Title

Two-Dimensional Boron Nitride and Related Materials: Synthesis, Vacancy Formation, and Applications for Nanopores and Nanomachines

Permalink

https://escholarship.org/uc/item/9xv5064w

Author

Gilbert, Stephen Matthew

Publication Date

2019

Peer reviewed|Thesis/dissertation

Two-Dimensional Boron Nitride and Related Materials:
Synthesis, Vacancy Formation, and Applications for Nanopores and Nanomachines

by

Stephen Matthew Gilbert

A dissertation submitted in partial satisfaction of the

requirements for the degree of

Doctor of Philosophy

in

Physics

and the Designated Emphasis

in

Nanoscale Science and Engineering

in the

Graduate Division

of the

University of California, Berkeley

Committee in charge:

Professor Alex Zettl, Chair
Professor Feng Wang
Professor Luke P. Lee

Fall 2019

Abstract

Two-Dimensional Boron Nitride and Related Materials:
Synthesis, Vacancy Formation, and Applications for Nanopores and Nanomachines

by

Stephen Matthew Gilbert

Doctor of Philosophy in Physics

Designated Emphasis in Nanoscale Science and Engineering

University of California, Berkeley

Professor Alex Zettl, Chair

Without changing a material's chemical composition, lattice geometry, or orbital structure, the physical properties of a material can be drastically modified by changes to its dimensionality. Two-dimensional materials are therefore an ideal platform for exploring the role of reduction in material geometry because they can be stacked to form three-dimensional structures or etched to form one- and zero-dimensional features.

In this dissertation, I explore the methods for isolating two-dimensional hexagonal boron nitride (h-BN) and related materials, for controlling their three-dimensional structural properties synthetically, and for using irradiation to locally reduce their dimensionalities through vacancy formation. After discussing these techniques and their underlying physics, I investigate the applications of etched two-dimensional materials for nanopore sequencing and nanomachines.

In Chapter 2, I outline the techniques for isolation of two-dimensional materials by both exfoliation from bulk crystals and by synthetic deposition. I delve into the mechanics of chemical vapor deposition synthesis of h-BN graphene and establish methods for controlling their three-dimensional stacking.

In Chapter 3, I investigate the effects of electron irradiation on h-BN. I show that accelerated electrons induce specific vacancy geometries in h-BN depending on its stacking sequence and develop a method for creating atomically precise nanopores. I explore the application of these nanopores for DNA sequencing.

In Chapter 4, I similarly characterize the effects helium ion irradiation on two-dimensional materials. I explore the damaging effects on the lattice of h-BN and MoS_2 while assessing the controlled use of these helium ions to etch one- and zero-dimensional nanostructures.

In Chapter 5, I study the use of patterned graphene for softened mechanical actuators. I show that micron scale graphene can be used as an acoustic transducer and demonstrate a novel electron beam driven rotational actuator.

1

To Mom, Dad, Ryan, and Claire,

and

To everyone who wants to know everything I learned
without working nearly as hard as I did to learn it,

Table of Contents

List of Figures

Acknowledgements

The opportunity to pursue my Ph.D. in the Physics Department at UC Berkeley has been an amazing experience, and I owe a debt of gratitude to a number of people who have enriched my time as a graduate student.

I would first like to acknowledge my research advisor, Professor Alex Zettl, for serving as my mentor for the past several years, for providing scientific guidance, and for giving me access to the vast resources in his group. Without his balance of support and allowing me to forge my own path, my time in graduate school would have been far less rewarding and productive. I will always appreciate the lessons I have learned about science, leadership, and discovery.

The work in this thesis has also been shaped dramatically by my labmates in the Zettl Group who both aided me scientifically and made my time working a joy. I owe a tremendous gratitude to Thang Pham, Ashley Gibb, and Gabe Dunn for serving as my mentors and friends; despite how much you all had to do, I always felt like I could ask for help with anything, scientific or otherwise. Thank you all for teaching me so much.

I would also like to thank the rest of graduate students who have worked in the lab with me: Brian Shevitski for always sparing huge amounts of time for ambitious scientific discussions, helping with TEM, and inspirational words; Sally Turner for sparing huge amounts of time for discussions about cats, qualifying exams, coffee, and surviving graduate school; Scott Meyer and Derek Popple for bringing an intense positive outlook to the lab and for generosity with their time; Aidin Fathalizadeh for teaching me the best part of a Ph.D. very well may be the hours and the pay; Michael Rousseas and (though not a graduate student at the time) Willie Mickelson for teaching me to carefully consider my portfolio of work in the lab and introducing me to all of the tools in the Zettl Group; Onur Ergen for encouraging me to explore out of the box ideas about the applications of low-dimensional materials; Seita Onishi for setting the pace in the lab with his work ethic; and Donez Horton Bailey for collaborating with me on difficult projects.

I am also deeply grateful for the undergraduate who have worked with me over the years. Thank you to Gabe Schumm, Alex Ungar, Adam Molnar, Yasmeen Mustafa, Jonathan Jackson, Rachael Klaiss, Stanley Liu, Edgar Dimitrov, Dilveen Goraya, Jacob Norman, Lakshika Ruwanpiranthana, Matthew Sorensen, Raymond Truong, Andy Zhang, and Owen Chen. Much of the work in this thesis is shared with them; I hope it is a testament to their work as much as mine. I appreciate all of their hard work; it often felt that with them on my team that I was able to do >200 hours of work each week.

Thank you to the postdocs in the lab for working tirelessly and still finding time to collaborate and mentor me. Thank you to Vivek Adiga, Kyunghoon Lee, and Jongmin Yuk for serving as mentors to me and teaching me experimental techniques. Thank you to Amin Azizi for collaborating with me, helping with TEM, and for personal discussions. Thank you to Wu Shi and Aiming Yan for being great officemates and friends. Thank you to Hamid, Jiyoung, Qin, Hu, Jeff, Haider, Claudia, and Oscar for all of your advice and friendship.

I would like to acknowledge the department staff who kept everything running seamlessly throughout the years so that I had the luxury to focus on my studies. Thank you to Jon Deasy, Laura King, and Gee Gee Lang for taking care of all of the administrative tasks that were probably my responsibility, making sure I got paid and my orders got placed, and for doing this

all with incredible positivity. Thank you to Anne Takizawa for making sure I got my admissions letter after the original email bounced, for helping with PGSA, and for helping with all of the little trials of graduate school.

I would like to thank my classmates for teaching me about the breadth of physics, giving me new ideas for my work, proofreading all of my various applications and coming to my practice talks, helping with problem sets, making graduate school a joy, and going camping, watching football, doing yoga, and hanging out with me. Special thanks to Crystal Noel, Vinay Ramasesh, Halleh Balch, Stephanie Mack, Justin Gerber, Alejandro Ruiz, Nityan Nair, Chris Benson, Steve Drapcho, Neil Goeckner-Wald, Erik Urban, Kyle Boone, Brendan Folie, Chris Olund, Sam Kohn, Mike Yen, and Clio Sleator.

Most importantly, I would like to thank my family for supporting me through this process. Thank you to my parents and brother for always encouraging me to pursue my out of the ordinary interests, letting me cycle through various hobbies and pursuits, encouraging me through all of the math and science over the year, taking pride in my recent work even when I couldn't explain what it was I was doing, and for everything you have done for me. I hope this work means as much to you as it does to me. Thank you to my grandfather for always reminding me how much he brags about my accomplishments and for always asking me the right questions. Thank you to Claire for her patience, advice, and encouragement through this whole process; doing a Ph.D. is a lot of work, and I am grateful for all of the work you have done by my side to make mine possible.

Lastly, I would like to acknowledge my collaborators. Science is a collaborative effort, and much of the work in this thesis belongs to you all as much or more than it belongs to me. I have carefully denoted in the text where I have worked with others, and I hope that I have fully given credit where credit is due. Thank you to Thang Pham, Ashley Gibb, Gabe Dunn, Brian Shevitski, Mehmet Dogan, Nishita Deka, Amin Azizi, Kyunghoon Lee, Zhenglu Li, Adam Molnar, Donez Horton Bailey, Peter Ercius, Steven Louie, Marvin L. Cohen, and Alex Zettl for allowing me to include work we did together in this thesis.

Chapter 1

Introduction

1.1 Introduction to Two-Dimensional Materials and to This Thesis

Without changing a material's chemical composition, its lattice shape and spacing, or even its molecular orbital structure, the physical properties of the material can be drastically modified by changes to its dimensionality. Classic pedagogical examples illustrate this effect such as the difference in phase between the one-dimensional and two-dimensional Ising model or difference in energetic properties between a free electron, a 'particle in a box', and a 'particle in a ring'. By confining the number of spatial dimensions in these examples through hard boundaries, periodic boundary conditions, or simply removing a dimension, new phase transitions and energy gaps arise.

While there is not yet a straightforward path to experimentally increase the number of spatial dimensions of a substance beyond three, lower dimensional systems are routinely realized. Low-dimensional materials – defined as materials that have at least one physical dimension near the atomic scale – have been the subject of intense research interest for decades. [1] This class includes zero-dimensional, one dimensional, and two-dimensional materials. These low-dimensional materials can vary tremendously from their three-dimensional counterparts: effects like quantum confinement can induce or increase their bandgaps, high surface-to-area ratios allow for enhanced doping and field penetration schemes, and new electronic phases and other emergent behaviors can arise. [2–6]

A prototypical example of a system that can be used to realize zero-, one-, two-, and three-dimensional geometries is sp^2-bonded carbon. The three-dimensional phase of sp^2-bonded carbon is graphite, a commonly-used naturally-occurring mineral that is well known for its use in pencils and as a dry lubricant. Three-dimensional graphite is what is known as a layered material because it is comprised of atomically-thin layers with weak interlayer adhesion that stack to form a bulk crystal. [5,7] A single layer of graphite is known as graphene, the monolayer two-dimensional phase of sp^2-bonded carbon. Unlike graphite, graphene demonstrates strong adhesive properties in ambient conditions and electrically is a Dirac zero-gap semiconductor in which the electrons possess a linear energy-momentum dispersion relation (similar to photons).

There are two one-dimensional forms of sp^2-bonded carbon, carbon nanotubes (CNTs) and graphene nanoribbons (GNRs). CNTs are effectively a rolled-up sheet of graphene with a diameter near the atomic scale (i.e. approximately 1 – 10 nm) while GNRs are narrow strips of graphene with widths near the atomic scale. Unlike graphite and graphene, CNTs and GNRs can be semiconducting or metallic depending on their width and chirality or edge termination. Unlike graphite, graphene, and CNTs, GNRs are not strictly a sp^2-bonded carbon due to their edges. The

zero-dimensional geometry of sp^2-bonded carbon is the fullerenes. These molecules are ball shaped meshes of generally 20 to 90 atoms. The emergence of the sp^2-bonded carbon family of low-dimensional materials began with the discovery of the zero-dimensional C_{60} (known as buckminsterfullerene due to its geodesic dome structure) by Curl, Kroto, and Smalley in 1985 [8] and continued with the first synthesis and correct identification of carbon nanotubes by Iijima in 1991. [9]

While three-dimensional layered materials such as graphite have been used for millennia, until 2004 it was unclear if it would ever be possible for a single two-dimensional sheet to exist on its own due to the Mermin-Wagner theorem. [5,10,11] This rule suggested that long-range ordering in two-dimensions would be impossible, and this would prevent the stability of monolayers of two-dimensional materials. However, upon the first isolation and identification of graphene (a monolayer of graphite) by Novoselov and Geim and later upon the first preparation of suspended graphene samples, it became clear that two-dimensional crystals could be stable in the monolayer limit and that there would be a much larger family of them than just graphene. [5,12,13]

Since the first isolation of single layer graphene, dozens of other two-dimensional materials and vast literature to support them have emerged. However, beyond just their intrinsic properties, the ability of two-dimensional materials to span different dimensionalities has become an active research area. By patterning monolayers in plane, one dimensional features like nanoribbons or zero-dimensional features like antidots or artificial atoms can be generated.[14,15] Because these sheets are only one atom thick to begin with, this is a shortcut to creating lower dimensional structures. Moreover, because these features can be embedded in a larger two-dimensional sheet, systems hybrid low-dimensionalities can be explored such as nanomeshes (two-dimensional sheets of one-dimensional ribbons), [16] antidot arrays (two dimensional sheets of zero-dimensional wells), [17] or van der Waals heterostructures (three-dimensional stacks of two-dimensional sheets). [18,19]

In this thesis, I focus on synthetically controlling the properties of two-dimensional materials and understanding how electron and ion irradiation can be used to induce nearly atomically-precise zero- and one- dimensional features. I also further explore the implementation of these patterned materials for nanopore and nanomechanical applications

In the rest of this chapter, I introduce the three materials studied in thesis, graphene, hexagonal boron nitride *(h-*BN), and MoS_2, and the electron microscopy techniques I use to characterize them. In Chapter 2, I describe my work to control the properties of *h*-BN and graphene synthetically and provide a detailed account of how I prepare samples of these materials. Specifically, I focus on tuning the interlayer geometry of these materials in order to create an alternative stacking sequence for *h*-BN and to later understand how this impacts vacancy formation. In Chapter 3, I explore the effect of electron irradiation under conditions on *h*-BN and study how it is impacted by the stacking of the material. I also develop a method for near atomically-precise fabrication of nanopores and outline our work to implement them for DNA sequencing. In Chapter 4, I explore the how helium ion irradiation impacts and can be used pattern two-dimensional materials and their heterostructures. Finally, in Chapter 5, I demonstrate two new geometry for two-dimensional material transducers.

1.2 Introduction to Graphene, *h*-BN, and MoS$_2$
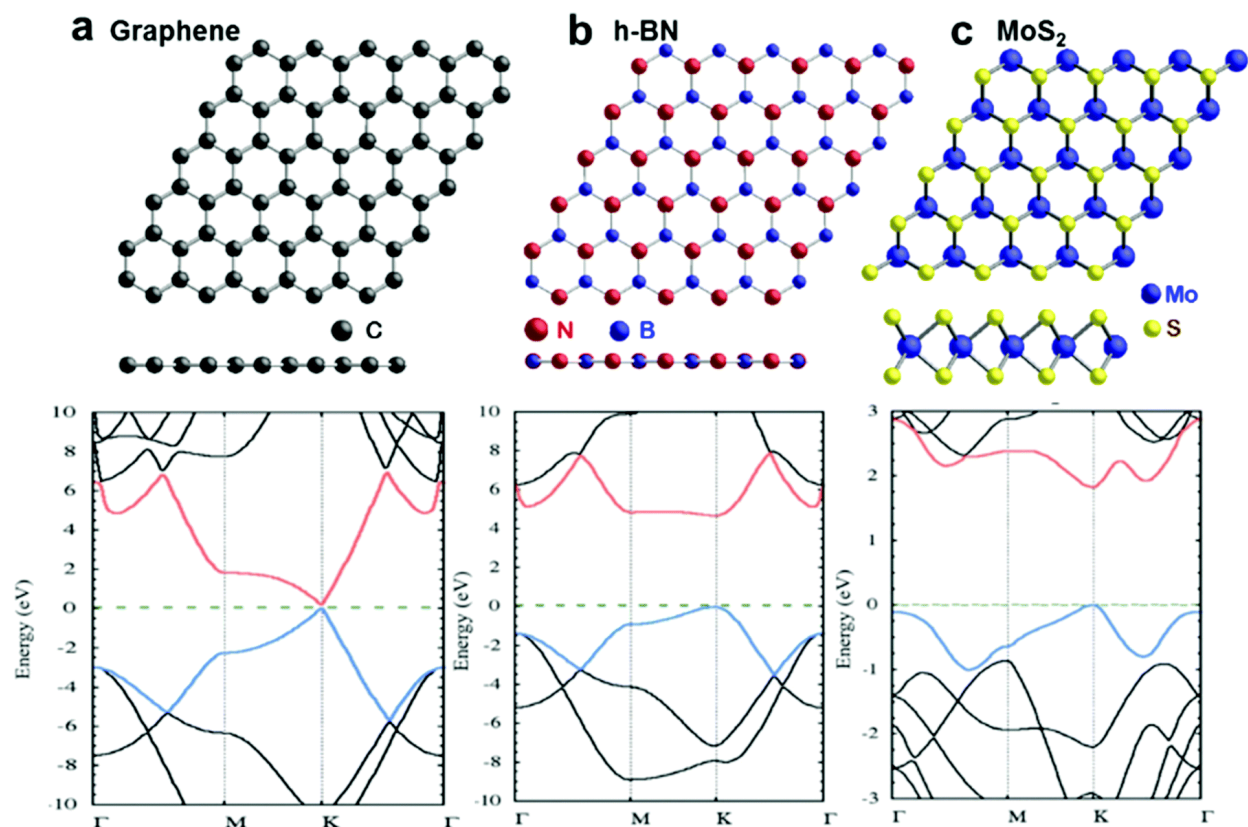
Figure 1.1 Graphene, *h*-BN, MoS$_2$ – Atomic schematics and band structures. (a)-(c) The atomic structures of graphene (a), *h*-BN (b), and MoS$_2$ (c). (d)-(e) The band structures for the Dirac zero-gap semiconductor graphene (d), insulating *h*-BN (e), and semiconducting MoS$_2$ (f). Figure is reprinted from Solís-Fernández et al in Reference [20].

In using two-dimensional materials as a shortcut for the creation of lower dimensional structures, the properties of the various of materials studied dictates the ingredients that can be used. As of 2017, there had been two-dimensional materials isolated as monolayers comprised of more than 23 different elements. These sheets range wildly in their chemical, electrical, and mechanical properties.[21,22] However, as much of modern device physics is based only on the availability of conductors, insulators, and semiconductors, in this thesis I will focus on one of each: graphene, *h*-BN, and MoS$_2$. These species represent the three most studied two-dimensional materials; all three are air stable and can be isolated in monolayer form using standard laboratory equipment.

Graphene (shown in Figure 1.1(a)), which was introduced in the previous section, is a single layer of sp^2-bonded carbon in a hexagonal honeycomb configuration. Monolayers of graphene were first isolated in 2004 by mechanical exfoliation (explained in Section 2.1) of bulk graphite.[5] As previously discussed, these monolayers were demonstrated to be Dirac zero-gap semiconductors in which the band structure is comprised of two linear 'V-shaped' bands that meet with no energy gap as shown in Figure 1.1(a). [5,7,20] The Fermi level for intrinsic graphene lies at the Dirac point where the two bands meet. Because of its linear dispersion, the charge

3

carriers in graphene possess a variety of peculiar effects for impurity scattering of charges, but these are outside of the scope of this thesis. [23] Intrinsic graphene possesses a high-carrier mobility of 200,000 cm^2 V^{-1} s^{-1} [24] and gating can be used to tune the number density and type of carriers.

Graphene is also notable for its mechanical and chemical properties. Graphene is the strongest material ever characterized with a Young's modulus of 1 TPa, comparable to only carbon nanotubes, diamond, and h-BN. [25] Like bulk graphite, graphene is stable in ambient conditions; however, because of its high surface area and exposed edges, graphene can be readily functionalized and chemically modified. [26]

Hexagonal boron nitride (h-BN), sometimes industrially and colloquially known as white graphite, is an sp^2-bonded structural analog to graphite. [18] Monolayer h-BN, first isolated in 2008 by mechanical exfoliation, [27] is structurally similar to graphene but replaces a two-carbon atom unit cell by alternating boron and nitrogen atoms as shown in Figure 1.1(b). Due to the asymmetry of the boron-nitrogen unit cell, an ionic-covalent bond forms and induces a 4-6 eV bandgap as shown in Figure 1.1(b). [28–30] Because of this wide bandgap and the relatively low defect densities of h-BN crystal syntheses, h-BN is a popular dielectric substrate and encapsulation layer for other two-dimensional materials. [31,32] In this way, h-BN increases the mobility/potential homogeneity of other two-dimensional materials and provides chemical stability to air sensitive materials.

Of the two-dimensional materials, h-BN is possibly the most chemically inert. h-BN is stable in air up to at least 1100 ºC and in vacuum up to at least 1800 ºC. [33] Because it is so inert, it has proven difficult to induce chemical functionalization to h-BN; [34] however, because it is so stable, cleaning techniques such as high temperature annealing and UV/ozone can be used on h-BN. [35,36]

Unlike graphene and h-BN, MoS$_2$ does not have an sp^2-bonded honeycomb structure. As shown in Figure 1.1(c), each molybdenum is bonded to six sulfur atoms, requiring d-orbital hybridization. MoS$_2$ in both its monolayer and bulk form is a semiconductor with a bandgap of 1.8 eV as shown in Figure 1.1(c). As MoS$_2$ is thinned from multilayer to monolayer, this bandgap changes from indirect to direct, leading to enhancement in the photoluminescence of MoS$_2$ monolayers. [37] MoS$_2$ has been demonstrated as an excellent transistor material with on/off ratios of 10^8, [38] and gate lengths as small as 1 nm. [39]

MoS$_2$ is a member of the larger transition metal dichalcogenides (TMD) family in which a single transition metal bonds to two Group VI elements to form the unit cell of a layered material. [40] This class includes charge density wave materials such as TaS$_2$, superconductors like NbSe$_2$, and topological insulators such as WSe$_2$. However, in this thesis, I will only consider MoS$_2$.

Samples of Graphene, h-BN, and MoS$_2$ are obtained through either mechanical exfoliation of bulk crystals or by chemical vapor deposition. These processes are described in detail in Chapter 2.

1.3 Introduction to Electron Microscopy

While optical characterization techniques such as Raman spectroscopy and photoluminescence or electrical characterization techniques such as low-temperature transport are popular for studying the bulk properties of two-dimensional materials, higher spatial resolution is needed for studying the local nanoscopic geometry. In this thesis, I primarily rely on electron microscopy to characterize our two-dimensional materials. I primarily refer to two distinct types of electron microscopy: scanning electron microscopy (SEM) and transmission electron microscopy (TEM).

In SEM, a condensed electron beam with energy generally ranging from 1-30 kV is scanned across a sample. As the accelerated electrons collide with the sample, secondary scattered electrons (SE) and backscattered electrons (BSE) are generated and measured by electron detectors above the sample. Scattered electrons are counted at each pixel along the beam path, and the number of electrons at each point defines the grayscale contrast for the SEM image.

When a conducting material is scanned, electrons are absorbed and dissipated through the sample and into the stage. This produces a small number of scattered electrons and thus a dark contrast. When an insulating material is scanned, charge cannot be dissipated into the stage. and electrons therefore accumulate in the insulator. This produces a large number of scattered electrons and thus a bright contrast. This is illustrated by the SEM image of a multilayer flake of insulating h-BN on conducting iron foil shown in Figure 1.2(a).

The resolution in SEM is limited by the nominal probe size and aberrations of the electron beam. In practice, the minimum feature size that can be resolved ranges from 10-100 nm. Because SEM relies on secondary scattered and backscattered electrons measured above the sample, the measurement is highly surface sensitive, depending on the electron penetration depth in the material.

In TEM, an accelerated electron beam that generally ranges from $60 - 300$ kV in energy is transmitted through an electron transparent sample to generate image. TEM techniques can be used to image materials with $0.1 - 5$ nm resolution, perform electron diffraction, and study the atomic composition and material band structure spectroscopically. Depending on which specific instrument is used and in what mode it is operated, different underlying mechanisms are used for TEM imaging.

The first mode (and the one which is generally referred to with the simple TEM acronym) is bright-field TEM. In this mode, a diffuse, collimated electron beam illuminates a sample and the unscattered electrons produce an image directly on a camera or phosphorescent screen. Bright-field TEM creates a projection based image in the same way an overhead projector produces a display on a wall; spatial variations in the electron transparency of the sample (due to thickness, atomic mass, or density among other factors) results in a spatial variation in the number of unscattered electrons in the image plane.

The number of electrons in each position along the screen or CCD camera detector defines the grayscale contrast of a bright-field TEM image. Therefore, a less electron transparent (thicker, higher-Z, higher density, etc.) region will produce darker contrast while a more electron transparent region produces brighter contrast. For homogeneous two-dimensional materials, brighter contrast generally corresponds to thinner areas of the material. Figure 1.2(b) shows a

representative bright-field TEM image of a terraced h-BN. As the thickness decreases from approximately ten layers (along the edges) to vacuum (inside of the small triangle), the contrast decreases.

While it is not strictly a separate mode of TEM, the way in which high-resolution TEM (HR-TEM) produces contrast varies from bright-field TEM. As the resolution for a given TEM approaches or exceeds the atomic size and spacing, individual atoms and the space between them can be resolved. HR-TEM images are produced by combining both the scattered and unscattered electrons to form a phase-contrast image. For this type of imaging, the wavelike nature of the electron produces real-space interference patterns which lead to spatial variation in collected electrons. Because of this, the contrast of a given feature depends heavily on the focus of the microscope. However, as one example, an individual atom and the open space around it behave analogously to the classic double slit experiment in the proper focus; this thereby produces a local maximum electron transmission below the center of the atom and gives the atom its bright contrast. This is shown in Figure 1.2(c)

TEM can also be used to perform electron diffraction and collect reciprocal space information about a crystal. By rearranging the objective and intermediate lenses, the diffraction plane can be focused onto the camera or phosphorescent screen of a TEM. An aperture is placed in the first image plane (above the diffraction plane) to select a small area of the sample for diffraction, giving this technique the name of selected area electron diffraction (SAED). The position, intensity, and shape of a diffraction pattern can be used to understand the configuration of a crystal in the TEM. Figure 1.2(d) shows a representative SAED pattern of h-BN; the hexagonal structure of the peaks arises because the Fourier transform of h-BN's trigonal lattice is a hexagon. Techniques such as dark-field TEM (DF-TEM) and high-angle annular dark-field scanning TEM (HAADF-STEM) are used to collect the diffracted electrons to produce images. These techniques are described in more detail in Sections 3.2.4, 3.2.5, and 4.2.
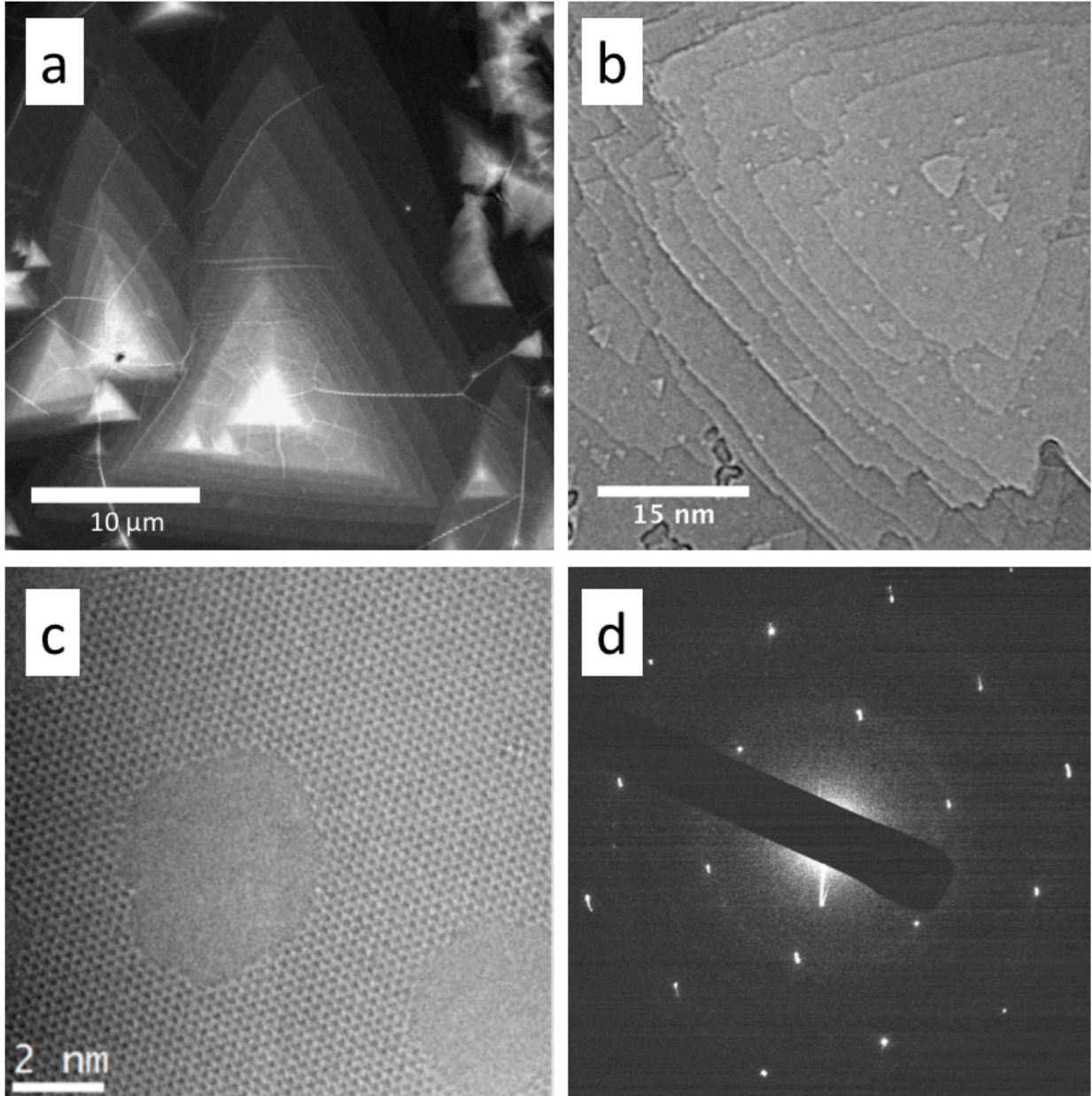
Figure 1.2 Electron microscopy examples. (a) An SEM image of triangular multilayer *h*-BN flakes on iron foil. (b) A TEM image of a terraced *h*-BN region. The brightest contrasted triangle is vacuum while the darkest contrast is approximately 10 layers. (c) An HR-TEM image of a holey single layer of graphene. (d) An SAED pattern from a region of *h*-BN. The peaks are arranged in a hexagonal structure because the Fourier transform of *h*-BN's trigonal lattice is a hexagon. (a) & (d) are reprinted from our previously published work in References [41] & [42] respectively. (b), (d) are unpublished experimental data.

Chapter 2

Bulk crystal exfoliation, CVD synthesis, and sample preparation of two-dimensional boron nitride and related materials

The methods used for sample preparation or synthesis of a material can vastly affect its properties without disturbing its overall composition. Factors such as domain size and stacking, defect density, built-in stress, and cleanliness can have major impacts on a material. In order to better understand and control the properties of the two-dimensional materials, in this chapter, I explore how single to few-layer graphene, h-BN, and MoS_2 are prepared and transferred to arbitrary substrates. In particular, I take I deep dive to explore how the stacking sequence of h-BN can be controlled during its growth, and I further draw a strong comparison between the growth mechanisms for h-BN and graphene.

First, I start by introducing how high-quality, thin flakes can be isolated from bulk crystals by mechanical exfoliation. Next, I explain how these materials are synthesized at large scales by chemical vapor deposition (CVD) on transition metal foils; I focus on how my work towards understanding how the growth mechanics of these processes can allow for the tuning of both the thickness and interlayer stacking of these layered materials. Based on this understanding, I present an original method for the synthesis of the previously unobserved Bernal stacking of h-BN.

Finally, I present several methods used for the transfer of graphene and h-BN. I primarily focus on three methods 1.) a polymer assisted wet transfer, 2.) a polymer free wet direct transfer, and 3.) a dry aligned transfer. I show how each of these methods perform in the fabrication of TEM samples and demonstrate how our dry transfer methods allow us to create large scale arrays of vacuum sealed cavities.

2.1 Bulk Crystal Exfoliation of Two-Dimensional Materials

Due to their weak interlayer bonds, one popular method for obtaining single and few layers of graphene, h-BN, and other two-dimensional materials is to cleave them from bulk single-crystals of the layered material.[12] This process, known as mechanical exfoliation, was the first technique used to isolate single-layer graphene,[5] h-BN,[27] and the several of the TMDs.[12,37,38,43]

Because high-quality bulk crystals of these materials are either naturally abundant (in the case of graphene and MoS_2)[5,12,38,43] or can be readily synthesized[32,40,44–46] (in the case of h-BN and several other TMDs), mechanical exfoliation generally yields the highest quality single crystal flakes of two-dimensional materials as identified by high-carrier mobility in graphene,[24,32] and narrow optical linewidths in the TMDs and h-BN.[44,46]
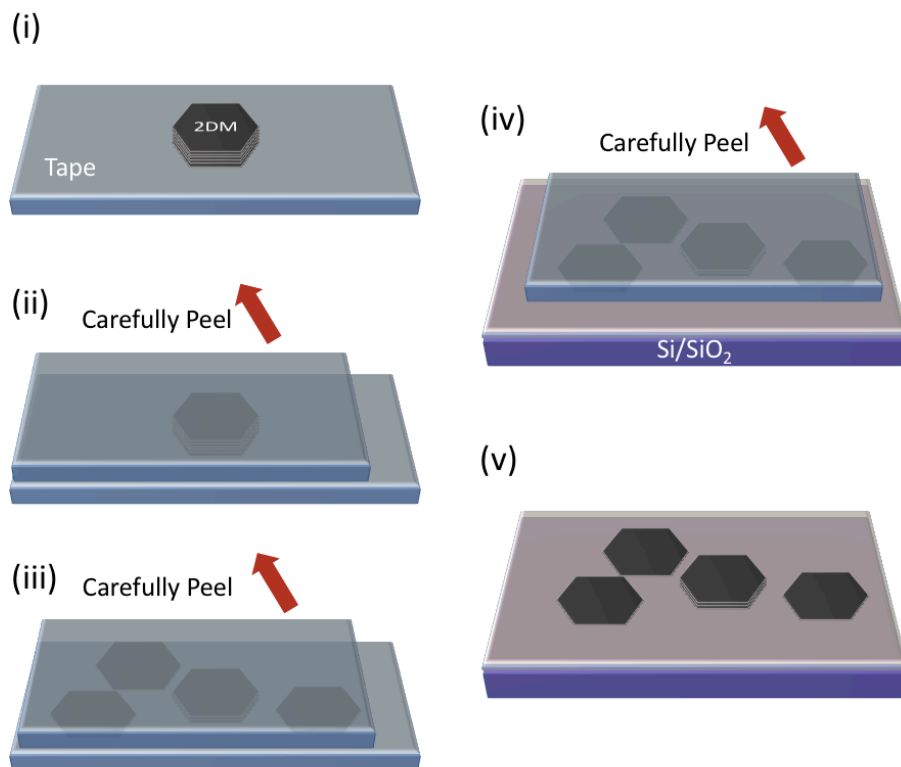
Figure 2.1 The process flow of mechanical of exfoliation of two-dimensional materials. (a) Single crystals are adhered to a piece of tape. (b) The tape is folded and peeled several times. (c) Several thin flakes are observed on the tape. (d) The tape is carefully adhered to a target substrate. (e) The tape is slowly peeled leaving behind thin flakes.

The process flow for mechanical exfoliation is shown in **Figure 2.1**. First, a bulk crystal of a two-dimensional material is fixed on an adhesive surface such that the basal plane is parallel to the surface. Usually, the adhesive is either scotch tape or blue wafer tape, but others such as PDMS can be used.

Next, a second piece of the adhesive (or a folded section of the first) is stuck to and carefully peeled from the first. This results in an interlayer cleavage of the two-dimensional material and thereby yields thinner crystals on both pieces. This peeling is continued until a high-coverage of thin flakes are obtained; this judgement is highly subjective and still seems to rely heavily on individual preference and experience. An important factor to consider in this step is the ratio between the interlayer adhesion and in-plane strength. Repeated peeling is necessary in order to obtain thin flakes of layered materials; however, if the crystal is too fragile in plane, the flakes will break laterally, and the exfoliated crystals will be too small.

After thin crystals are obtained, they can be transferred to a substrate directly using the adhesive. The adhesive is carefully applied to the substrate (while avoiding trapped air bubbles) and slowly peeled off. Traditionally in this step, flakes are either transferred to SiO_2 on Si or PDMS. To enhance the transfer, the substrate surface can be treated; for example, SiO_2 on Si surfaces can be exposed to oxygen plasma, increasing the adhesion to graphene flakes. However, plasma treating can make it difficult to remove the exfoliated flake later on using the methods outlined in Section 2.3.3.
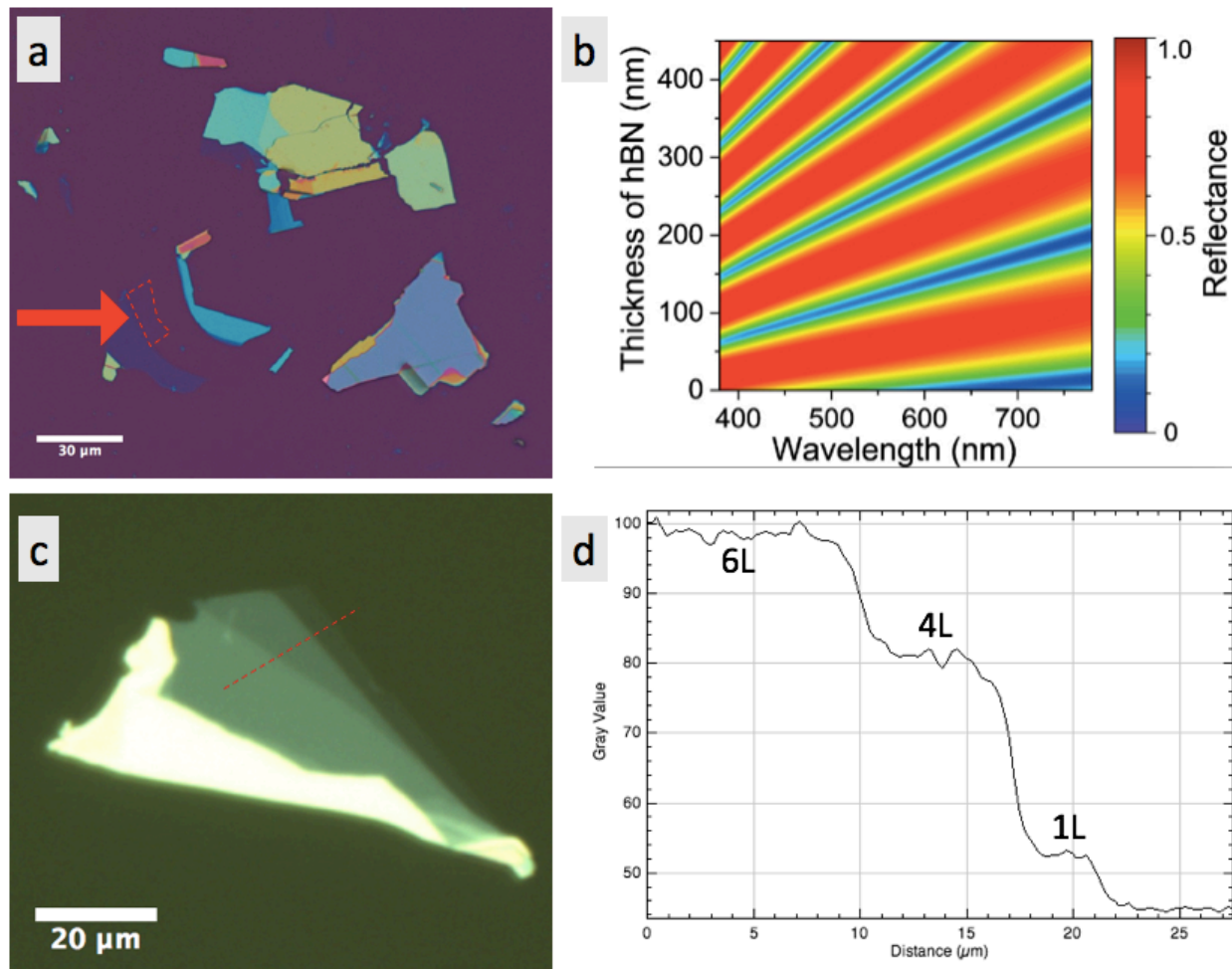
Figure 2.2 Optical identification of flake thickness. (a) An optical image of exfoliated *h*-BN flakes on 285 nm SiO$_2$ on Si. The region indicated by the arrow is a monolayer and can be distinguished by its color and contrast. (b) A reflectance versus film thickness and wavelength plot on 285 nm SiO$_2$ on Si. This can be used to determine the color of a flake based on *h*-BN thickness. (c) An optical image of an exfoliated MoS$_2$ flake on PDMS as it tapers from multilayer to monolayer. The thickness can be deduced by the grayscale reflectivity under white light. (d) The reflectivity profiled of the MoS$_2$ flake in (c), labelled with layer numbers. (a), (c), and (d) are from my unpublished work. (b) is reprinted from Anzai et al in Reference [47]

The size and thickness of exfoliated flakes can be identified optically. [47–50] Figure 2.2 shows representative exfoliated *h*-BN flakes on Si/SiO$_2$ (a) and MoS$_2$ flakes on PDMS (c). The thickness of the *h*-BN can be identified by color contrast; due to thin film interference, different thicknesses of *h*-BN result in different colors. [49] Figure 2.2(b) shows a plot of reflectivity versus thickness for *h*-BN. [47] For monolayer samples, it shows only blue light is reflected with white light irradiation. As the sample becomes thicker, higher wavelengths are reflected resulting in teal, green, yellow, orange, then red flakes in order. Therefore, the monolayer region in Figure 2.2(a) (denoted by the arrow) can be identified by its faint blue color.

By contrast, the thickness of the thin MoS$_2$ flake exfoliated on PDMS shown in **Figure 2.2**(c) can be identified by its gray scale contrast. From bottom left to top right, the intensity of the reflected light decreases as the MoS$_2$ becomes thinner. In the few layer limit, the contrast falls

off linearly with layer number. In **Figure 2.2**(d), the single layer contrast is approximately 10 counts; therefore, the thinnest region is monolayer, the next thinnest region is 4-layer, and the next region is 6-layers.

2.2 Synthesis of *h*-BN by Chemical Vapor Deposition (CVD)

Due to the relatively small size (tens to hundreds of microns laterally) of flakes of *h*-BN, graphene, and other two-dimensional materials generally produced by exfoliation, it is not yet practical to use this technique at scale. Therefore, despite the high quality of materials produced by exfoliation, it is worthwhile to consider other synthetic methods that lend themselves to more readily to producing high-coverage of thin flakes and films.

Chemical vapor deposition (CVD) is a process in which a catalytic target substrate is exposed to a gaseous precursor, causing the precursor to react with or decompose onto the substrate surface, thereby producing the desired film. These processes can range across a variety of temperatures, pressures, and precursor volatilities.

CVD has been demonstrated to quickly produce full coverage of single to few layer films and flakes of two-dimensional materials over large areas on a variety of substrates. Since the initial demonstration of CVD synthesis of monolayer graphene by the Li et al in 2009, [51] monolayers of *h*-BN, [52,53] and MoS$_2$ and a total of 47 TMDs (including alloys), [54–56] to name a few, have all been produced by CVD.

In addition to producing a large number of materials, CVD synthesis also delivers on producing material properties out of the range of bulk crystal growth. Full coverage monolayer graphene has been grown at the meter scale, [57,58] single crystals of graphene and *h*-BN have been prepared at the wafer scale, [59] and centimeter sized flakes of these materials have been synthesized. [60] Covalently and non-covalently bound in-plane heterostructures of various two-dimensional materials have been prepared and pristinely stacked vertical heterostructures have been achieved. [61–65] While the quality of CVD material is not yet consistently equal to bulk crystal growths (in terms of defect density, mobility, and optical properties), CVD two dimensional materials can be prepared with high quality and properties unattainable in exfoliated flakes.

In this chapter, I consider the low-pressure CVD (LP-CVD) syntheses of *h*-BN and graphene. In these processes, relatively non-volatile precursor molecules (BH$_3$NH$_3$ and CH$_3$ for *h*-BN and graphene respectively) are catalytically decomposed on a transition metal surface at high temperature (>1000 °C). [51,52] As the precursor molecules decompose, they react with one another on the surface forming flakes or films of the desired two-dimensional material.
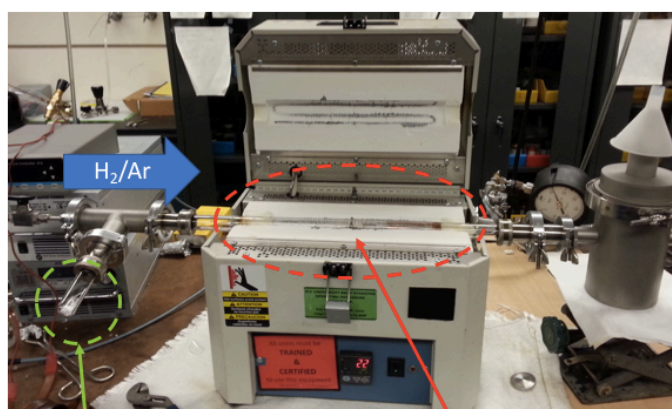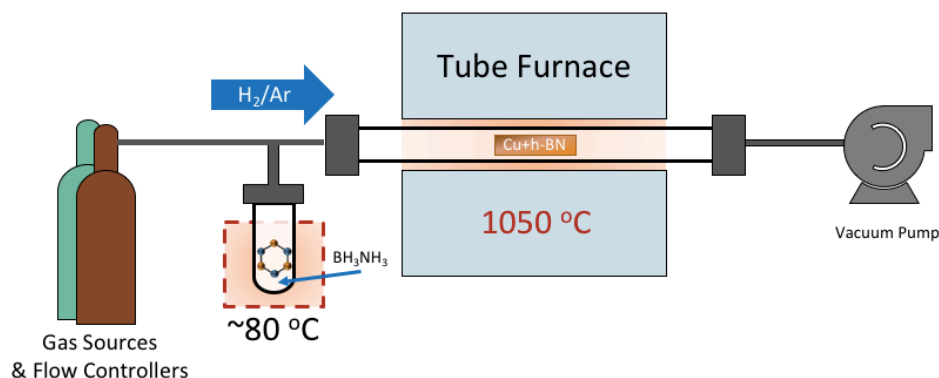
Figure 2.3 A schematic (top) and photo (bottom) of an *h*-BN CVD furnace. From left to right, the schematic and picture show 1.) hydrogen and argon sources (tuned by a mass flow controller) feed the carrier gases toward the reaction area, 2.) solid ammonia-borane (BH_3NH_3) is thermally degraded and its gaseous byproducts are pushed by the carrier gas, 3.) a transition metal foil is heated in a quartz tube as *h*-BN grows on its surface, and 4.) the gases are removed using a mechanical roughing pump (which is chemically isolated using a liquid nitrogen cold trap as seen in the photo). Figure based on our previously published work in Reference [41].

    Figure 2.3 shows a schematic (top) and picture (bottom) of one of the LP-CVD furnace systems used in this work. Both are shown as configured for *h*-BN synthesis, but graphene growth can be substituted by adding methane gas and removing the solid ammonia borane (BH_3NH_3) precursor. In this particular *h*-BN CVD process, a copper foil is heated under low-pressure mixed argon/hydrogen gas flow. In this first step, the sample is annealed (>1000 °C for 0.5 – 12 hours) to reduce oxygen defects, burn off hydrocarbons, smooth the foil surface, and increase the domain size of the polycrystalline foil. After annealing, precursor molecules are introduced. In the case of *h*-BN synthesis shown, ammonia borane precursor is heated and thermally decomposed at ~80 °C. Precursor molecules are then carried by the Ar/H_2 flow towards the copper catalyst. The precursor then further decomposes on the catalyst surface and reacts to form *h*-BN.

    After the growth, samples of *h*-BN and graphene are characterized by SEM, TEM, Raman spectroscopy, and atomic force microscopy (AFM). In this chapter, however, I will mainly consider only SEM and TEM imaging.
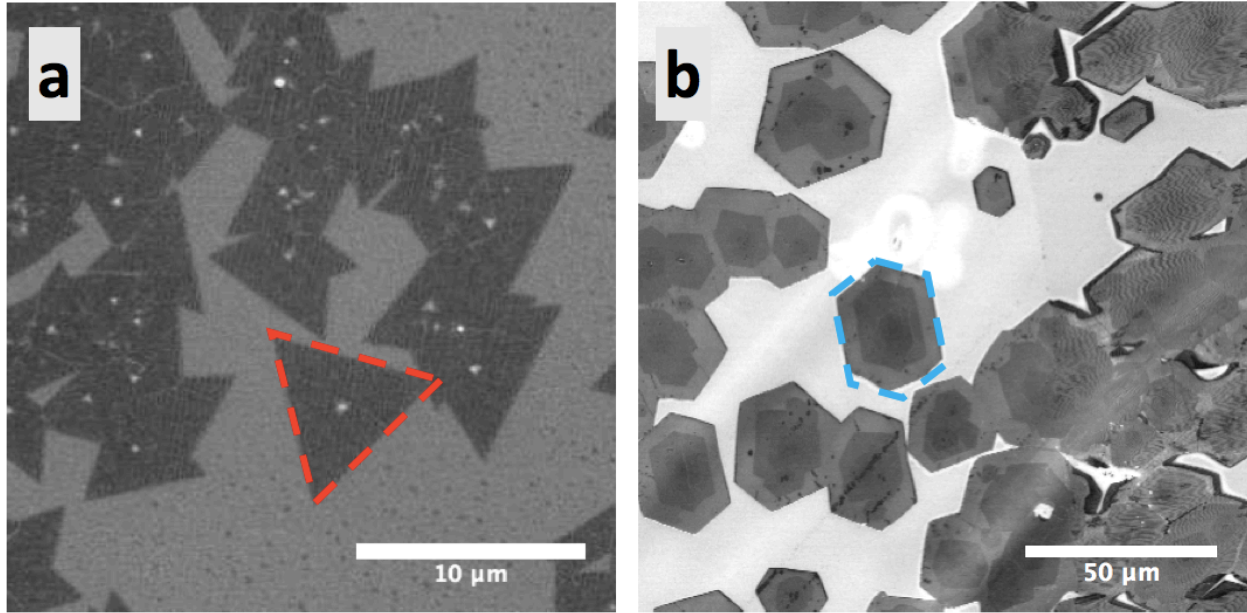
Figure 2.4 Characterization of CVD *h*-BN and graphene. (a)-(b) Representative SEM images of few layer CVD *h*-BN (a) and graphene (b). (a) In the *h*-BN sample, a dark triangle (highlighted by the red dashes) can be seen on a light background. The light background is a copper foil and the dark triangle is an *h*-BN monolayer. The concentric light triangle is an *h*-BN ad-layer (a spot where the *h*-BN is locally multilayer). The arrow points to a line along a region where multiple monolayers have merged. This line is a wrinkle in the *h*-BN and can be used to detect full coverage layers from SEM images. (b) In the graphene sample, a dark hexagon (highlighted by the blue dashes) is seen on a light background. The light background, again, is the copper foil, and the dark hexagon is a single layer graphene flake. The concentric dark hexagon within the larger hexagon is a multilayer region of graphene. (a) is reprinted from my previously published work in Reference [41]. (b) is original unpublished data.

Figure 2.4(a) and (b) show what *h*-BN and graphene look like through SEM imaging. As introduced in Section 1.3, SEM generates an image by scanning a focused electron beam across a sample and measuring the backscattered electrons from each point. Therefore, contrast from SEM is generated based on how readily electrons backscatter from a material. For example, highly electron charged materials (e.g. insulators under an electron beam) will appear bright while metals that can disperse charge will appear dark.

In **Figure 2.4**(a), the single layer flake of *h*-BN is identifiable based on its dark contrast versus the brighter surrounding copper, as is consistent with the literature,[52,66,67] despite its insulating nature. Conversely, the multilayer *h*-BN triangle (the concentric triangle at the center of the single layer flake) is identifiable by its bright contrast. This leads to the counterintuitive conclusion that monolayer *h*-BN on copper produces darker contrast and scatters fewer electrons than the copper itself which in turn produces darker contrast and scatters fewer electrons than multilayer *h*-BN.

I propose this contrast occurs because for monolayers of *h*-BN, the entire monolayer is in contact with (and potentially covalently bonded to) the copper substrate; therefore, when electrons are injected by the SEM, they are efficiently moved into the copper foil without charging the *h*-BN. The *h*-BN can simultaneously block backscattering from the copper surface. This lack of charging and backscattering allows the single layer *h*-BN to appear dark relative to

13

both the copper and multilayer *h*-BN. For the multilayer *h*-BN, only the bottom layer is in contact with the copper. Therefore, the insulating top layers of *h*-BN cannot disperse their charge and appear bright by SEM. The partial coverage *h*-BN flakes grow as triangles due to the three-fold rotation symmetry of the lattice.

In **Figure 2.4**(b), both the single layer and multilayer flakes of conducting graphene are identifiable based on their darker contrast. Graphene flakes grow as hexagons due to the six-fold symmetry of their lattice. However, the shape of the graphene crystals does not form as perfectly as the *h*-BN triangles due to the speed and stochastic nature of the growth.

2.2.1 Synthesis of *h*-BN Monolayers by CVD

This section is based on our previously published work in Reference [41].

Similar to what has been previously observed in CVD synthesis of graphene, we find that *h*-BN CVD on copper foil using ammonia borane as a precursor is limited to monolayers over a large range of growth times, temperatures, precursor flows, and pressures. In graphene, it is understood that this monolayer growth proceeds by the following steps [51,68,69]:

1. Precursor molecules (typically methane) are chemically decomposed on the surface of the copper foil catalyst
2. Carbon atoms dissolve into the metal until the solid solution is locally saturated.
3. Graphene domains begin to nucleate as additional molecules decompose or precipitate from the bulk
4. Individual graphene domains continue to grow and merge into a polycrystalline film
5. The monolayer film grows to fully cover the foil and growth terminates as the precursor no longer has access to the catalyst

In principle, multiple layers can grow; in fact, multilayered ad-layers frequently form at the nucleation site of the crystal, in both graphene and *h*-BN. [52,67,70] However, under normal growth conditions, the catalyst is fully covered by the monolayer film and the growth is fully arrested before a high coverage of multilayer flakes forms.

We observe similar mechanics for the CVD growth of *h*-BN to that of graphene as depicted schematically in **Figure 2.5** and shown in the SEM images in **Figure 2.6**. First, triangular domains of monolayer *h*-BN form about a nucleation site at the triangles centroid as shown schematically in **Figure 2.5**(a) and in the SEM image in **Figure 2.6**(a). These triangular crystals grow laterally and eventually merge into polycrystalline sheets as shown in **Figure 2.5**(b) and in **Figure 2.6**(a). These sheets continue to grow and merge with other monolayer crystals to ultimately comprise a full coverage monolayer sheet.

Once a full-coverage monolayer sheet forms as shown in **Figure 2.5**(c) and in **Figure 2.6**(b)-(c), the growth is terminated as ammonia borane precursor molecules can no longer access the catalyst where they decompose. As a result, growths of both 30 minutes and 60 minutes result in monolayer films with few multilayer regions in **Figure 2.6**.
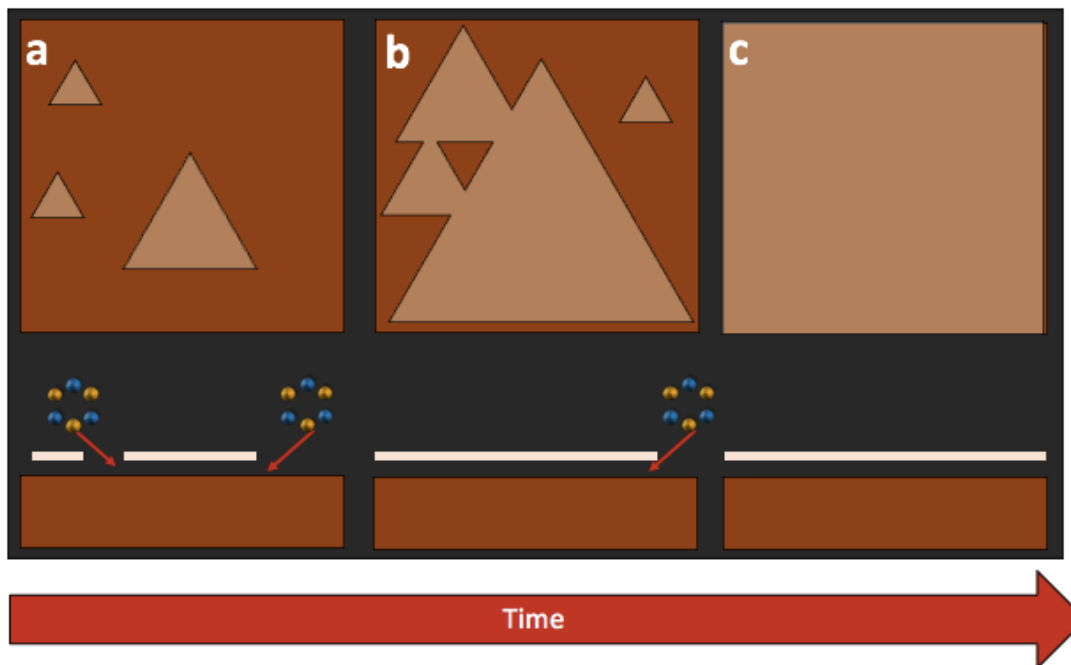
Figure 2.5 A cartoon illustrating the CVD synthesis of monolayer _h_-BN. (a) Initially, triangular monolayer single crystals form as precursor molecules adsorb and react on the transition metal catalyst surface. (b) As the monolayer crystals grow, their growth fronts collide and the crystals merge, forming polycrystalline films. (c) Eventually, the catalyst becomes fully covered by a polycrystalline monolayer film and the precursor no longer has access to the foil. This terminates the growth with the single layer sheet of _h_-BN. Figure based on our previously published work in Reference [41].
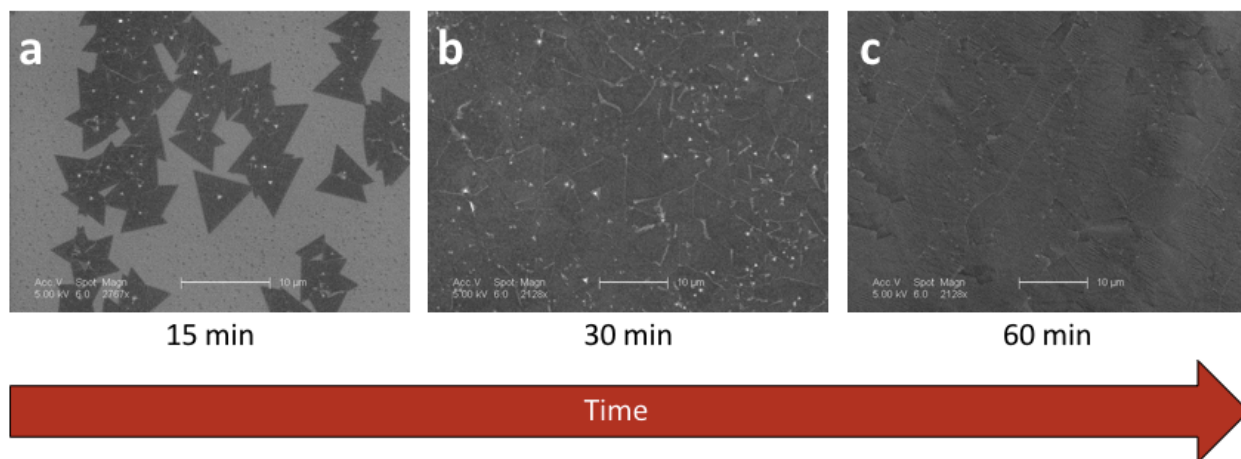
Figure 2.6 Growth progress of monolayer _h_-BN. SEM images are shown of three separate CVD syntheses of _h_-BN on copper foil that are prepared under identical annealing, temperature, precursor, and carrier gas flow (20 sccm H_2 and 80 sccm Ar) conditions. The growth time is varied between 15 minutes (a), 30 minutes (b), and 60 minutes (c). (a) After 15 minutes, triangular monolayer _h_-BN crystals have formed and some have begun to merge. (b) After 30 minutes, a full coverage polycrystalline monolayer film has formed from the merging of the _h_-BN crystals. Wrinkles (white lines) and ad-layers (white triangles) are visible. (c) After 60 minutes, there has been no additional growth versus 30 minutes because the growth has terminated. There are no additional ad-layers versus 30 minutes. Scale bars are 10 μm. Figure based on our previously published work in Reference [41].

2.2.2 Multilayer *h*-BN and its Stacking Sequences

This section is based on our previously published work in Reference [41]. Theoretical calculations are performed by Dr. Mehmet Dogan under the supervision of Prof. Marvin L. Cohen.
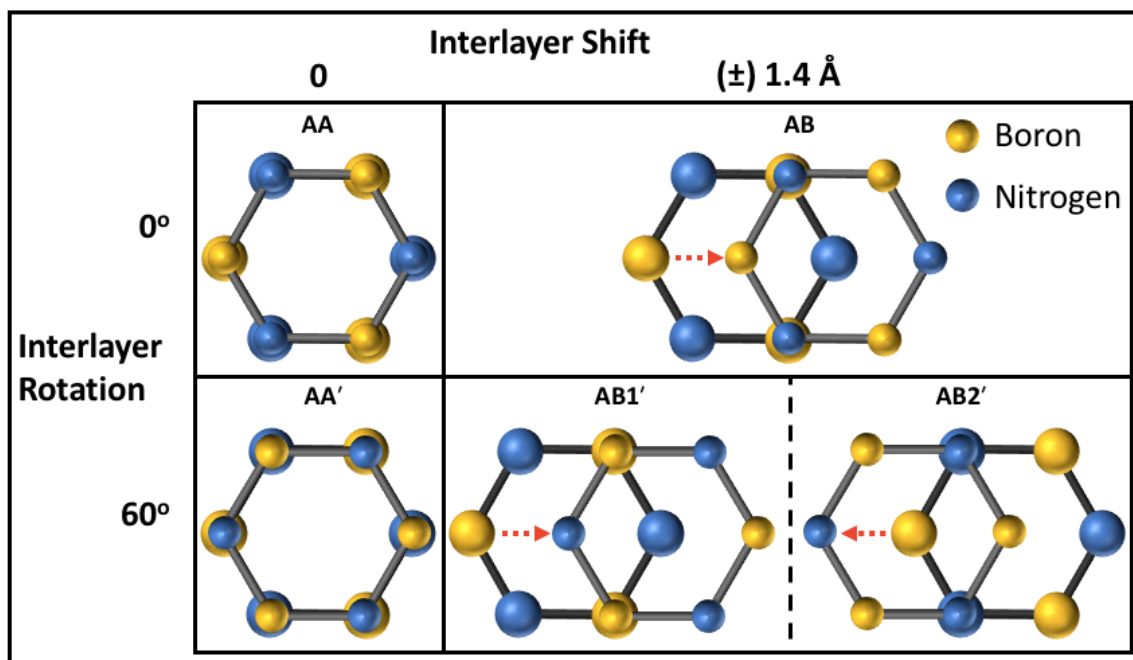
Figure 2.7 Schematics of the 5 high-symmetry stackings in bilayer *h*-BN. In the top half of the figure, the rotationally aligned stacking configurations, AA and AB, are shown. AA is formed by stacking B to B and N to N in two aligned layers. AB is formed by translating one layer by a single bond length (1.4 Å)[71] to stack N to B as shown by the red arrow. In the bottom half of the figure, the rotationally anti-aligned stacking configurations, AA', AB1', and AB2', are shown. AA' is formed by stacking two anti-aligned layers B to N and N to B. AB1' is formed by translating one layer such that the layers stack B to B while AB2' is formed by translating one layer such that they stack N to N. Figure reprinted from our previously published work in Reference [41].

Multilayer two-dimensional materials can take on a variety of twist angles and stacking sequences; generally, however, these materials take on high symmetry stacking sequences during high-temperature chemical synthesis. In this section, the possible stacking sequences for *h*-BN synthesized by CVD are considered.

Figure 2.7 schematically shows the five high-symmetry stacking sequence possibilities for multilayer *h*-BN. Boron and nitrogen atoms are indicated in gold and blue, respectively. In each schematic, only two superposed atomic sheets or layers are shown, and for visual clarity atoms in the top layer have been drawn slightly smaller than atoms in the bottom layer. Because there is no nomenclature consensus in the literature for all of these stacking sequences, a naming convention is adopted where "prime" denotes a 60° rotation, and the letters A and B are used in the standard way as for graphite.

AA is the simplest stacking sequence; here the atoms in consecutive layers exactly align (B on B, and N on N). AA′ is obtained from AA by rotating every other layer by 60° and aligning the hexagons (B on N). AB is obtained from AA by shifting every other layer, as demonstrated by the red arrow in the upper right panel of the figure, which yields a structure where half of the B atoms align with half of the N atoms, and the remaining half of the atoms align with the centers of the hexagons in the neighboring layers. Shifting every second layer in AA′, as demonstrated by the red arrows in the lower right two panels of Fig. 1, yields AB1′ and AB2′. In AB1′ (AB2′), all the B (N) atoms are aligned, and all the N (B) atoms align with the centers of the hexagons in the neighboring layers. Applying to AA the same lateral shift as gives AB2′ from AA′ yields an equivalent structure to AB; therefore, there are a total of five physically distinct structures that preserve the three-fold symmetry. Despite the existence of these five total distinct structures, AB stacking, also called Bernal stacking, is the stacking sequence most prevalent in naturally-occurring crystalline graphite,[72] while virtually all *h*-BN produced today and used in laboratories worldwide has the stacking sequence AA′. [71,73–75]

In order to understand the energetics for *h*-BN stacking, we collaborate with the group of Marvin L. Cohen to theoretically describe the stacks. The total cohesive energy, electronic band structure, and dielectric response tensor for the infinite crystal (bulk) and bilayer forms of *h*-BN, in the five physically distinct stacking sequences were calculated by Dr. Mehmet Dogan (under the supervision of Prof. Cohen and in collaboration with Dr. Sehoon Oh) using density functional theory (DFT). Similar calculations for total energy and band structure had been published previously by various other groups, but because the results are highly sensitive to the computational details such as the exchange-correlation functional and the van der Waals scheme, they yield inconsistencies.[76–81]

Table 2.1 presents the total energies of bulk and bilayer *h*-BN in the different stacking sequences, as computed using DFT. Because it is most commonly observed in the literature, we take the AA′ stacking to be the reference and set its energy to zero. The results from previous studies are also included in Table 2.1 for comparison. We find AB to be the ground state (i.e. it has the lowest overall energy) for both bulk and bilayer *h*-BN. However, AA′ is quite close in energy (3 meV per unit cell higher for bulk). AB1′ is next closest in energy (8 meV per unit cell higher for bulk). This hierarchy is consistent with some reports in the literature[78,81] but at odds with others[76,79]. We also find that AA and AB2′, while close to each other in energy, are significantly higher in energy than the other three stackings. This can be understood by simple arguments such as those suggested in Ref. [82]. Aligning negatively charged nitrogen atoms with large electron clouds causes a repulsive Pauli interaction between the layers, increasing the total energies and the interlayer distances to 3.64 Å for AA and 3.54 Å for AB2′ (from 3.33 Å for AA′, AB and AB1′). We note that these two high-energy stackings are also energetically unstable, i.e. they do not correspond to local energy minima in the configuration landscape and relax to one of the stable configurations when the atoms are slightly perturbed.

	Energy (meV per cell)	Method	AA	AA$'$	AB	AB1$'$	AB2$'$
bulk	Present	GGA+TS vdW	48	$\equiv 0$	-3	5	42
	Liu (2003)[77]	LDA	56	0	0	8	48
	Ooi (2006)[76]	LDA	51	0	6	25	48
	Hu (2011)[78]	LDA	52	0	-2	6	47
	Constantinescu (2013)[79]	LMP2	80	0	3	25	82
bilayer	Present	GGA+TS vdW	21	$\equiv 0$	-2	2	18
	Riberio (2011)[80]	GGA	13	0	0	3	10
	Constantinescu (2013)[79]	LMP2	40	0	0	9	33
	Fujimoto (2016)[81]	LDA	24	0	-2	2	22

Table 2.1 Computed total energies of the five high-symmetry stackings of *h*-BN in its bulk and bilayer forms. We use density functional theory (DFT) with the Perdew-Burke-Ernzerhof generalized gradient approximation (PBE GGA)[37] and norm-conserving pseudopotentials. To include the interlayer van der Waals (vdW) interactions, we have used the Tkatchenko-Scheffler (TS) correction as described in the supplement. Energies are referenced to the commonly known AA' stacking, and are in meV per unit cell (two B and two N atoms). Calculations performed by Mehmet Dogan under the supervision of Prof. Marvin Cohen. This table is presented in our previously published work in Reference [41].
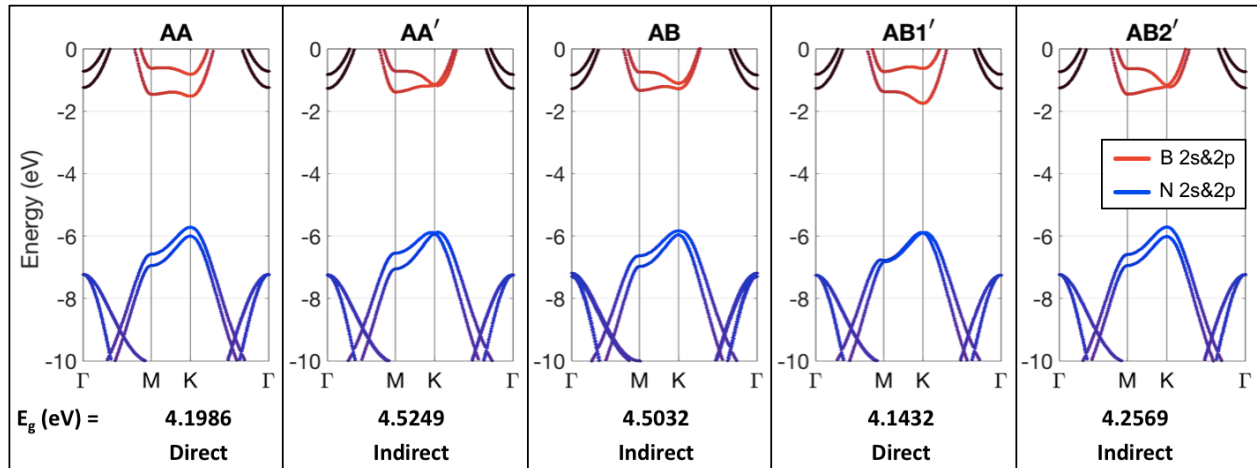
Figure 2.8 Band structures of high symmetry *h*-BN stackings. The electronic structure and bandgaps of the five physically distinct high-symmetry stackings of bilayer hexagonal boron nitride, AA, AA', AB, AB1', and AB2', are shown from left to right. The red (blue) coloring of a band indicates the boron (nitrogen) 2s or 2p character of that band. Calculations performed by Mehmet Dogan under the supervision of Prof. Marvin L. Cohen. Figure reprinted from our previously published work in Reference [41].

Figure 2.8 shows our calculated band structure for *h*-BN bilayers of each high-symmetry configuration (assumed suspended in vacuum). The zeros of the energy levels are set to the vacuum level for each structure so that there is a common reference between the plots. For additional insight, we have projected the Kohn-Sham wave-functions onto the atomic orbitals for each point along the bands we have computed. The resulting atomic orbital characteristics are designated by red (blue) coloring for boron (nitrogen) n=2 (2s & 2p) orbitals. We observe that the top of the valence band mostly consists of nitrogen n=2 orbitals, and the bottom of the conduction band mostly consists of boron n=2 orbitals, which verifies the ionic character of the intra-layer bonds in *h*-BN, and is consistent with a large-gap insulator.

The band gaps we have obtained for *h*-BN in its bulk and bilayer forms are summarized in Table 2.2. Due to the underestimation of band gaps in DFT, the values tabulated are expected to be much lower than experimental measurements, which are in the 4 to 7 eV range. [76] However, the relative values of the computed gaps can be expected to be mostly accurate. For instance, in Refs. [83] and [78], the bandgaps are computed with and without a GW correction, respectively, and it is found that the GW correction adds about 1.6 eV to the value of each gap. We also expect the shapes of the bands to be correctly predicted by DFT; therefore, the predictions as to whether a band gap is direct or indirect are reliable. We find that both AA′ and AB have indirect gaps. However, the AB structure allows an optical transition at the K point with an energy only 1% larger than the band gap. This is a key feature distinguishing the electronic structure of AB stacking from AA' stacking in *h*-BN.

Table 2.3 summarizes our calculations for the dielectric tensor of bilayer and bulk *h*-BN, for the five selected stacking sequences. Because of the high symmetry of *h*-BN, the dielectric tensor only has two distinct non-zero values: the in-plane $\varepsilon_{xx}=\varepsilon_{yy}$ (which we denote as $\varepsilon_{\parallel}$), and the out-of-plane ε_{zz} (which we denote as $\varepsilon_{\perp}$). We compute the dielectric tensor in two frequency limits: ε_{∞} and ε_0, for high and low frequency, respectively. In the Born-Oppenheimer approximation, for high-frequency electric field response, the nuclei can be thought of as stationary, and the electronic response dominates. In this case, the dielectric response is described by ε_{∞}, which we compute via the density functional perturbation theory. [84] For low-frequency electric-field response, ε_0, we compute the relaxed-ion dielectric tensor, following the methodology proposed by Ref. [85].

We find that the dielectric tensor values for AA′, AB and AB1′ are very close, and larger than the values for AA and AB2′ by 0.2 to 0.4. This simple trend can be understood as a result of the difference in the interlayer distance between these two groups of stackings. In the former group, which has smaller interlayer distances, the dielectric material simply occupies a larger portion of the space, leading to a larger dielectric tensor. Our results for the relaxed-ion tensors indicate that the response of the nuclei to a finite electric field does not significantly depend on the stacking, further emphasizing the weakness of the interlayer ionic interactions. We have also compared our results with Ref. [86] for the AA′ stacking, which, to our knowledge, is the only available calculation of these values in the literature. Our results are in good agreement for the in-plane dielectric constant values, and in reasonable agreement for the out-of-plane values. For the ε values in the bilayer case, we have carefully corrected for the existence of vacuum in our simulations by applying the combined capacitor rules, as described in Ref. [86]. For the slab thickness, we have used twice the value of the interlayer distance in each stacking.

Band gap (eV)		Method	AA	AA$'$	AB	AB1$'$	AB2$'$
bulk	Present	GGA+TS vdW	3.7248 (d)	4.2932 (i)	4.3751 (i)	3.6470 (i)	3.6245 (i)
	Liu (2003)[77]	LDA	3.226 (i)	4.027 (i)	4.208 (i)	3.395 (d)	3.433 (i)
	Ooi (2006)[76]	GGA	3.12 (d)	4.28 (i)	4.39 (i)	3.66 (i)	3.23 (i)
	Hu (2011)[78]	LDA	3.352 (i)	4.015 (i)	4.202 (i)	3.407 (i)	3.369 (i)
	Hu (2012)[83]	GW	4.96	5.73	5.87	5.01	4.96
bilayer	Present	GGA+TS vdW	4.1986 (d)	4.5249 (i)	4.5032 (i)	4.1432 (d)	4.2569 (i)
	Riberio (2011)[80]	GGA	4.23	4.69	4.60	4.29	4.52
	Fujimoto (2016)[81]	LDA	4.05 (d)	4.34 (i)	4.36 (i)	4.01 (d)	4.08 (i)

Table 2.2 Electronic band gaps for *h*-BN in its five high-symmetry stackings, listed for the bulk and bilayer cases. Indirect and direct band gaps are denoted by "(i)" and "(d)", respectively. Calculations performed by Mehmet Dogan under the supervision of Prof. Marvin Cohen. This table is presented in our previously published work in Reference [41].

		AA	AA$'$	AB	AB1$'$	AB2$'$	AA$'$ [Laturia2018][86]
$\varepsilon_{\parallel,\infty}$	Bulk	4.41	4.71	4.80	4.78	4.49	4.98
	bilayer	4.40	4.68	4.74	4.75	4.43	4.97
$\varepsilon_{\parallel,0}$	bulk	6.58	6.88	6.96	6.95	6.53	6.93
	bilayer	6.41	6.87	6.95	6.95	6.45	6.86
$\varepsilon_{\perp,\infty}$	bulk	2.28	2.64	2.66	2.61	2.30	3.03
	bilayer	2.27	2.61	2.66	2.60	2.29	2.91
$\varepsilon_{\perp,0}$	bulk	2.80	3.17	3.15	3.02	2.59	3.76
	bilayer	2.54	3.07	3.12	3.00	2.57	3.44

Table 2.3 The high frequency (clamped-ion) and low frequency (free-ion) dielectric tensor elements for the five high-symmetry stackings of *h*-BN. The values are relative to vacuum permittivity (ε vacuum=1). Calculations performed by Mehmet Dogan under the supervision of Prof. Marvin Cohen. This table is presented in our previously published work in Reference [41].

2.2.3 Synthesis of Bernal Stacked *h*-BN

This section is based on our previously published work in Reference [41].

The original synthesis of *h*-BN by Balmain in 1842[87,88] yielded material with AA' stacking, and this situation continues today: virtually all *h*-BN produced by all synthetic routes has the AA' stacking sequence. However, our total energy calculation results presented in Table 2.1 suggest that of the 5 high symmetry stacking sequences of *h*-BN, only AA and AB2' structures are likely highly unstable. The remaining three sequences, AA', AB, and AB1' are relatively close in energy, with AB representing the ground state. This begs the question, is a synthesis route possible that allows access to the distinct AB Bernal ground state structure, or possibly the slightly higher energy AB1' configuration?

Apart from the properties discussed above, AB Bernal-stacked *h*-BN has been predicted to possess a tunable bandgap, along with other unique optical features.[89–91] Previous experimental studies have observed tantalizing small pockets of AB-stacked bilayer *h*-BN.[90,92–94] Therefore, we are motivated to develop a viable synthetic route for the reliable synthesis of AB-stacked *h*-BN, a new form of two-dimensional insulator.

We employ LP-CVD on a transition metal surface to select the stacking growth sequence of *h*-BN. We find that the growth can be tuned from conventional AA' growth to exclusively Bernal AB growth, on both Cu and Fe substrates. High-Resolution Transmission Electron Microscopy (HRTEM) and Selected Area Electron Diffraction (SAED) are used to reveal the Bernal-stacking of the resulting multilayer flakes.

Figure 2.3 shows the furnace setup used for the synthesis. Similar to Ref. [52] and our previous work[42,95], we employ a two-zone heating approach in which the gaseous thermal decomposition products of solid ammonia-borane (heated at 70-90 ^{o}C in region T_0 in Fig. S1) react to form *h*-BN on a transition metal catalyst (heated at 1025 ^{o}C in region T_1 in Fig. S1). Our synthesis method for Bernal-stacked *h*-BN differs from previous ammonia-borane based LP-CVD growths of *h*-BN in its combination of relatively low precursor temperatures (75-85 ^{o}C) and high hydrogen gas flows (100-200 sccm). [52,53,66,96] Additional details on the growth are available in the supplementary methods sections of Refs. [41,42].

Figure 2.9 shows two representative SEM images of few-layer *h*-BN flakes grown on Fe via the LP-CVD method (30 min, 100 sccm H_2). The concentric triangular shape and 40+ μm size of the flakes are representative of those grown over much of the entire metal substrate, with an average total substrate coverage by *h*-BN of approximately 50-90% depending on the growth conditions. Generally, AB-stacked *h*-BN is expected to grow as concentric triangles due to alignment between the layers. AB-stacking in *h*-BN and MoS_2 has been previously identified based on the presence of concentric triangles. [96,97]
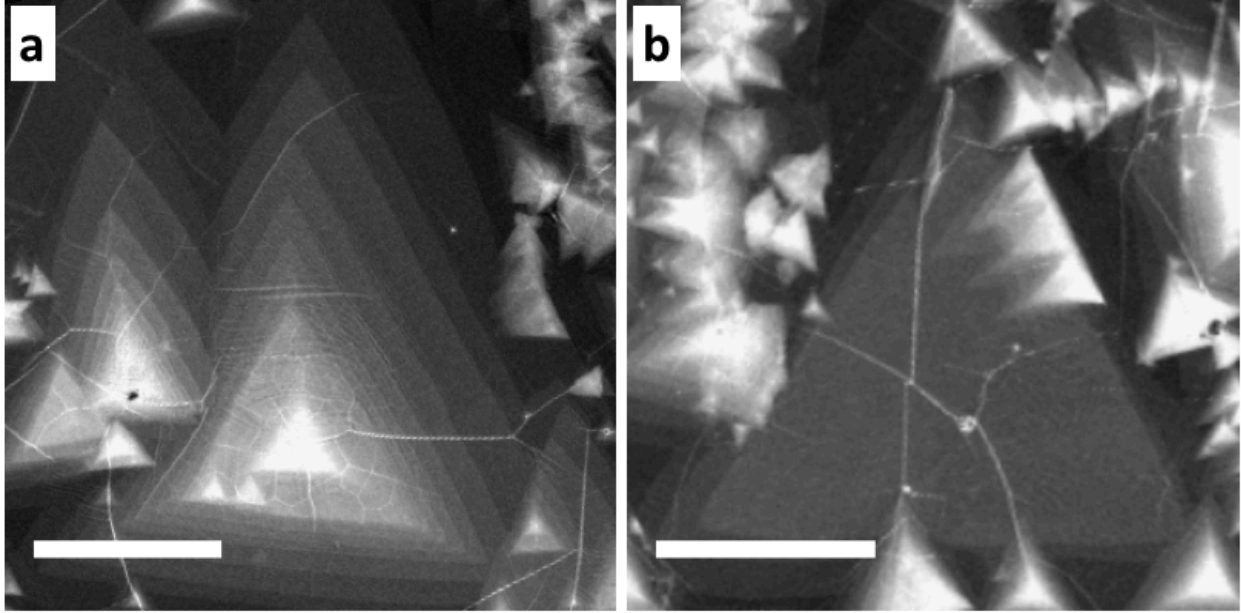
Figure 2.9 SEM of AB-stacked *h*-BN on iron foil. (a,b) SEM images of multilayer *h*-BN crystals as-grown on iron foil for 1 hour under 100 sccm H_2. The *h*-BN single crystals are bright contrasted concentric triangles on a dark background of iron. Concentric triangles are additional layers stacked together. Brighter contrast indicates additional layers. (a) shows >10 separate layers stacked together with a large variation in width (2-30 µm) while (b) shows a more continuous region of multilayer *h*-BN over ~40 µm that is surrounded by smaller thicker *h*-BN triangles. Scale bars are (a) 10 µm, (b) 15 µm. Figure based on our previously published work in Reference [41].

We examine the stacking sequence of the *h*-BN by SAED and HRTEM. Electron diffraction can be used to deduce the stacking sequence of a layered material because it is a probe of the structure factor of the crystal.[98,99] For low order diffraction peaks, the intensity *I(q)* of a given peak at a given inverse lattice coordinate $q = hb_1 + kb_2$ is given by:

$$I(q) \approx \varphi(q, T, E) \left| \sum_i f_i e^{-q \cdot R_i} \right|^2$$

Where R_i and f_i are the atomic position and scattering factor for the *i*-th atom in the unit cell. $\varphi(q)$ is an exponentially decaying function that describes how the intensity of the beam falls off due to lattice vibrations for increasing **q** as a function of beam energy and temperature. For the purposes of these calculations, we assume that $f_B = f_N = f_{BN}$.

For AA' (or AA) stacked *h*-BN, the intensity of a given diffraction peak **q** is:

$$I(q) \approx N^2 f_{BN}^2 \left| 4 \cos\left(\frac{1}{2} q \cdot R\right) \right|^2 = 16 N^2 f_{BN}^2 \cos^2\left((h+k)\frac{\pi}{3}\right)$$

Therefore:

$I(\mathbf{q}) = 4 N^2 f_{BN}^2 \varphi(q)$ for $h + k \neq 0$ mod 3

$I(\mathbf{q}) = 16 N^2 f_{BN}^2 \varphi(q)$ for $h + k = 0$ mod 3

Using the above relationship, the ratio of the first order diffraction peaks to the second order diffraction peaks is:

$$R_{AA'} = \frac{I_1(\mathbf{q})}{I_2(\mathbf{q})} = \frac{1}{4} \frac{\varphi(q = <0\,1\,0>)}{\varphi(q = <1\,2\,0>)}$$

For AB (or AB1'/AB2') stacked *h*-BN, the intensity of a given diffraction peak **q** is:

$$I(q) \approx N^2 f_{BN}^2 |2 + 2\cos q \cdot R|^2 = 4N^2 f_{BN}^2 \left(1 + \cos\left((h+k)\frac{2\pi}{3}\right)\right)^2$$

$I(\mathbf{q}) = N^2 f_{BN}^2 \varphi(q)$ for $h + k \neq 0$ mod 3

$I(\mathbf{q}) = 16 N^2 f_{BN}^2 \varphi(q)$ for $h + k = 0$ mod 3

And that the ratio of the first order diffraction peaks to the second order diffraction peaks is:

$$R_{AB} = \frac{I_1(\mathbf{q})}{I_2(\mathbf{q})} = \frac{1}{16} \frac{\varphi(q = <0\,1\,0>)}{\varphi(q = <1\,2\,0>)}$$

This shows that the ratio R_{AB} is 4 times smaller than $R_{AA'}$. Therefore, the ratio of the first order to second order intensity of AB stacked *h*-BN should be 4 times as small as in AA'.
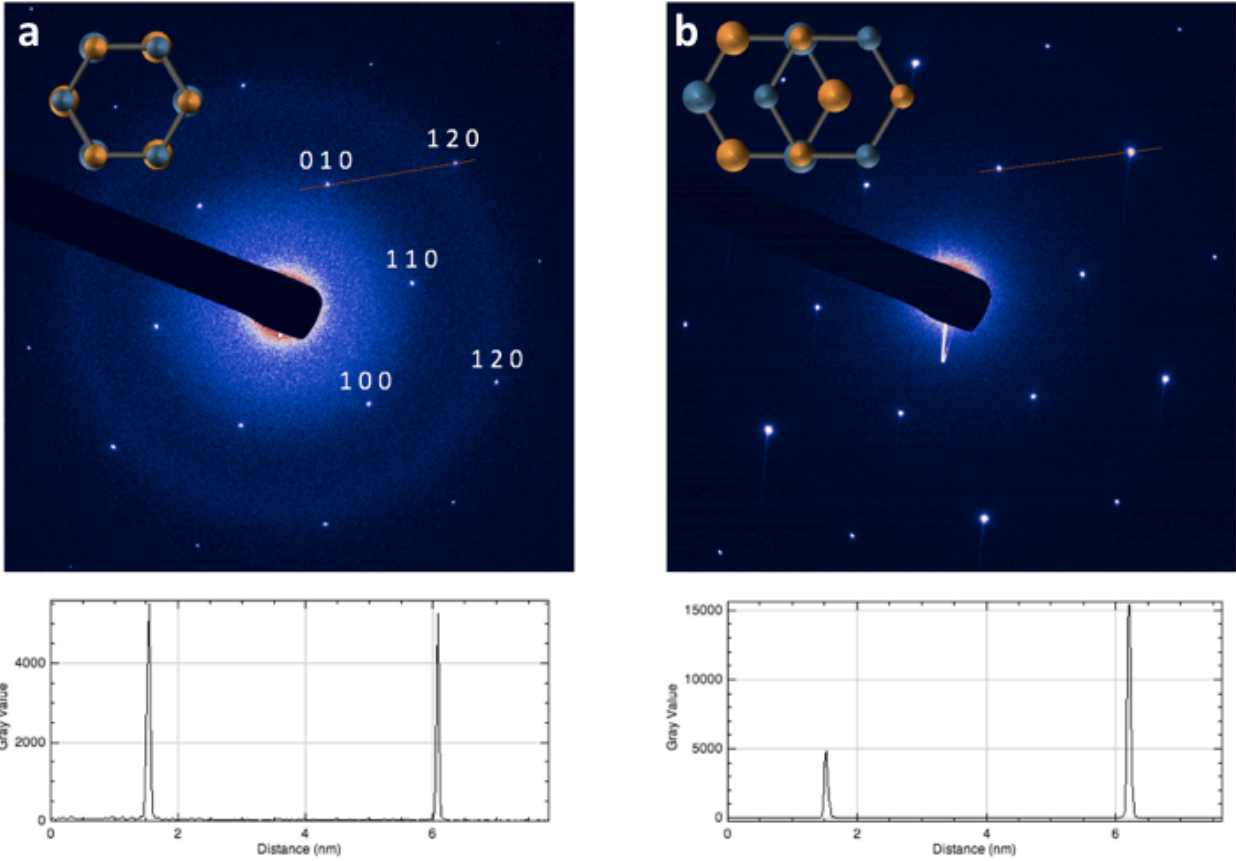
Figure 2.10 A comparison of representative SAED patterns in AA' and AB stacked *h*-BN. (Top) A comparison of representative SAED patterns for a thick regions of multilayer exfoliated AA' (a) and LP-CVD AB stacked *h*-BN (b). The diffraction peak indices are written as < h k l > where $q = hb_1 + kb_2 + lb_3$. (Bottom) The ratio of the intensities of the first-order <010> and second order <120> peaks are compared to determine the stacking order of the *h*-BN. The ratios of ~1.1 on the right is indicative of AA' stacking and the ration of ~0.3 on the right indicative that the stacking is AB, AB1', or AB2' as detailed in the text. Figure based on our previously published work in [41].

Figure 2.10 compares the SAED patterns of an *h*-BN flake originally grown via LP-CVD on an Fe substrate (a) to that of a standard exfoliated AA' stacked sample (b). In our samples, for the AA'-stacked sample, the ratio of these intensities is ~1.1 while for the CVD grown Bernal stacked sample, the ratio of the intensities of the first-order <010> and second-order <110> diffraction peaks is ~0.3 as shown in the bottom of **Figure 2.10**. This is roughly consistent with our prediction that the ratio $R_{AA'}$ should be 4 times larger than the ratio R_{AB}.
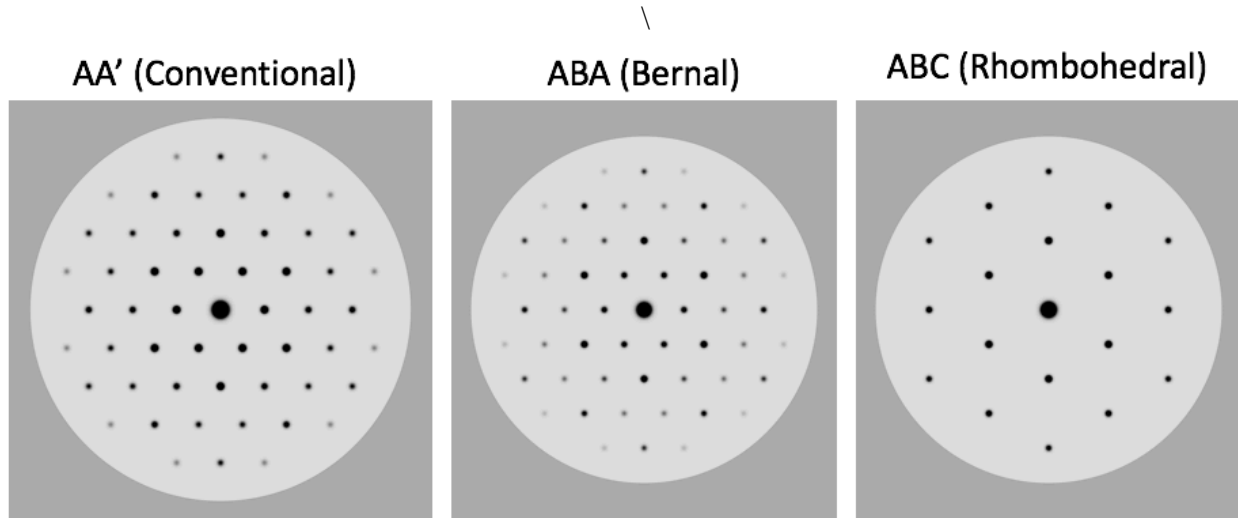
Figure 2.11 Simulated Electron Diffraction in *h*-BN. (Left) A simulated diffraction pattern for bulk AA' stacked *h*-BN using the Single Crystal software package. (Center) A simulated diffraction pattern for bulk AB stacked *h*-BN. (Right) A simulated diffraction pattern for bulk ABC stacked rhombohedral BN. For the AA′ stacked *h*-BN, the first-order <010> and second order <110> peaks are approximately equal. For the Bernal stacked *h*-BN the first order peak is smaller and thereby less intense than the second order peak. For the rhombohedral BN there is no first order peak. Figure prepared by Brian Shevitski and reprinted from our previously published work in Reference [41].

We simulate the diffraction patterns of the stable bulk configurations of *h*-BN with AA′ and AB stackings using the Single Crystal software package (as shown in Fig. S2) and compare with our measured values. Although ABC-stacked rhombohedral BN does not belong to the *h*-BN class, we also simulate the diffraction patterns for it to rule out this stacking in our material.[100,101] The experimental first-order to second-order ratio of ~0.3 is consistent with the simulated ratio of 0.28 for AB stacked *h*-BN while the simulation of AA′ yields a ratio of 1.1 and ABC yields a ratio of 0. These ratios of intensities are comparable to results in graphene.[99] This result indicates that the as grown *h*-BN is either AB, AB1', or AB2' stacked, as they possess similar intensity ratios.
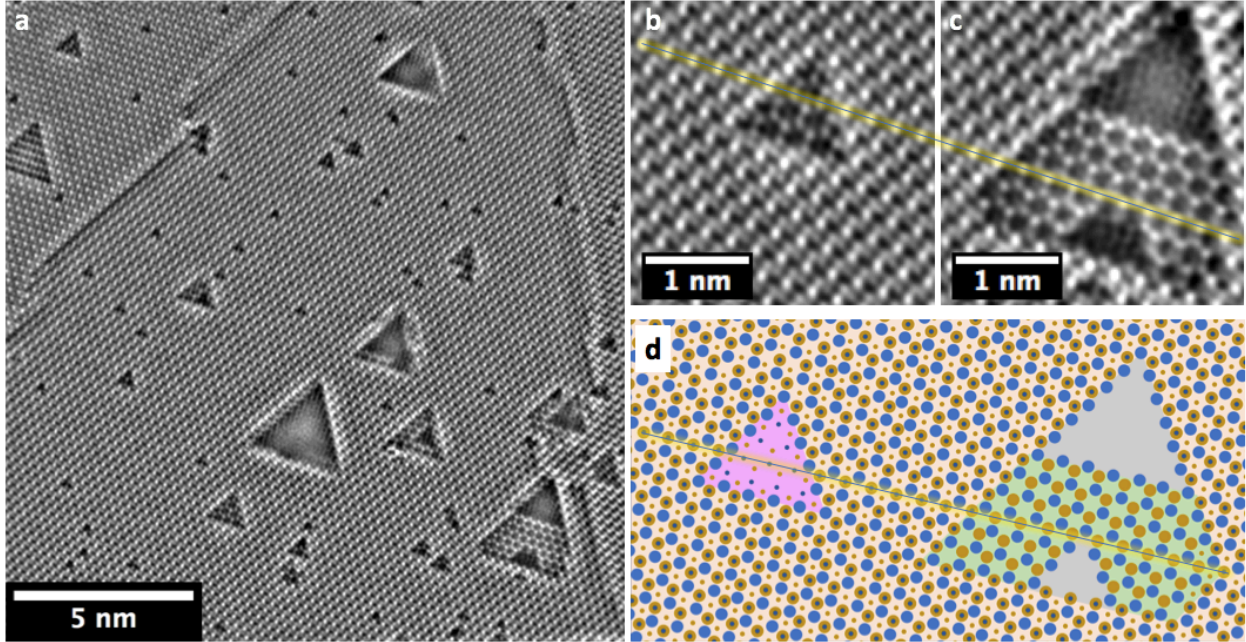
Figure 2.12 HR-TEM of AB stacked *h*-BN. (a) An aberration corrected HR-TEM focal series reconstruction of a region of Bernal stacked *h*-BN. (b)-(c) Two nearby mixed bilayer/monolayer regions of *h*-BN as cropped from the full image shown (a). The red-dashed triangles denote the boundary between the monolayer/vacuum(inner) and the bilayer(outer) areas. (d) A schematic of the position of each atom in (b)-(c). The atomic positions are deduced as described in the text. The opaque yellow lines in (b)-(d) trace the line of stacked atoms in the bilayer region to highlight the alignment of the left and right monolayer regions. Figure reprinted from our previously published work in Reference [41].

To differentiate between these stackings, we perform HR-TEM on a bilayer region of material. **Figure 2.12**(a) shows an aberration corrected HR-TEM focal series reconstruction acquired at 80 kV. Two nearby mixed monolayer/bilayer regions of the multilayer *h*-BN as cropped from the full image are shown in **Figure 2.12**(b)-(c). The atomic positions in each region are deduced from **Figure 2.12**(b)-(c) and are sketched in **Figure 2.12**(d). Based on the atomic positions as sketched, the two layers are AB stacked. We deduce the atomic positions as shown by assuming that all edge-atoms of the triangular holes are nitrogen terminated as is reported in the literature at ambient conditions. [42,71,102–105] We thereby determine the position of all other atoms in both layers of the bilayer area accordingly.

It is worth noting that the monolayer regions in **Figure 2.12**(b)-(c) are areas of two different layers. The atoms of the monolayer in **Figure 2.12**(b) which align with the referenced yellow line connecting bright contrast spots running through the entire bilayer area (the bright contrast spots are attributed to the overlapping of two atoms in the top and bottom layers), are all B. On the other hand, the atoms of the monolayer, which also align with the referenced yellow line as indicated in **Figure 2.12**(c)., are all N. As a result, we conclude these monolayer regions reside in different layers. More importantly, one layer translates with respect to the other by a single atomic bond length (1.4 Å)[71] along the yellow reference line. This translation reflects AB (Bernal) stacking as shown in Fig. 1. This is the first conclusive observation to our knowledge of non-overlapping vacancies in two separate layers of a two-dimensional material.
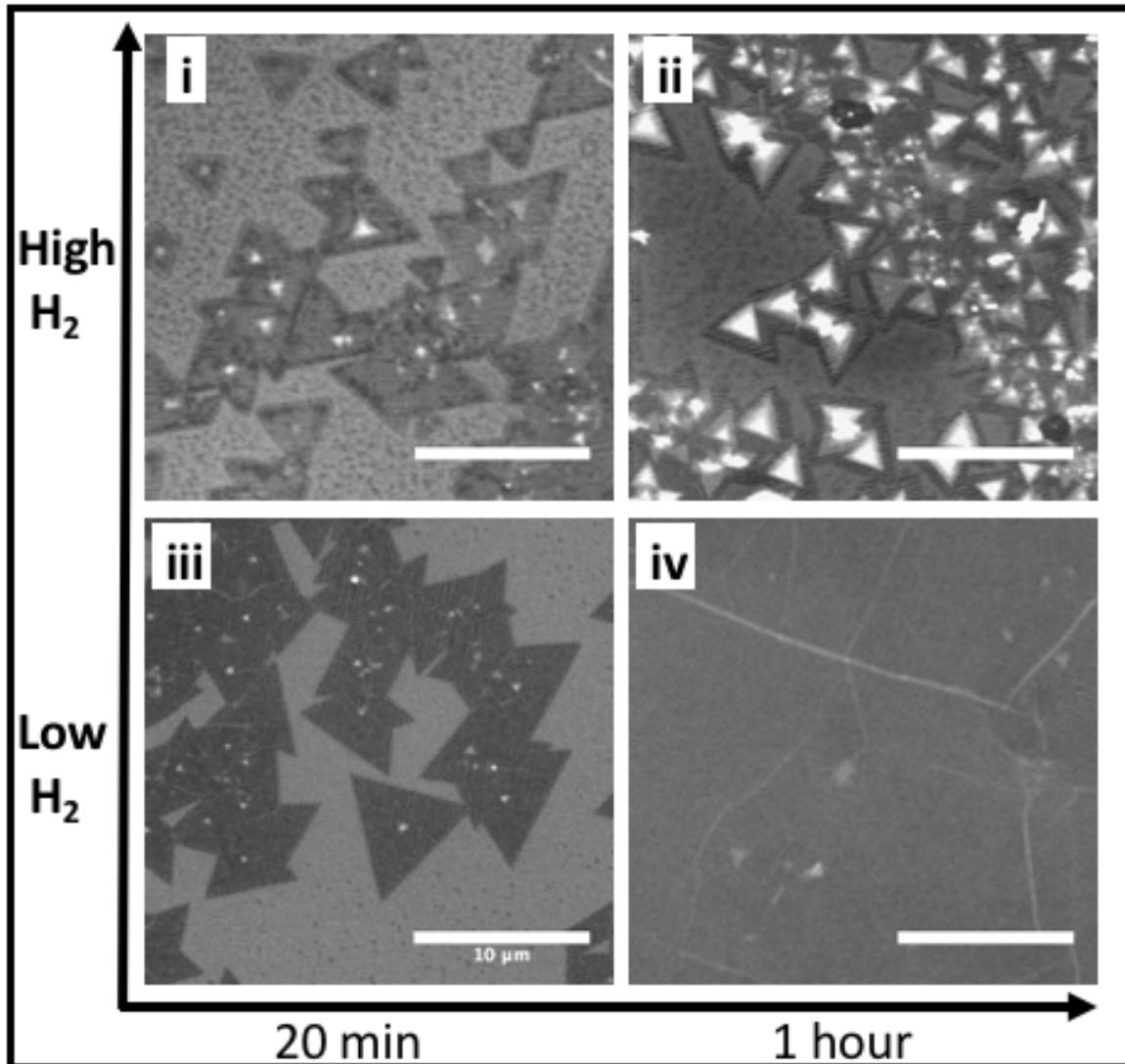
Figure 2.13 *h*-BN growth progress with varying hydrogen flows. SEM images of multilayer *h*-BN crystals grown on copper with varying times (20 min and 1 hour) and hydrogen flows (20 sccm and 200 sccm). (i) shows 3 μm triangular *h*-BN domains with small ad-layers (white) that are representative of a 20 minute growth with 200 sccm H_2. (ii) shows that after 2 hours the ad-layers grow larger while the monolayer *h*-BN triangle remains a similar size under 200 sccm H_2. (iii) shows 5 μm triangular *h*-BN domains that are representative of a 20 minute growth with 20 sccm H_2. (iv) shows that after one hour with 20 sccm H_2, the *h*-BN crystals merge to a full-coverage film with only minimal multi-layer coverage. Figure reprinted from our previously published work in Reference [41].

In order to elucidate the growth mechanism for Bernal-stacked *h*-BN, we explore the role of this increase in hydrogen. **Figure 2.13** shows SEM images of four *h*-BN samples grown on Cu with varying hydrogen gas flows (low 20 sccm, high 200 sccm) and growth time (20 min and 1 hour). In **Figure 2.13** (iii-iv), low hydrogen flows, when combined with low precursor temperatures, lead to monolayer *h*-BN domains that merge into continuous films with additional growth time. While some small regions of ad-layer *h*-BN are present (white dots or triangles within the larger, darker *h*-BN monolayer triangle), the multilayer regions do not appear to grow with increased times once the film fully covers the catalyst (as shown in **Figure 2.6**).

27

Conversely, for higher hydrogen flows the crystals quickly reach their final lateral size and then ultimately do not merge into films as shown in **Figure 2.13** (i-ii). For short growth times (20 min), the triangular *h*-BN domains grown with high hydrogen flow (**Figure 2.13** (i)) are slightly smaller in comparison to those with low hydrogen flow (**Figure 2.13** (iii)), but these smaller crystals have a higher coverage of multilayered ad-layers. As the growth time is increased, the *h*-BN crystals grown with high hydrogen-flow do not significantly increase in size, but the size and coverage of multilayers increases as shown in **Figure 2.13** (ii).

We attribute the preference towards forming multilayer flakes rather than continuous monolayer films to the etching properties of the hydrogen gas. Hydrogen gas is known to etch the edges of *h*-BN domains at high temperatures. [66,106] Therefore, by utilizing a high hydrogen flow as in **Figure 2.13** (iii-iv), the edges of the *h*-BN flakes are etched throughout the growth, and the domains are prevented from merging into films after reaching their equilibrium lateral size. While both the low and high hydrogen flow case lead to ad-layer formation, it appears their growth is halted once a continuous film has formed.

Based on this observation, we propose an under-layer growth model for Bernal-stacked *h*-BN, as sketched in **Figure 2.14**. This type of mechanism has been previously described for multilayer graphene and *h*-BN. [70,107–109] In our LP-CVD process, low flows of precursor gas and high flows of hydrogen cause the edges of the *h*-BN domains to be continuously etched. This prevents the formation of a full coverage layer and allows the gaseous precursor to access the transition metal catalyst for the entire length of our procedure. The precursor gas can thereby adsorb onto or dissolve into the metal and form ad-layers below the first layer.

It has been previously reported that an *h*-BN layer grown on metal foil by CVD will have its orientation uniquely determined by the local configuration of the catalyst at the nucleation site of the *h*-BN.[110] Since each layer of *h*-BN grows directly on the catalyst in our process, its rotation can be controlled by the metal. Generally, we find that the layers of our Bernal-stacked *h*-BN grow as aligned triangles with a common centroid; this suggests the layers all form at a common nucleation point, forcing each layer to align to the metal. This mechanism, as sketched in **Figure 2.15**, results in aligned (0° interlayer rotation) layers that relax into the AB ground state by interlayer sliding on the order of 1 Å at the elevated growth temperatures. This process also therefore excludes the stable AA' and AB1' stackings which have anti-aligned (60° interlayer rotation) layered structures. We therefore suggest that our relatively high hydrogen gas flows allow successive *h*-BN layers to form below the existing layers where they align to the metal resulting in Bernal-stacked *h*-BN. Since this process relies on the metal only to serve as a catalyst and alignment template, other metal catalysts used for *h*-BN CVD beyond Fe and Cu (such as Ni, Pt, Rh, or Ir) may also support the growth of Bernal stacked *h*-BN.[110–113]

This growth mechanism suggests that we could grow heterostructures of different materials with aligned stacking or single crystals with arbitrary twist angles by similar processes. By changing the precursor during the growth, the composition of the under-layer could be changed. By inducing nucleation at the grain boundaries of a polycrystalline metals, the orientation of the under-layer could be tuned.
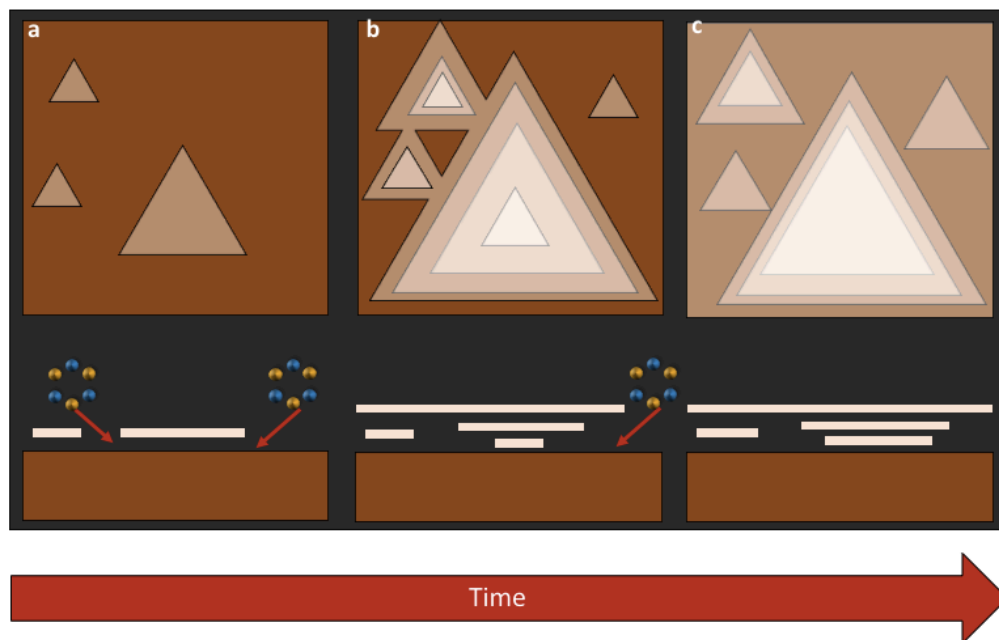
Figure 2.14 A cartoon illustrating the growth mechanism for Bernal-stacked *h*-BN. The top-view is shown above and the side-view is shown below. (a) depicts the seeding and growth of *h*-BN monolayers. (b) shows the growth of the *h*-BN monolayers and the seeding of ad-layers underneath the original monolayer. (c) shows the *h*-BN film achieving full coverage thereby stopping the growth. Figure reprinted from our previously published work in Reference [41].
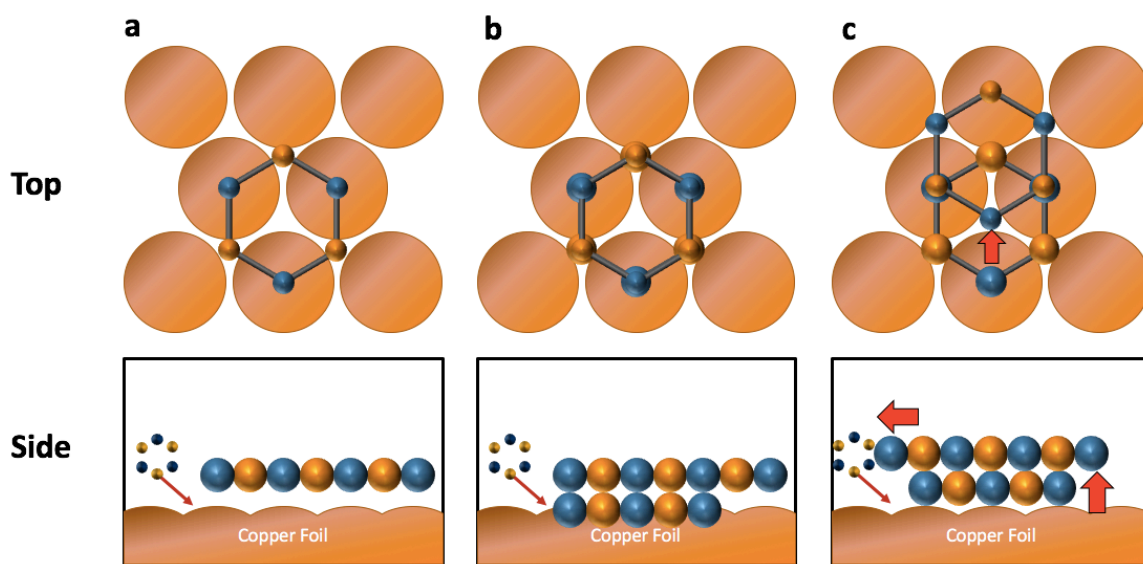
Figure 2.15 Proposed mechanism for the alignment of multiple layers of *h*-BN. (a)-(c) show a chronological representation of the proposed mechanism for how an underlayer growth can produce interlayer aligment and thereby Bernal stacking. (a) First, a single layer of *h*-BN forms on the surface of the copper catalyst such that the nitrogen atoms align to the copper lattice as described in Reference [114]. (b) Next, a second layer forms below the first, aligning to copper via the same mechanism. (c) Finally, as the second layer forms, the top layer relaxes into the ground state for 0˚ rotation, AB stacking, relax by sliding 1.4 Å due to the elevated temperature (>1000˚ C). Figure based on my unpublished analysis of Reference [41].

29
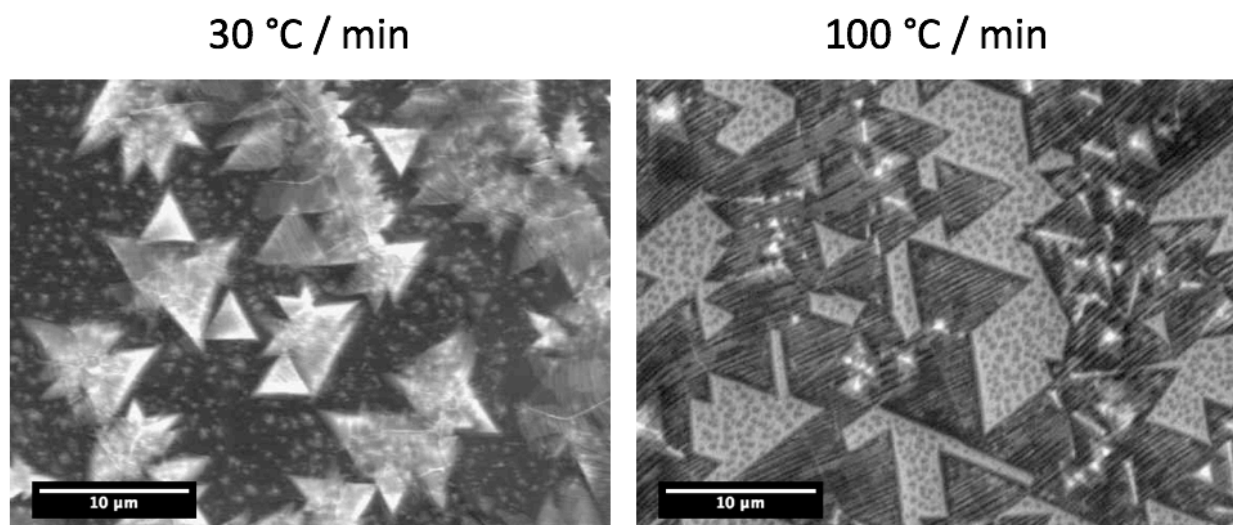
Figure 2.16 *h*-BN synthesis by CVD with varied cooling rates. Two SEM images of *h*-BN grown with high H_2 flow under identical annealing, temperature, precursor, and carrier gas flow (100 sccm H_2) conditions. The first image (Left) shows an *h*-BN sample cooled slowly (30 °C/min) after growth. Thick multilayer crystals form and can be identified by their bright contrast. The second image (Right) shows an *h*-BN sample cooled quickly (100 °C/min) after growth. The *h*-BN crystals are thinner (based on their darker contrast) except for their ad-layer at their centroids and are only partial coverage. Figure based on my unpublished experimental data.

Multilayer formation can also be promoted in this synthesis process by reducing the cooling rate after the growth. Figure 2.16 compares two separate *h*-BN samples prepared on copper with different cooling rates after termination of the precursor flow. The slower cooling rate (30 °C/min) yields a higher coverage of thicker crystals embedded in a full coverage film while the faster rate (100 °C/min) leads to the formation of an incomplete coverage of thinner flakes with multilayer ad-layers at their centroids.

This highlights the role of precipitation of precursor dissolved in the bulk of the catalyst for forming multilayer *h*-BN flakes. During the growth, precursor molecules decompose on the surface of the transition metal foil; while some of these molecules react to form *h*-BN crystals on the catalyst and some dissolve into the bulk. In the fast cooling process, only a small portion of the precursor precipitates from the foil to form small multilayer flakes as seen on the right in Figure 2.16. However, in the slow cooling process, as shown on the left of Figure 2.16, a greater amount of the dissolved precursor precipitate into *h*-BN films on the surface.

2.2.4 CVD Synthesis of *h*-BN on Iron Enabled by Phase Segregation

This section is based on my unpublished experimental results.

100 °C / min	30 °C / min
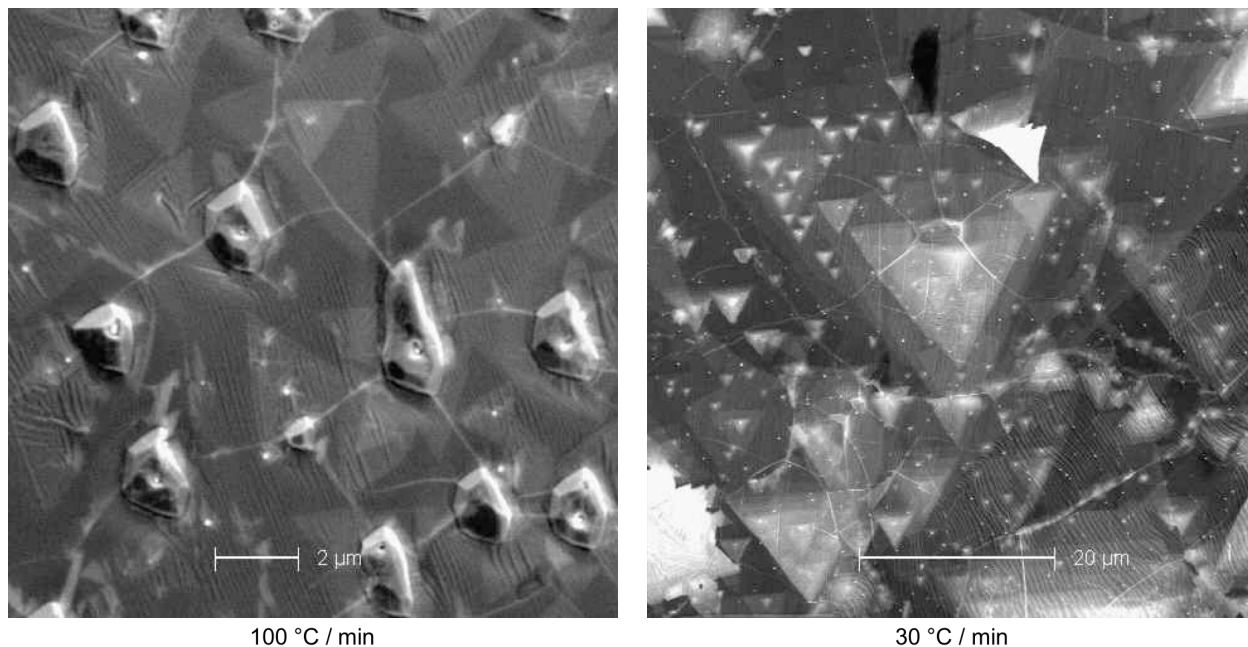
Figure 2.17 SEM images of *h*-BN on Iron versus cooling rate. Two SEM images of separate *h*-BN samples prepared on iron by CVD under identical annealing conditions, temperature (1100 ˚C), gas flow, and growth time (1 hour) are shown with varied cooling rates. (Left) The quickly cooled sample yields smaller (2-5 µm) and thinner (1-3 layer) flakes embedded in a full coverage monolayer with visible 1-3 µm 3D crystals. (Right) The slowly cooled sample yields larger (>20 µm) and thicker (>5-10 layer) flakes. Scale bars are 2 µm (left) and 20 µm (right). Figure based on my unpublished experimental data.

CVD synthesis of *h*-BN on iron demonstrates a similar but exaggerated dependence on cooling rate. **Figure 2.17** shows two separate *h*-BN samples prepared on iron under identical annealing conditions, temperature (1100 ˚C), gas flow, and growth time (1 hour) but different cooling rates. When the sample is cooled quickly (100 ˚C/min), small (2-5 µm) and thin (1-3 layers) flakes of *h*-BN emerge, surrounded by a full coverage monolayer of *h*-BN as depicted in **Figure 2.17** (left). However, notably, a large number of 1-3 µm elevated crystalline features appear on the surface. When the sample is cooled slowly (30 ˚C/min), large (>20 µm) and thick (>5-10 layers) flakes of *h*-BN form as shown in **Figure 2.17** (right). Moreover, the elevated crystalline features do not appear for slowly cooling growth.
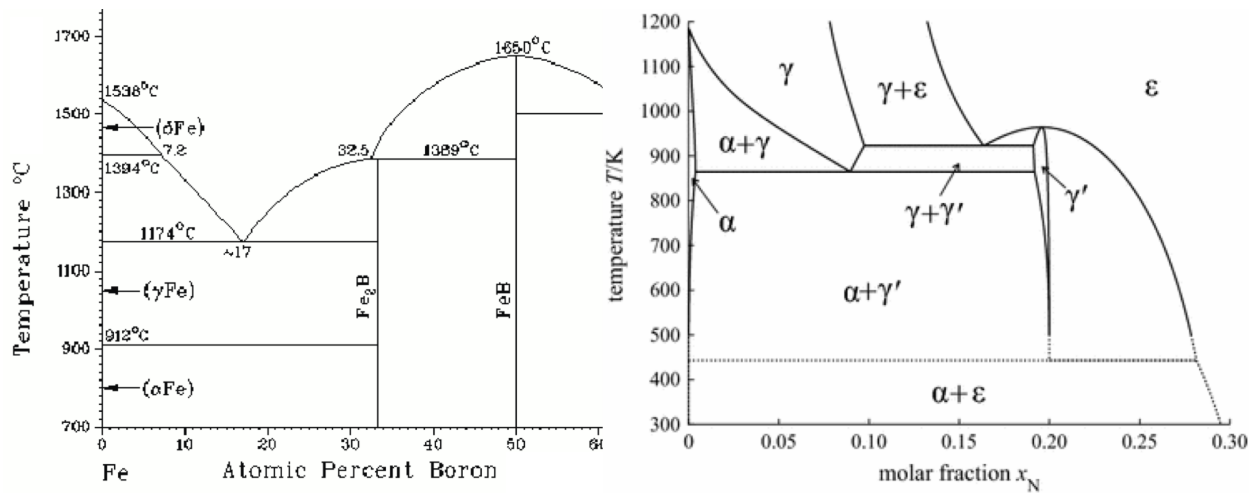
Figure 2.18 Binary iron phase diagrams with boron and nitrogen. (Left) Boron in Iron Binary phase diagram. (Right) Nitrogen in Iron Binary Phase diagram. α-phase iron is the preferred room temperature body-centered cubic (BCC) phase, and γ-phase is the high temperature (>900 ˚C) face-centered cubic (FCC) phase. Phase diagrams reprinted from References [115,116].

I propose the results shown in **Figure 2.17** are due to a high temperature iron phase transformation. **Figure 2.18** shows the binary phase diagram for boron and nitrogen in iron. When iron settles slowly to room temperature, it adopts a body-centered cubic (BCC) α-phase, but when it is heated above 900 ˚C, it reconfigures to the face-centered cubic (FCC) γ-phase. [115,116] This γ-phase, based on the nitrogen phase diagram, will dissolve a larger amount boron nitride precursor. It therefore seems likely that in **Figure 2.17** the three-dimensional crystals on the iron in the quick-cooling sample are γ-phase iron that is near saturation with boron and nitrogen. When it is cooled quickly, the annealing of the iron is quenched and the configuration is locked. When the sample is allowed to cool slowly, the γ-phase iron crystals are able to reconfigure into the bulk α-phase, and the dissolved *h*-BN precursor precipitates on the surface forming large triangular flakes of *h*-BN.

2.2.5 Similarities of Graphene and *h*-BN Synthesis by CVD and Synthesis of *h*-BN/Graphene Heterostructures

This section is based on my unpublished experimental results.

In addition to *h*-BN, the CVD synthesis of graphene has been reported extensively in the literature.[51,58,68,70] In this section, I present evidence that the discussion in Sections 2.2.1 and 2.2.3 also apply to graphene CVD. I conclude that these CVD processes are deeply analogous and that understanding of one can promote that of the other. I further explore how this can be applied for the fabrication of synthetic *h*-BN/Graphene heterostructures.
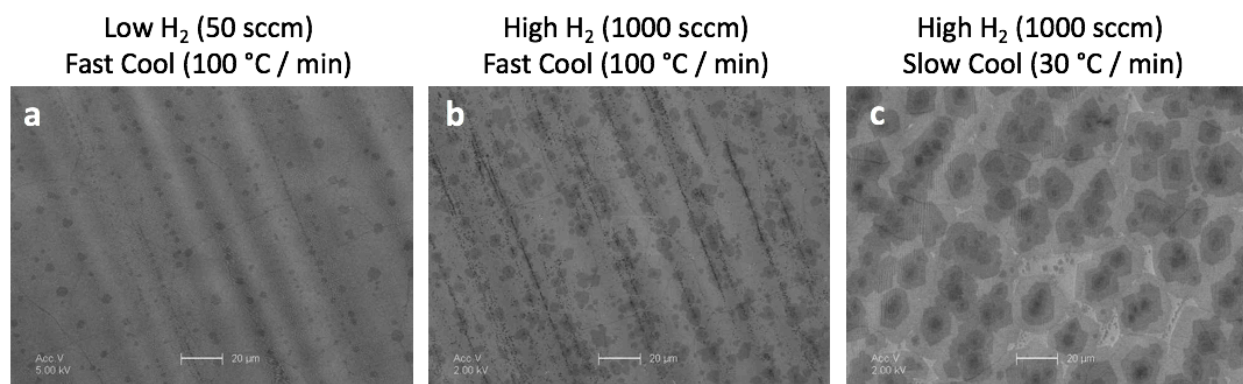
Figure 2.19 SEM images of graphene grown on Cu via CVD under varying cooling rates and hydrogen flow conditions. (a) Graphene synthesized with low hydrogen flow (50 sccm) and a fast cool down (100 ˚C/min). A full coverage monolayer of graphene is visible with low coverage of small (~5 μm) bilayer domains. (b) Graphene synthesized with high hydrogen flow (1000 sccm) and a fast cool down (100 ˚C/min). A full coverage monolayer of graphene is visible with moderate coverage of small (~5 μm) bi- and trilayer domains. (c) Graphene synthesized with high hydrogen flow (1000 sccm) and a slow cool down (30 ˚C/min). A nearly full coverage monolayer of graphene is visible with moderate coverage of large (~20 μm) two to five layer hexagonal domains. All growths occur at low pressure over 1 hour at 1030 ˚C with 2.5 sccm of methane flow. All scale bars are 20 μm. Figure based on my unpublished experimental data.

Figure 2.19 shows SEM images of graphene synthesized by CVD under varying conditions in the same furnace shown in **Figure 2.3**. The growth conditions are identical to those used for the *h*-BN growth except the ammonia borane precursor is replaced for methane and higher flows of hydrogen are observed to be necessary. The graphene in **Figure 2.19**(a) is grown under low hydrogen flow (50 sccm) and terminated with a fast cool down (100 ˚C/min). Similar to *h*-BN grown in this way, a full coverage monolayer forms on the foil with a low coverage of bilayer ad-layers.

By increasing the hydrogen but maintaining a fast cooling rate (**Figure 2.19**(b)), multilayer growth is promoted and moderate coverage of bilayer flakes appears over the sample. This is similar to what is observed for increased hydrogen flows for *h*-BN in **Figure 2.9**. Based on this observation, it is likely that the multilayer regions form by the same growth mechanism in graphene as in *h*-BN in which hydrogen etching allows the precursor to continue to access the

foil throughout the growth and grow additional layers below the first as shown **Figure 2.14**. It is worth noting that the necessary hydrogen flow to achieve this growth is an order of magnitude larger than in the *h*-BN growth. This is because the minimum partial pressure of methane allowed by our mass flow controller is substantially higher than our maximum partial pressure of ammonia borane.

Slowing the cooling rate from 100 ˚C/min to 30 ˚C/min (**Figure 2.19** (c)) yields a moderate coverage of large (~20 μm) two to five layer hexagonal domains as dissolved carbon in the copper is able to precipitate to the surface. This is similar to the emergence of thick triangular flakes at slow cooling rates in *h*-BN as shown in **Figure 2.16** and further confirms that these CVD growths are highly analogous.

A major goal explored throughout the literature for both graphene and *h*-BN CVD synthesis is the growth of their heterostructures.[18,61,64,65,117,118] Since *h*-BN is an ideal substrate and capping layer for graphene, the ability to prepare pristine and rotationally aligned vertical heterostructures through CVD promises to enhance the quality of graphene devices at large scales.[32,119] The ability to grow lateral heterostructures illuminates new methods for manipulating the physical and electrical properties of the films and to create novel atomically thin electronics.[61,65]

An understanding of the similarities in the growth mechanisms of graphene and *h*-BN suggests that pristine samples of both lateral and vertical heterostructures of the two can be prepared in a single process. After first controllably growing partial coverage graphene flakes, *h*-BN can be synthesized around and below the flake in a subsequent step by exploiting our under-layer growth technique.

Figure 2.20(a)-(b) shows an SEM image of a CVD grown heterostructure of graphene and *h*-BN on copper foil prepared in a single process (shown in **Figure 2.20**(c)). First the graphene flakes are seeded with a small amount of carbon contamination in the CVD setup. After annealing for 1-2 hours, ammonia borane is precursor heated to begin the growth of *h*-BN. Because the graphene flakes are only grown in partial coverage, the *h*-BN precursor can access the copper foil to grow both around and under the graphene. The foil is cooled slowly to allow the remaining dissolved precursor to precipitate on the surface.

This process results in both vertical and lateral heterostructures of graphene and *h*-BN. In **Figure 2.20**(a)-(b), bright *h*-BN triangles can be seen overlapping and surrounding the darker graphene six-fold symmetric flower-shaped flake. Moreover, the mirror symmetry lines for both the graphene and *h*-BN are parallel, suggesting that the flakes are aligned. A full coverage monolayer of *h*-BN embeds the graphene flake. Because this sample is fabricated in a single growth process, the interfaces for the material will be pristine. However, further TEM characterization and electrical transport are needed to understand the properties of these heterostructures.
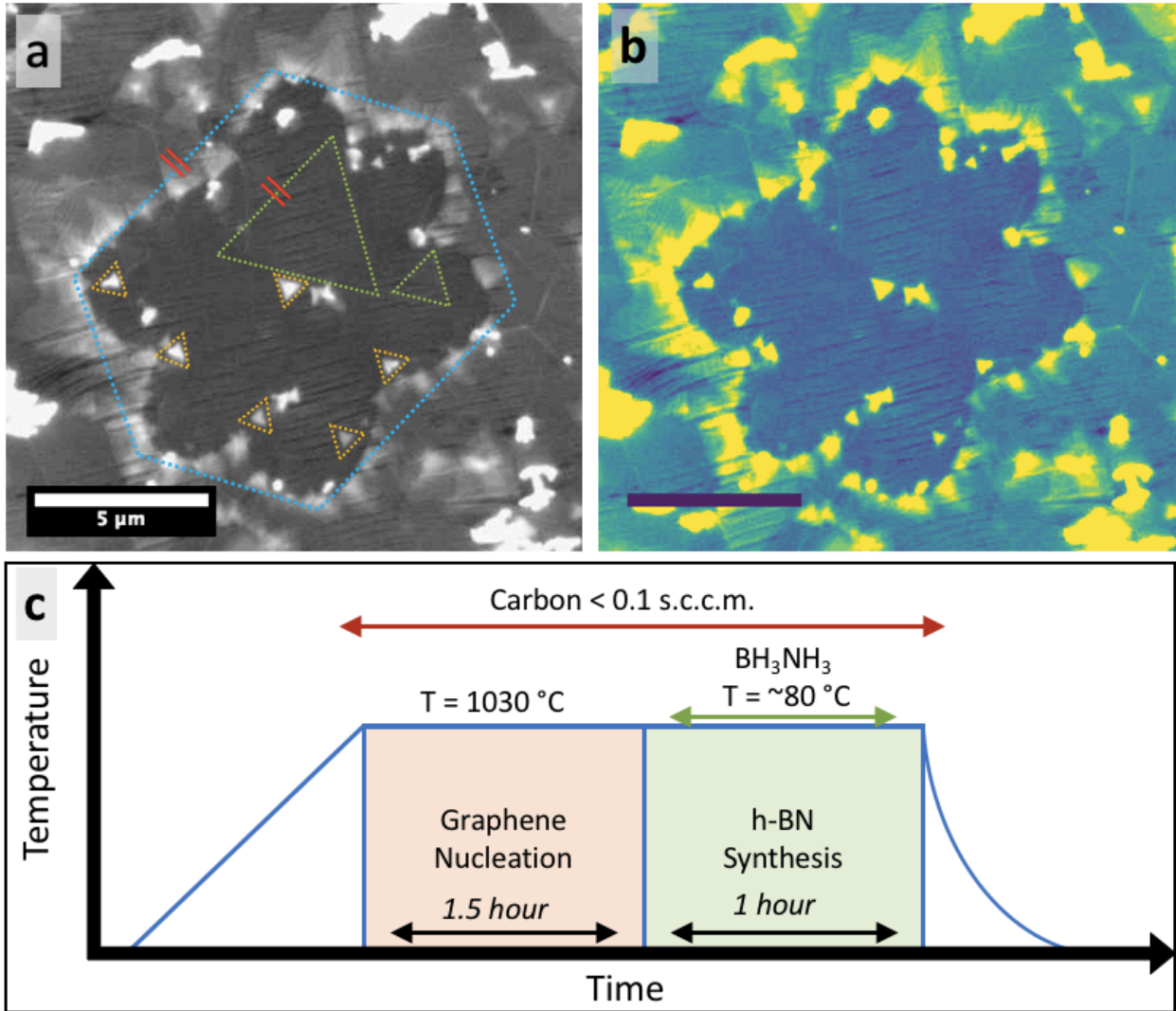
Figure 2.20 CVD grown graphene/*h*-BN heterostructure on copper foil. (a)-(b) An SEM image of CVD grown graphene/*h*-BN heterostructure shown in grayscale (a) and viridis (b). A dark domain of graphene (six-fold symmetric flower highlight by a blue hexagon) is embedded in a full coverage monolayer of *h*-BN. Triangular ad-layers of *h*-BN surround and overlap the graphene. The overlapping *h*-BN triangles are outlined in the grayscale image (thinner flakes in green and thicker flakes in yellow) and the Viridis color scale is used to enhance optical clarity. The red lines indicate that the edge of the hexagon is parallel the edge of the triangle. (c) shows the process flow for the synthesis as described in the text. Figure based on my unpublished experimental data.

2.2.6 Synthesis of AA' Stacked *h*-BN using Borazine Precursor

This section is based on experimental work performed in collaboration with and independently (published in Reference [111]) by Dr. Ashley Gibb under the supervision Prof. Alex Zettl and on unpublished theoretical calculations performed by Dr. Mehmet Dogan under the supervision of Prof. Marvin L. Cohen.

In Sections 2.2.1 & 2.2.3, we demonstrated that CVD synthesis of *h*-BN using ammonia borane as a precursor (under specific geometric, precursor and growth temperatures, pressure, and pretreatment conditions) is monolayer limited for low hydrogen flows and selectively produces Bernal stacked *h*-BN for high hydrogen flows. This is in stark contrast to all other methods of *h*-BN synthesis which preferentially form AA'-stacking

Based on the computed total energies in Table 2.1, both AA' and AB stacked *h*-BN have comparable energies and are unlikely twist 60° from one to the other even under high temperatures. Given the low transition probability between these two stackings, this suggests that the interlayer order relies on the growth mechanics. While we have proposed that AB-stacking arises from each successive layer aligning to the growth substrate independently, this leaves unanswered what causes the necessary anti-alignment to grow AA' multilayered *h*-BN.

To address underlying mechanics for the emergence AA' stacking, we consider additional studies on the CVD synthesis of *h*-BN using borazine precursor. Borazine or $B_3H_6N_3$ shown in **Figure 2.21**(a) is a cyclic compound that alternates BH and NH groups in a six-membered ring. Borazine is isostructural and isoelectronic to benzene, and, like Benzene, it is a liquid at and near room temperature. Liquid borazine is loaded in a one-end sealed quartz tube and chilled between -20 and -10 ˚C to control its vapor pressure. A needle valve is used to precisely control its flow rate into the reaction area. The rest of the setup is identical to that in **Figure 2.3**.

To study the stacking of the *h*-BN grown with Borazine, HR-TEM and SAED of the material are presented in **Figure 2.21**(b)-(c) as grown and characterized by Dr. Ashley Gibb under the supervision of Prof. Alex Zettl. In **Figure 2.21**(b), a mixed mono-, bi-, and tri-layer region of *h*-BN is shown. Consistent with AA' stacking, the honeycomb structure of the *h*-BN is clearly aligned between the different layer number regions. In the inset, a zoomed in picture of the bilayer region is given. In contrast to **Figure 2.12**, there are no additional atoms at the center of the honeycomb, each atomic position is of similar brightness, and the atomic spacing is consistent with the expected B-B/N-N and B-N distances for *h*-BN. The SAED shown in **Figure 2.21**(c) shows that the first order and second order diffraction peaks are of comparable intensities. These details rule out AB, AB1', and AB2' stacking and are consistent with either an AA or AA' configuration. Because AA stacking is unstable based on Table 2.1, we conclude that this CVD synthesis using borazine as a precursor results in multilayer AA' stacked *h*-BN. This is despite the fact that all other details of the synthesis are similar to those discussed in Section 2.2.3.
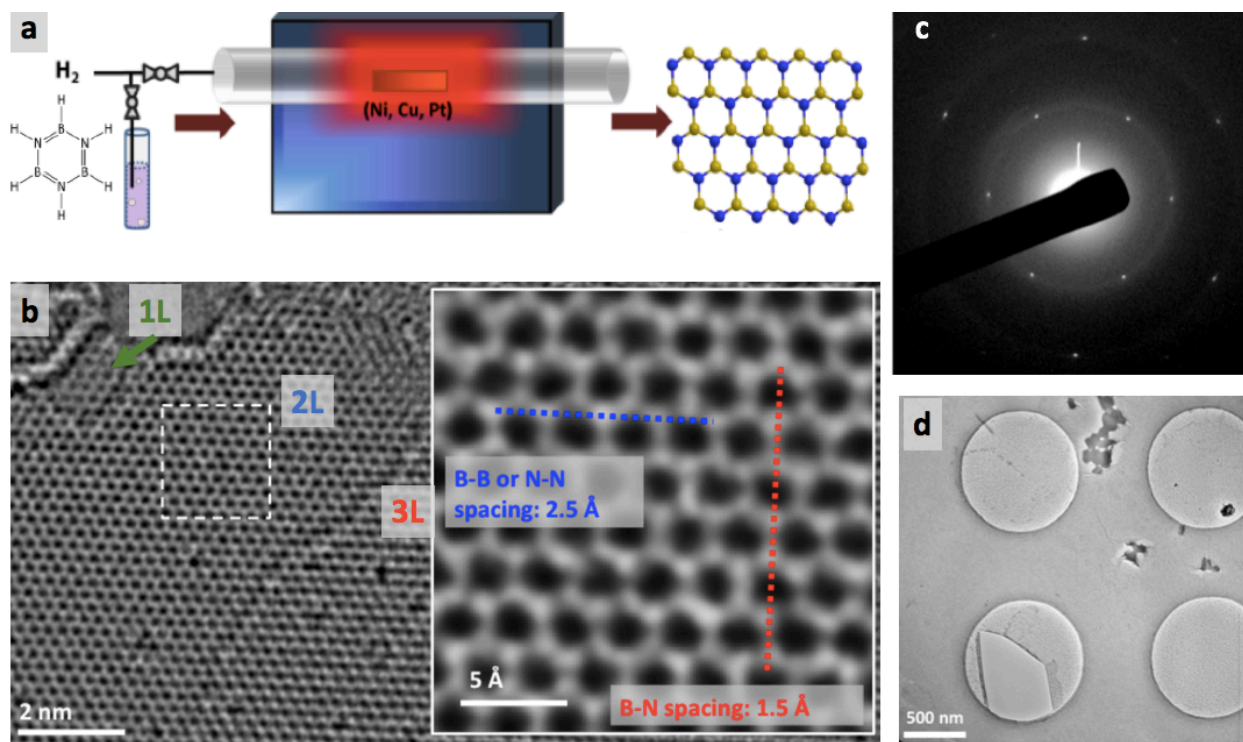
Figure 2.21 AA′-stacked *h*-BN grown by CVD with Borazine precursor. (a) A schematic of Borazine precursor based *h*-BN synthesis technique. The furnace setup is identical to the one shown in Figure 2.3 except a liquid borazine precursor replaces the solid ammonia borane. The liquid borazine is chilled to control its vapor pressure and a leak valve is used to control its flow into the reaction area. (b) An HR-TEM image of the resulting *h*-BN. The *h*-BN honeycomb structures are clearly aligned across the monolayer (1L), bilayer (2L), and trilayer (3L) regions. The inset zooms in on the boxed area of bilayer *h*-BN; the regular hexagonal positions of the atoms with no additional atom at the center of the hexagon rules out AB, AB1', and AB2' stacking. (c) SAED of *h*-BN grown with Borazine. The first order and second order diffraction peaks are of similar intensity. (d) An SEM image showing the thick suspended *h*-BN produced in this way. (a-d) were prepared by Dr. Ashley Gibb based on her experimental data. (a), (c), and (d) are from Gibb et al in Reference [111].
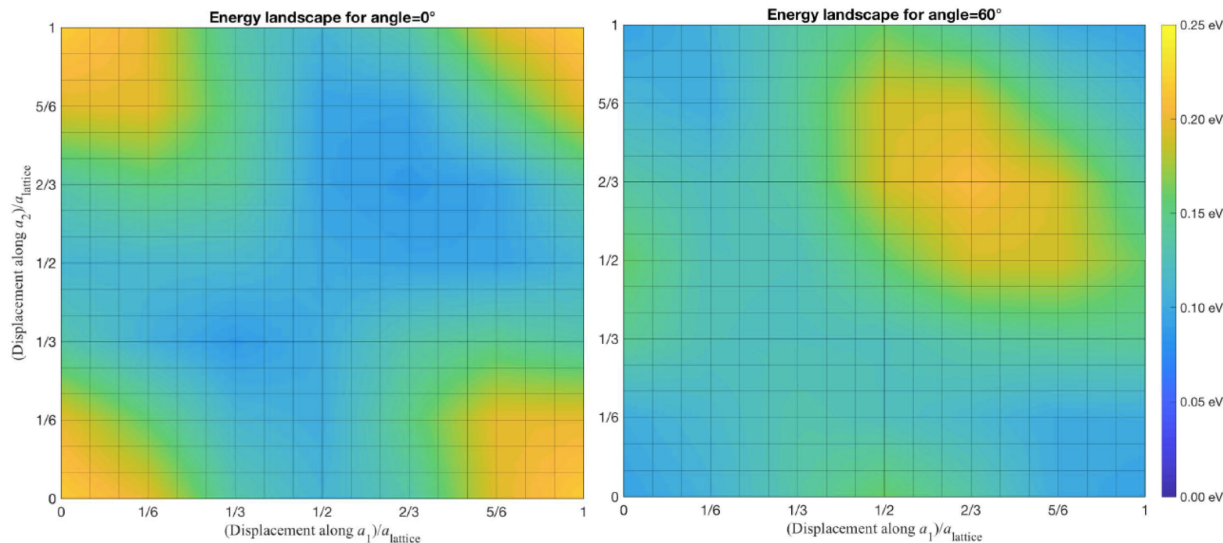
Figure 2.22 Energy landscapes for borazine adsorption on *h*-BN. (Left) Energy landscape for borazine adsorption on *h*-BN with a 0˚ rotation angle. The ground states are for boron stacking on top of nitrogen (AB) and nitrogen stacking on top of boron (BA) at 0.09 eV. (Right) Energy landscape for borazine adsorption on *h*-BN with a 60˚ rotation angle. The ground state is at 0.09 eV for AA' stacking. Figure based on DFT calculations performed by Mehmet Dogan under the supervision of Prof. Marvin Cohen.

I propose that this AA' stacking emerges due to a tendency of the borazine molecules to adsorb stably anti-aligned on *h*-BN. **Figure 2.22** shows the relative energy landscape for adsorption of borazine on *h*-BN at 0˚ (aligned) and 60˚ (anti-aligned) as calculated using DFT by Dr. Mehmet Dogan in the Marvin L. Cohen Group. The minimum energy (relative scale) is 0.09 eV for each case, suggesting that it is equally favorable to adsorb in each orientation. However, due to the two ground states for 0˚ alignment (AB with boron on top of nitrogen and BA with nitrogen on top of boron), the energy landscape is flatter than for the 60˚ case which has a single ground state (AA' alignment).

As a result, the adsorbed molecules are more mobile for the former while the latter is more stable. Moreover, from the AA' ground state (0 displacement), ~0.2 eV is required to rotate to from 60˚ to 0˚ while from the bottom from the bottom left AB stacked ground state, only ~0.05 eV is required to rotate to from 0˚ to 60˚. Given that k_BT is ~0.1 eV under our growth conditions, the AA' ground state is significantly more stable.

38

2.3 Graphene and *h*-BN Transfer and Sample Preparation

After a two-dimensional material is exfoliated or grown, it is often necessary for it to be transferred to a separate substrate to be characterized or used. For example, in order for *h*-BN to be characterized by TEM as in Section 2.2, it is necessary for the flakes to be suspended on a TEM compatible substrate. This transfer requires careful consideration about how best to 1.) remove the material from its initial substrate, 2.) place it on a target substrate, and 3.) post-process for cleanliness.

In this section, I highlight three major transfer techniques used throughout this thesis to transfer graphene, *h*-BN, and other two-dimensional materials. I compare them in terms of applications, strengths, limitations, and cleanliness. In particular, I put an emphasis on using these transfer techniques for the preparation of TEM samples.

2.3.1 Polymer Based Wet Transfer

In the first report of the CVD synthesis of monolayer graphene, Li et al provided a transfer method for the graphene as grown on copper foil.[51] Notably, this method would become the standard technique for transferring CVD two-dimensional materials grown on metal foils for the next decade and was only described in the supplementary materials.

In this method, a thin layer (~100-300 nm) of PMMA (or another similar polymer) is coated on top of a two-dimensional material as-grown on a metal foil. Any material grown on the other side of the foil is then etched (generally by plasma) to expose the bottom surface of the foil. Next, the metal foil is dissolved in a wet etching solution. In order to remove any salt that adsorbs during the metal etching, the PMMA on two-dimensional material stack is transferred to one or multiple water baths. Finally, the stack is scooped from a final water bath onto a target substrate directly from the water, and after drying, the PMMA is removed by some combination of solvent dissolution and/or annealing. This process is illustrated in **Figure 2.23**.

When using this process to transfer *h*-BN grown on copper foil to TEM grids, we use the following specific parameters:

1. PMMA A4 950k is spun on the desired side of *h*-BN on copper foil
2. The PMMA is soft baked at 95 °C for 5 minutes
3. Any *h*-BN on the backside is NOT etched
4. The PMMA/*h*-BN stack is floated on $Na_2(SO_4)_2$ solution (1 mg/ml) until the copper dissolves (approximately 3 hours)
5. The PMMA/*h*-BN stack is transferred sequentially to three water baths (>30 minutes each) using a glass slide.
6. The stack is scooped directly onto the target grid and left to dry (>1 hour).
7. The grid is baked in air on a hot plate at 50 °C for 5 minutes and 95 °C for 5 minutes
8. The PMMA is removed by annealing at 350 °C for 3 hours under 100 sccm H_2 and 300 sccm Ar
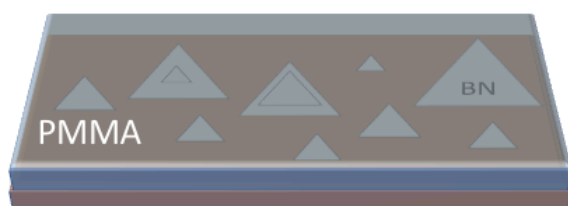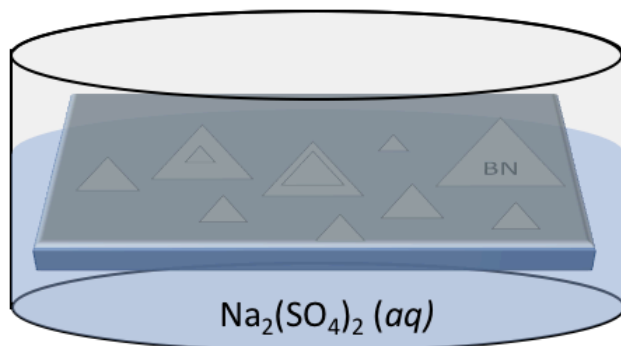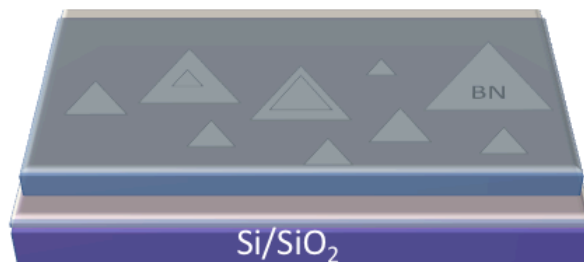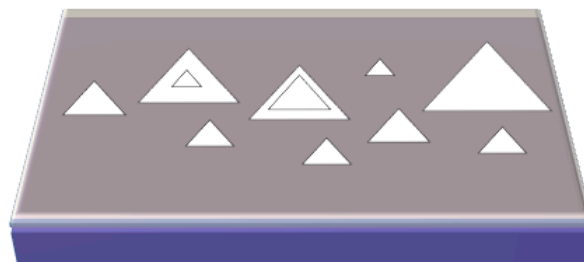
Figure 2.23 Wet Transfer Method. (i)-(ii) PMMA is spun on *h*-BN on copper foil. (iii) The stack of PMMA on copper foil is floated on $Na_2(SO_4)_2$ to dissolve the copper. The copper is removed, leaving the *h*-BN on the polymer. (iv) The polymer/*h*-BN stack is scooped onto a substrate (in this case Si/SiO$_2$) and dried. (v) The polymer is removed by solvent or annealing leaving the *h*-BN on the substrate.

The major strength of using the wet transfer method is that it allows for large continuous films (or flakes) over large areas to be adhered to virtually any water-compatible substrate. Moreover, all that are required to implement this technique are some basic laboratory chemicals and a spin coater. The versatility and ease of this method generally offset its weaknesses; however, for some applications the use of polymer and solvents can be too aggressive and too dirty.

First, of the commonly used transfer methods, the wet transfer is the dirtiest. Because polymer is necessary to support layers of two-dimensional materials, a residue that is difficult or impossible to remove is generally left behind. Moreover, when the stack is scooped out of water, contaminants (or even liquid water) can be trapped between the film and the substrate. These contamination mechanisms prove deleterious for the electrical properties of graphene (reduced mobilities) and can prevent high-resolution TEM imaging.

Second, the methods to remove the polymer are often quite aggressive for certain substrate materials and two-dimensional films. In order to use the wet transfer technique, the substrate needs to be both water compatible (for the scooping) and robust in organic solvents or high-temperatures (for the polymer removal). In this process, fragile substrates and the suspended two-dimensional materials can be broken. This can result in low yields for suspended structures and rule out certain substrates.

Variation: Electrochemical Bubbling Transfer

The wet transfer method can be modified in order preserve the underlying transition metal catalyst. This is important for metals which are difficult to dissolve cleanly (e.g. iron) or expensive (e.g. platinum). In this modified wet transfer process, evolution of hydrogen bubbles between the metal catalyst and the two-dimensional material are used to peel the PMMA supported sheets from the substrate.[120]

After PMMA is spun as described above, the metal substrate is connected as the anode in a water splitting cell. A 5-10 V difference is applied between the sample and a platinum cathode which sit in a common NaOH (0.1 M) bath. The voltage is tuned until hydrogen bubbles visibly form and begin to peel the PMMA. After the PMMA/two-dimensional material stack is fully removed it is transferred to water as in the conventional wet transfer.

2.3.2 Direct Transfer to Quantifoil TEM Grids

While the wet transfer method described in Section 2.3.1 can be used to transfer CVD graphene and *h*-BN to a wide variety of substrates, the need to remove PMMA can often be too aggressive and contaminating for TEM sample preparation. In order to avoid the application and removal of polymer using CVD graphene, Regan et al developed a direct transfer for two-dimensional on metal substrates to TEM grids. [121]
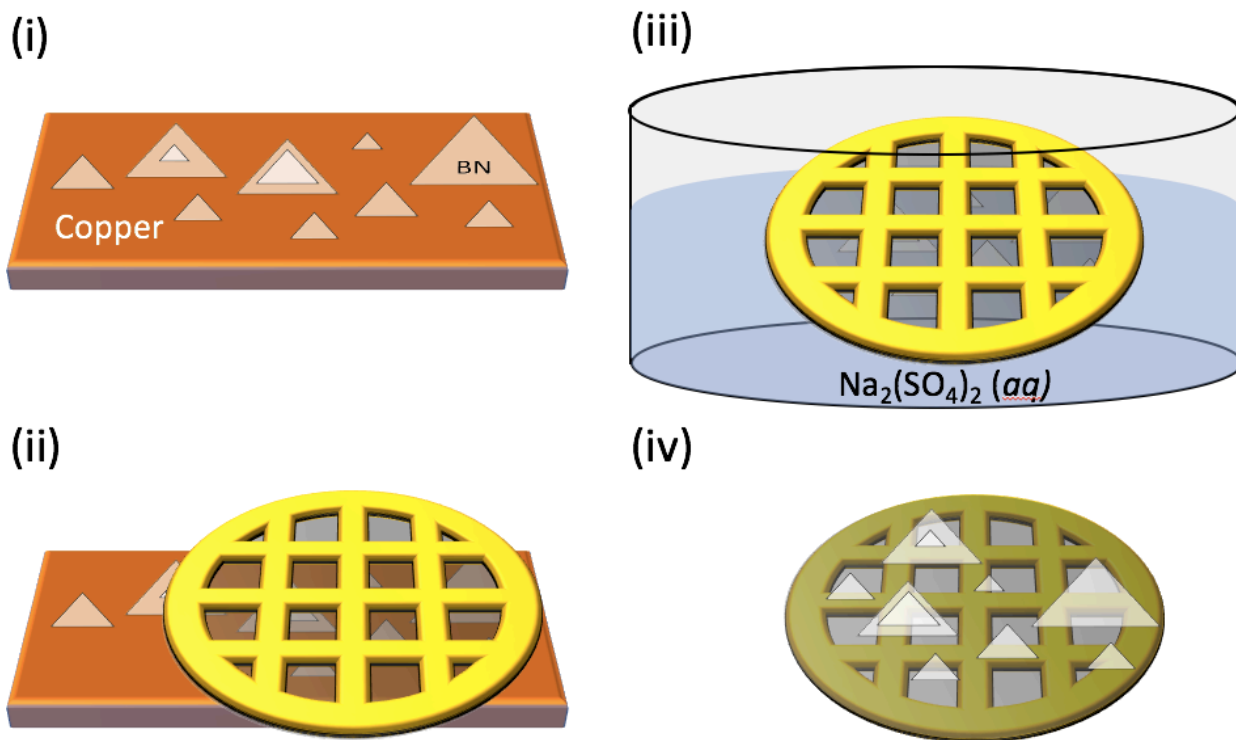
Figure 2.24 Direct Transfer Method. (i)-(ii) a holey carbon TEM grid is adhered to *h*-BN on copper foil using a drop of isopropanol. (iii) The stack of TEM grid on copper foil is floated on $Na_2(SO_4)_2$ to dissolve the copper. The copper is removed, leaving the *h*-BN on the grid. (iv) The grid is removed from the water and left to dry. The *h*-BN is suspended on the grid and ready to be imaged.

In this method (shown in **Figure 2.24**), a holey carbon TEM grid is adhered to a (flattened) metal foil with graphene or *h*-BN on its surface using a drop of isopropanol. As the isopropanol evaporates, the holey carbon is pulled into intimate contact with the layered material on the metal surface. After the sample is dry, the foil is floated in etchant solution, grid side up, until the foil has fully dissolved. The grid can then be transferred to water solutions for removal of any ionic contaminants and removed to dry.

When using this process to transfer *h*-BN grown on copper foil to holey carbon TEM grids, we use the following specific parameters:

1. Without any backside etching, *h*-BN on copper foil pieces are cut to 4x4 mm
2. The foils are rolled flat with a vial and pressed flat with two microscope slides
3. A drop of isopropanol is placed on the foil. Liquid is added until the surface tension of the drop breaks and the foil is evenly wet.
4. A Quantifoil (R 0.6 or R 1.2) TEM grid (Gold 300 Mesh) is placed carbon side down on the wet copper foil.
5. As the foil dries, the sample is monitored under an optical microscope to \ check for adhesion. This is observed visibly as a darkening of the contrast of the grid.
6. After the sample is dried, the foil/grid stack is inverted to check that the grid is adhered to the foil.
7. The foil/grid stack is floated on $Na_2(SO_4)_2$ solution (1 mg/ml) until the copper dissolves (approximately 3 hours)
8. The stack is transferred sequentially to three water baths (>30 minutes each) using a glass slide.
9. The grid is removed directly from the water using sharp inverted grip tweezers and left to dry for at least 20 minutes.

The direct transfer method is particularly useful for its two main strengths. First, the transfer has relatively high-yields for suspending two-dimensional materials on TEM grids. For monolayer graphene, the direct transfer consistently suspends on >90% of the holes on an R2/2 TEM grid. Second, this technique is generally cleaner the wet transfer method. While this is not the cleanest transfer method due to the necessity of wet metal etchants, carbon residues can be avoided, and samples produced are generally clean enough that they can be imaged at high-resolution after beam showing.

However, the direct transfer technique suffers two main weaknesses. The first major weakness is that the direct transfer method is highly limited in scope. This technique can really only be used to transfer from a rigid flat growth substrate onto flexible TEM grid. While it could potentially be modified to transfer from any rigid substrate to any flexible substrate, the number of use cases for this technique are limited. The second limitation is that the use of metal etchant solutions and water still lead to some contamination on the sample. While the contamination is not generally enough to interfere with TEM imaging, chemical adsorbates and residues need to be accounted for.

Variation: Transfer from Si/SiO₂

A similar direct transfer technique can be implemented to transfer two-dimensional materials from Si/SiO$_2$ substrates. This method involves adhering a flexible amorphous carbon TEM grid to the surface of the substrate and then intercalating or etching the two-dimensional material SiO$_2$ interface.

First, using a drop of IPA, a holey carbon TEM grid is adhered to the surface of Si/SiO$_2$ chip covered with flakes of graphene, *h*-BN, or MoS$_2$. Next, the sample is left to dry to form an intimate seal between the grid and the chip. A small drop 1 M NaOH is placed near the edge of the TEM grid. The drop then slowly seeps below the grid peeling the flakes up with it. The chip is then dipped in water and the grid floats on the surface. The grid is then cycled through water baths in order to clean the sample.

2.3.3 Polymer Based Dry Transfer

The final major transfer technique I focus on in this thesis is the aligned, dry transfer. This technique, as described by Reference [122–124], allows for single to few flakes of almost any two-dimensional material to be lifted from an initial substrate and placed on virtually any flat, mechanically rigid target. This technique is necessary for 1.) aligning h-BN flakes to single holes on a TEM grid, 2.) creating stacks of heterostructures, 3.) cleanly transferring exfoliated flakes to TEM grids, and 4.) removing h-BN or MoS_2 from TEM grids.

In this method (shown in Figure 2.25), a polymer stamp is used to lift flakes from a substrate and then be placed on a desired target. First, a polymer stamp is prepared; generally, we use PDMS coated with polypropylene carbonate (PPC). This combination gives the stamp the mechanical flexibility of PDMS coupled with the temperature dependent adhesive properties of PPC. Next, a specially designed transfer stage is used to align and lift the two-dimensional flake onto the stamp. Here, an XYZ stage is used to control the relative position of the polymer stamp with respect to a two-dimensional material flake on a substrate. The stamp is then lowered onto the flake and then lifted to pick up the material. Finally, the flake is aligned and transferred to the desired substrate. A temperature controller is used to tune the adhesive properties of the stamp at each step.

Specifically, when using this process to transfer h-BN grown on iron foils to silicon nitride TEM grids, we use the following steps:

1. A ~1x1x1 mm stamp of PDMS (Gel Pak X4) is placed on a glass slide
2. A piece of transparent Scotch tape is placed over the PDMS stamp. Pressure is carefully applied to avoid forming bubble and to create a smooth curve in the PDMS.
3. 15% PPC in anisole is spun at 1500 RPM for 1 minute on top of the tape
4. Using a transfer stage, the apex of the PDMS stamp is aligned to the desired flake of h-BN on iron foil.
5. The stamp is lowered to contact the sample slowly at 90 °C.
6. The sample/stamp stack is heated to 110 °C and let to sit for 5-10 minutes.
7. The sample is cooled back to 90°C.
8. The stamp is slowly lifted, bringing the flake with it.
9. The target TEM grid (Norcada holey silicon nitride) is loaded in place of the iron foil below the stamp on the transfer stage. Usually the grid is exposed to a light oxygen plasma to enhance its adhesion to the h-BN.
10. The h-BN flake is aligned and lowered into contact with the TEM grid at 90 °C.
11. The temperature is raised to 130 °C and the stamp is slowly lifted, leaving the flake on the grid.
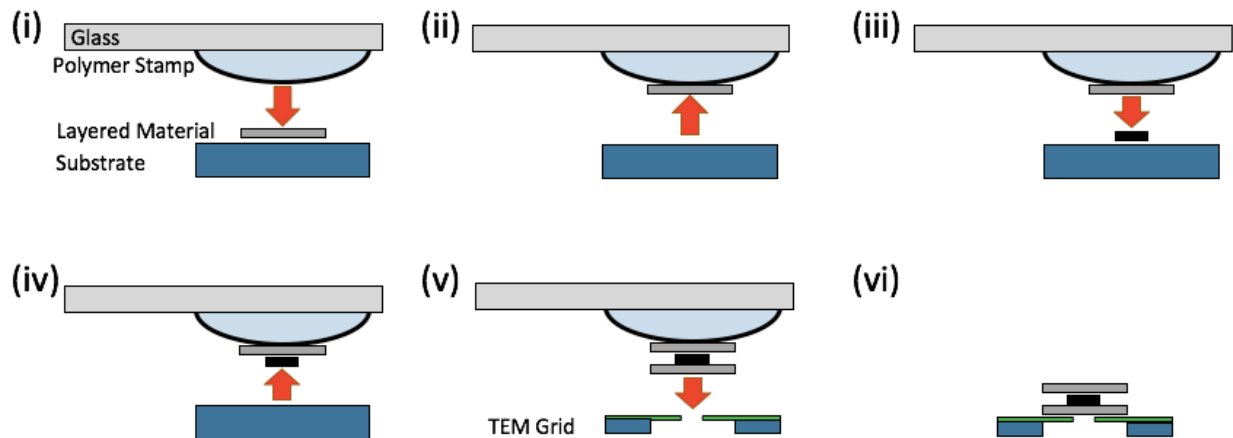
Figure 2.25 Aligned Dry Transfer Technique. (i) A polymer stamp on a glass slide is aligned to a flake of layered material on a substrate. The stamp is then lowered on to the flake. (ii) The stamp is lifted slowly bringing the flake with it. (iii)-(iv) Steps (i) & (ii) are repeated to pick up the desired stack of two-dimensional materials. (v) The two-dimensional material stack is aligned to a substrate and lowered to adhere the stack to the membrane. (vi) The stamp is lifted leaving the stack on the desired substrate. Note: In each step, the temperature and raising/lowering speed are controlled to determine if the flakes adhere to the stamp or substrate.
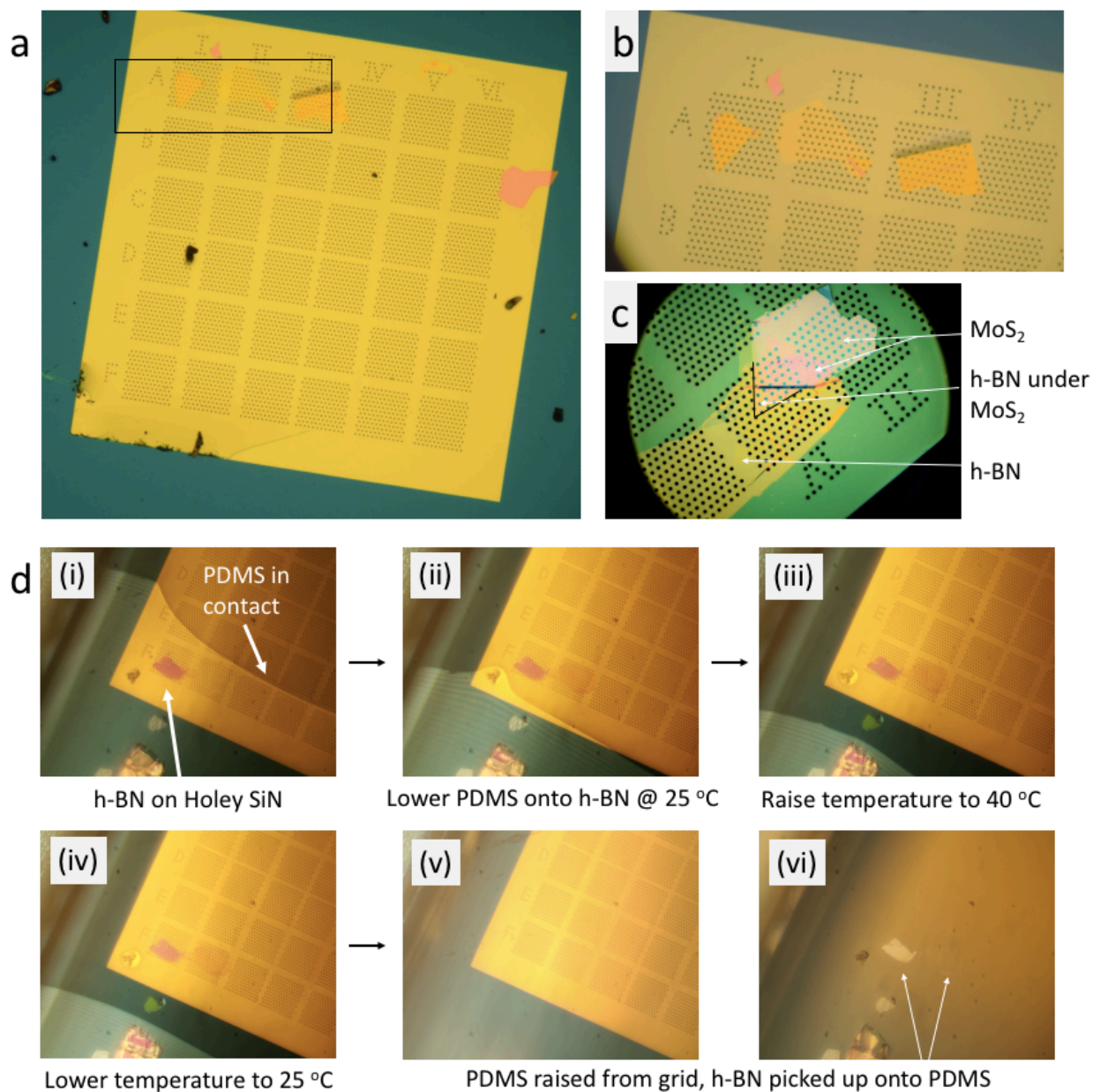
Figure 2.26 Aligned, Dry Transfer Results. (a)-(b) Three few-layered flakes of *h*-BN transferred separately onto a silicon nitride TEM grid. (c) shows an *h*-BN/MoS$_2$ stack transferred onto a silicon nitride TEM grid. Two large separate regions and one overlapping region are formed deliberately to study the materials both together and separately by TEM. (d) The process of lifting an *h*-BN flake from a silicon nitride TEM grid. (i)-(ii) A PDMS stamp is slowly lowered onto the *h*-BN at 25 °C. (iii) After the flake is covered by the PDMS the temperature is raised to 40 °C. (iv) After 5 minutes, the temperature is cooled back to 25 °C, and the stamp is lifted. (v)-(vi) When the stamp is lifted, the *h*-BN flake is removed from the grid and remains on the stamp. Figure based on my unpublished experimental data in collaboration with Gabe Schumm.

46

Figure 2.26(a)-(b) shows an example of exfoliated few-layered *h*-BN flakes transferred to silicon nitride TEM grids. Three flakes on A-I, A-II, and A-III have been aligned and transferred separately. This sample emphasizes the ability of this technique to accurately transfer multiple flakes onto the same sample. It also shows that the method can be used to suspend flakes on TEM grids without compromising the grid. **Figure 2.26**(c) shows a representative image of a stack of MoS_2 and *h*-BN transferred to a TEM grid. Regions of each material are deliberately separated while maintaining a region of overlap in the middle. This is only attainable over the length scales shown due to the accuracy of the aligned transfer method. **Figure 2.26**(d) highlights that the dry transfer technique can be used not only to transfer flakes of two-dimensional materials onto TEM grids but also off of them. This creates an ability to modify and image suspended structure using electron or ion microscopy (as in Section 4.2)and then to transfer them to a different substrate. **Figure 2.26**(d)(i)-(iv) show a flake of *h*-BN being contacted by a PDMS stamp. The PDMS stamp is then lifted leaving a bare grid in **Figure 2.26**(d)(v) and the *h*-BN on the PDMS stamp in (vi).

The aligned, dry transfer technique has several advantages over the first two techniques described. First, this method can be used to produce the cleanest samples.[122] A significant amount of contamination is avoided because no liquid is needed in the process. Second, the aligned, dry transfer method enables new applications that are not accessible for the other techniques. By aligning the sample, precise heterostructures with pristine interfaces can be fabricated, and single flakes can be aligned directly to specific holes on a TEM grid or features on a substrate. Another new application enabled by this method is the use of liquid incompatible substrates. For example, if a wet transfer is used in Section 2.3.5, liquid will be trapped in the wells, leaving the devices useless. Finally, by using this method several times in sequence, flakes can be moved between samples as in Section 4.2, allowing for correlative characterization.

However, the level of complexity and specificity of this technique introduce a few major limitations. First, the setup for implementing the aligned, dry transfer can be difficult to build and quite costly (as described in Reference [124]). Other than a spin-coater (common in nanoscience laboratories), there is no specialized equipment needed for the polymer assisted wet transfer and none at all needed for the direct transfer. Second, a flat and robust sample is needed otherwise the transfer will fail. Finally, as compared to the other techniques, this aligned transfer is very labor intensive. While the other techniques can transfer to 10s of samples in parallel and cover square centimeters over the course of a few hours, the aligned transfer is limited to transferring only a few 100s of square microns per hour. Because the technique is both labor intensive and highly technical, transfers can often frequently fail, further reducing the yield or producing dirty samples.

Variation: Direct Exfoliation with PDMS

For use with exfoliated materials, this technique can be made even cleaner by directly exfoliating with and transferring from PDMS. In this variation, two stamps of PDMS are used to exfoliate flakes of a two-dimensional crystal. For flakes with particularly weak interlayer bonds (e.g. MoS_2), monolayer can be achieved by repeatedly peeling apart two stamps of PDMS with a crystal in the middle. Once monolayer flakes are observed on the PDMS, they can be transferred as normal as described above. This process yields clean films that are never exposed to a carbon-based polymer.

2.3.4 Comparison of Transfer Techniques
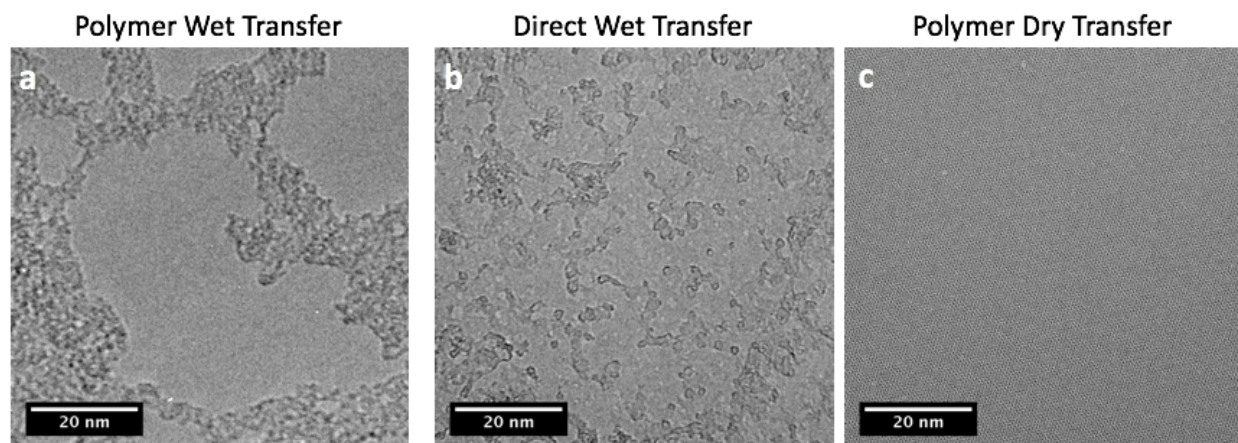
Figure 2.27 Cleanliness of the transfer methods. TEM images of suspended *h*-BN fabricated by polymer wet transfer (a), direct wet transfer (b), and polymer dry transfer (c). Figure based on my unpublished experimental data.

Figure 2.27 shows a TEM comparison of the three transfer techniques described above. Each sample has been prepared carefully and cleaned by annealing at 350 °C under mixed argon (300 sccm) and hydrogen (100 sccm) flow for 3+ hours. Clean areas are preferentially selected for imaging. In the polymer wet transfer shown in **Figure 2.27**(a), a large network of relatively thick contamination forms. While the film is covered by a larger amount of amorphous material than the sample prepared by direct wet transfer (**Figure 2.27**(b)), the distribution of the contaminants leaves large open areas that are convenient for TEM imaging and can be reduced by beam showering.

The polymer dry transfer shown in **Figure 2.27**(c) produces the cleanest sample of the three techniques. The flake shown is exfoliated directly using PDMS and transferred to a silicon nitride TEM grid. Within the image shown, there is no contamination at all; however, on the sample there are sparse networks that resemble the polymer wet transfer. Two vacancies are visible in the top of the image and a moiré pattern is visible due to the twisting of multiple layers.

2.3.5 Mixed Wet and Dry Transfer for Vacuum Sealing

This section is based on unpublished experiments in collaboration with and led by Nishita Deka under the supervision Prof. Vivek Subramanian and Prof. Kristofer Pister as well as Alexander Ungar under the supervision of Prof. Alex Zettl.

It has been previously shown that graphene can be used to seal the pressure of a small cavity in a Si/SiO$_2$ chip.[125,126] By mechanically exfoliating graphene flakes onto an SiO$_2$ well, Boddeti et al found that the pressure inside the hole could be controlled.[127] By leaving the chip in a desired pressure for several days, the pressure inside the well equilibrates by gas diffusion through the SiO$_2$. When the chip is returned to ambient pressure, the well retains its changed state for multiple hours.

However, because graphene can also be used to seal liquids,[128] only dry techniques can be used to prepare a sealed cavity that is devoid of liquid. Therefore, if a large arrays holes (>1000 μm^2) is to be sealed, either a large number of flakes must be transferred in succession or a film scale dry transfer must be implemented.
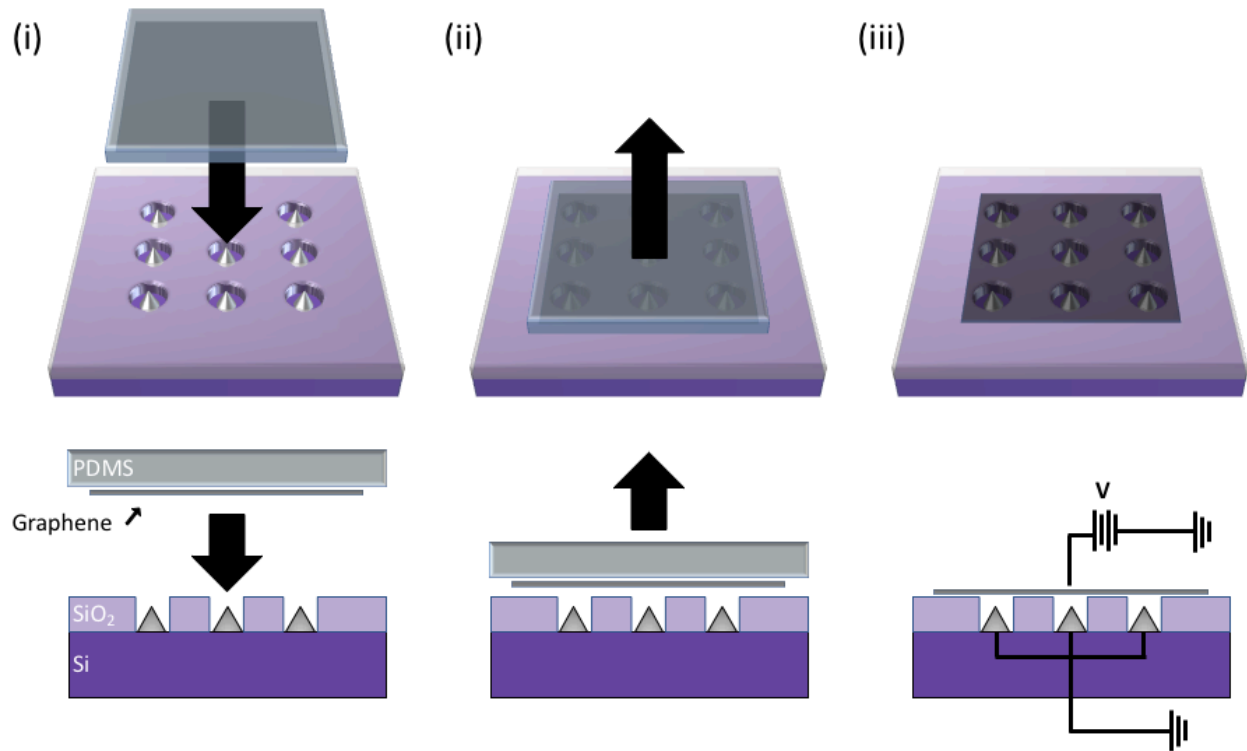
Figure 2.28 The mixed wet and dry transfer method for vacuum sealing. (i) A bilayer graphene membrane transferred to a PDMS stamp is cut to 1 x 1 mm and aligned to an array of conical titanium tips embedded in SiO_2 wells. The stamp is slowly contacted to the chip at 50 ˚C. (ii) The stack is heated to 90 ˚C for 5-10 minutes then the stamp is lifted slowly, leaving the graphene behind. (iii) After the transfer, the graphene is left suspended above the titanium tips. The tips remain grounded as a voltage is applied to the graphene, forming a conventional Fowler-Nordheim field emitter.

Here we explore the use of a novel mixed wet and dry transfer of graphene as an electron transparent electrode for a vacuum electron-emitter. In this technique, three layers of full coverage CVD grown graphene are transferred to a PDMS stamp using a conventional PMMA assisted wet transfer. The PDMS stamp is then cut to 1 mm x 1 mm and used to transfer the graphene as shown in Figure 2.28. The graphene/PDMS stamp is aligned to a Si/SiO_2 chip containing an array of conical titanium tips embedded in SiO_2 wells fabricated and studied by Nishita Deka under the supervision of Profs. Vivek Subramanian and Kristofer Pister. The stamp is slowly brought in to contact with the chip at ~50 ˚C and then heated to ~90 ˚C for 5-10 minutes. The chip is then cooled back to ~50 ˚C and the stamp is slowly lifted.

For the proper execution of this technique, we find that it is important to control the layer number of the graphene and size of the stamp. Using monolayer graphene, we observe by SEM that only low-coverage of torn sheets is adhered; by contrast tri-layer graphene yields a full coverage of mixed mono-, bi-, and tri- layer graphene on the sample. We control the layer

number by transferring additional layers of graphene directly to monolayer graphene on the copper growth substrate.

We also find it is critical to carefully control the size of the PDMS stamp. After transferring ~5 x 5 mm graphene layers to the PDS, the stamp is cut to ~ 1 x 1 mm. This is important because 1.) it is necessary for the graphene layers transferred to be significantly smaller than the target substrate and 2.) larger films are more difficult to delaminate from the PDMS.

Figure 2.28(iii) shows the geometry of the graphene electrode capped emitter device after the transfer. A voltage is applied to the graphene membrane which is suspended ~200 nm above a grounded titanium tip. This forms a conventional Fowler-Nordheim field emitter.
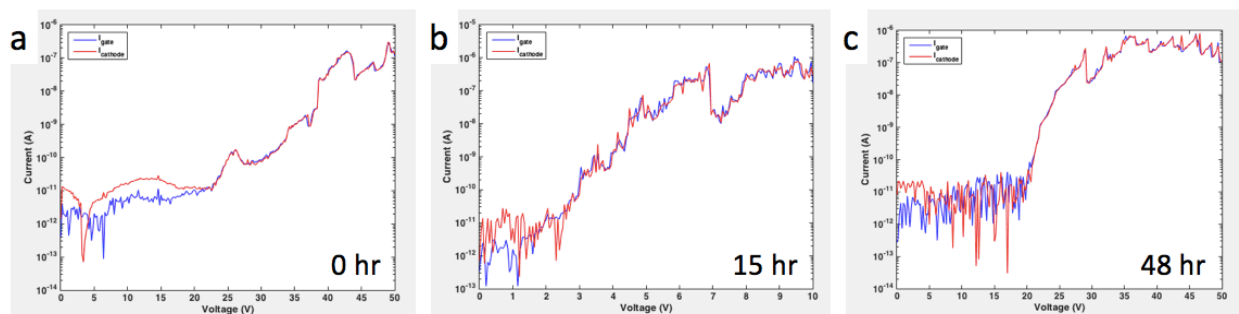
Figure 2.29 I-V characteristics of bilayer graphene-electrode emitter devices. Gate (blue) and cathode (red) currents after no pumping (0 hours), 15 hours, and 48 hours of pumping at high vacuum. Figures courtesy of Nishita Deka.

Figure 2.29 compares the current-voltage characteristics for the bilayer graphene-electrode emitter device across the 200 nm gap from the titanium tip to the graphene drain when it has been pumped down and removed from high-vacuum after 0, 15, and 48 hours. When the sample has not been pumped down at all (0 hours), the current trace has characteristics indicative of a mix of air ionization and field emission. We observe four distinct regions in which the slope is discontinuous and local peaks emerge as would be expected for an emitter in air.[129]

After 48 hours of pumping, the I-V curve takes on the behavior typical Fowler-Nordheim diode. Between 0 to 20 V, there is effectively no current. Suddenly after the onset voltage of 20 V, there is an abrupt increase between 20 to 25 V in current followed by saturation. The contrast between these two measurements indicates that despite both measurements taking place in ambient pressure, the 48 hour pumped sample appears to retain its high vacuum.

Figure 2.29(b) also shows the resulting I-V characteristics after 15 hours of pumping on the same sample. After only 15 hours of pumping, the behavior is not clearly typical of air ionization current or Fowler-Nordheim emission. This suggests that the pressure is at an intermediate state and requires more than 15 hours to fully convert from air ionization current to Fowler-Nordheim.

Chapter 3

Electron beam induced vacancies in *h*-BN: Properties, formation, and nanopore applications

Vacancy defects in two-dimensional materials are comprised of one to several missing atoms in a lattice. As alluded to in Chapter 1, these vacancies represent a hybrid of a zero-dimensional and two-dimensional system as they can have their own unique electronic, optical, and mechanical properties while remaining embedded within the larger two-dimensional sheet. In this chapter, I explore the formation of electron beam induced vacancies in *h*-BN and reveal how it is impacted by both its interlayer stacking and irradiation conditions.

I begin by motivating the study of vacancy defects in two-dimensional materials due to their physical properties and their opportunities to advance research in DNA sequencing, molecular sieving, and artificial atoms. I next describe how *h*-BN vacancies form under electron irradiation and show that these vacancies can be controlled with geometric precise geometric precision. I then take a deep dive into describing the varieties of defects that form in *h*-BN in different conditions including varied stacking sequences, material laminations, and temperatures. Finally, I outline a new method for fabricating nanopore ranging from 0.5 – 5 nm with near atomic precision and detail our efforts to use these nanopores for DNA sequencing.

3.1 Vacancy Defects in 2D materials and Their Applications

Vacancy defects in two-dimensional materials are zero-dimensional features with properties that vary vastly from the bulk. These defects can have different optical and electronic properties from the pristine sheets (e.g. their bandgaps, charge state, and electron scattering) and they can change the emergent measurable properties of the material (e.g. resistivity and tensile strength).[130–134] Moreover, these vacancies represent a physical structure in which there is a small hole in an otherwise impermeable membrane.

Simultaneous advances in atomic resolution TEM and in the isolation and large scale synthesis of two dimensional as outlined in Chapter 2, has resulted in a rapid increase in the understanding of vacancy defects in two-dimensional materials.[71,135,136] These vacancies have been studied in both their naturally occurring and artificially induced forms, and they have been extensively structurally characterized.[100,103,131,137–139]

The fundamental properties of vacancy defects in two-dimensional materials have led to their investigation for the following research directions:

Nanopores for DNA Sequencing

Nanopore sequencing is an emerging, direct-read DNA sequencing technique. Unlike earlier popular techniques, the DNA does not require to be cloned, arbitrarily long read lengths can be achieved, and DNA can be sequenced at a rate of hundreds of bases per second.[140–143] As of this

writing in 2019, commercially available units from Oxford Nanopore using biological nanopores have achieved continuous read lengths of 2.3 Mb at speeds of >450 bases per second.

In the nanopore sequencing method, DNA dispersed in ionic solution is pushed electrophoretically through a few-nanometer pore in an otherwise impermeable membrane. As the DNA translocates through the pore, the ionic current across the pore is continuously measured. The conductivity of the nanopore fluctuates based on the current blockage due to the DNA. The exact current blockage is a direct function of which nucleotide bases are inside of the pore. For a membrane with a thickness comparable to the ~0.3 nm length of a single base, the current blockage maps directly to the species (ATCG) of the nucleotide base that is passing through the nanopore. Therefore, a DNA sequence can be read off directly by measuring the ionic current as the strand moves through the nanopore.

To achieve pore thicknesses that are similar to the length of a single base in DNA, two strategies have been employed. The first of which is to use a tapered pore in a thicker membrane.[144,145] In this way, an hour glass shaped pore is formed in which the central hole is less than a nanometer thick. This is employed for both naturally occurring biological pores as well as solid state silicon nitride pores.

The second strategy is to use a membrane that is roughly as thick as the length of a single DNA nucleobase.[141,146–148] Much of the research on nanopores in two-dimensional materials has therefore focused on their application for DNA sequencing because their few-atom thicknesses lend themselves naturally to forming thin pores. However, these nanopores have never been successfully used to sequence DNA. Efforts to improve the use of two-dimensional material nanopores have focused on more carefully controlling the geometry of the nanopore and the rate of the DNA translocations

Quantum Emission from Defects in 2D Materials

Over the past decade, Nitrogen Vacancy (NV) centers in diamond have sparked an enormous interest in "artificial atoms" in solid-state systems.[149] These defects behave as a stable and optically addressable two-level quantum state, and due to their long coherence times at room temperature, applications such as quantum information storage and transmission, magnetometry, and quantum sensing. However, for noise from dangling bonds and contaminants at the surface can drive decoherence.[150]

In the past several years, research on artificial atoms in solids has seen a major breakthrough in the discovery of quantum emission from point defects in 2D materials at room temperature.[151] It is predicted that these sites are analogous to NV centers. These defects should possess unique advantages; namely, they can simultaneously be on the surface while sitting a large distance from the dangling bonds present at the edge of the material. This avoids obstacles associated with shallow defects in diamond and suggests that these defect states could serve as more sensitive quantum sensors and have longer coherence times.

While it is still unclear which point defects are the source of quantum emission or what is the exact mechanism by which they emit, vacancy defects are still a prime candidate. Further study of the optical properties of vacancy defects in two-dimensional materials promises to advance applications of artificial atomic systems.

Nanoporous materials also lend themselves naturally for use in molecular sieving.[152–155] In this application, the size distribution of a large number of pores in an impermeable membrane is controlled to selectively exclude the passage of molecule or ions greater than a selected size. Therefore, this allows for the filtration of gasses or liquids and can even be used to control the ionic selectivity of a membrane.

Nanoporous two-dimensional materials, either using fabricated or native defects, have been explored for water desalination, gas and ion separation, and electronic transport.[156–159] Controlling the size of the pores in a graphene membrane has resulted in the ability to selectively exclude gases including H_2, CO_2, Ar, N_2, and CH_4.[152,160] Recent advances have allowed for large scale nanoporous graphene membranes to be used as filters for dialysis.[161]

3.2 Formation of Defects in *h*-BN under Electron Irradiation

For the applications described in the previous section, vacancy size and geometry are critical for determining the utility of nanopores and vacancies. While high energy electron beams and ion beams have been used to create the smallest pores observed,[137,146,162] the shape and size of nanopores is limited by the beam geometry. For graphene nanopores, for example, pore size has traditionally been limited to 3 nm or greater and their shapes can only be minimally controlled.[146]

One method that has been used to create structures below the minimum resolution limit of a patterning technique is to leverage the intrinsic etching properties of a material. For example, to pattern sub-10 nm radius AFM tips, a diffraction limited SiO_2 (~1 µm) pad is patterned using photolithography. The SiO_2 is then undercut using a KOH etch of the underlying silicon. In this step, the silicon is anisotropically etched to its crystallographically favored facet to form a ~ 10 nm radius tip at the center of the SiO_2 pad (which subsequently falls off). This technique allows for features to be made substantially below the resolution limit of the lithography technique used and is the predominant method used to make AFM tips.

Analogously in a two-dimensional system, it has been previously demonstrated that when *h*-BN is exposed to 80 kV electron irradiation in TEM, vacancies are etched and atomically precise edges are formed along the sheet's favored nitrogen zig-zag direction.[71,104,105,138,163,164] The size and shape of these defects are determined by the material properties and not the geometry of the beam.

Figure 3.1 shows HR-TEM images comparing vacancies formed by an 80 kV electron beam in graphene and *h*-BN. The edges of the vacancy created in graphene are highly irregular, with no preferred edge termination. This results in a pore that has a vaguely round but ultimately non-deterministic shape and a difficult to control size. The vacancies *h*-BN, by contrast, have a deterministic triangular shape. The two vacancies shown in the monolayer region of *h*-BN are parallel triangles, terminated by nitrogen zig-zag edges as sketched in Figure 3.2 below.
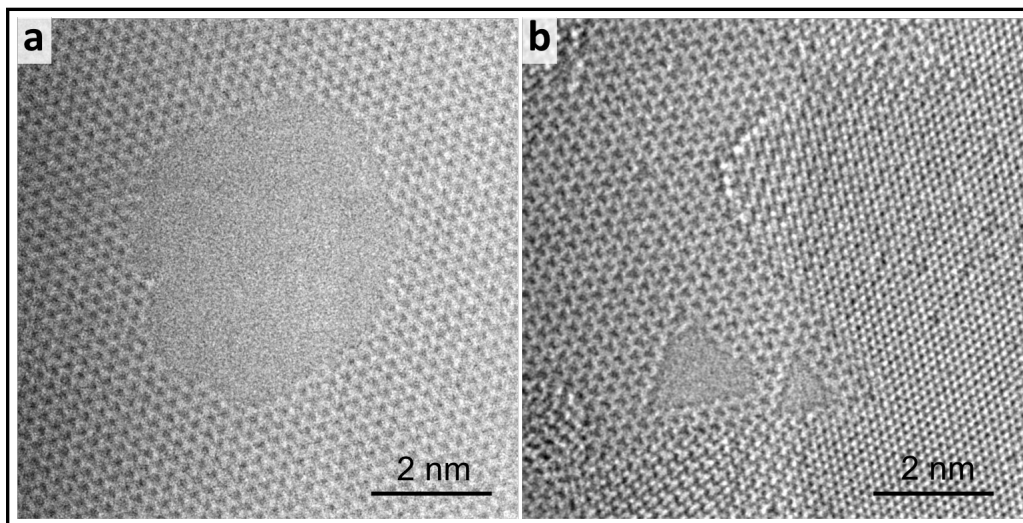
Figure 3.1 Electron beam induced vacancies in Graphene and *h*-BN. Vacancies produced in graphene (a) and *h*-BN(b) in-situ under diffuse electron irradiation using TEM mode on the TEAM 0.5 aberration corrected HR-TEM at 80kV. The graphene nanopore has irregular edges with no preferred termination whereas the *h*-BN pore has pristine zig-zag edges. Figure reprinted from our previously published work in Reference [42].

3.2.1 Atomic Ejection by Electron Knock-on Damage

The most widely accepted (though not without controversy) mechanism for the formation of defects and pores in two-dimensional materials is electron knock-on damage.[103,104,138,165,166] In this effect, high energy electrons collide with and transfer their kinetic energy to atoms in a crystal. When the energy of the electron is above a minimum threshold, the scattering of the particle can eject atoms from the lattice. The minimum electron energy for the ejection of a given atom (known as the knock-on threshold) is met when the maximum energy transfer (based on conservation of momentum) exceeds the minimum ejection energy of the atom. The maximum kinetic energy transfer for a given electron beam energy and atomic mass is found by reducing the following equations to solve for the final kinetic energy of the atom:

Definition of relativistic total energy:

$$E^2 = (pc)^2 + (mc^2)^2$$

Definition of relativistic kinetic energy:

$$T = E - mc^2$$

Conservation of energy:

$$E_e + E_a = E_e' + E_a'$$

Conservation of momentum:

$$p_e + p_a = p_e' + p_a'$$
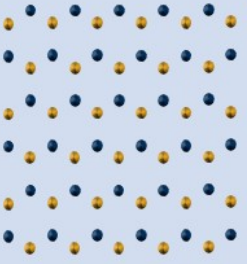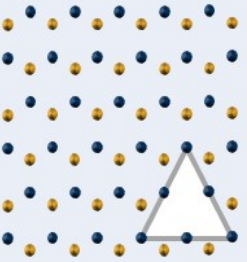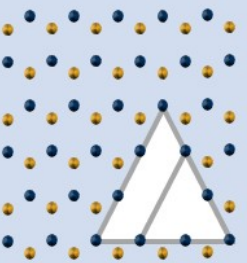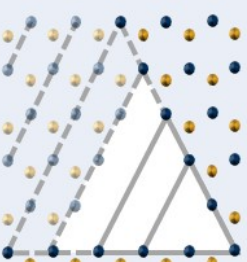
This gives a maximum total kinetic energy transfer of:

$$T_{max} = \frac{2E(E + m_e c^2)}{m_a c^2}$$

Where E_e and E_a are the energy of the electron and atom respectively, p_e and p_a are their respective momenta of the electron, and m_e and m_a are their respective masses. The prime symbol differentiates the final energy or mass from the initial. From the equation above, the total kinetic energy that can be transferred to an atom is inversely proportional to the mass of the atom. Therefore, lighter atoms can receive more energy from an electron beam, and the maximum kinetic energy transfer increases with increasing mass.

While every bulk and edge carbon atom in graphene have the same binding energy and mass and, therefore, knock-on threshold, the diatomic lattice of *h*-BN has different knock-on thresholds for different atoms. For *h*-BN, the knock-on threshold for sp^2-bonded bulk Boron is 74 kV while the knock-on threshold for Nitrogen is 84 kV.[166] For an electron beam between these energies, only boron will be ejected in a pristine sample. Once a boron mono-vacancy forms, the knock-on threshold for the under-coordinated edge nitrogen atoms is below 80 kV, and it too can be ejected (in addition to any undercoordinated edge borons) by the 80 kV TEM.

3.2.2 Defect Formation in *h*-BN Monolayers

Index	Image	Area
N = 0		$A = 0$
N = 1		$A = (2a_o)^2 \dfrac{3\sqrt{3}}{4}$ $= 0.11 nm^2$
N = 2		$A = (3a_o)^2 \dfrac{3\sqrt{3}}{4}$ $= 0.25 nm^2$
N = n		$A = ((n+1)a_o)^2 \dfrac{\sqrt{3}}{4}$ $= (n+1)^2 * 0.027 nm^2$

Figure 3.2 Cartoon of electron beam induced vacancy growth in monolayer *h*-BN. Vacancies in monolayer *h*-BN grow as quantized triangles to retain the nitrogen zig-zag edge termination. For each quantized triangular pore size, an image shows the atomic configuration of the pore and its area. Nitrogen and boron atoms are shown in blue and gold respectively. The interatomic spacing, a_o, is 1.45Å. Figure reprinted from our previously published work in Reference [42].
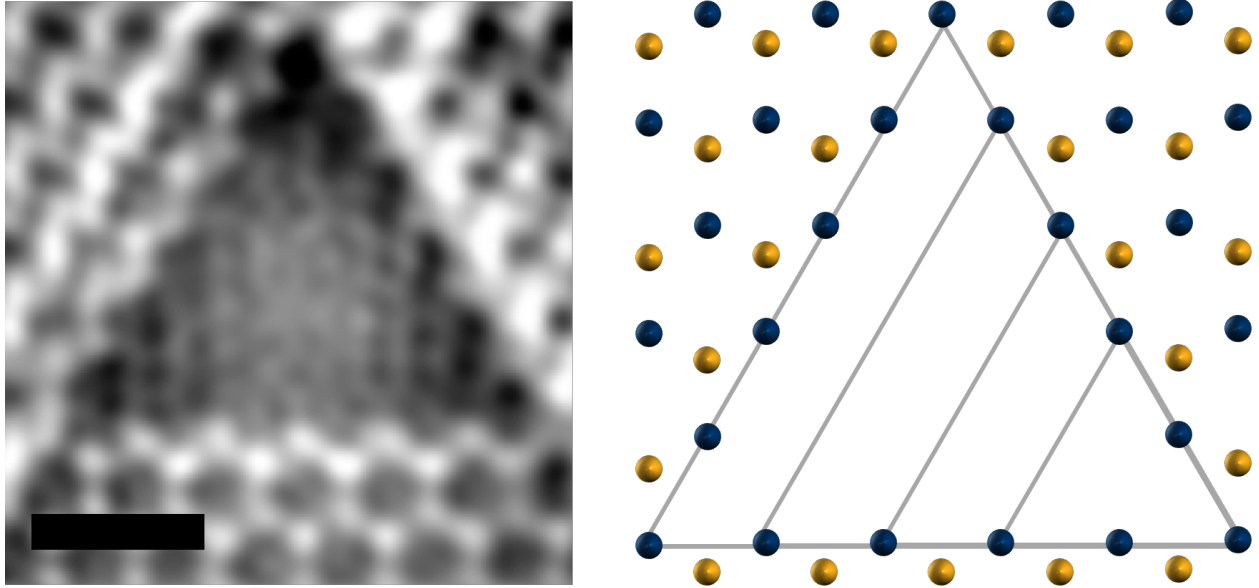
Figure 3.3 An HR-TEM image (left) of an *h*-BN vacancy with one monolayer edge (the bottom) and a schematic (right) of monolayer vacancy of the same size. The scale bar is 0.5 nm. Figure based on our previously published work in Reference [41].

Because for an 80 kV electron beam, sp^2 bonded bulk nitrogen atoms are not ejected while bulk boron atoms are, and because edge boron atoms are ejected immediately while edge nitrogen atoms are ejected more slowly, the vacancies in monolayer hexagonal boron nitride form the predictable geometries shown schematically in **Figure 3.2** and in HR-TEM in **Figure 3.3**. Triangular vacancies form by the process illustrated in **Figure 3.2** as follows:

1. A boron is ejected forming a monovacancy
2. A single under-coordinated nitrogen adjacent to the boron monovacancy is ejected in a slow step (order 10s-100s of seconds at 80 kV)
3. The ejected Nitrogen brings its bonded boron in a fast step leaving a nitrogen zig-zag edge (quasi-immediately)
4. Steps 2-3 repeat until the beam is turned off

This leads to the formation of triangular vacancies with perfect nitrogen terminated zig-zag edges. These triangular vacancies can be fabricated from 1 to ~40 atoms in side length, comprising an atomically precise nanopore of 0.25 to 10 nm. This gives rise to a quantized area given by the following equation:

$$A = \frac{\sqrt{3}}{4} a_0 (n + 1)^2 = 2.7 \text{ Å}^2 \ (n + 1)^2$$

Where n is any integer value and denotes the number of nitrogen atoms along the edge and a_0 is the boron to nitrogen bond length.

Figure 3.3 shows an example HR-TEM focal series reconstruction of a triangular *h*-BN vacancy along with a schematic. The bottom monolayer edge can be clearly seen to be a zig-zag edge. Moreover, closer inspection shows that the lattice is comprised of alternating darker and brighter atoms at every other site. The dark atoms, which are nitrogen, form the zig-zag edge.

3.2.3 Defect Formation in Bernal Stacked *h*-BN

This section is based on my original unpublished experimental data and supporting unpublished theoretical results from Dr. Mehmet Dogan and Prof. Marvin L. Cohen.

In the previous section, I described the formation of nitrogen zig-zag terminated vacancies in monolayer *h*-BN and demonstrated how they form precise triangular holes in the material due to the preferential ejection of boron. In multilayer samples, however, the vacancy defects are able to interact with adjacent layers.[132] This can affect the types and shapes of vacancies in the sheets.

For example, in AA′-stacked *h*-BN, interlayer interactions have been shown to dominate the properties of its electron irradiation induced defects. Out-of-plane covalent bonds are found to form across layers at boron mono-vacancy sites in bilayers.[132] Also, along the edges of extended vacancies in these bilayers, covalent bonds form between the layers and the edge relaxes to resemble a boron nitride nanotube with an extremely short radius of curvature. Theoretical calculations show that the local atomic structure at these defects and edges has a massive impact on the electronic properties of the material with the interlayer coordination determining if it is a metal or insulator.

Because each lattice site in AA′-stacked *h*-BN contains a boron directly on top of a nitrogen, interlayer covalent bonds are available at each site in the crystal. However, by forming these bonds, the three-fold rotational symmetry of the lattice is lost and the vacancy shape is no longer deterministic. In Section 2.2.3, I described a new synthesis technique for producing Bernal stacked *h*-BN; for this stacking, the relative shift and rotation between the layers leaves only half of the lattice sites with a stacked boron and nitrogen. Moreover, because the layers are aligned, defects may preferentially preserve the plane *p3* symmetry of the monolayer.

In this section, I consider the role of Bernal-stacking in the electron beam induced formation of extended vacancies in *h*-BN. While previous studies of AA′-stacked *h*-BN have characterized the geometry and edge-termination of multilayer vacancies using atomic resolution TEM and unveiled their electronic properties using first principle calculations, there have only, so far, been a limited number of structural studies on vacancies in AB stacked *h*-BN. Therefore, little is currently known about the differences between the extended vacancies in these two configurations and what role the stacking plays.

Here, I describe how we characterize the formation of vacancies in AB-stacked *h*-BN using conventional TEM and study their atomic structures using aberration-corrected, sub-angstrom resolution TEM. Based on these experimental studies, first principle calculations are performed to deduce the electronic properties of the vacancies.
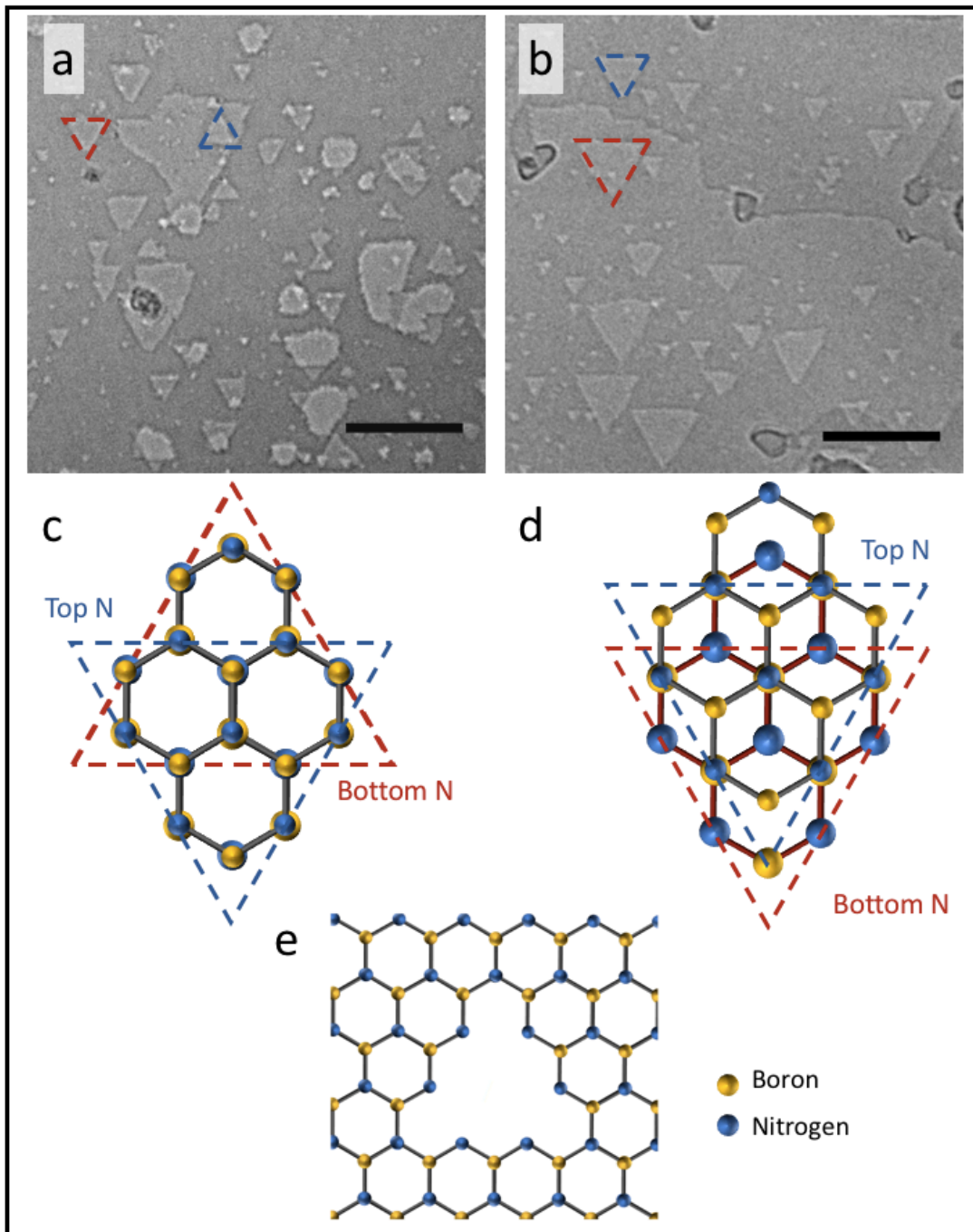
Figure 3.4 Vacancies in AA′- and AB-stacked *h*-BN. (a) and (b) show conventional TEM images of vacancies formed under 80 kV electron irradiation in AA′- and AB-stacked *h*-BN respectively. (a) In the AA′-stacked *h*-BN, we observe anti-parallel triangular vacancies in separate layers, highlighted by red and blue triangles. We also observe bilayer vacancies with no preferred shape or edge termination. (b) In the AB-stacked *h*-BN, we observe only parallel triangles in every layer as highlighted by red and blue triangles. (c) A schematic of bilayer AA′-stacked *h*-BN. The nitrogen zig-zag edges are highlighted in the top (blue) and bottom (red) layers. (d) A schematic of bilayer AB-stacked *h*-BN. The nitrogen zig-zag edges are highlighted in the top (blue) and bottom (red) layers. (e) A schematic of a prototypical monolayer *h*-BN nitrogen zig-zag edge terminated triangular defect. (c-e) Boron is shown in gold and nitrogen is shown in blue. Figure based on my unpublished experimental data. Scale bars are 10 nm.

Figure 3.4 illustrates the differences between vacancies that form in AA′- and AB-stacked *h*-BN, schematically and imaged using conventional TEM with a beam energy of 80 kV (JEOL 2010). In the AA′-stacked sample shown in Figure 3.4 (a), we observe triangular vacancies that form with two anti-parallel orientations as denoted by the red and blue triangles. This is consistent with the observations in References [71,138,167]. Vacancies with irregular edge structures are also observed as highlighted by the purple circle in Figure 3.4 (a). Because the change in contrast across the edge of these vacancies is double that of the triangular vacancies, we infer that the irregular vacancies are bilayer.

By contrast, in the AB-stacked *h*-BN shown in Figure 3.4 (b), all of the triangular vacancies that form are parallel. Moreover, the edges of each vacancy are nearly straight, and we do not observe any irregular shaped vacancies.

We attribute the difference in the vacancy morphology to the difference in interlayer orientation. For AA′-stacked *h*-BN, the adjacent layers are rotated by 60° and registered such that the boron and nitrogen atoms in the top layer sit directly above the nitrogen and boron atoms in the bottom layer respectively as shown in Figure 3.4 (c). Due to the 60° rotation between the layers, the triangles defined by the three nitrogen-terminated zig-zag edges in each pair of adjacent layers are anti-parallel as sketched. Because the nitrogen terminated zig-zag edges define triangular vacancies (as described shown in Figure 3.4 (e)), these vacancies in adjacent layers of AA′-stacked *h*-BN should be anti-parallel. This agrees directly with our experimental observation.

When vacancies in two layers of AA′-stacked *h*-BN overlap, Alem *et al* showed that interlayer covalent bonds form.[132] This interlayer covalent bond breaks the threefold rotational symmetry of the *h*-BN layers and disturbs the preferential formation of triangular vacancies. Because the nitrogen-terminated zig-zag edges in each layer are offset by a 60° rotation, multi-layer vacancies do not preferentially form triangles. As observed in Figure 3.4 (a), these multilayer vacancies do not have a deterministic shape.

By contrast, AB-stacked *h*-BN is comprised of aligned layers in which each successive layer is offset by one atomic bond length as shown in Figure 3.4 (d). Because every single layer in the lattice is now aligned, the triangles defined by the nitrogen zig-zag edges and the vacancies they define are now parallel in each separate layer as sketched. This explains the formation of exclusively parallel vacancies as observed in Figure 3.4 (b).

The parallel orientation of these vacancies allows for the deterministic fabrication of vacancies in *h*-BN. This process is described in Section 3.3 and Reference [42]. It also allows for the fabrication of nested triangular vacancies as shown in Figure 3.5.
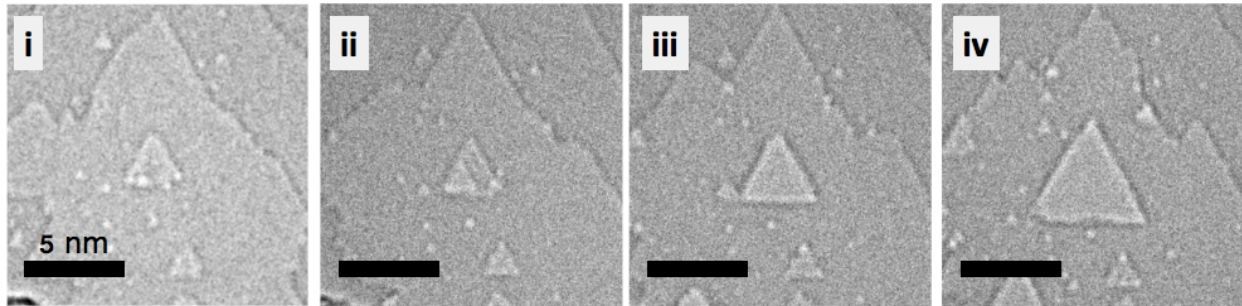
Figure 3.5 Growth of a bilayer nanopore in AB-stacked *h*-BN. (i)-(iv) shows the growth of a bilayer nanopore from a few-atom monolayer vacancy to a 6 nm bilayer pore. (i) Initially, the vacancy starts as a one-edge bilayer few atom defect. (ii) Then, the pore grows to ~1.5 nm with two bilayer edges. (iii) The vacancy grows to 4 nm with three bilayer edges. (iv) The pore grows to 6 nm retaining its bilayer edges. No edge ever reverts to monolayer. All scale bars are 5 nm. Figure based on my unpublished experimental data.

Because in AB-stacked *h*-BN adjacent layers share the same three-fold *p3* symmetry (just as in monolayer *h*-BN), the intersection of triangular vacancies also preserves this symmetry, thus allowing for the formation of bilayer triangular vacancies. Figure 3.5 shows the growth of a vacancy in a monolayer of *h*-BN as it merges with a larger vacancy in the next layer to form a bilayer AB-stacked *h*-BN nanopore.

In Figure 3.5 (i), a small single- or few-atom vacancy has formed within a triangular monolayer region that is embedded within a bilayer area (~2 nm triangle). By panel (ii), the vacancy has grown to ~1.5 nm and two of its edges have aligned with the large vacancy to form bilayer edges. In panel (iii), the vacancy in the two layers have merged to form a ~4 nm triangular bilayer vacancy. In panel (iv), the triangular bilayer vacancy has grown to ~6 nm while retaining its bilayer edges and triangular geometry.

Unlike the irregular multilayer vacancies that form AA′-stacked *h*-BN, stable bilayer triangular pores form in the AB-stacked sheets in when irradiated under the same conditions. These bilayer edges keep their triangular shape and bilayer edges as they continue to grow as shown in Figure 3.5 (iii) & (iv). Moreover, the edges never revert to two separate monolayers or merge to form a trilayer edge.

While the interlayer orientation is sufficient to describe the alignment of vacancies in multiple layers, it does not fully explain why the vacancies should merge to preferentially form a bilayer edge. We suggest two mechanism by which bilayer edges emerge. The first possible mechanism is that bare monolayers of *h*-BN are less stable under electron irradiation. This could be because a second layer provides protection from chemical sputtering from the electron beam or because the second layer increases the kinetic scattering threshold for the layers among other reasons. In this scenario, whenever a small monolayer region of *h*-BN is exposed, the layer is etched back to form a bilayer edge.

The second mechanism we suggest is that a covalent bond forms between the edge atoms. In this scenario, as the triangular vacancies in the top and bottom *h*-BN layers intersect, the edge atoms covalently bond together. This would form a stable edge that maintains its structure as it is irradiated and reforms as it is etched. These two mechanism can be distinguished by their structural properties as in Reference [132].
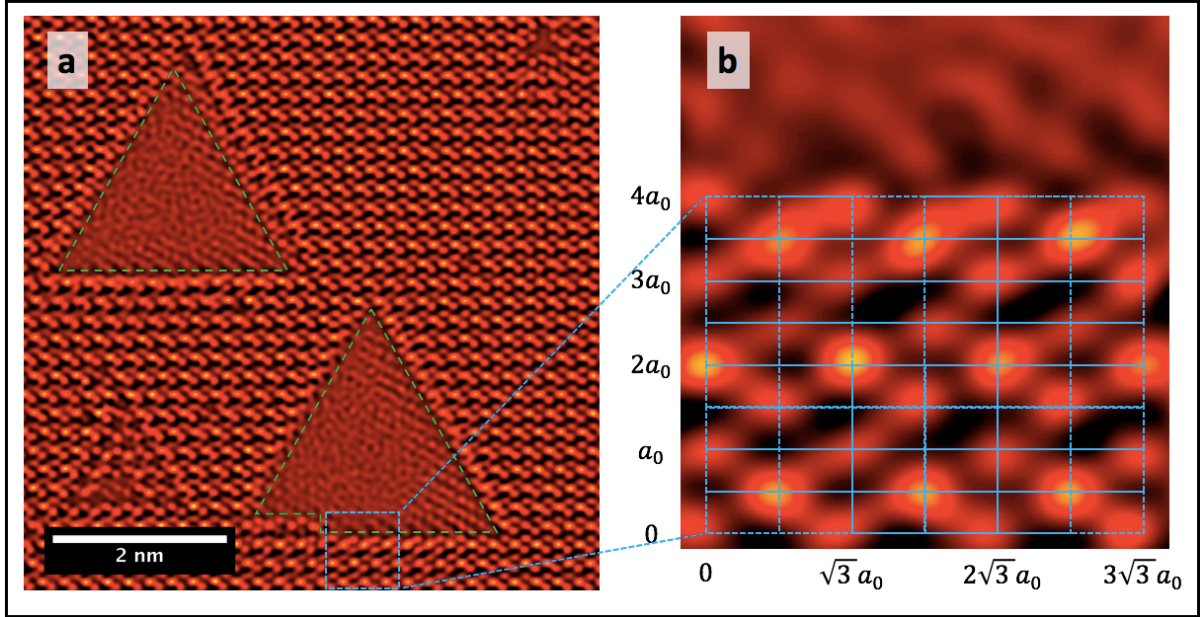
Figure 3.6 HR-TEM of triangular vacancies in AB-stacked *h*-BN. (a)Triangular vacancies produced in *h*-BN under 80 kV electron irradiation using TEM mode on the National Center for Electron Microscopy's TEAM 0.5. Two 3 nm bilayer pores (highlighted in green) are present with several smaller monolayer vacancies. The image is presented using the 'Fire' lookup table to distinguish between vacuum (black and dim red), single boron and atoms (bright red dots), and stacks of boron and nitrogen (yellow dots). (b) A zoomed in section of the edge highlighted by blue dashed box in (a). An overlaid grid denotes spacings of half the interatomic distance ($a_o/2$) in y and (($\sqrt{3}$)$a_o/2$) in x; all of the positions for the relaxed, undisturbed lattice fall on this grid. Figure based on my unpublished experimental data.
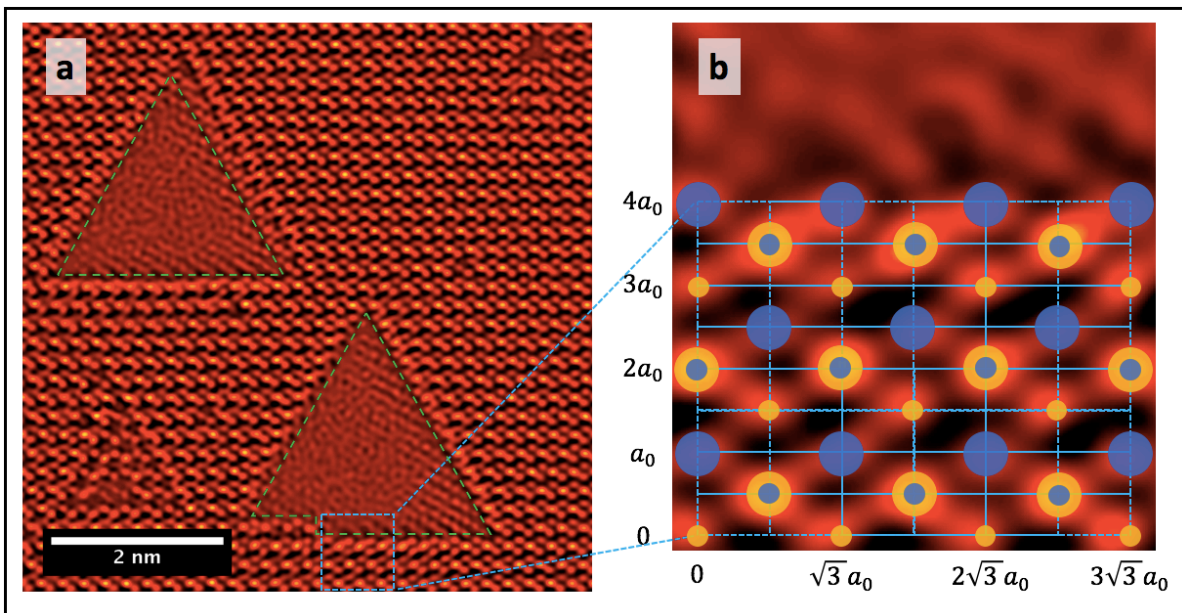
Figure 3.7 HR-TEM of triangular vacancies in AB-stacked *h*-BN with overlaid atoms. (a) The same TEM focal series reconstruction from **Figure 3.6**(b). The same zoomed in section of the edge from Figure 3.6 with the atoms species overlaid. Boron is shown in yellow while Nitrogen is shown in blue. Atoms in the 'top' layer are shown smaller than the 'bottom' layer. Figure based on my unpublished experimental data.

In order to understand the structure of its edges, we performed HR-TEM on vacancies in bilayer AB-stacked *h*-BN using the TEAM 0.5 microscope at Lawrence Berkeley National Laboratory. Figure 3.6 shows the exit wave reconstruction (mac tempas) of a focal series stack (-10 nm to 70 nm) of 80 monochromated TEM images acquired at 80 kV. The image is presented using the 'Fire' lookup table to distinguish between vacuum (black and dim red), single boron and atoms (bright red dots), and stacks of boron and nitrogen (yellow dots).

Figure 3.6(a) shows an overview of two 3 nm bilayer vacancies in the AB stacked *h*-BN as highlighted by the green triangles. Multiple smaller monolayer vacancies are also present. The edge highlighted by the blue dashed box is presented in Figure 3.6(b). An overlaid grid denotes spacings of half the interatomic distance ($a_o/2$) in **y** and (($\sqrt{3}$) $a_o/2$) in **x**; all of the positions for the relaxed, undisturbed lattice fall on this grid.

We find that each double atom stack of boron and nitrogen falls exactly on the grid of the undisturbed lattice, independent of how close they fall to the edge. In Reference [132], Alem et al show = that the curvature induced by covalent bonding at the edge of bilayer AA′-stacked *h*-BN compresses the measured in-plane interatomic distance for atoms near (not at) the edge by approximately ($a_o/4$). For our measurement, as shown in Figure 3.6, we can exclude this possibility.

At the edge, in Reference [132], Alem et al show (that the measured in-plane interatomic distance is compressed by an even larger ($a_o/3$). In our measurement, however, it is more difficult to precisely assign atomic position at the edge. This is because for the single atoms, including those that comprise the edge, distortions to their shapes and positions from the reconstruction introduce uncertainty to the measurement. However, despite this uncertainty, the positions of the single atoms appear to fall much closer to their relaxed position than the ($a_o/3$) compression observed in Reference [132].

Figure 3.7 reveals the atomic species near the edge as deduced from the positions of the boron-nitrogen atomic stacks and monolayer vacancies. We observe that the edge is comprised of a single nitrogen zig-zag chain in only one of the layers (shown as the bottom layer); the other layer terminates at its nitrogen zig-zag edge along the boron-nitrogen stack zig-zag. Each layer therefore appears to terminate independently with only one layer reaching the edge of the vacancy.
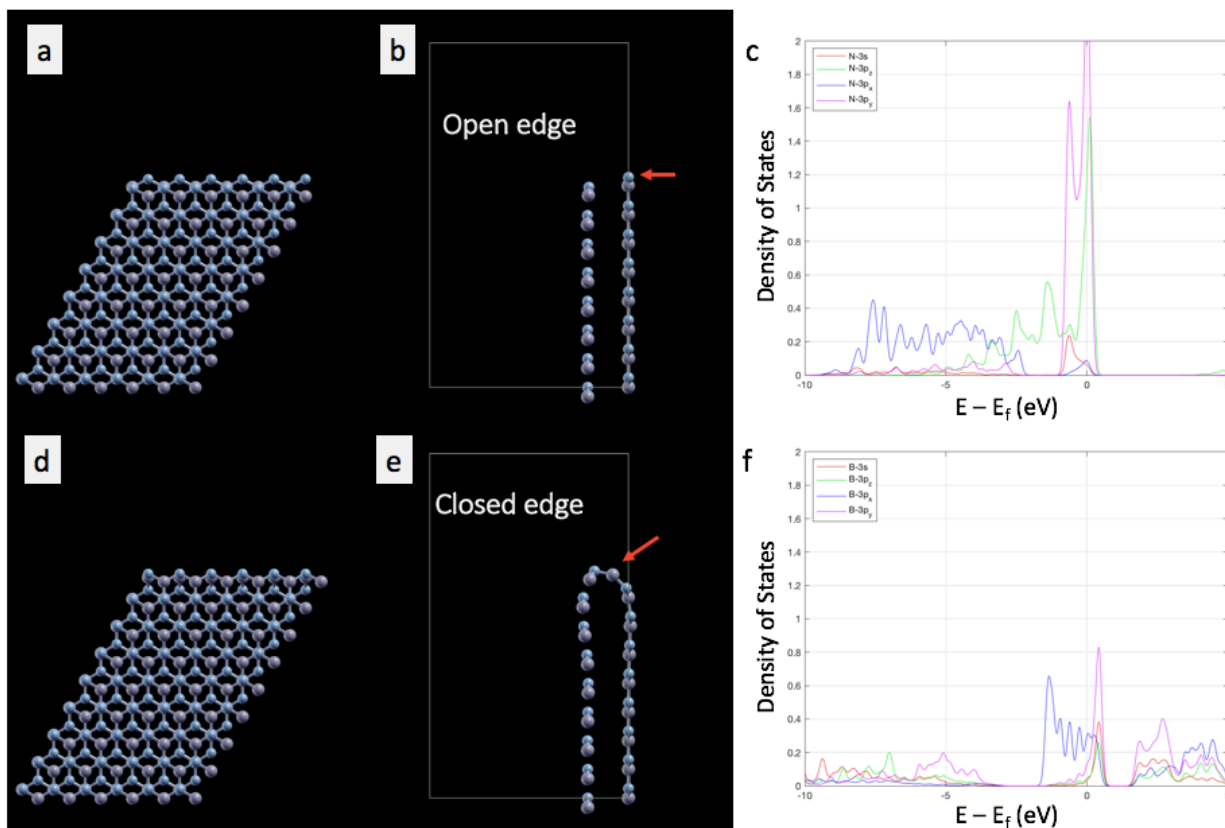
Figure 3.8 Simulated edge structures and electronic structures in AB stacked bilayer *h*-BN. Two possible edge structures that exhibit no in-plane compression away from the edge and their density of states plotted versus energy. (a)-(b) Schematics from the top (a) and side (b) of the 'open edge' structure for bilayer *h*-BN in which two layers terminate in adjacent nitrogen zig-zag edges, and no interlayer covalent bond forms. (c) The density of state plotted versus energy for the nitrogen zig-zag edges. (d)-(e) Schematics from the top (d) and side (e) of the 'closed edge' structure in which in which two layers terminate in adjacent nitrogen zig-zag edges, and an additional chain of boron atom inserted in between forms a covalent bond between the layers. (f) The density of states plotted versus energy along the boron edge. This figure is prepared based on unpublished theoretical work by Dr. Mehmet Dogan under the supervision Prof. Marvin Cohen.

To further understand the properties of the edges of the AB-stacked bilayer vacancies, we again collaborate with Dr. Mehmet Dogan and Prof. Marvin L. Cohen. In order to explore the possible atomic and electronic structures, the Cohen group simulated the structures using density functional theory (DFT). Atomic models for >12 possible edge configurations, both with and without interlayer covalent bonds, were modelled based on the HR-TEM reconstruction shown in Figure 3.7. Using DFT, the structures were simulated and structurally relaxed to minimize the lattice strain energy. Then, the electronic band structures were calculated. We parsed the possible structures to find candidates that demonstrated no in-plane distortion of the atoms near the edge.

Figure 3.8 shows the two bilayer edge configurations that result in virtually no in-plane compression or curvature for the lattice other than for the atoms at the edge. The first structure is the 'open edge' case in which two monolayer edges sit directly on top of one another without bonding. The model for this structure) matches directly with our observed atomic species and positions in Figure 3.7. Figure 3.8(c) shows the calculated density of states for the open edge

structure. Unlike the edges studied in AA′ stacked *h*-BN,[132] we find a large occupied density of states at the fermi energy, suggesting that these edges are metallic.

The second structure we found that does not exhibit in-plane distortions is shown in Figure 3.8(d)-(e). In this 'closed edge' case, an additional boron atom at the edge allows for a covalent bond to form between the nitrogen zig-zag edges. Consistent with our HR-TEM study, the only observed lattice compression in this conformation is for the single chain of nitrogen atoms along the edge. However, we do not observe an additional boron atom along edge of the vacancy, and the atomic positions in Figure 3.8 do not match those in Figure 3.7. In contrast to the AA′-stacked *h*-BN studied in Reference [132], we find an occupied density of states at the fermi level for this covalently bonded edge.

Our observations suggest that the bilayer edges formed under 80 kV electron irradiation in AB-stacked *h*-BN vary markedly from those that form in AA′-stacked *h*-BN.[132] First, the bilayer edges in AB-stacked *h*-BN appear to be metallic while those in the conventional AA′-stacking are insulating. This is an important difference as it suggests that AB-stacked *h*-BN could potentially be used for its 1D conducting edges. Second, the formation of bilayer edges in AA′-stacked *h*-BN occurs because of stable interlayer, but the formation of bilayer edges in AB-stacked *h*-BN appears to be a kinetic effect. This highlights that both the roles of the chemistry in the TEM column and knock-on effects have major roles in determining defect geometry in materials.

In addition to studying the bilayer edges of AB-stacked *h*-BN, we also considered monolayer vacancies in a single layer of the two-layer stacks. Figure 3.9 shows two such monolayer vacancies as imaged in TEM and modelled theoretically. In the first (shown in Figure 3.9(a)-(c)), 10 boron atoms and 6 nitrogen atoms are missing from one layer in a bilayer AB-stacked *h*-BN. The relaxed theoretical model (which contains no interlayer covalent bonds) matches the experimental HR-TEM structure almost exactly. Based on these theoretical calculations (again performed by Dr. Mehmet Dogan under the supervision of Prof. Marvin L. Cohen), we find that the edges of this vacancy are metallic.

In the second vacancy (shown in Figure 3.9(d)-(f)), 3 boron atoms and 1 nitrogen atom are missing. Again, our experimental HR-TEM is fully consistent with the relaxed theoretical model with no interlayer covalent bonding. When this smaller structure is modelled theoretically, however, we find that the edge is semiconducting with a 1.86 eV gap. This result suggests that tuning vacancy size in AB-stacked *h*-BN is a new method for tuning the gap of its vacancies. The ability to create vacancies with tunable bandgaps in the visible range may be useful for *h*-BN in optoelectronics and photon emission.[134,151,168]
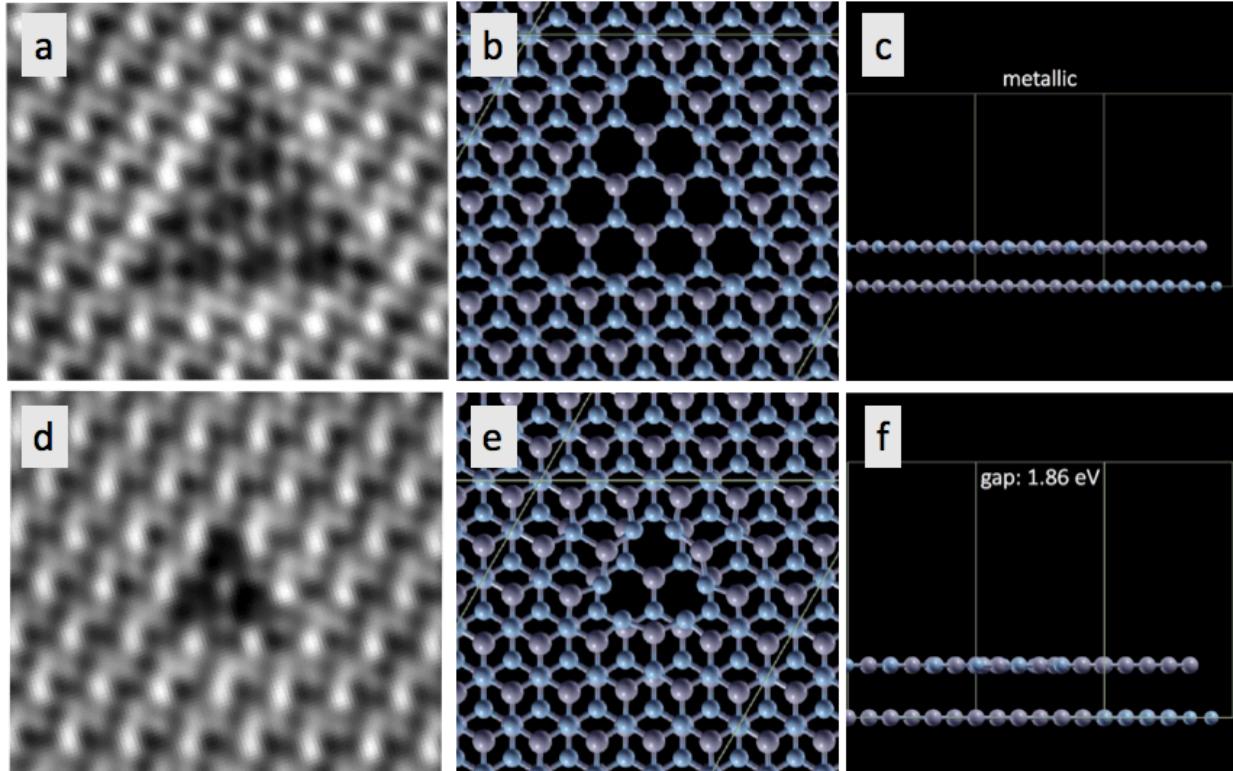
Figure 3.9 Vacancies in one layer of a bilayer AB-stacked *h*-BN. (a) An HR-TEM focal series reconstruction of a vacancy produced in a single layer of a bilayer AB-stacked *h*-BN, comprised of 10 missing boron atoms and 6 missing nitrogen atoms. (b) A fully relaxed atomic schematic of the vacancy in (a). (c) A side view of the stack in (b) and a 'metallic' label denoting that at the edge of the vacancy there is no bandgap at the fermi level. (d) An HR-TEM focal series reconstruction of a vacancy in a bilayer comprised of 3 missing boron atoms and 1 missing nitrogen. (e) A fully relaxed atomic schematic of the vacancy in (d). (f) A side view of the stack in (e) and a '1.86 eV' label denoting that at the edge of the vacancy there is a 1.86 eV bandgap at the fermi level. Scale: The frames of (a) and (d) are 2 nm wide. This figure is prepared based on unpublished theoretical work by Dr. Mehmet Dogan under the supervision Prof. Marvin Cohen.

66

3.2.4 Graphene on *h*-BN Defects

This section is based on my original unpublished experimental results.

While *h*-BN and its vacancies are of interest for their own applications and properties, *h*-BN has most widely been studied as a substrate, dielectric, or encapsulation layer for graphene and other two-dimensional materials. As a supporting material, *h*-BN has consistently been used to demonstrate the highest mobilities in graphene,[32,119] to maintain the chemical stability of volatile materials,[31,169–171] and to explore sensitive physical phenomena such as quantum metallic and superconducting states. [172,173]

Recently, it has been shown that manipulating the dielectric environment exerts major control over the electronic properties two-dimensional materials. [174,175] Because the members of this class of materials are only one or a few atoms thick, the surface it sits on has direct access to the entire 'bulk' of the material. This can be implemented by either carefully selecting a substrate's dielectric constant [174,175] or by spatially patterning the dielectric.[17,176] This scheme can also be used to tune the potential landscape for a two-dimensional material. For example, patterning a trigonal lattice in an SiO_2 layer beneath a graphene/*h*-BN heterostructure has been shown to generate an artificial graphene superlattice band-structure and to yield additional Dirac cones in the graphene's band structure.[176]

In the Section 3.2.2, I showed that the vacancies in *h*-BN grow to atomically precise triangles; these vacancies represent ultimate limit for tuning the geometry of a dielectric layer for the two-dimensional material family.

Here, I suggest a novel route for the direct fabrication of atomically precise vacancies in *h*-BN/graphene heterostructures. Fortuitously, the knock-on thresholds for both boron and nitrogen in *h*-BN are lower than that of carbon in graphene. At 80 kV, it has been demonstrated that carbon is not readily ejected from graphene while vacancies in *h*-BN form as described in Section 3.2.2. Therefore, it is possible to irradiate graphene/*h*-BN heterostructures to form vacancies in *h*-BN without disturbing the graphene.

By laminating pristine graphene directly on *h*-BN and forming *h*-BN vacancies by irradiation, the carriers in graphene can be directly exposed to the modulations in the *h*-BN due to the intimate contact of the layers. The carriers will thereby experience atomically-sharp potential variations across the surface from the charge on the edge atoms of the patterns and the variation in doping of the graphene caused by the vacancies.
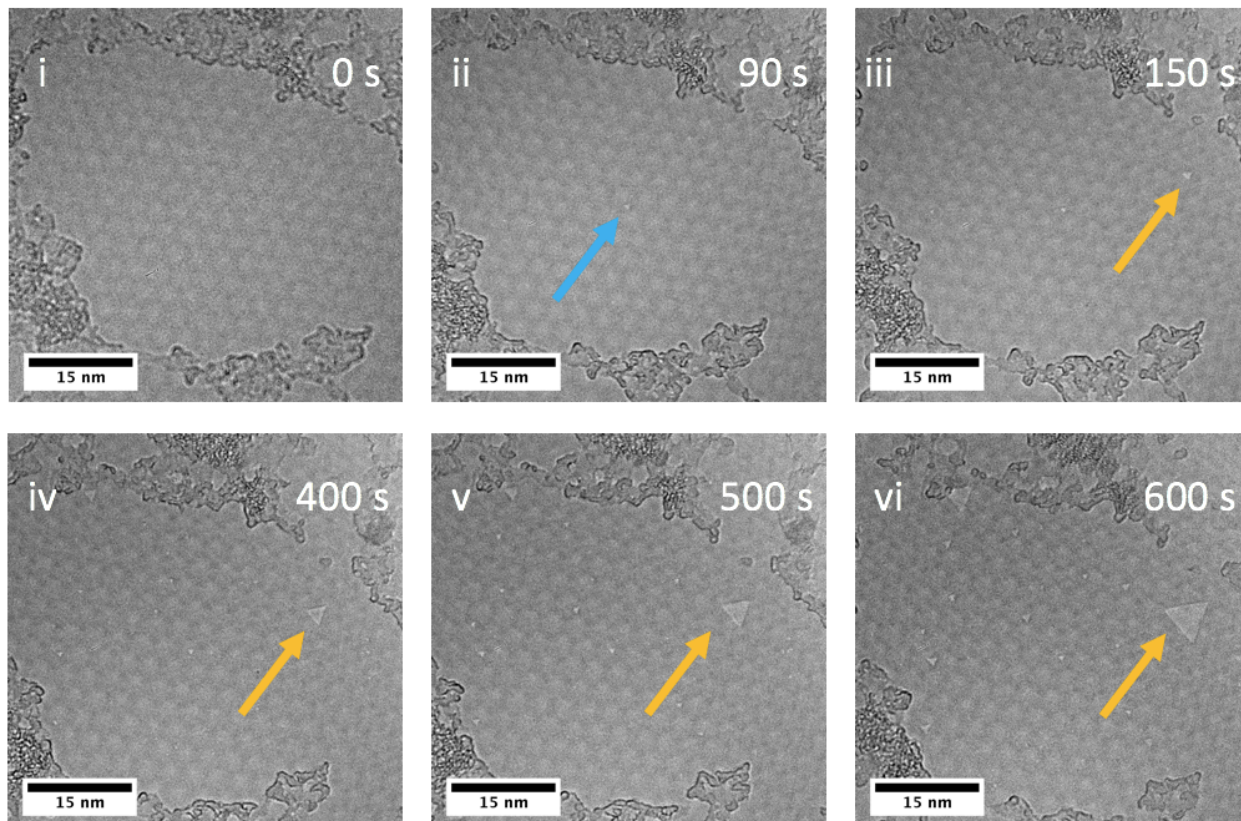
Figure 3.10 TEM imaging the formation of vacancies in graphene/*h*-BN heterostructures. (i)-(vi) A time series showing the evolution of defects in a stack of graphene and multilayer AB-stacked *h*-BN while it is irradiate by 80 kV electrons at 7 A/cm^2. (i) Initially, no vacancies are present at 0 s. (ii) After 90 seconds, a single vacancy has formed. (iii)-(v) Vacancies continue to nucleate and grow. (vi) After 600 seconds, a single vacancy has grown to 8 nm and all other vacancies are clearly triangular. Figure is based on my unpublished experimental data.

Figure 3.10 shows the formation of vacancies in the *h*-BN layer of an *h*-BN/graphene heterostructure. In panel (i), the overlapping graphene and *h*-BN is identified based on the presence of a moiré pattern; the periodic trigonal array of bright contrasted spots spaced by approximately 4 nm is produced by the twisting between the graphene and *h*-BN layers as described later in Section 3.2.5.

There are no visible defects in **Figure 3.10** (i), but after 90 s of irradiation with the 80 kV electron beam at 7 A/cm^2, a single few atom vacancy has formed at the center of the panel as shown **Figure 3.10**(ii). As the region is irradiated more defects form (**Figure 3.10**(iii)) and begin to grow (**Figure 3.10**(iv)). In the time series shown, a single vacancy grows from a few missing atoms in panel (ii) to an 8 nm triangular vacancy. This process is observed *in situ* and is amenable to being controlled due to its slow growth rate of 1 nm/min.

After 600 seconds of irradiation in **Figure 3.10**(vi), it is clear that all of the vacancies observed are triangular (and aligned). Because graphene (i) has never been observed to support triangular vacancies, (ii) does not exhibit a three-fold rotational symmetry, and (iii) has a higher knock-on threshold than *h*-BN, this strongly suggests that all of the vacancies have formed in the *h*-BN.
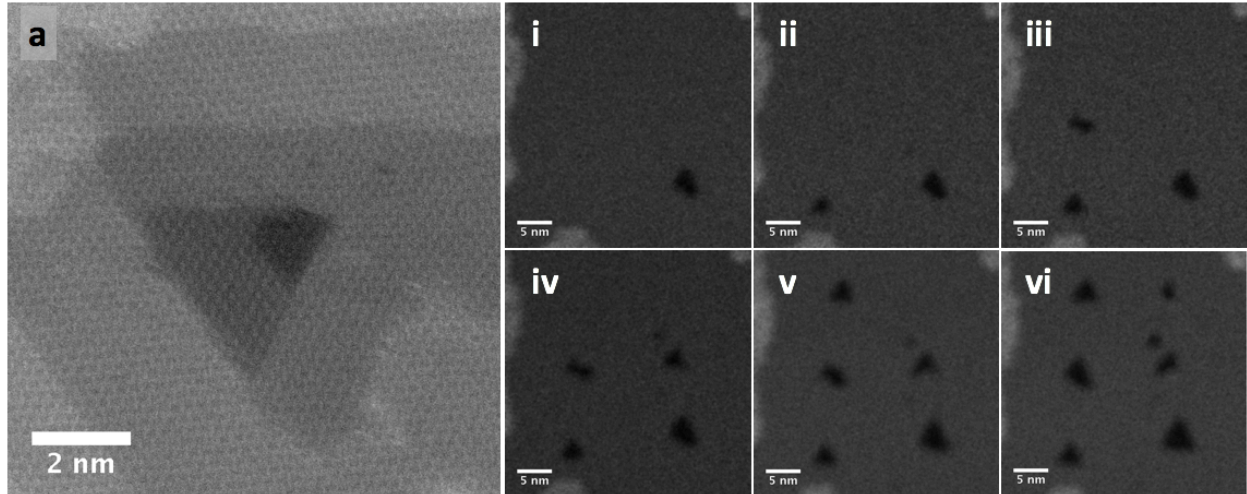
Figure 3.11 Fabrication of *h*-BN vacancy array using STEM. (a) Triangular vacancies in several layers of AB-stacked *h*-BN as fabricated and imaged in STEM mode using the TEAM 0.5 microscope. (i)-(vi) The sequential fabrication of single triangular vacancies in a monolayer *h*-BN using STEM mode on the TEAM 0.5 microscope. Figure is based on my unpublished experimental data.

To create an array of vacancies in *h*-BN with precise and deliberate locations, we irradiate the material using the scanning TEM (STEM) mode of the TEAM 0.5 microscope. In contrast to TEM mode which uses broad illumination with parallel electron trajectories to produce a projection image, STEM uses a converged electron beam with a sub-Å probe size. The probe is rastered, and transmitted (bright-field) or scattered electrons (dark-field) are measured at each point to generate an image. This is analogous to other scanning microscopies (e.g. SEM, AFM, HIM, etc.) which generate images using similar rastering techniques.

Figure 3.11(a) shows a representative vacancy fabricated in AB-stacked multilayer *h*-BN using STEM. Parallel triangular vacancies form across the multiple layers as observed using TEM mode in Section 3.2.3. Moreover, the edges of the triangles are parallel to a zig-zag edge based on the position of the lattice fringes. We note that it is not obvious this should be the outcome; because the beam has a Gaussian profile that is only approximately 1 Å in diameter, the beam could preferentially form pores based on its own geometry or locally favor nitrogen based on the location of the beam's peak intensity.

To create arrays of precisely-placed vacancies we turn off the rastering function of the STEM and place the condensed beam for 10-20 seconds on a monolayer region of *h*-BN. By positioning the beam at pre-specified locations, we are able to create an array point-by-point as shown in **Figure 3.11**(b)(i)-(vi).

Specifically, we are able to create an array of <5 nm vacancies with a 15 nm pitch. While the shape is not yet fully controlled, further dose optimization and shuttering the beam between exposures (as we did) may improve this.

69

3.2.5 Vacancy Formation in Twisted Multilayer *h*-BN

This section is based on my original unpublished experimental results.

In Section 3.2.3, I compared electron irradiation effects in AA′- and AB-stacked *h*-BN and found that the orientation of layers controlled the shape of the vacancies formed. Because the angle between the nitrogen zig-zag edge changes based on the interlayer rotation, both the relative orientation between the vacancies in the individual layers (antiparallel vs. parallel) and the nature of bilayer vacancies (triangular vs. amorphous) change.

While the high symmetry orientations represent the thermodynamic ground states, twisted multilayers of two-dimensional materials can be fabricated at room temperature. These twisted multilayers have become subject of intense research interest as of late with controlled stacking angle giving rise to exciting new electronic and optical phenomena.

Here, I show these twisted multilayers can also be of interest for controlled formation of vacancies in *h*-BN under electron irradiation. Like in AA′-stacking, the nitrogen zig-zag edges in layers of twisted multilayer *h*-BN will vary from layer allowing new vacancy angles. However, unlike in the AA′-stacking, in the twisted material each atom will no longer stack to form covalent bonds at every site. This allows for the formation of new unexplored vacancy shapes.

In this study, twisted multilayer *h*-BN regions that form spontaneously during the transfer of AB-stacked *h*-BN from foil to TEM grid are found using the STEM mode of the TEAM 0.5 microscope.
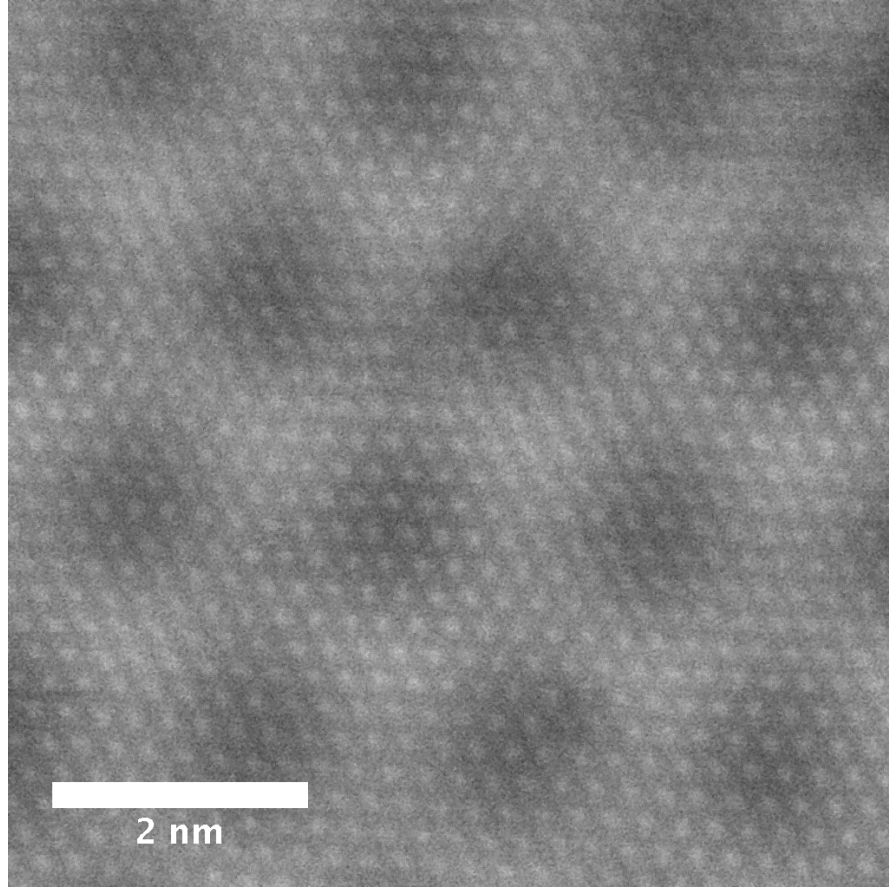
Figure 3.12 Moiré patterns in twisted multilayer *h*-BN. A STEM image of a moiré pattern in a twisted multilayer of *h*-BN comprised of two distinct 7° twisted regions of AB-stacked *h*-BN. Figure is based on my unpublished experimental data.

Twisted multilayer regions are identified from the presence of moiré patterns as shown in **Figure 3.12**(a). In this image, two overlaid trigonal lattices are visible: The lattice comprised of 1 Å spots with 2.5 Å pitch is due the constituent AB stacked layers, and the lattice comprised of 1 nm spots with a 2 nm pitch is the moiré pattern.

Moiré patterns arise in twisted multilayers due to a local shift in the areal density of atoms as illustrated. Because STEM measures the presence of atoms with a rastering probe, lighter regions indicate that a larger areal density is covered while darker areas indicate that the atoms are more closely aligned.

If the lattice constant is known, the spacing of the moiré spots can be used determine the interlayer rotation. The wave vector of the moiré pattern is given by the difference of the two nearest wave vectors of the constituent layers. Therefore, the moiré spacing can be expressed as a function of the lattice constant and interlayer twist by:

$$D = \frac{2\pi}{|k_1 - k_2|} = \frac{a}{2 \sin\left(\frac{\theta}{2}\right)}$$

For the lattice constant of *h*-BN (*a* = 0.25 nm) and the 2 nm moiré spot spacing, the twist angle θ is approximately 7°.
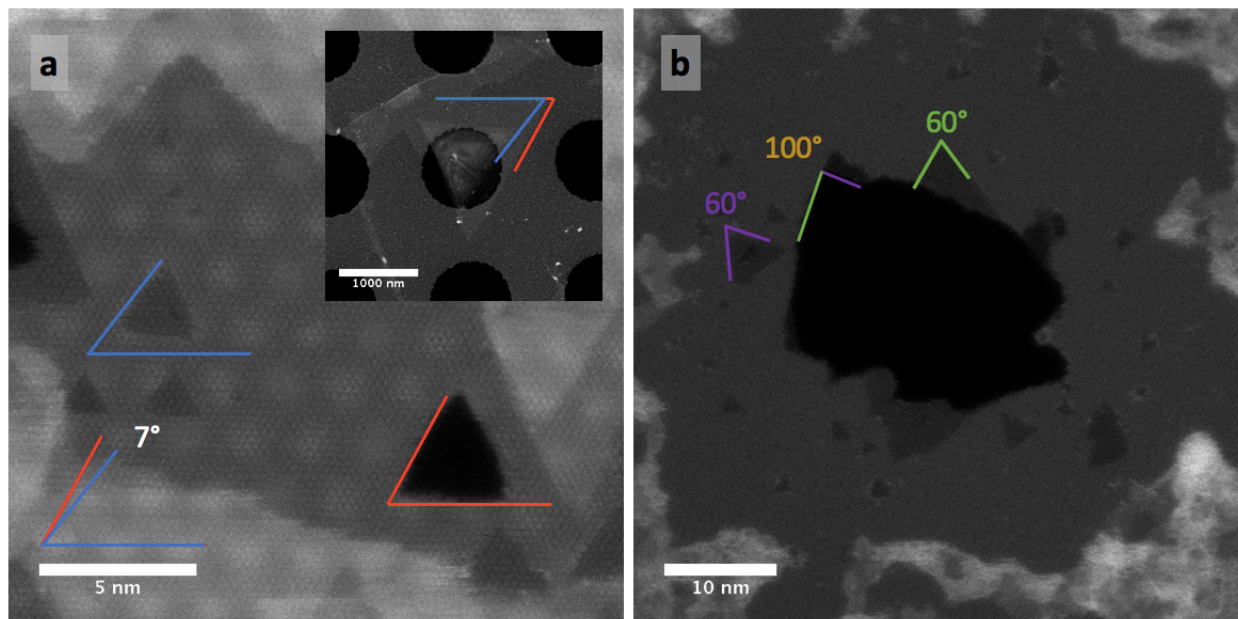
Figure 3.13 HR-STEM images of two twisted areas of *h*-BN with varying thicknesses in which vacancies have been induced. (a) A >3 layer region of AB-stacked *h*-BN with a 7°. The twist angle is visible in the inset and based on the spacing of the moiré pattern. Distinct triangular vacancies are visible with a 7° difference in their orientation (red and blue). (b) A bilayer region of twisted *h*-BN containing several vacancies. Two small triangular vacancies that are rotated from each other by 40° have edges parallel to that of a large bilayer vacancy. Figure based on my original unpublished experimental data.

After identifying a twisted region of *h*-BN in STEM, we irradiate with 80 kV electrons to investigate the vacancies that form. **Figure 3.13**(a) shows the emergence of vacancies in two distinct orientations of triangle defects in the twisted multilayer *h*-BN. These defects are offset by 7° as illustrated by the red and blue lines. This rotation angle agrees with the 2 nm spacing of the moiré pattern and the observed angle between the triangular domains shown in the low-magnification TEM image in the inset. The rotation between the vacancies confirms that their orientation can be controlled using interlayer twist in multilayer *h*-BN.

Figure 3.13(b) shows a bilayer region of twisted multilayer *h*-BN that has been irradiated to induce both monolayer vacancies and a large bilayer pore. As highlighted by the purple and green lines, the monolayer vacancies have a 60° corner as is standard for the triangular features, but they are oriented in different directions.

The bilayer hole, on the other hand, is comprised of a variety of edges. Notably, however, many of these edges are straight and can be correlated to the edges of the triangular vacancies in the individual layers. For example, in the bilayer hole, a 100° corner is highlighted by the intersection of a green line and a purple line. The green line is parallel to the left edge of the green 60° angle and the purple line is parallel to the right line of the purple 60° angle. This suggests that it is the nitrogen zig-zag edges of the individual layers that define the bilayer hole.

This suggests that twisted *h*-BN layers can be used to unlock new vacancy geometries. By carefully selecting the interlayer orientation different corner angles and numbers of sides in a vacancy may be tuned.

3.2.6 Defect Formation in *h*-BN at Elevated Temperatures

This section is based on our previously published work in Reference [177]. Experimental work was performed in collaboration with and led by Dr. Thang Pham and Dr. Ashley Gibb under the supervision of Prof. Alex Zettl, and theoretical calculations were performed by Dr. Zhenglu Li under the supervision of Prof. Steven G. Louie.

One important parameter for tuning the structural properties of atomic vacancies is material temperature. By thermally exciting the lattice, the constituent atoms are mobilized, allowing them to more readily anneal into the ground state of the vacancy's edge, or potentially changing the vacancy's ground state altogether. This is analogous to phase transitions and annealing in bulk materials. Additionally, as adsorbates and other surrounding are excited, the chemical environment can also be changed.

One example of temperature impacting the morphology of vacancies in two-dimensional materials is in those that form under electron irradiation in graphene.[178] We have seen at room temperature (in **Figure 3.1** that electron induced vacancies in graphene have no preferred termination; however, when the sample is heated above 500 °C, some zig-zag edges can form preferentially This suggests that heating can be used in *h*-BN as well to tune its vacancy geometry.

In this section, I investigate the role of material temperature on its electron irradiation induced defect formation and evolution. *h*-BN samples prepared by Dr. Thang Pham by carbothermic reduction of highly oriented pyrolytic graphite (HOPG) with boron oxide and nitrogen gas are studied with high-resolution TEM (80 kV) at elevated temperatures (500 – 1000 °C). Simultaneous atomic resolution TEM and heating is performed using the TEAM 0.5 microscope with an Aduro TEM holder that allows for stable joule heating during imaging.
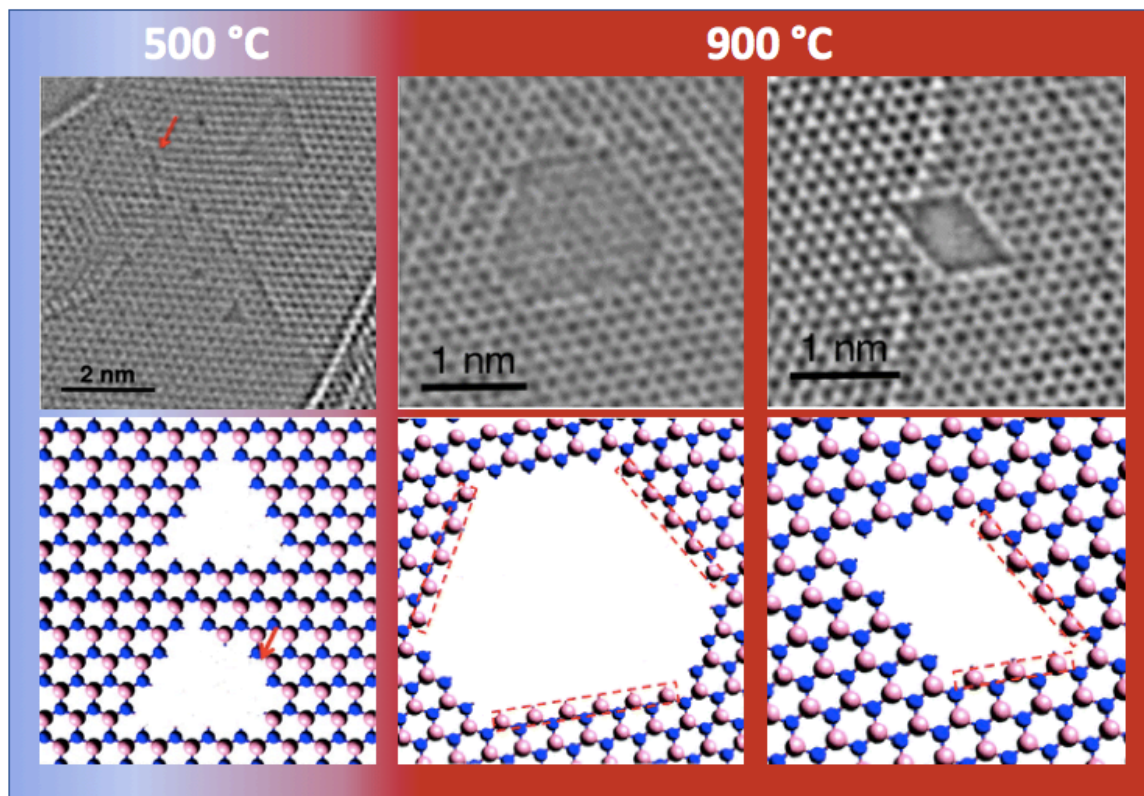
Figure 3.14 _h_-BN Defect shape versus temperature. Representative high resolution TEM images (top) and their corresponding atomic structures (bottom) are shown versus temperature. At 500 °C and below (left), triangular vacancies with nitrogen terminated zig-zag edges are formed preferentially. At 900 °C (right and center), boron zig-zag edges begin to appear in defects, allowing for the formation of hexagonal (center) and parallelogram (right) vacancies. Based on experimental data collected by Dr. Ashley Gibb under the supervision of Prof. Alex Zettl as presented in our previously published work in Reference [177].

Figure 3.14 shows representative high-resolution TEM images collected by Dr. Ashley Gibb and corresponding atomic schematics highlighting the effects of increasing temperature on the structure of vacancies in _h_-BN. At 500 °C (**Figure 3.14** (left)), we continue to observe the exclusive formation of triangular defects (as we do at room temperature). As shown in the atomic structure (**Figure 3.14** (bottom left)), this suggests that nitrogen zig-zag terminated triangles form preferentially up to at least 500 °C.

From 600 to 1000 °C, we begin to observe the appearance of hexagonal defects. While small triangular vacancies do still form, they quickly become unstable and reconfigure to hexagonal morphology. **Figure 3.14** (center) shows a representative hexagonal vacancy observed at 900 °C and its atomic schematic. We note that these hexagonal vacancies are comprised of both nitrogen and boron zig-zag edges separated by 120° corners. While we also observe the formation of parallelogram shaped vacancies **Figure 3.14** (right) at 900 °C, these defects are far outnumbered by their hexagonal counterparts. For both of these shapes, the perimeters must be composed of exactly half each of both nitrogen terminated and boron terminated edges that coexist within the same defect and all edges have a zig-zag conformation. Prior to this finding, all other defects in the _h_-BN literature have been observed to be exclusively nitrogen or boron terminated.
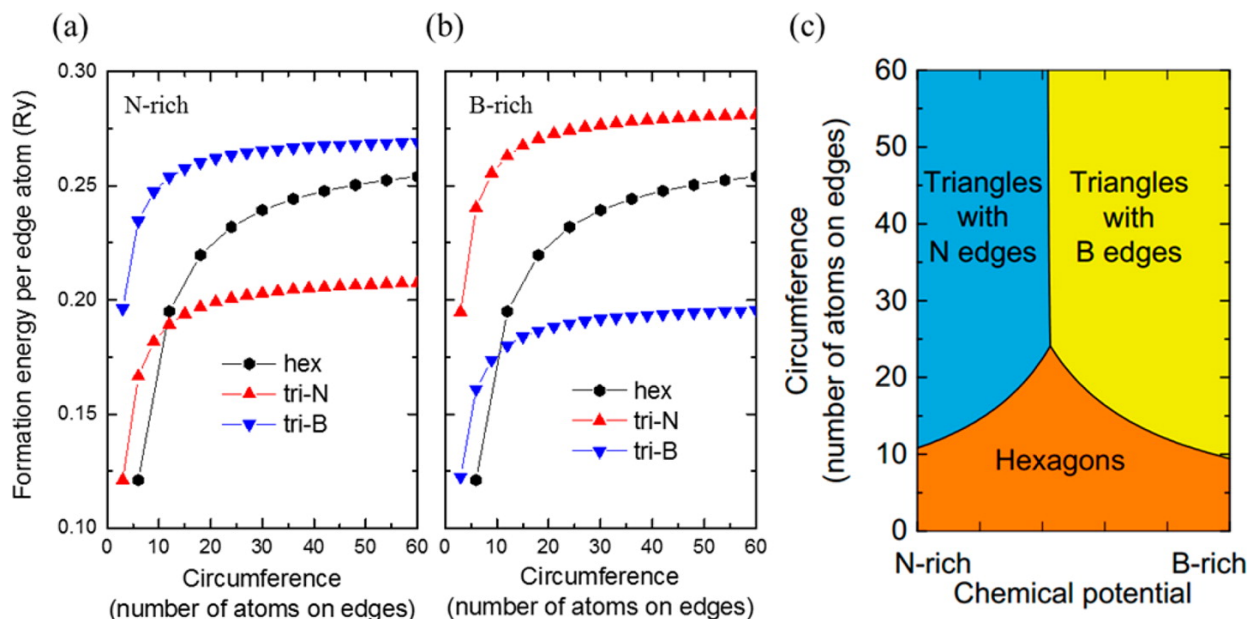
Figure 3.15 Enthalpy of formation for *h*-BN vacancies. The enthalpy of formation per unit length vs. number of edge atoms ((a)-(b)) and corresponding phase diagram (c) for hexagonal, nitrogen terminated triangle (tri-N), and boron terminated triangle (tri-B) *h*-BN vacancies in (a) nitrogen rich and (b) boron rich environment. In both chemical limits, hexagonal vacancies are preferred for small circumferences (n < 20). In the phase diagram as shown in (c), hexagonal vacancies are preferred with larger edges for a more even mix of boron and nitrogen. Based on theoretical calculations performed by Dr. Zhenglu Li under the supervision of Prof. Steven G. Louie as presented in our previously published work in Reference [177].

At the elevated temperatures studied, the evolution of hexagonal vacancies suggests that there is a strong temperature dependence to the energetic preference of boron versus nitrogen termination in the edges. In collaboration with Zhenglu Li and Professor Steven G. Louie, we use first principle calculations in the Quantum ESPRESSO package to compute the enthalpy of formation for different defect shapes in order to gain understanding of the defect formation mechanism.

Figure 3.15 (a)-(b) show the resulting calculated total formation energy per edge atom for hexagonal, nitrogen terminated triangle (tri-N), and boron terminated triangle (tri-B) *h*-BN vacancy geometries. First, the enthalpy of formation of edge atoms and corner atoms are calculated for each geometry. Then the enthalpy of formation is averaged across the entire structure. At small circumferences, the formation energy per atom is lower because there is appreciable energy minimizing structure reconstruction near the corners. In the hexagonal structures, we find that the 120° corner has lower energy than the 60° boron or nitrogen terminated corner in either triangular geometry.

For small vacancies in both nitrogen (**Figure 3.15** (a)) and boron rich environments (**Figure 3.15** (b)), we find that hexagonal vacancies are energetically preferred. Experimentally, we observed the presence of hexagonal defects with the size (circumference) in the range of n = 6 to n = 26, which fall within the hexagonal defect dominated space in the phase diagram in **Figure 3.15** (b) for our expected near even mix of boron and nitrogen.

This, however, predicts that hexagonal defects should be predominant for all temperatures and chemical environments. Therefore, we believe that for high temperatures the defect geometry is governed by the enthalpy of formation as described in the phase diagram while the geometry in the low temperature case is governed kinetically. Because lattice atoms are more mobile at higher temperatures (> 600 °C), they are able to anneal into the energetic ground state, favoring hexagonal defects. However, for lower temperatures (< 500 °C), atoms are less mobile and the preference of boron ejection by the knock-on kinetics favors triangular vacancies.

3.3 Fabrication of Subnanometer-Precision Nanopores in *h*-BN

This section is based on our work in Reference [42].

In this section, I describe and establish a procedure for the fabrication of individual nanopores in few-layer *h*-BN with atomically precise control of pore size from few-atom vacancies to several nanometer side-length through careful control of transmission electron microscope (TEM) electron beam conditions. It has been previously demonstrated that when *h*-BN is exposed under 80 kV electron irradiation in TEM that regular atomically precise triangle defects form[71,104,105,138,163,164]. Due to the preferential ejection of boron, attributed either to electron knock-on effects or selective chemical etching by atomic species present in the TEM, metastable nitrogen terminated zig-zag edges form and preserve a triangular shape under the electron beam. As these undercoordinated nitrogen atoms are ejected a new nitrogen zig-zag edge is exposed allowing for the precise quantized growth of the triangle defect[103,164].

In the earlier literature on *h*-BN vacancies, however, the defects studied, despite growing at precise increments, were not controlled in number or size; many defects were formed and the rate of growth was left uncontrolled.[103,163,167] In other studies, in which the number and position of the defects in *h*-BN were controlled for nanopore studies, the defects formed were irregular in shape and larger than 5 nm due to the use of high currents or voltages in order to readily create single pores[36,179].

Here, I present a method that combines the strengths of these approaches by allowing for both the nucleation of single nanopores and for the precise growth of these defects in *h*-BN from few atom vacancies to several nanometer side-lengths. This process can be simply accomplished in a conventional TEM by only modifying the beam conditions and does not need an advanced aberration-corrected TEM.

AB-stacked *h*-BN, prepared by chemical vapor deposition on copper foil, is transferred to quantifoil holey carbon grids via a direct transfer method. Sub-nanometer precise pores are then fabricated using a JEOL 2010 TEM at 80 kV as detailed below.
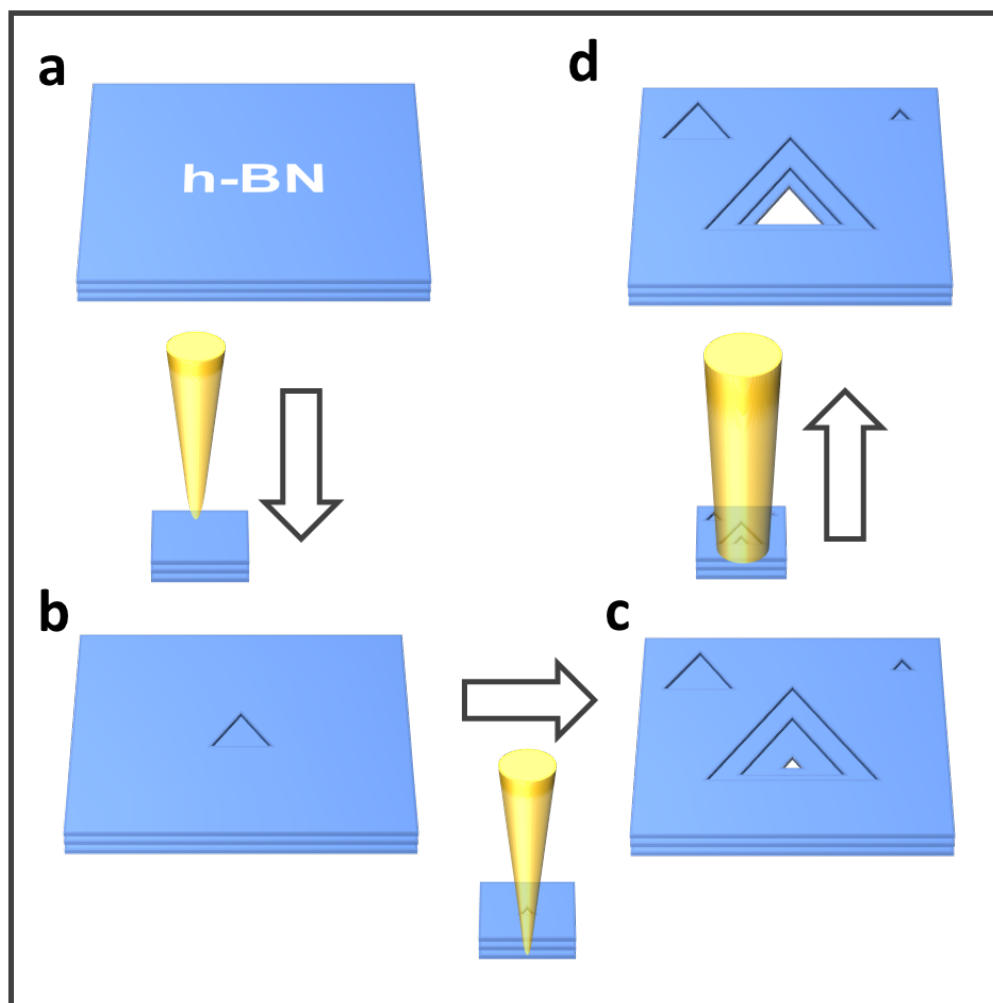
Figure 3.16 Schematic of our nanopore fabrication method. (a) Starting from pristine *h*-BN a TEM electron beam is condensed to 10-20 nm area. (b) Triangular defects form under the condensed beam, mostly near the center, allowing for the stripping of the *h*-BN layer by layer. (c) After the formation of a single few-atom vacancy in the final layer, the beam is spread. (d) Under a lower beam energy density, the pore is grown to the desired size. Figure reprinted from our previously published work in Reference [42].

Our process for creating an individual nanopore is shown schematically in Figure 1, and consists of two main steps.

First, with a high current density (>20 A/cm^2) focused electron beam, we strip away layers of *h*-BN over a small area until we are left with a single few-atom vacancy in a small single-layer region. The high current density allows for the quick milling of *h*-BN multilayers. While these beam currents do not produce nice triangular vacancies, they do preferentially form new vacancies. This results in a thinning of the *h*-BN.

Second, the electron beam is spread to a lower current density (<10 A/cm^2). In this beam current regime, triangular vacancies grow preferentially. The size of the growing nanopore is monitored *in* situ under the diffuse electron beam. Based on our observations, the formation of additional vacancies and pores is suppressed due to the low current density. Further studies are necessary to understand why this happens.
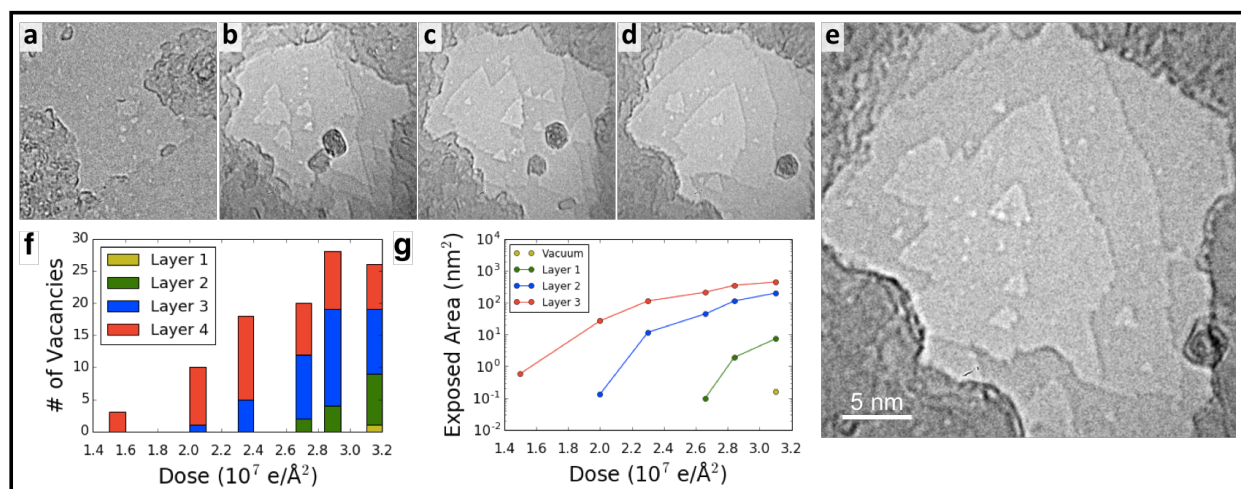
Figure 3.17 Layer by layer stripping of multilayer _h_-BN. (a)-(e) TEM time series showing the formation of defects and stripping of layers at doses of (a) 0, (b) 2.0×10^7 e/Å^2, (c) 2.3×10^7 e/Å^2 (11 min), (d) 2.8×10^7 e/Å^2 (15 min), and (e) 3.1×10^7 e/Å^2 (18.5 min) under a 10-20 nm condensed electron beam with a current density of 37 A/cm^2. (f) The number of continuous vacancies present in each layer of the sample as a function of dose. (g) A graph depicting the amount of area exposed of a given layer or below, note that the area exposed of each layer or below goes asymptotically towards probe size. The difference between layer 1 and vacuum is larger than between other layers. The size in nanometers of frames (a)-(e) are constant. This figure is reprinted from our previously published work in Reference [42].

In order to prepare individual nanopores in multilayer _h_-BN, our first step strips away layers in a localized region by milling using the condensed, high-current density (>30 A/cm^2) electron beam in the JEOL 2010 TEM. As shown in **Figure 3.17**(a)-(e), by using a beam condensed to a diameter of 10-20 nm at a current density of 37 A/cm^2, vacancies are readily formed in each layer sequentially and steadily grow with dose, effectively stripping away layer by layer. The dose dependence is illustrated in **Figure 3.17**(f). Under these beam conditions, this process proceeds fairly slowly giving a good deal of control.

Figure 3.17 (g) shows the area of the sample exposed for a given layer or below. In this experiment, it requires a dose of approximately 6×10^6 e/Å^2 or 4.5 minutes to strip to each successive layer under the condensed beam.

Vacancies in the final single-layer region of the _h_-BN can be identified by a larger contrast difference. **Figure 3.18** shows that the difference in grayscale counts between a 1 L region and vacuum is nearly four times as great as difference between any other two layers. This allows us to identify when a pore reaches vacuum and to stop the milling after an isolated vacancy has been introduced in the single-layer region.
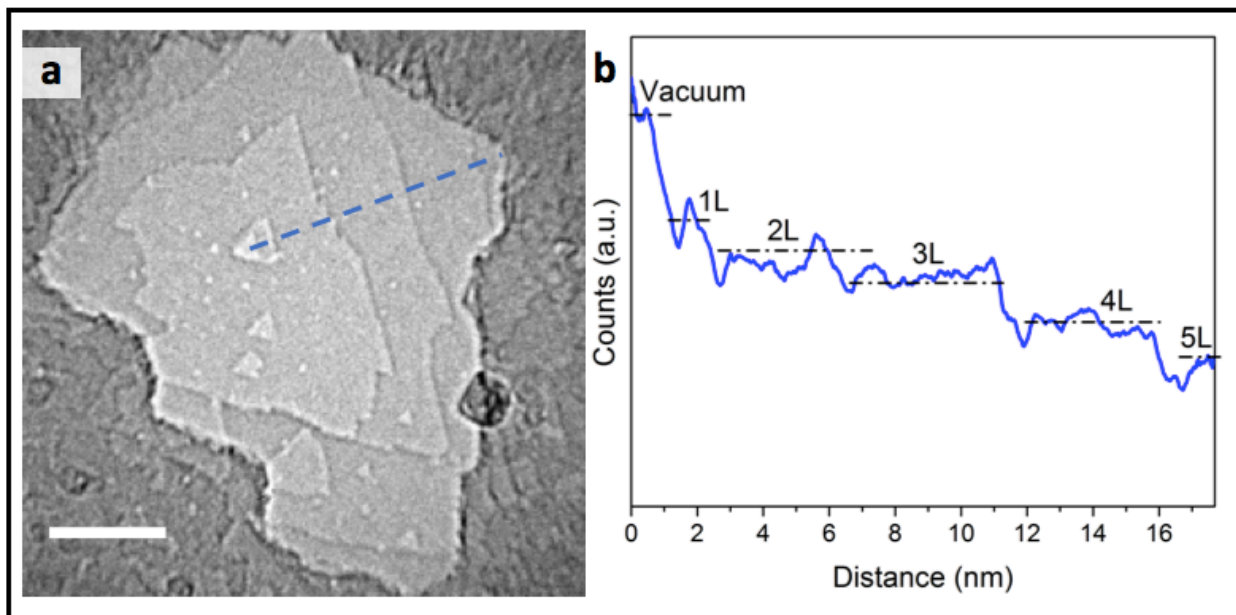
Figure 3.18 TEM image of a single 1.5 nm *h*-BN nanopore and its grayscale contrast. (a) A TEM image of a single 1.5 nm nanopore in AB stacked *h*-BN that is formed after the time series in **Figure 3.17** . The pore has two bilayer edges and one monolayer edge. The thickness along the blue dashed line varies from 0 to 5 layers of *h*-BN. (b) Grayscale count profile along the path along the line in (a). The difference between layer 1 and vacuum is larger than between other layers. This figure is reprinted from our previously published work in Reference [42]. Scale bar is 5 nm.
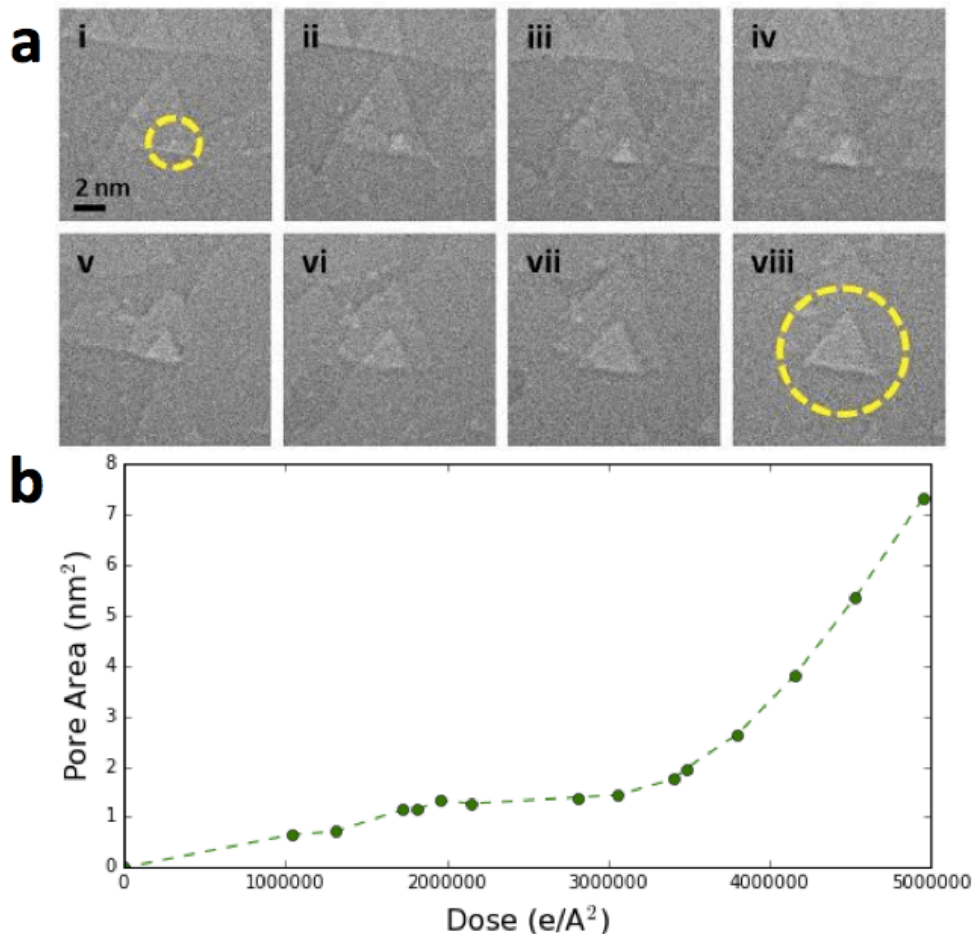
Figure 3.19 Size vs dose Metastable quantized growth of triangular nanopores. (a) (i)-(viii) A time series showing the quantized growth of a triangular nanopore in *h*-BN from a few-atom vacancy (i) to approximately 8 nm^2 (viii) under a beam current of 6 A/cm^2. Mono to few-atom vacancy formed in bottom *h*-BN sheet, circled in yellow in (i). Images are taken at roughly 2 minute intervals. (b) A plot of pore area versus dose for the images shown in (a). Figure based on our work in Reference [42].

After a small vacancy has been produced, a lower energy density beam allows us to grow the nanopore in quantized triangles of precise size, while new vacancy formation is inhibited. As the nanopore grows, it favors a triangular geometry and is metastable at each quantized triangle size, allowing for easily reproducible, highly regular pore geometry. **Figure 3.19**(a) shows an example of the growth of a single nanopore from a few-atom vacancy to 8 nm^2 with the beam current density reduced to 6 A/cm^2. The pore growth as a function of dose can be seen in **Figure 3.19**(b).

As has been described previously, electron knock-on effects and/or selective chemical etching due to gases present in the TEM column preferentially eject boron atoms and preserves nitrogen zig-zag edge termination[71,104,138,163,164,180]. Hence, each of the triangular pores created is reliably nitrogen terminated, desirable for many nanopore applications where controlling end-group chemistry is critical. When the nanopore has reached its desired size, the beam can be fully expanded or blanked to cease pore growth.
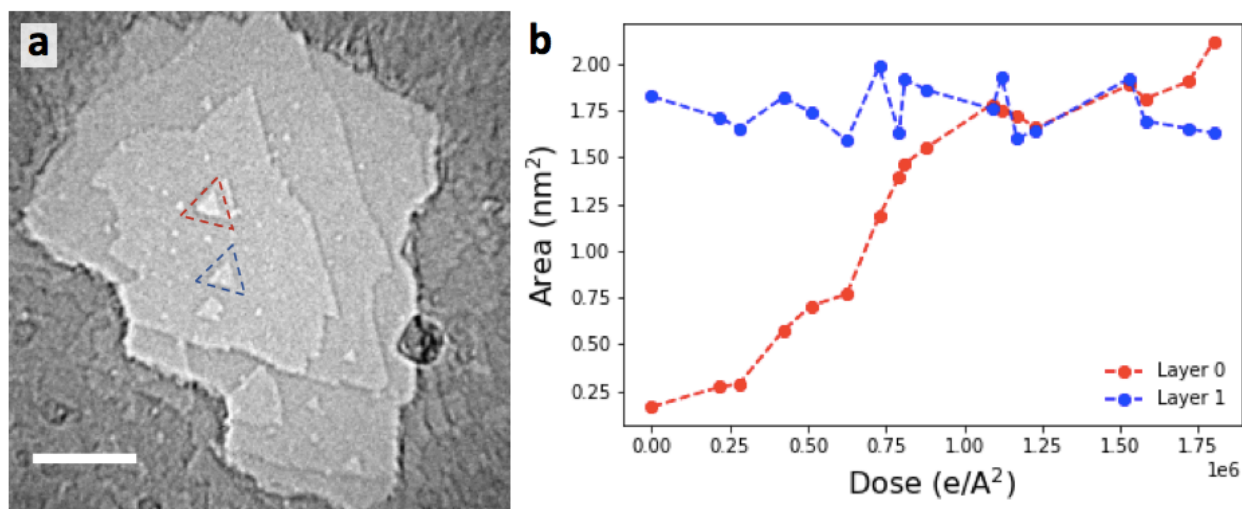
Figure 3.20 Comparison of vacancy growth by layer. Pore area versus dose for the nanopore shown in **Figure 3.18** compared to a neighboring vacancy of similar size in the second layer. Unlike the pore that spans the full thickness of the h-BN, the vacancy that sits on top of another layer of h-BN does not grow at an appreciable rate. Figure based on our work in Reference [42]. Scale bar is 5 nm.

By further lowering the beam current density, the nanopore in the single-layer region can be preferentially grown while similar defects in the multilayer region remain static. This is possible because vacancies in multi-layer regions appear to be stabilized, with inhibited further evolution, by the supporting h-BN layers. This is shown in **Figure 3.20**, where over the course of exposing the sample with a total electron dose of 1.8×10^6 e/$Å^2$ over 16 minutes at beam current of 3 A/cm^2, the pore that spans the bottom layer grows by 10-fold while the similar vacancy in the second layer remains constant in size.

While we demonstrate that high precision nanopore can be created using conventional TEM, the TEM irradiation process may be difficult to scale for applications requiring more than one nanopore. However, chemical routes such as hydrogen annealing have demonstrated the ability to form triangle vacancies in h-BN[66]. By optimizing such a chemical process or by applying local heating as Nam et al[181], number and size of defects could be controlled outside of the TEM at much larger throughput. Other groups have also shown that defects in h-BN can be produced at lower accelerating voltages using a scanning electron microscope (SEM)[168]; further studies of this process might allow standard electron beam lithography exposures to create precise nanopores in h-BN.

In summary, we have developed a method for fabricating individual h-BN nanopores with pore sizes that can be controlled with atomic precision. By careful control of beam conditions, electron beam irradiation can be used to strip away h-BN layers and create vacancies, or it can be used for nanopore growth. Under the correct beam conditions, this pore growth is limited to pores in single-layer h-BN and is inhibited in multi-layer regions. The pore geometry and end-group chemistries are both highly regular and controllable. Furthermore, we demonstrate in this work that these atomically precise nanopores can be created using a conventional TEM. Using an aberration corrected TEM allows refined characterization. h-BN nanopores with tunable pore size and geometry can find application in DNA sequencing (*e.g.* the pores <2 nm have approximately same dimensions as single-strand DNA) and molecular sensing[144,146] where smaller pores and more precise end-group functionalization could increase sensitivity and

performance respectively, in water desalination where better tailored pore sizes and functionalization could improve performance and efficiency[159], and in molecular separation, where precise pore size and end group control would allow for better discrimination between like chemical species[160].
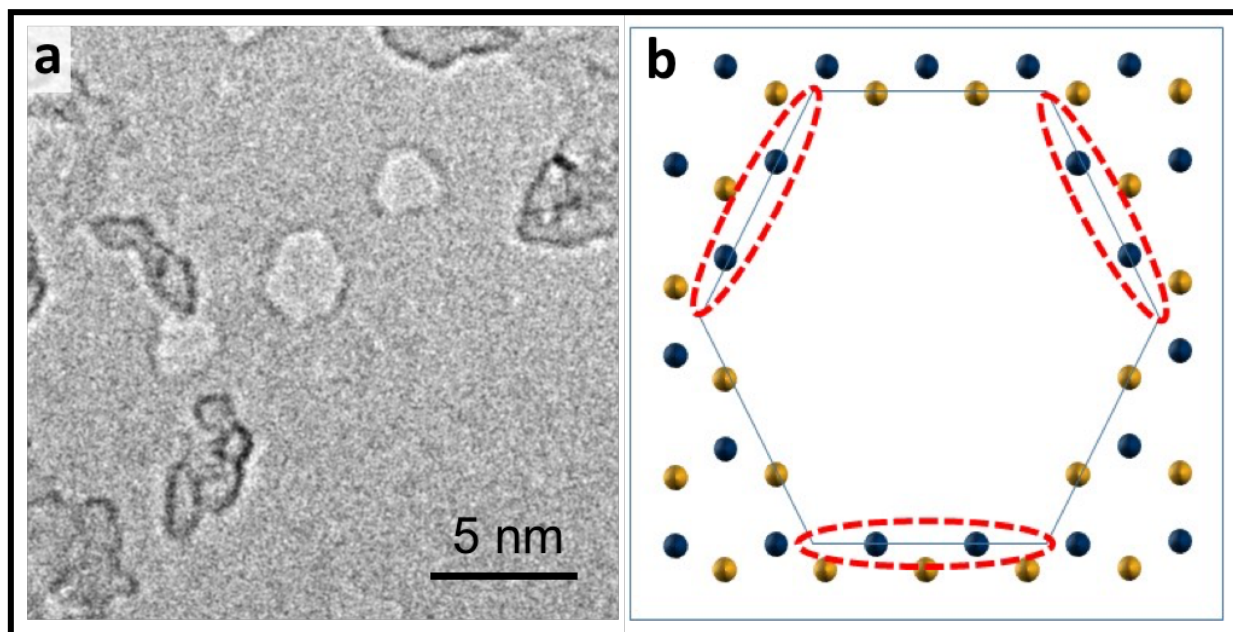
Figure 3.21 Formation of hexagonal vacancies at high beam currents. (a) Hexagonal *h*-BN pore created by condensing the beam at higher spot sizes to achieve higher current density. (b) Alternating boron and nitrogen facets as demonstrated in Reference [177]. Boron and Nitrogen represented in gold and blue respectively. The nitrogen terminated facets that normally form the edges of a triangular nanopore are circled in red and are stable at low beam currents while the boron terminated edges are not. Figure reprinted from our work in Reference [42].

The nitrogen terminated triangular defect geometry described above is not the only stable geometry possible for *h*-BN under electron irradiation; other pore geometries and end groups can be formed under different conditions. [102,163,180,182] In particular, in previous work it has been shown that by elevating the temperature of the *h*-BN while it is exposed that hexagonal defects can be formed. [102,180] The formation of these hexagonal defects is justified by the revelation that there is an energy barrier between the hexagonal and triangular states which the heat provides the energy to overcome in these prior works.

Here, we show that by increasing the beam current density we are also able to form hexagonal defects using a conventional TEM. By using a smaller spot size to increase the condensed beam current to approximately 70 A/cm^2, hexagonal defects are formed, as shown in figure 5. As has been described elsewhere, in order to create hexagonal defects, both boron and nitrogen edges must be present. [102] These hexagons likely form because the extra beam current compensates for the energy difference between boron and nitrogen zig-zag edge similar to how heating has provided this extra energy in the prior literature. [102,180] The hexagonal pores can be steadily increased in size if the beam current remains around 70 A/cm^2.
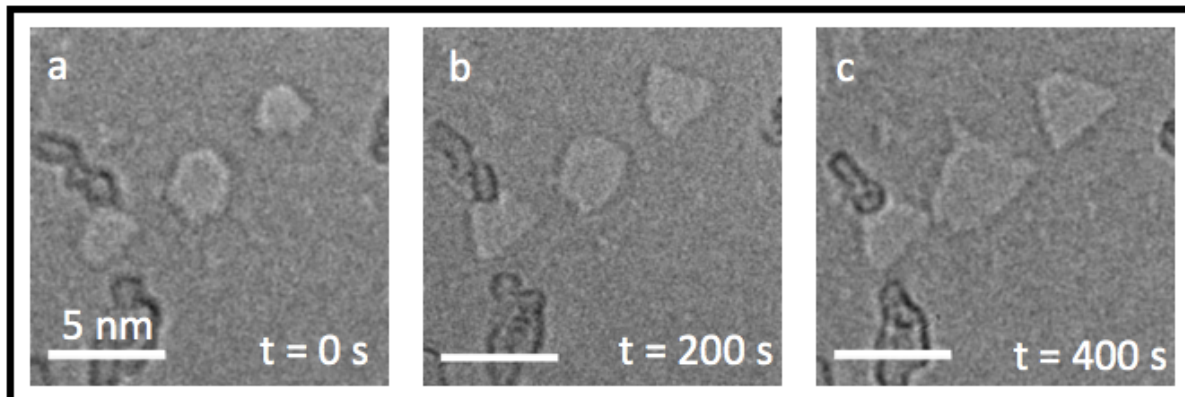
Figure 3.22 Evolution of hexagonal vacancies in *h*-BN. A time series of the evolution of hexagonal *h*-BN nanopores after the beam is reduced from ~70 A/cm^2 to ~20 A/cm^2 at time t = 0. Frames (a), (b), and (c) respectively show the sample after 0 seconds (image taken almost immediately upon spreading the beam), 200 seconds, and 400 seconds of exposure under the ~6 A/cm^2 beam. After the hexagonal shapes are formed at the the high beam current density, the vacancies grow into a triangle shape at the lower beam current density. All scale bars are 5 nm. Figure reprinted from our work in Reference [42].
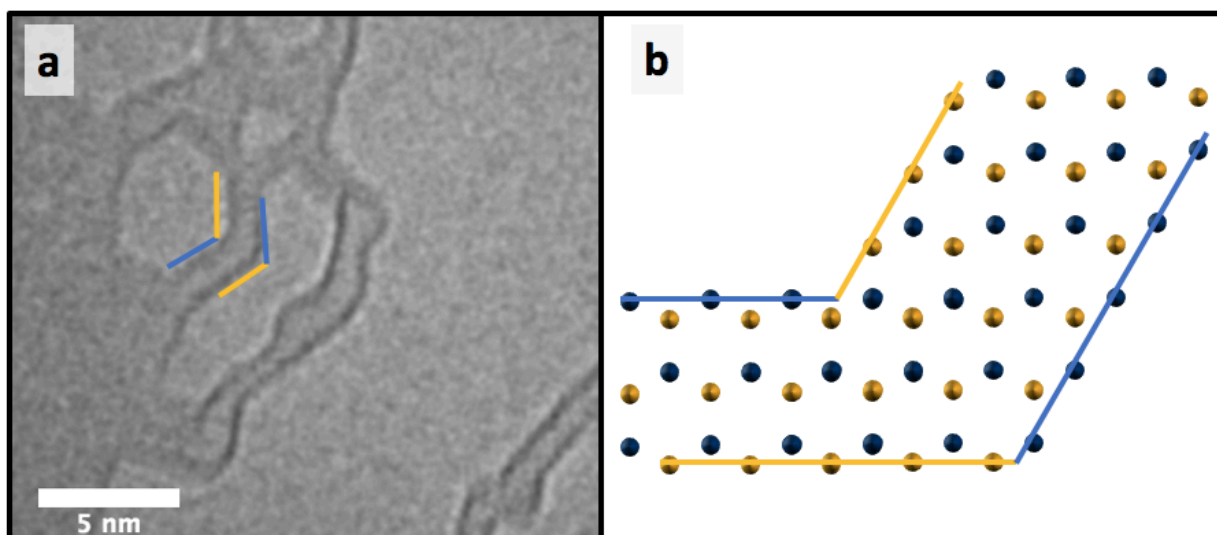
Figure 3.23 *h*-BN nanoribbons formed by TEM irradiation. A TEM image of an *h*-BN nanoribbon formed by creating multiple hexagonal vacancies in close proximity in AA' stacked *h*-BN. The width of the ribbon is ~1 nm implying that it is less than 6 atoms across. Since the chevron in the middle measures 120°, it is implied that the edge termination varies between boron and nitrogen as shown schematically in in (b.) Boron is shown in blue and nitrogen in yellow. Figure based on my unpublished experimental data.

However, if the beam current is the hexagonal pores revert towards a triangular shape. **Figure 3.22** shows the evolution of hexagonal vacancies formed in AB-stacked *h*-BN at a beam current of ~70 A/cm^2 as they revert to a triangular shape at ~10 A/cm^2.

The ability to fabricate hexagonal vacancies unlocks the potential to create structures with both nitrogen and boron terminated edges. **Figure 3.23**(a) shows a TEM image of a monolayer *h*-BN nanoribbon fabricated at an elevated beam current. Based on its geometry, the ribbon must have both boron and nitrogen terminated zig-zag edges. On either side of the 120° junction, the edges flip termination as shown in **Figure 3.23**(b).

3.4 h-BN Nanopores for DNA Sequencing

This section is based on unpublished experimental work performed in collaboration with Dr. Gabriel Dunn under the supervision of Prof. Alex Zettl.

The Bernal stacked *h*-BN nanopores described in Sections 3.2.3 and 3.3 have an ideal set of properties for the DNA sequencing method outlined in Section 3.1. First, unlike graphene, few-layered *h*-BN is chemically inert.[29] Covalently bound functional groups such as oxides and alkyls that are commonly found in graphene and on graphene nanopores are absent in *h*-BN.[183]This may lead to a reduction in DNA sticking and increase the stability of the pore geometry. Moreover, because few-layered *h*-BN is inert, nanopore bearing sheets of the material can be cleaned using standard UV-ozone treatments to tune the cleanliness and hydrophilicity of the membrane.[36]

Second, bilayer edges with deterministic edge termination preferentially form in the electron induced *h*-BN nanopores. Based on our observations and predictions shown in Section 3.2.3, these bilayer edges are highly stable and may be caused by interlayer covalent bonding, as seen in previous TEM studies. Two to three layer nanopores have been predicted to be optimal for DNA sequencing, and if these edges are covalently bonded, the negative effects of the DNA-edge interaction can be minimized.[184]

Finally, the shape and size of *h*-BN nanopores are both deterministic and controllable.[42] Previous studies of two-dimensional material nanopores have struggled to produce pores with predictable geometries; this has a profound impact on the ionic current blockage caused by DNA translocation events.[146] In Section 3.3, I showed that *h*-BN nanopores can be fabricated from ~0.5 to 5 nm with approximately 0.2 nm resolution and that these pores can be exclusively equilateral triangles.
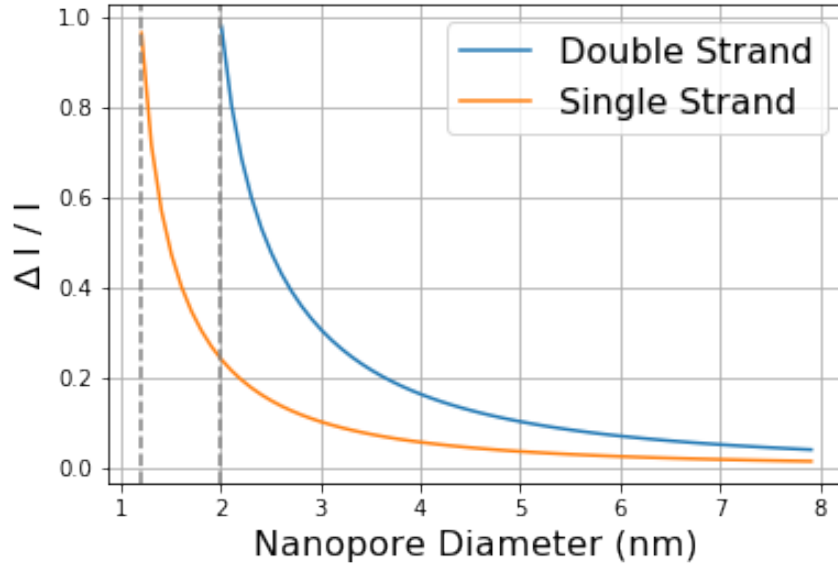
Figure 3.24 Calculated proportional current blockage for DNA translocation versus nanopore diameter. Proportional current drop due to the translocation of single strand (orange) or double strand (blue) DNA through a monolayer nanopore. Figure based on formula in Reference [144].

The significance of the ability to control the size of nanopores can be understood by considering its effect on the proportional current drop, $\Delta I/I_{open}$, due to a DNA translocation event. In Reference [144], Kowalczyk et al find the change in conductivity for a nanopore based on its size is given by the following equation where σ is the conductivity of the electrolyte, l is the thickness of the pore, d is the diameter of the pore, and r is the diameter of the DNA:

$$G_{open} = \sigma \left(\frac{4l}{\pi d^2} + \frac{1}{d} \right)^{-1}$$

$$G_{blocked} \approx \sigma \left(\frac{4l}{\pi(d^2 - r^2)} + \frac{1}{\sqrt{d^2 - r^2}} \right)^{-1}$$

Figure 3.24 plots $\Delta I/I_{open}$ for translocation of single and double strand DNA versus nanopore size for a graphene or *h*-BN monolayer. For single strand DNA, there is a greater than 50% blockage in current for translocation events through pores smaller 1.5 nm. When the pore is larger than 3 nm, as most two-dimensional material nanopores reported in the literature are, the current blockage is less than 15%. For a 1 nA base current, a pore less than 1.5 nm will produce a blockage signal of around 0.5 nA whereas those greater than 3 nm will produce signals less than 0.1 nA. Given that our *h*-BN nanopore production method allows for the fabrication of pores with 0.2 nm precision between 1-2 nm, this represents a potential gain of one order of magnitude in the ionic current blockage signal.

Because the common fabrication techniques produce nanopores greater than 3 nm, double strand DNA is typically studied. As shown in **Figure 3.24**, pores between 3 and 4 nm give a blockage current of approximately 25%. However, using nanopores, there is no way to sequence double strand DNA, and therefore, smaller pores are favorable.
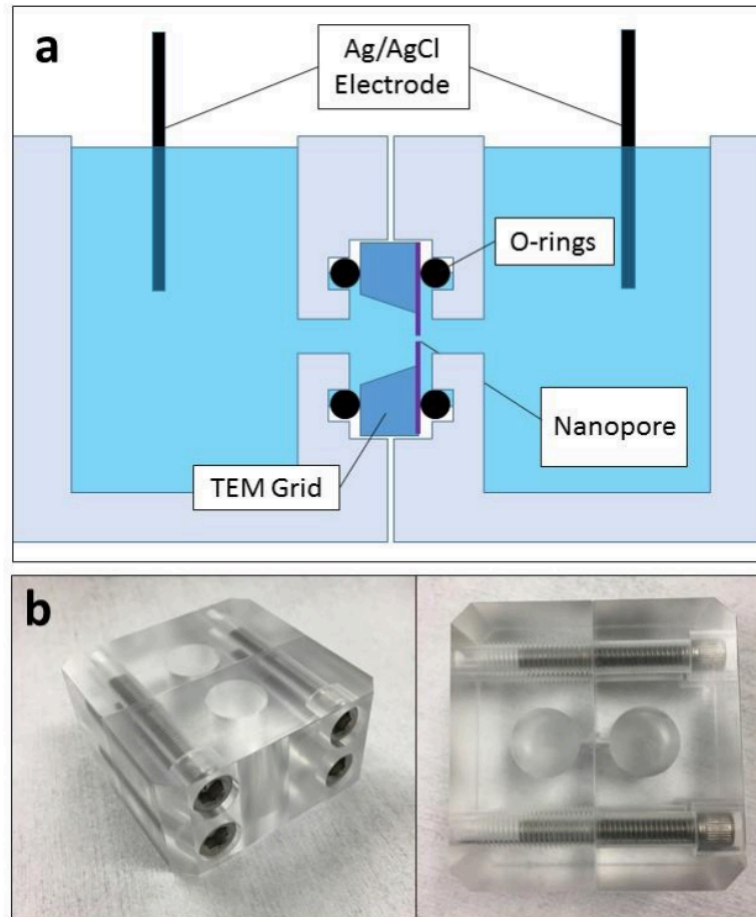
Figure 3.25 Schematic (a) and photograph (b) of the acrylic fluidic cell for nanopore measurement. Figure prepared by Dr. Gabriel Dunn.

In order to measure the *h*-BN nanopores produced by the method outlined in Section 3.3, we designed and constructed an acrylic fluidic cell as shown in **Figure 3.25**. In this design, a nanopore bearing TEM chip is sandwiched between two nearly identical half cells. The half cells are composed of an acrylic block with a 10 ml cylindrical reservoir and a 1mm deep, 2 mm diameter cylindrical channel that connects to the nanopore.

Silicone O-rings or a PDMS gaskets are used to form a liquid tight seal around the chip by applying pressure using 4 screws. Before wetting, the whole assembly is briefly exposed to oxygen plasma (10 seconds, 20-50 watts, 10 sccm O_2) to increase its hydrophilicity. The reservoirs are then wetted with 50% ethanol in deionized water and refilled with 0.1 – 1 M KCl. The whole fluidic assembly is then degassed by pumping down (using house vacuum) to remove any air bubbles in the system.

Homemade Ag/AgCl electrodes are prepared by soaking silver wire in bleach (Clorox) for at least 30 minutes and connected to the head-stage of an Axopatch 200B patch clamp amplifier. For electrical measurements, the fluidic cell is placed in a double Faraday cage. The inner cage is a block of solid aluminum which encloses the acrylic cell and the electrodes while the outer cage is an aluminum case that surround both the inner cage and the head-stage.
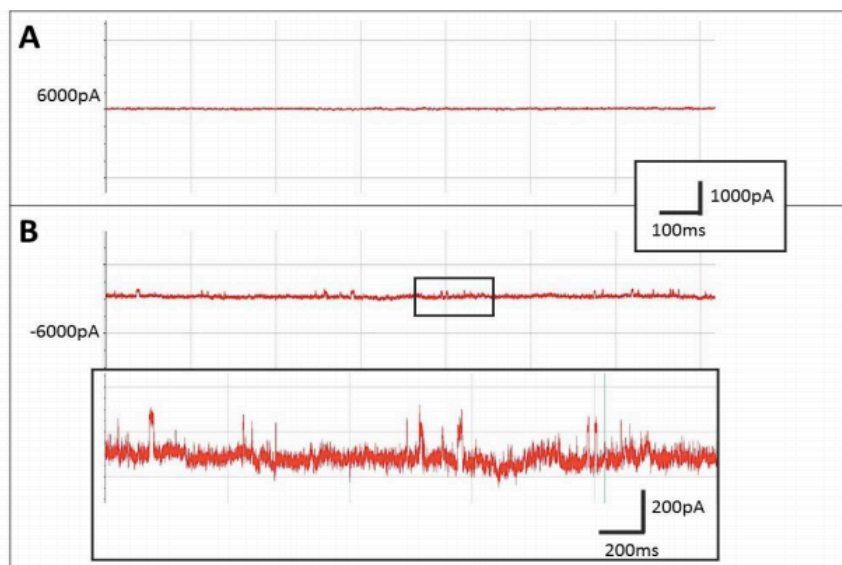
Figure 3.26 Current trace for DNA translocation in a SiN nanopore. Current trace plotted versus time for the transmembrane current of a 6 nm diameter, 10 nm thick nanopore at +100 mV (a) and -100 mV (b) as measured with Axopatch 200b. DNA is loaded in the live trans-reservoir. (a) At +100 mV, the current trace is flat with no DNA translocation events. (b) At -100 mV, 50 millisecond, 200 pA reductions in current are observed as highlighted in the magnified region. Data taken in collaboration with and figure prepared by Dr. Gabriel Dunn.

Figure 3.26 shows a representative current trace for the fluidic cell with a loaded 6 nm diameter, 10 nm thick SiN nanopore as collected in collaboration with Dr. Gabriel Dunn. Double strand λ-DNA(48.5 kbp) is loaded into the fluidic cell reservoir connected to the live terminal of the head stage (trans-reservoir). At a positive voltage of 100 mV, a positive ionic current of ~6 nA (6000 pA) flows between the terminals as a net current of negative chlorine ions from the ground terminal (cis-reservoir) flow into the live reservoir and deposit on the electrode. Because negative charge flows from the cis-reservoir to the trans-reservoir, the negatively charged DNA stays put in the trans-reservoir, leading to a flat current trace as seen in **Figure 3.26**(a).

When the voltage is flipped to -100 mV, negative charges flow from the trans-reservoir to the cis-reservoir. This leads to DNA translocation through the nanopore. Corresponding to these DNA translocations, 50 millisecond, 200 pA reductions in the absolute current occur intermittently as shown in **Figure 3.26**(b). These spikes represent a ~3% reduction in the overall current; this is consistent with what we would expect from 10 nm thick, 6 nm diameter pore as described by the equation following **Figure 3.24**.

To date, we have been unsuccessful in our attempts to observe translocations of DNA through our atomically precise *h*-BN nanopores. A major hurdle we have faced has been designing a protocol that allows for consistent wetting of the *h*-BN. To allow for consistent wetting, the aspect ratio of the channel leading up to the nanopore bearing grid and PDMS gasket needs to be reduced. In the current setup, the combined thickness of this stack is nearly 2 mm while its width is less than 1 mm. The thickness need not be more than 0.5 mm and the width can be up to 2mm for our grid size. Reducing the thickness and increasing the width will allow for the channel to wet more easily. Tuning the hydrophobicity of the pore as in reference[36] will also be of use.

Chapter 4

Helium ion milling of two-dimensional materials

In this chapter, I study the impact of helium ion bombardment on two-dimensional materials using a helium ion microscope (HIM) and how it can be used to pattern these materials. In this technique, a focused helium ion beam with nominal probe size of 0.5 nm and 25 kV irradiates a sample and ejects atoms from our two-dimensional lattices. The focused helium ion beam is generated and controlled using a Zeiss ORION helium ion microscope. An HIM functions analogously to an SEM in which the electron source is replaced by a He$^+$ source. A helium ion beam is generated by heating tungsten 'trimer' filament in which only three exposed tungsten atoms terminate the tip in a low-pressure helium gas. Ionized helium atoms are then accelerated to 25 kV and condensed to a ~0.5 nm probe using conventional electromagnetic optics. The beam is then scanned across the sample and secondary scattered electrons are measured as a function of beam position to image the sample.

Though lower beam energies are used in HIM than in our TEM experiments (described in Chapter 3), the larger mass of the He$^+$ particles allows for kinetic ejection of atoms in the two-dimensional materials by the helium beam. Under imaging conditions, this results in some material damaging. However, by increasing the dose and steering the beam in predefined patterns using an external software, arbitrary cuts can be generated in our materials. In this section, I show that pores and ribbons can be generated in few-layer h-BN and MoS$_2$ with feature sizes smaller than 5 nm. By using few-layer samples instead of monolayers, amorphization of the edges can be mitigated. I further explore this technique for the fabrication of heterostructures and assess the use of heating to reconfigure edges milled using HIM.

4.1 Nanopatterning *h*-BN with HIM

This section is based on our previously published work in Reference [95].

The ability to pattern and etch h-BN has been explored for a variety of purposes to aid in its role in graphene electronics. Patterned h-BN has been demonstrated as a growth template for CVD graphene.[61] Stacks of h-BN/graphene/h-BN have been etched to create edge contacts for the encapsulated graphene.[122,185] Holes through h-BN stacked on graphene have been used to create point contacts for the graphene.[31] Moreover, nanostructures in insulating materials are being studied for their role in the production of superlattices in two-dimensional materials; the ability to pattern and etch h-BN for this purpose could enhance the results in the existing literature by moving the electronic 2D material closer to the periodic potential.[176]

The patterning and etching of h-BN has also been studied for several stand-alone applications. Nanopores etched in h-BN have been shown to confer several advantages for DNA sequencing over their graphene counterparts.[36,42] h-BN nanoribbons etched from boron nitride nanotubes have also been explored due to their interesting magnetic and electronic properties.[4,186,187]

Here we demonstrate the use of helium ion milling for the controlled fabrication of nanostructures in few-layer h-BN. Specifically, we show using a direct-write lithographic system that nanopores with diameters as small as 4 nm and ribbons with 3-10 nm width can be attained – roughly a factor of 5 smaller than what can be made by conventional electron beam lithography.[188] This method of nanopore formation achieves comparable sizes to milling in a TEM but at a much higher throughput.[36,146,189–191]

The high precision and rapid rate of pore production suggests that this method may be useful for scaling up the fabrication of nanopore sensors, producing point contacts for h-BN encapsulated devices, or for testing applications that require a large number of holes on a sample such as water desalination[156,157] or dielectric superlattices.[176] The ability to produce sub-10 nm ribbons demonstrates that this technique could be a straightforward method for studying the properties of h-BN nanoribbons. Furthermore, the demonstration ribbons at these sizes shows that other h-BN nanostructures can be created with minimal damage even at these small dimensions, allowing for the production h-BN deposition/etch masks, beams and cantilevers, and patterned dielectric layers.

Few-layered h-BN used for the suspended structures in this study was prepared by chemical vapor deposition (CVD) on copper following references[42,52]. The synthesis method in this work produces 3-5 layers of h-BN, ideal for creating near atomically-thin yet mechanically-stable suspended films. To prepare for the CVD growth, 1 cm x 4 cm copper foils are rinsed in glacial acetic acid for 10 minutes followed by 3 deionized water baths. A foil is then loaded into a tube furnace and annealed for 2 hours at 1020 °C under a gas flow of 300 sccm of Ar and 100 sccm of H_2 at 1 Torr. After the 2 hours of annealing, the Ar gas flow is turned off and 100 mg of ammonia-borane powder (Sigma Aldrich 97%), located in an upstream one-end sealed quartz tube, is heated to 80 °C for 30 minutes, allowing the BN precursor to diffuse to the copper catalyst where h-BN grows on the surface. The ammonia-borane is then cooled quickly to end the growth while the copper foil cools slowly at a rate of 10 °C/min.

Suspended samples of h-BN are then prepared by direct transfer as described in reference[121]. h-BN coated copper foils are cut into 4 mm x 4 mm pieces and a drop of isopropanol is used to adhere a holey-carbon TEM grid to the h-BN surface. The stack is then floated (grid on top) in 10% weight-per-volume sodium persulfate solution and underlying copper is dissolved, leaving behind an h-BN coated holey-carbon grid. The sample is removed from the sodium persulfate, floated in deionized water briefly to remove any residual copper etchant, and then is ready for use.

h-BN nanostructures are prepared from the suspended sheets by locally etching with the focused helium beam of a Zeiss ORION NanoFab helium ion microscope (HIM). The microscope is operated at 25 kV with a beam current of ~1 pA. Features to be etched are defined using a direct-write lithography software that precisely controls the position of the beam and dose delivered. We find that it is necessary to use suspended h-BN in order to prevent the re-deposition of etched species on a substrate. In order to protect the sample from uncontrolled etching, imaging of the h-BN using the HIM is minimized;[130,192] therefore, characterization is performed *ex situ* by TEM using a JEOL 2010 operated at 80 kV.
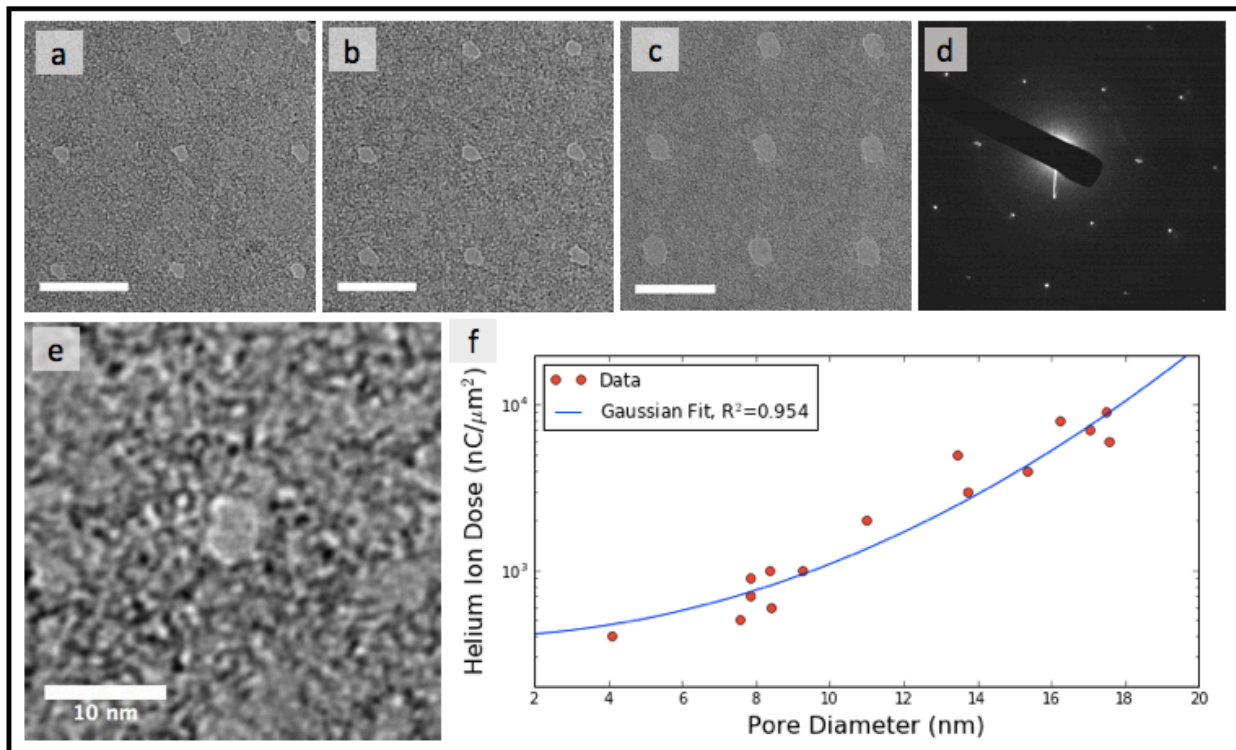
Figure 4.1 Dose dependence of _h_-BN nanopore formation by HIM. (a)-(c) Arrays of holes in _h_-BN produced by spot exposures at (a) 500, (b) 1000, and (c) 5000 nc/μm^2 as imaged by TEM. (d) Selected area electron diffraction taken on a hole array with spot exposures of 1000 nc/μm^2. (e) A single nanopore produced by a spot exposure with 400 nc/μm^2 irradiation as imaged by TEM. (f) Average pore diameter versus helium ion dose for 6x6 arrays of holes produced by spot exposures ranging from 400 - 10000 nc/μm with an overlaid Gaussian fit with R^2 = 0.954. Scale bars are: (a) – (c) 50 nm, (e) 10 nm. Figure is reprinted from our previously published work in Reference [95].

To explore the relationship between helium ion dose and minimum etch-feature size, the suspended _h_-BN sheets are irradiated using point exposures at varying doses. 6 x 6 arrays of points, spaced by 60 nm, are exposed (with a constant ion dose for all points) using the focused helium beam. Doses for each array range from 100 – 10,000 nC/μm^2 over a nominal probe size of 0.5 nm in diameter, typically requiring less than 1 second (up to 1000 nC/μm^2) to 10 seconds (up to 10,000 nC/μm^2) per spot exposed.

Figure 4.1(a)-(d) show the resulting pores formed by the helium ion point exposures. The sizes of all of the pores in a 6 x 6 array are measured and averaged as plotted in Figure 4.1 (f). Similar to previous results that investigate the etching of graphene using helium ion milling, we find that the variation of the size of the _h_-BN pores with total ion dose can be attributed to the Gaussian profile of the beam.[162,192] This is confirmed by the Gaussian dependence of the required helium ion dose versus pore radius shown in Figure 4.1(f). Figure 4.1(e) shows selected area electron diffraction (SAED) from an irradiated region; the regular crystal structure without strong presence of rings suggests that the _h_-BN is not substantially disordered by the etching.

In this study, the smallest pores formed were approximately 4 nm as shown in **Figure 4.1**(e). Pores this size were formed by irradiating the sample at 400 nC/μm^2. At spots exposed with lower doses, no pore formation was observed. These 4 nm pores are highly irregular in geometry

and seem more elliptical than circular (major diameter = 5 nm, minor diameter = 3 nm) likely due to either beam/sample drift or beam stigmation. The irregular geometry suggests that further characterization and optimization is required to understand the edges. Nanopores of this size in MoS_2 have been previously used to discern single nucleotides, suggesting that this too is possible with the *h*-BN pores formed in this way.[190]
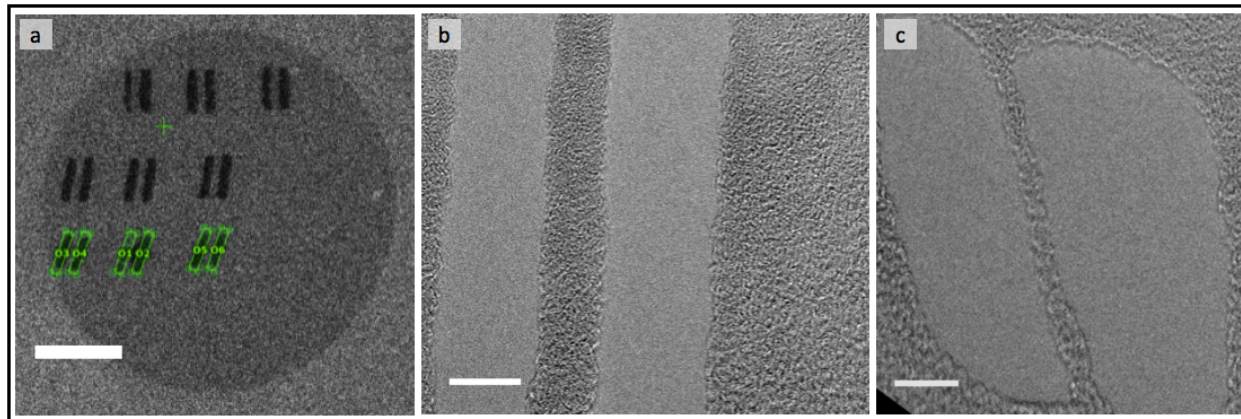
Figure 4.2 Fabrication of nanoribbons in *h*-BN by HIM. (a) A HIM image of rows of 70 x 15 nm *h*-BN ribbons with different rotation angles. The *h*-BN region is suspended over the center circle while the outer region is backed by holey-carbon. The green rectangles overlaid on the bottom row depict the region exposed to produce the ribbons as shown in the computer aided design software. b.) A TEM image of a 7 nm width *h*-BN nanoribbon (b) next to a 30 nm width ribbon (c). (c) A TEM image of a 3 nm width *h*-BN nanoribbon. Scale bars are: (a) 150 nm, (b) and (c) 10 nm. Figure is reprinted from our previously published work in Reference [95].

   h-BN ribbons were formed by irradiating two identical rectangular regions on either side of a narrow strip as shown in **Figure 4.2**(a). By varying the distance between the etched shapes, the width of the ribbon is tuned. A total dose of 1 nc/μm^2 was found to be the minimum dose to fully etch the selected region and was therefore used to minimize damage to the *h*-BN ribbon. As shown in **Figure 4.2**(b), sub-10 nm width ribbons can be fabricated in this way without incurring significant damage; this is reflected by the lack of obvious differences between the 7 nm width ribbon (b) and the center of the 30 nm width ribbon (c).

   By further irradiating the ribbons after etching by imaging the sample continuously with the HIM, the ribbons can be whittled down. This implies that the edge is more susceptible to etching than the rest of the suspended sample. Using this method, ribbons can be whittled to less than 3 nm as shown in **Figure 4.2**(c). However, these whittled ribbons appear significantly damaged.

   We have demonstrated that helium ion milling can be used to controllably fabricate sub-10 nm nanopores and nanoribbons in *h*-BN. With its high throughput and precision, this technique promises to advance studies requiring large numbers of nanostructures in an insulating layer such as those needed for nanopore arrays for DNA sequencing and for etched layers in van der Waals heterostructures.

4.2 Nanopatterning MoS$_2$ with HIM

This section is based on my unpublished experimental results obtained in collaboration with Dr. Amin Azizi, Dr. Kyunghoon Lee, and Brian Shevitski under the supervision of Prof. Alex Zettl.

While the etching of *h*-BN is of interest due to its use as a patterned dielectric or structural material,[17,32,176,185] the ability to directly induce nanoscopic patterns in electronic materials presents a different set of opportunities and challenges. [188,193,194] From an application-driven perspective, milling semiconducting two-dimensional materials with nanometer scale features is a promising route to realize the ultimate lower limits for transistor sizes and to create new geometries for sensors. From a basic-science perspective, engineering the geometries of conducting materials can influence both their bulk and edge electronic properties. Due to quantum confinement, the bandgap for materials like the TMDs and graphene can be tuned based on size and edge configuration.

In these situations, however, the impact of helium ion irradiation becomes critical. The performance of modern transistors requires defect densities to be below 0.1/cm^2, and much of the physics enabled by shrinking feature sizes can be dominated by imperfections in the crystal. HIM in particular has been previously observed to result in irregular edges and defect nucleation in two-dimensional materials.[130,195–197] Here, we fabricate nanoribbons in MoS2$_2$ using helium ion milling and characterize their crystalline properties near the edge using STEM.

Figure 4.3(a) shows our patterning scheme in which arrays of square holes are patterned to define narrow ribbons in the sheets. The distance between adjacent squares determine the width of the nanoribbon (denoted as 'x nm' in **Figure 4.3**(a)) while the size of the squares sets the length. **Figure 4.3**(b) shows 20 arrays of MoS$_2$ nanoribbons as defined by linear arrays of 5 square exposures of 1 nc/μm^2 at 1.6 pA beam current. Ribbons with widths varying from 2 nm to 50 nm and lengths varying from 20 to 50 nm are defined using HIM and characterized by TEM. Figure 4.3 (c)-(f) highlights four sets of these arrays in which 30 x 30 nm squares are set apart by 25 nm (c), 20 nm (d), 15 nm (e), and 10 nm (f). We observe that these ribbons are consistently narrower than intended. Each of the ribbons in in **Figure 4.3**(c)-(f) is 2 nm narrower than the distance set between adjacent square etches. This over-etching is consistent with the profile of the beam as highlighted in Section 4.2.

Due to the over-etching of the ribbon as well as the material mechanical stability, arbitrarily small ribbons cannot be produced. We find that the minimum ribbon width achievable is a strong function of the ribbon's length. In the bottom row of arrays, 50 nm x 50 nm squares are used to pattern 50 nm long ribbons that range from 25-50 nm in width. For ribbons that are 30 nm or wider, we find that there is a 100% yield for patterned ribbons. For the 25 nm ribbons, however, the yield drops to 75%. In the second row of arrays (from the bottom), 30 nm x 30 nm squares are used to fabricate 30 nm long ribbons; this length gives a 100% yield for ribbons 10 nm or wider. In the top two rows, 20 nm x 20 nm squares are etched to produce 20 nm long ribbons. For these, ribbons with widths of 4 nm or larger can be fabricated.
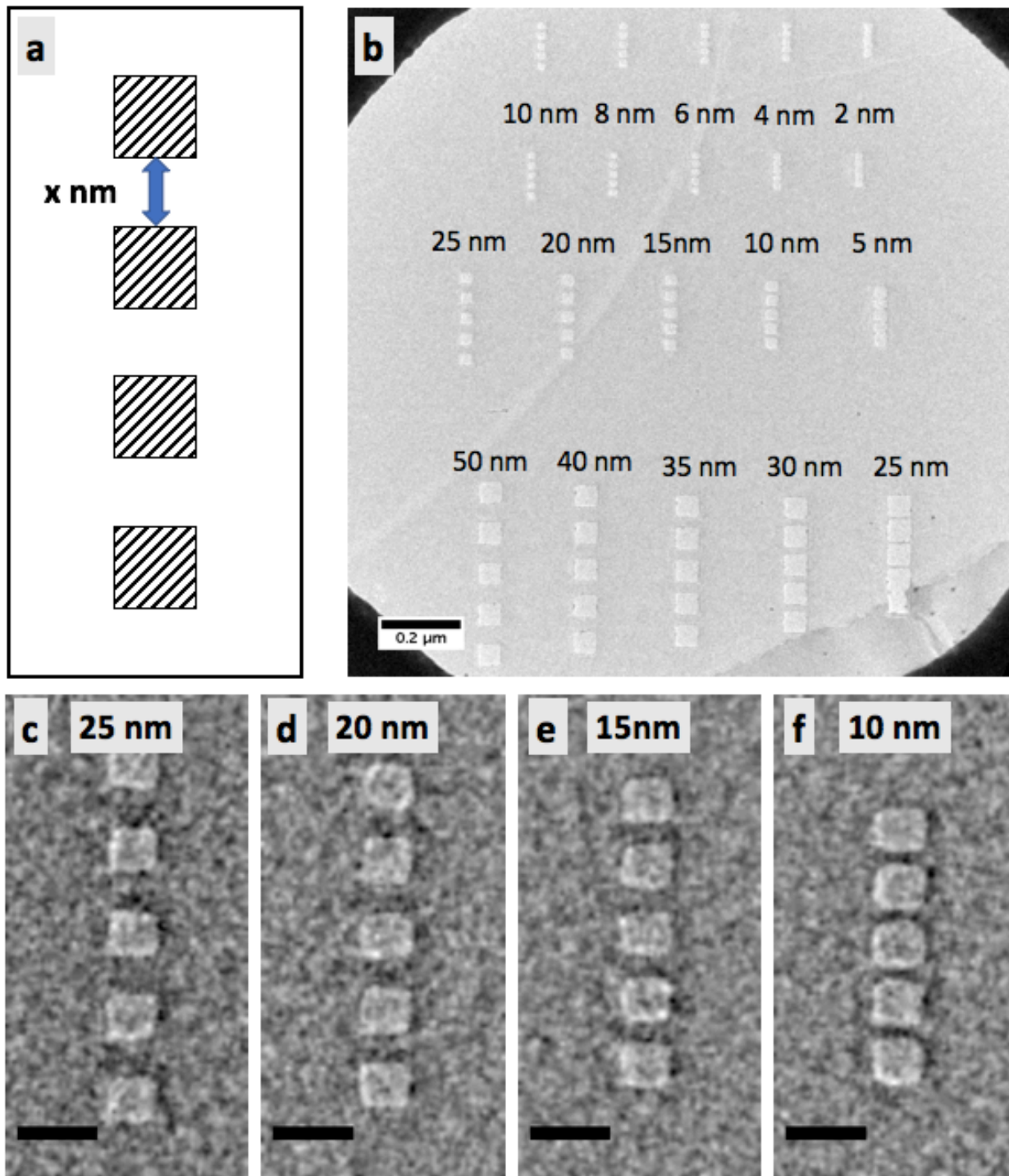
Figure 4.3 MoS₂ Nanoribbons fabricated by HIM. (a) A schematic of the etch pattern for the fabrication of nanoribbons. Square holes are etched in a linear array; the distance between the squares (labelled 'x nm') determines the width of the ribbon. The length of the pore is determined by the edge length of the square. (b) A bright field TEM image of MoS₂ nanoribbons with varying width (as labelled in the figure) and length. The bottom row is comprised of 50 nm length ribbons. The second row is comprised of 30 nm length ribbons. The top two rows are identical with 20 nm length ribbons. (c)-(f) Close up TEM images of the nanoribbons in the second row from the bottom. The width of the ribbon is labelled. (c)-(f) Scale bars are 50 nm. Figure is based on my original unpublished data.

93
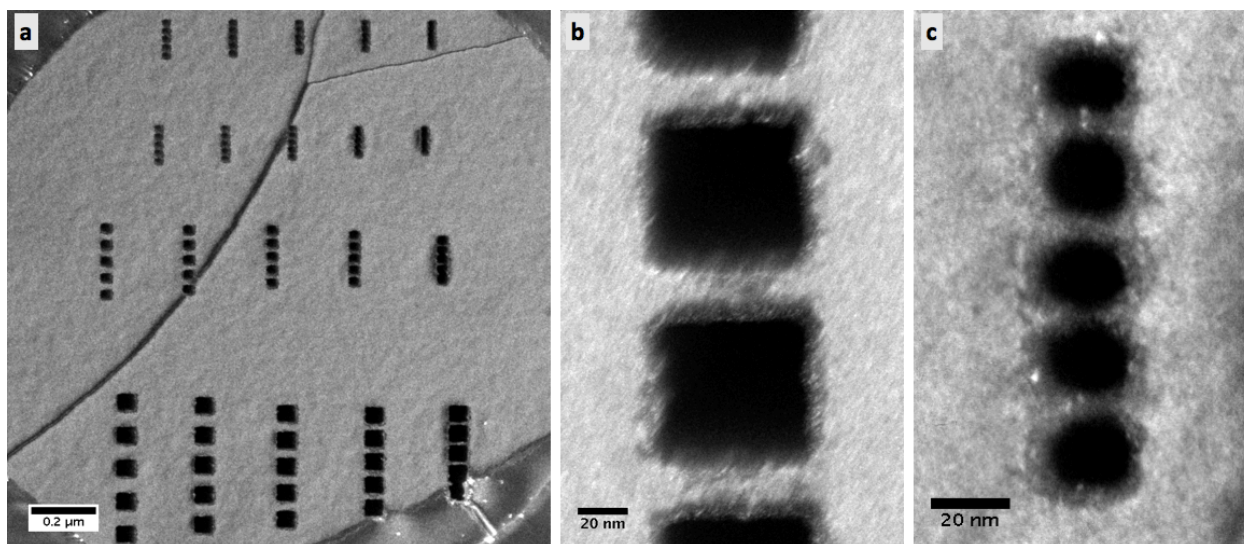
Figure 4.4 DF-TEM of MoS₂ nanoribbons fabricated by HIM. (a) A DF-TEM image showing the region in Figure 4.3(b). (b) A zoomed in DF-TEM image of an array of 30 nm x 50 nm ribbons in the lower right of (a). (c) A zoomed in DF-TEM image of an array of 6 nm x 20 nm ribbons in the top center of (a). Figure is based on my original unpublished data.

For electronic applications, the crystal structure and edge termination of nanoribbons is critical. In order to understand the effect of over-etching on the structural properties of the ribbons, we characterize the HIM etched MoS₂ nanoribbons by dark field TEM (DF-TEM) and high angle annular dark field STEM (HAADF-STEM). DF-TEM and HAADF-STEM work by physically filtering a real-space image for a specific region in an electron diffraction pattern. In the case of DF-TEM, an aperture is inserted in the diffraction plane of the TEM. Only electrons scattered into the selected diffraction peak form the real space image. Because the unscattered electrons are blocked, amorphous materials and vacuum appears dark while crystalline materials appear bright.

In HAADF-STEM, a ring-shaped detector is used to detect scattered electrons in STEM. Since only scattered electrons are detected, crystalline material appears bright while amorphous materials and vacuum appear dark. Because these two techniques allow for direct, high-resolution spatial discrimination between crystalline and amorphous materials, they are ideal for characterizing the effect of beam damage at the edge of nanoribbons.

Figure 4.4(a) shows a dark field TEM image of the MoS₂ nanoribbon arrays patterned by HIM and imaged by TEM in **Figure 4.3**. The MoS₂ film and ribbons has taken a bright contrast while the square holes and wrinkles have a dark contrast. **Figure 4.4**(b) and (c) zoom in on ribbon arrays defined by (b) 50 nm x 50 nm squares spaced by 30 nm and (c) 20 x 20 nm arrays spaced by 6 nm. For the 30 nm width ribbon (shown in **Figure 4.4**(b)), the cumulative total width is over-etched and reduced to 28 nm. The central 15 nm of the ribbon is bright in contrast implying that it is highly crystalline. However, a 6 nm border on each side has reduced contrast.

For the 6 nm ribbon shown in Figure 4.4(c), the entire ribbon is of reduced contrast versus the bulk of the film. However, it retains a bright contrast versus the vacuum level. The reduced contrast of 6 nm ribbon and border on the 30 nm ribbon could be due to 1.) amorphization, 2.) deposition of an amorphous coating, 3.) folding, or 4.) partial etching or change in chemical species.
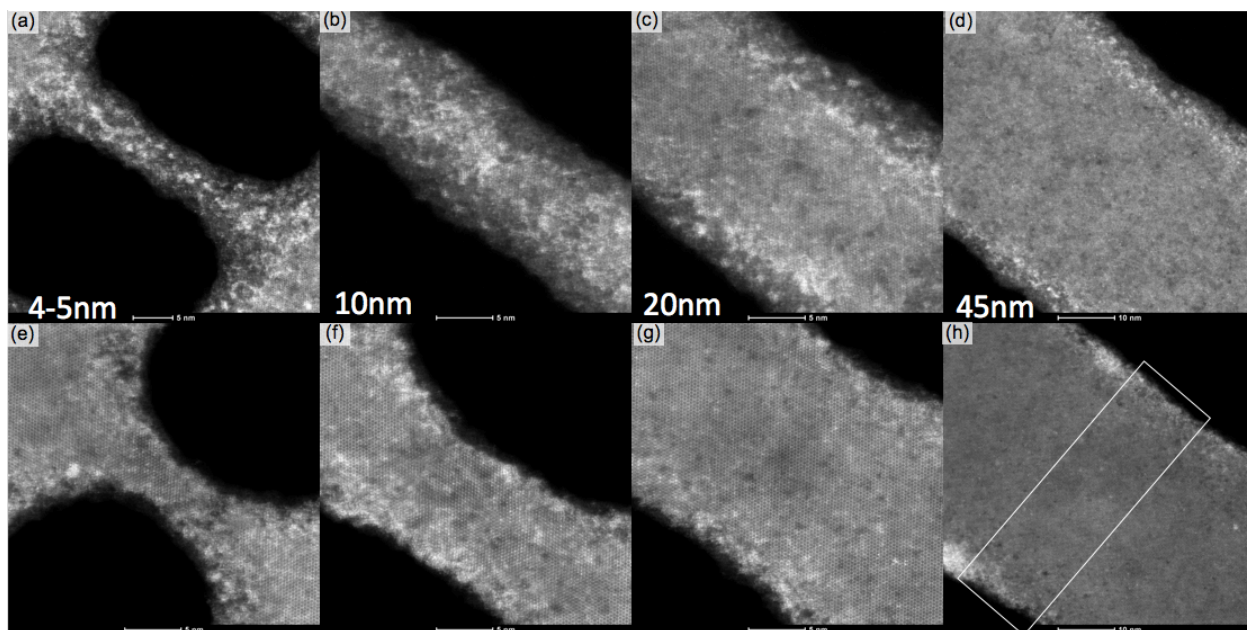
Figure 4.5 High resolution HAADF-STEM of monolayer and bilayer MoS$_2$ nanoribbons. (a)-(d) HAADF-STEM of monolayer MoS$_2$ nanoribbons. The width is labelled. (e)-(h) HAADF-STEM of bilayer MoS$_2$ nanoribbons. The width is labelled in the above image. Scale bars (a)-(c) & (e)-(g) 5 nm. (d) & (h) 10 nm. Figure prepared by and based on unpublished STEM data collected by Dr. Amin Azizi under the supervision of Prof. Alex Zettl.

To further probe the reduction in brightness from the DF-TEM near the edges of the MoS$_2$ ribbons, we performed high-resolution HAADF-STEM on both monolayer and bilayer nanoribbons fabricated under the same conditions described previously. **Figure 4.5** shows nanoribbons fabricated in monolayer (a)-(d) and bilayer (e)-(h) MoS$_2$ ranging from 4 – 45 nm in width. In the monolayer ribbons, there is visible inhomogeneity around the edges. For the 20 nm and 45 nm ribbons, the 2-3 nm nearest to the edge are comprised of a generally darker contrast with lighter dots and grains embedded. Based on previous work, it is likely that these strips near the edge are amorphous molybdenum mixed with MoS$_2$ or other metallic domains. For the narrower ribbons (4-5 nm and 10 nm), the entire ribbon has an inhomogeneous contrast. While these ribbons are structurally stable, they likely do not behave electronically as MoS$_2$. For monolayers, HIM etching is likely only suitable for ribbons >20 nm for transistor applications.

In the bilayer MoS$_2$ as shown in **Figure 4.5**(e)-(h), we do not observe substantial inhomogeneities in contrast near the edge. There is no major variation in contrast, and it is visibly clear that the ribbon is crystalline all the way to the edge. While some light and bright spots are visible throughout the 4-5 nm, 10 nm, and 20 nm, these do not compromise the crystallinity of the lattice; the light spots appear similar to carbon contamination on the ribbons while the dark spots appear similar to sulfur vacancies in the MoS$_2$.

Based on these observations, increasing the thickness from monolayer to bilayer stabilizes the edges of MoS$_2$ during HIM etching. This observation is consistent with the prior literature. We propose two possible mechanism for this stabilization. The first is that the addition of the second layer prevents kinetic scattering; for collisions the top layer, the bottom layer dissipates energy and prevents the atom from ejecting. Simultaneously, the top layer shields the bottom layer from helium ions. These effects result in an increase in the minimum scattering energy and results in

less etching and amorphization. The second mechanism we propose is that there is a chemical interaction between the top and bottom layer. When atoms are ejected from one layer, coordination between the layer may stabilize the vacancy, preventing additional etching and amophization. Because of these effects, the bilayer edges appear suitable for electronics applications.
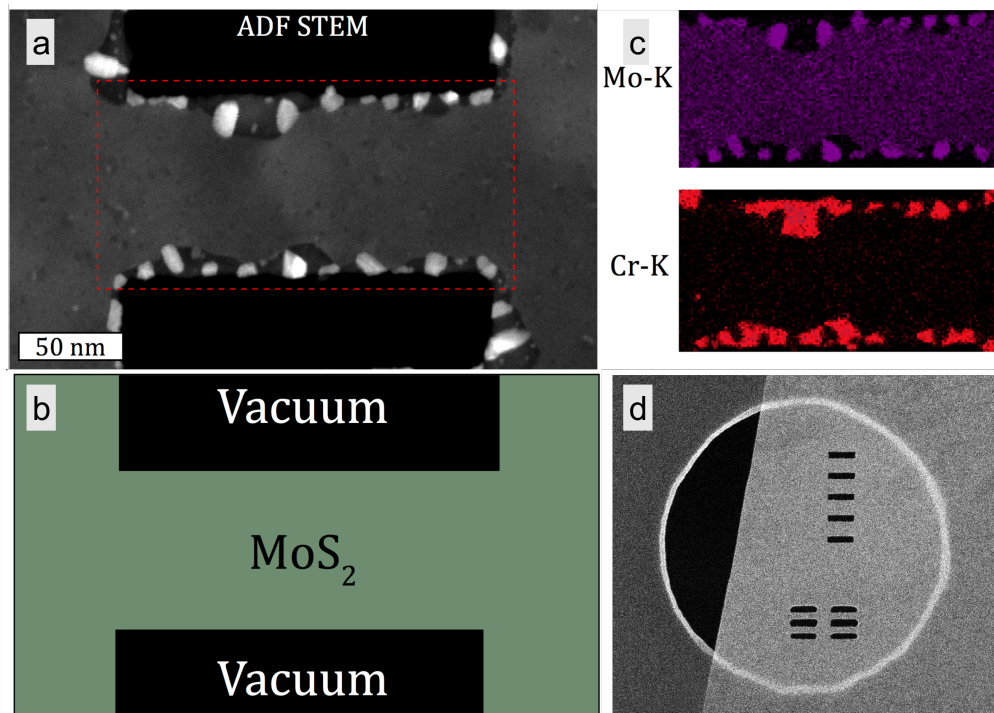
Figure 4.6 STEM and STEM-EELS of MoS$_2$ HIM ribbons after heating. (a) A multilayer MoS$_2$ ribbon after being heated to 900 ºC for 20 minutes. (b) A cartoon illustrating the position of the MoS$_2$ and the position of the vacuum in (a). (c) A STEM-EELS map showing the location of molybdenum (above) based on it K-peak and of chromium (below) based on it K-peak. (d) The multilayer MoS$_2$ ribbon sample suspended on a SiN TEM grid as imaged in the helium ion microscope. The circular hole is 2 μm. Figure based on unpublished data collected in collaboration with Brian Shevitski under the supervision of Prof. Alex Zettl.

Earlier experiments in graphene and *h*-BN have shown that heating under electron irradiation has have allowed their edges to heal and recrystallize.[102,178,198] In order to test if we can recover pristine MoS$_2$ edges in this same way, we heated our HIM milled nanoribbon samples during TEM characterization. Using an *in situ* heating holder, the multilayer MoS$_2$ is heated to 500 – 900 ºC and studied using STEM and electron energy loss spectroscopy (EELS). First, we heated the milled MoS$_2$ to 500 ºC for 20 minutes and observed no reformation of the edge.

Next, we increased the temperature to 700 - 900 ºC for 20 minutes and imaged the MoS$_2$ ribbons. **Figure 4.6**(a) shows a STEM image of the resulting MoS$_2$. Along the edges, bright 10-20 nm grains have formed within a dark background. STEM-EELS measurements (shown in the map in **Figure 4.6**(c)) demonstrate that the bright crystals are molybdenum-rich (even when compared to the bulk MoS$_2$) while the dark background in which they sit is chromium rich. This suggests that when the sample is heated, metals migrate and crystallize at the edges. Molybdenum exits the bulk of the MoS$_2$ and condenses near while chromium migrates from the substrate or TEM column.
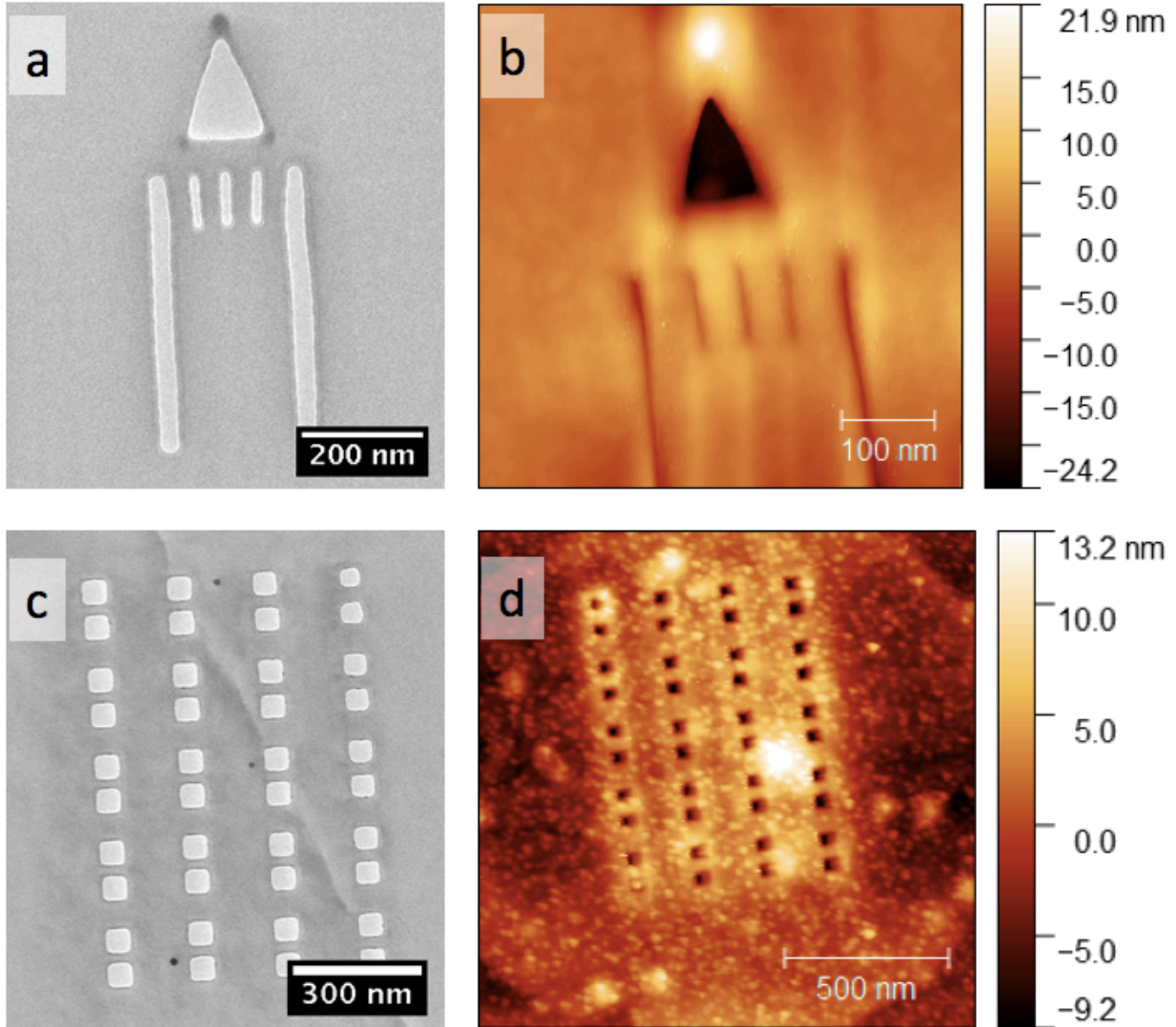
Figure 4.7 MoS$_2$ patterned by HIM before and after transfer off of a TEM grid. (a) and (c) show TEM images of patterns generated by HIM in multilayer MoS$_2$ on metallized SiN TEM grids (Norcada). (b) and (d) show AFM images of the same patterns (potentially from a different region of the sample) after they are moved to a Si/SiO$_2$ substrate by the dry transfer method described in Section 2.3.3. Figure is unpublished data collected in collaboration with Dr. Kyunghoon Lee and Dr. Amin Azizi under the supervision of Prof. Alex Zettl.

In order to characterize the HIM fabricated MoS$_2$ nanoribbons by electrical transport, it is important for the structures to be on a substrate compatible with standard lithography and contact techniques. After patterning, we demonstrate that the ribbons can be transferred from a SiN TEM grid using the transfer technique described in Section 2.3.3. **Figure 4.7** shows an array of multilayer MoS$_2$ nanoribbons (a) first while characterized by TEM while suspended on a grid and (b) then by AFM after the MoS$_2$ is picked up off of the grid and transferred to a Si/SiO$_2$ chip. We find that during the transfer the nanoribbons remain intact and can be moved between substrates. Using this technique, electrodes can be deposited to the MoS$_2$ nanoribbons using convention electron beam lithography and electronically characterized by transport.

4.3 Nanopatterning Graphene/*h*-BN Heterostructures with HIM

This section is based on my unpublished experimental results obtained in collaboration with Dr. Amin Azizi and Dr. Kyunghoon Lee under the supervision of Prof. Alex Zettl.

In Sections 4.1 and 4.2, I explored the ability of HIM to directly write nanostructures in two-dimensional materials. Moreover, it was shown that HIM can be used to reliably generate features as small as 4 nm in *h*-BN and MoS_2 and that multilayer samples can maintain their crystallinity near their edges. While patterning single species can have important impacts on their material properties, patterning one or multiple sheets in a stack can have additional effects arising from the interactions between the layers. Here, the use of HIM to produce patterned heterostructures in graphene/*h*-BN stacks is described. The ability to mill at the length scales already demonstrated in Sections 4.1 and 4.2 allows us to use patterns in *h*-BN to write periodic potentials for other two-dimensional materials. In this section, I consider the use of HIM to fabricate these types of heterostructures that can be used to create designer Hamiltonians.

Recently, there has been significant research interest in creating superlattice potentials for graphene.[17,173,176,199,200] Specifically, two types of lattices have been the subject of much of the focus of in both the Zettl Group and elsewhere. The first topic of interest is the use of superlattice potentials for the creation of 'artificial graphene'. By patterning a trigonal or hexagonal array in graphene or a dielectric substrate in contact with the graphene, additional Dirac cone band structures can be induced in the graphene shifted in energy and wave-vector. The position of these cones can be controlled within the energy-momentum space by controlling the spacing and depth of the overlaid potential.

The second system of interest is a one-dimensional superlattice overlaid on graphene. Several prominent theoretical predictions demonstrate that when superlattice potential comprised of parallel stripes is applied to graphene, an anisotropic electronic structure is induced.[200] These calculations have shown that there is a sharp decrease in the fermi velocity in the direction parallel to the potential stripes. With sufficiently sharp potential modulations, charge-carriers in graphene can thereby be focused and collimated without scattering. When current is flowed perpendicular to the stripes, this leads to a "supercollimation" effect in which electron waves can travel 100 microns before spreading even 500 nm. The ability to control the flow of ballistic electrons in graphene promises to be an exciting new platform for the development of low-dissipation and quantum coherent devices. These predictions remain unrealized, however, due to the large minimum feature sizes of conventional lithography.
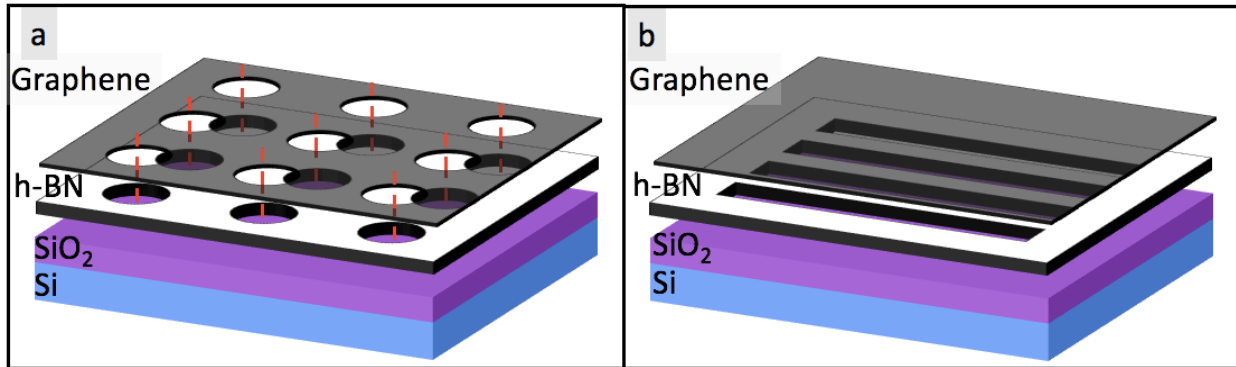
Figure 4.8 Schematics of two approaches for graphene/*h*-BN heterostructures. (a) Approach 1: the graphene/*h*-BN heterostructure on a Si/SiO$_2$ chip is assembled before patterning by HIM. Identical patterns are generated in the graphene and *h*-BN as shown by the aligned (denoted by red dashed lines) periodic holes. (b) Approach 2: Suspended *h*-BN is patterned using HIM prior to heterostructure assembly. After milling, the graphene is transferred to the *h*-BN before transfer to the target substrate.

Using HIM, we explore two paradigms for creating superlattices in graphene. **Figure 4.8** outlines our two approaches for fabricating these *h*-BN/graphene heterostructures. In the first approach (**Figure 4.8**(a)), graphene/h-BN stacks are assembled on an Si/SiO$_2$ substrate and patterned directly by milling with HIM. The geometry of the graphene and *h*-BN can then be modified to include new periodic structures such as anti-dot arrays.

In the second approach (**Figure 4.8**(b)), patterned *h*-BN gates are generated with nanometer scale precision in order to create custom energy landscapes. This patterning is achieved by milling using HIM on *h*-BN suspended on a TEM and then using a graphene flake to pick up the patterned *h*-BN in order to transfer the stack to the target substrate. By applying a gate-field through a patterned *h*-BN to a pristine conducting layer of a graphene, the charge carriers will experience atomically-sharp potential variations across the surface. This will induce modulations in doping and changes to the overall band structure, resulting in a versatile method for Hamiltonian design.[176]
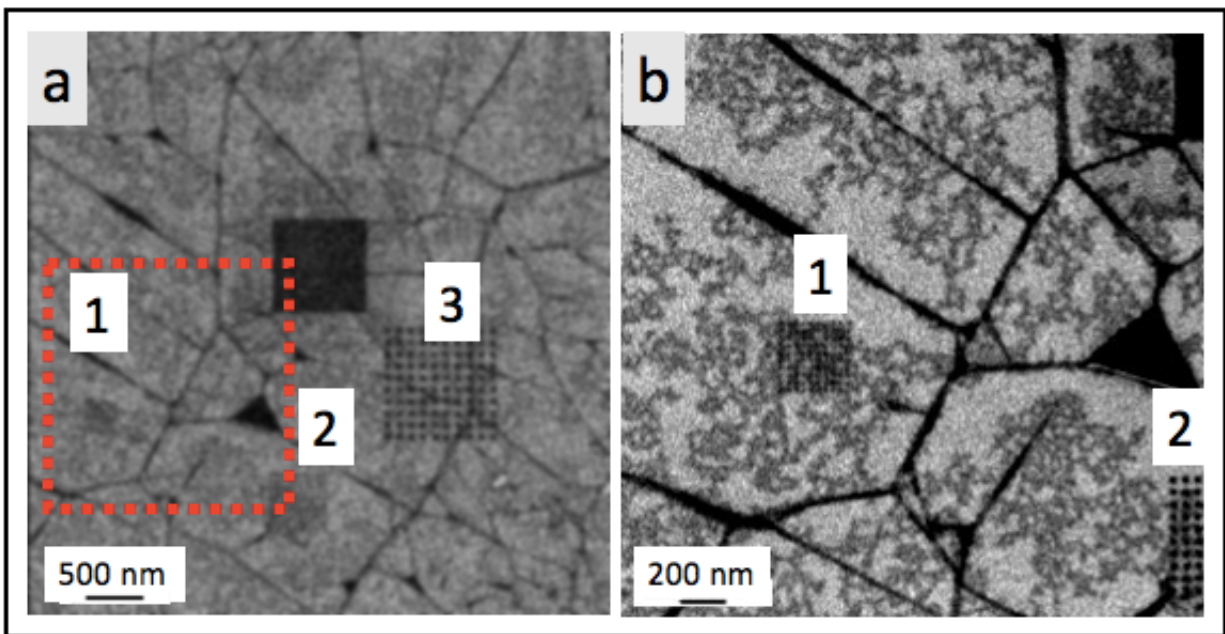
Figure 4.9 HIM images of nanopatterned anti-dot arrays on graphene/h-BN stacks. Holes in the graphene/*h*-BN stacks are etched by HIM after they are already on the target substrate. (b) shows a scan taken within the red-boxed region in (a.). Pattern 1 shows 10 nm hole formed at 20 nm pitch. Pattern 2 shows 20 nm holes formed at 50 nm pitch. Pattern 3 shows 50 nm holes formed at 100 nm pitch. Figure based on my original unpublished data.
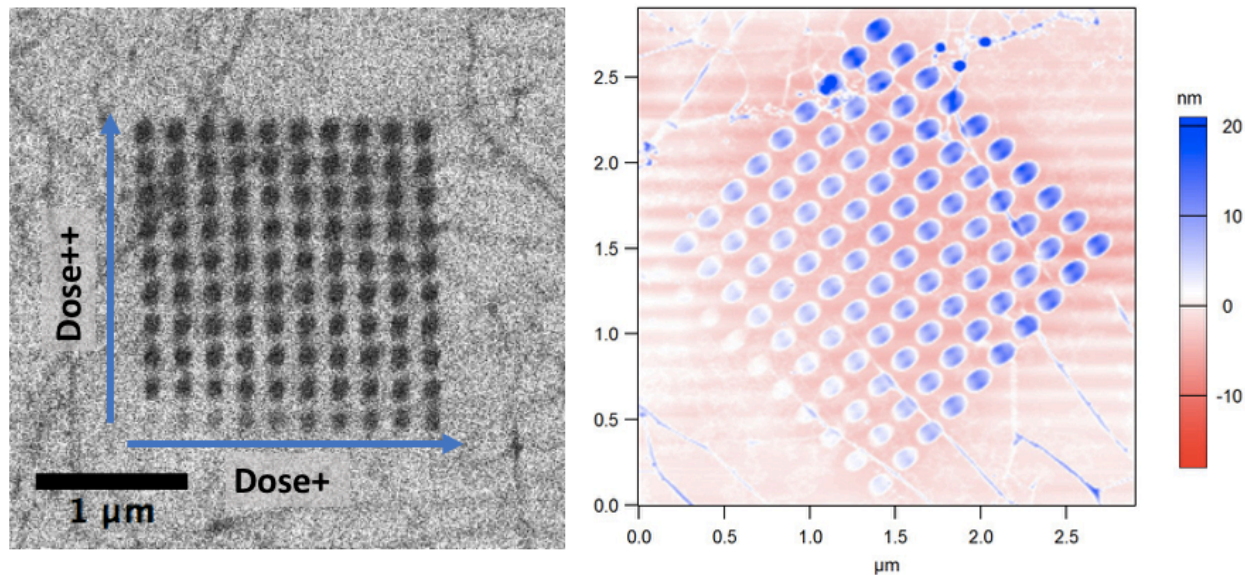
Figure 4.10 Helium ion dose effects on graphene/h-BN stacks. HIM (left) and AFM(right) images of a nanopatterned anti-dot array on a graphene/h-BN stack. The dose is increased from 0.1 to 10 nC/μm^2 in 0.1 nC/μm^2 (horizontal) and 1 nC/μm^2 (vertical) increments. Increasing the dose correlates to a darkening of the contrast in HIM (left) and an increase in vertical height (right) of the patterned dot. Figure based on my original unpublished data.

In **Figure 4.9** and **Figure 4.10**, we explore the first approach outlined in Figure 4.8 in which stacks of monolayer graphene on *h*-BN are patterned directly on a substrate. Films of monolayer graphene are transferred to exfoliated flakes of *h*-BN on 285 nm SiO2 on Si then anti-dot arrays are patterned in the graphene using HIM with a dose of ~1-5 nC/μm^2. **Figure 4.9** shows HIM images of three anti-dot arrays patterned in the graphene films with varying size and spacing. In panel (a), only array 3 can be resolved with 50 nm anti-dots and 100 nm pitch. In the zoomed in image in panel (b), arrays 1 and 2 are both visible. These arrays have 20 nm anti-dots with 50 nm pitch, and 10 nm anti-dots with 20 nm pitch.

While wrinkles and contamination on the film obscure the patterns, the arrays with these dimensions are clearly. In previous works exploring artificial graphene through direct patterning of graphene/*h*-BN stacks, satellite Dirac cone band structures are observed for trigonal arrays of anti-dots with hole and pitch size around 20 nm.[176]

One major concern for patterning two-dimensional materials, as explored in Sections 4.1 and 4.2, is the quality of the etched regions. Because characterization by TEM as in the previous sections requires an electron transparent substrate, atomic force microscopy (AFM) was used to characterize the helium ion milled anti-dot arrays. **Figure 4.10** shows an array of anti-dots patterned in the same sample described above with a dose varying from 0.1 to 10 nC/μm^2 imaged both using HIM (a) and AFM (b). In the HIM image, we observe that increasing dose results in an increase in both the size and darkness of an anti-dot. Performing AFM, we find that the anti-dots are actually raised relative to the sample with heights ranging from 5-25 nm.

The elevation of the exposed regions calls into question the effectiveness of patterning graphene/*h*-BN directly on the substrate. The increase in the height of the helium ion irradiate dots can be due to one of two reasons. First, the helium ion exposure may be etching redepositing material on top of the graphene. In this case, the dominant effect of the helium ion beam would be to add this additional layer. The second possibility is that the helium ion exposure may induce swelling in the Si/SiO$_2$ substrate. Additional experiments are necessary to investigate the quality of this etched heterostructure and assess its viability.
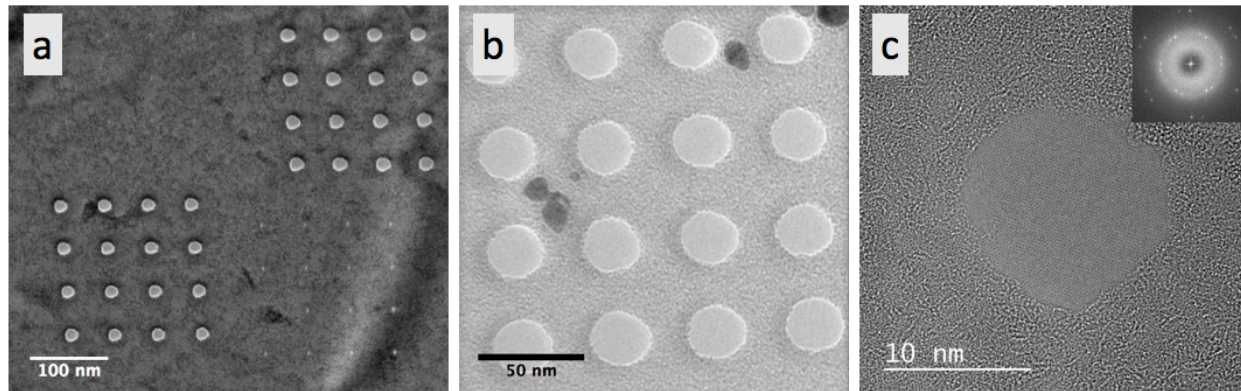
Figure 4.11 Heterostructures via graphene lamination over holes in *h*-BN. (a) Example TEM image of *h*-BN hole arrays generate by HIM. Arrays of 20 nm and 7 nm holes are shown with 50 nm pitch (b) Example STEM image of graphene transferred on top of an *h*-BN hole array in which 25 nm holes are spaced at a 50 nm pitch. (c) HR-STEM image of Graphene transferred on top of a 10 nm hole milled in *h*-BN using HIM. The inset shows a FFT of the image in which the lattices of both the graphene and *h*-BN are visible. The real space lattice of the graphene is apparent, and there is a clear layer of amorphous material between the graphene and *h*-BN. (b) and (c) are unpublished STEM data collected by Dr. Amin Azizi under the supervision of Prof. Alex Zettl.

In **Figure 4.11**, we explore the second approach outlined in **Figure 4.11** in which *h*-BN films are patterned using HIM and graphene is subsequently transferred. Unlike the patterning of anti-dots in graphene *h*-BN stacks, this technique can apply a periodic potential by changing the dielectric environment of the graphene across the *h*-BN or by applying a gate field that oscillates in strength due to the pattern in the *h*-BN. First, anti-dot arrays are milled in suspended multilayer CVD-grown *h*-BN on TEM grids as described in Section 4.1 and shown in Figure 4.11(a). Monolayer graphene is then transferred to the grid, directly on top of the *h*-BN as described in Section 2.3.1.

We characterize the suspended graphene/*h*-BN stacks by HR-STEM (Figure 4.11(b)-(c)). Figure 4.11(b) shows a STEM image of suspended graphene over an array of 20 nm holes in *h*-BN with a 50 nm pitch. From this lower magnification, we observe that the HIM fabricated holes are regular in size, shape, and position. **Figure 4.11**(c) shows a higher magnification image taken from a 10 nm hole in an array with 20 nm pitch. We can observe that graphene has adhered to the *h*-BN as its lattice is visible and because there are two distinct sets of hexagonal peaks in the FFT in the inset.

Based on the FFT, we observe that both the graphene and *h*-BN maintain their crystallinity, with the *h*-BN preserving its crystallinity up to its edge. A ring in the FFT and visible disorder indicate amorphous material in the image; however, the real and reciprocal space disorder is not localized near the HIM exposure and appears to be contaminants at the *h*-BN/graphene interface. This fabrication would therefore likely benefit from a cleaner transfer process.

Though we do not observe significant amorphization of the *h*-BN, the edges of the HIM milled holes do not appear perfectly regular. Electronic transport or more direct band structure measurements (ARPES or STM) are necessary to probe the effect of these irregular edges.

4.4 Graphene Mechanical Manipulation with HIM

This section is based on my original unpublished experimental results.

Helium ion milling suspended two-dimensional sheets provides a path towards strain engineering and fabrication of three-dimensional structures. By cutting and releasing sections of the membranes, sheets of graphene can be manipulated in the same ways as paper (by folding and wrinkling) or as an elastic tape (by stretching and sticking). Using conventional lithography, these types of three-dimensional manipulations have been achieved in Reference [201]; here, however, we demonstrate a direct-write method for mechanical manipulation of graphene by etching using HIM.
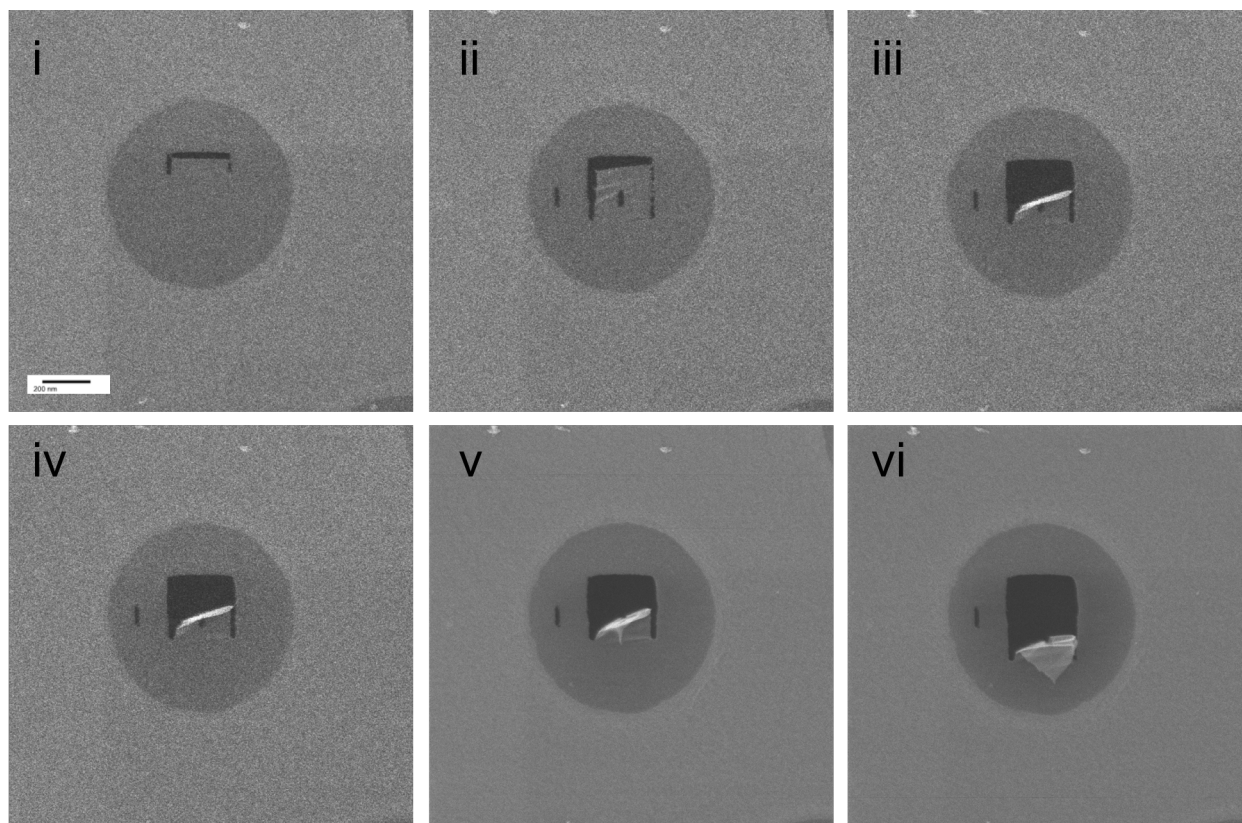
Figure 4.12 Direct-Write Folding of Graphene in HIM. HIM images of graphene as it folded using helium ion etching. The single layer graphene is suspended over a 0.6 μm diameter circular hole in an amorphous carbon TEM grid. (i) A horizontal slot is etched. (ii) Two vertical slots are etched surrounding the horizontal slot. (iii)-(v) The suspended graphene beam begins to sag. (vi) The graphene finally folds over due to its own adhesion. Figure based on my original unpublished data. Scale bar is 200 nm.

In Reference [202], Kim et al demonstrated that inducing folds in graphene results in a shift in the overall band structure and that the locally folded region (referred to as a 'grafold') is favorable for the intercalation of C_{60}. Here, we show that suspended graphene can be folded using direct-write helium ion milling. **Figure 4.12**(i)-(vi) shows graphene suspended over a 0.6 μm hole as it is cut, folded, and imaged using HIM.

In order to fold the graphene, first a horizontal cut is induced in **Figure 4.12**(i). Next two vertical slots are cut into the membrane to produce a freely suspended rectangular beam. The vertical slots are extended using the HIM until the rectangular until the sheet begins to sag as depicted in **Figure 4.12** (iii). The vertical cuts are extended until the self-adhesion of the graphene can overcome the bending stiffness of the sheet. At this point, the graphene will adhere to itself and produce a folded region as in **Figure 4.12**(vi).

Based on the angle and order of the cutting, the angle can be controlled. For example, in **Figure 4.12**, the left edge is cut first, resulting in a rightward shift for the fold. This could be used to produced twisted bilayer graphene using helium ion milling. The ability to fold suspended sheets of graphene can also be used to create 3D structures using kirigami as in Reference [201].
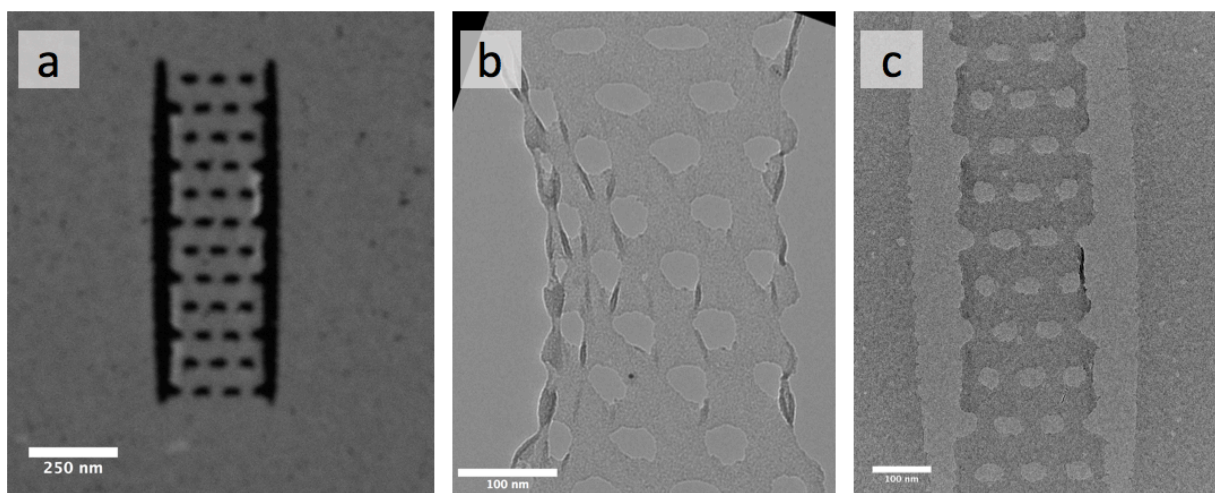
Figure 4.13 Strain engineered compression and wrinkling in graphene. (a) An HIM image of a slotted graphene ribbon produce by helium ion etching. (b)-(c) TEM images of slotted graphene ribbon produced by helium ion etching with holes that are (b) close together and overlapping in x-position and (c) further apart. Figure based on my original unpublished data.

The built-in tension in graphene can also be leveraged to control its morphology. By strategically cutting, strain can be relaxed to induce wrinkles, folds, and 3D structures. **Figure 4.13**(a) shows a slotted ribbon fabricated in suspended graphene as cut and imaged using HIM. By controlling the size and position of the slots, the strain relaxation in the ribbon can be controlled. **Figure 4.13**(b) and (c) show TEM images of ribbons produced with hole sizes and positions. When holes are produced close together such that the x-position overlaps between rows, compression and wrinkling out of plane in the ribbon is achieved (**Figure 4.13**(b)). For larger spacing between holes, only a small amount of compression results (**Figure 4.13**(c)).

Chapter 5

Mechanical transducers from patterned suspended graphene

In Chapter 4, I showed that by patterning suspended two-dimensional material membranes that their three-dimensional morphologies and mechanical properties are changed. In this chapter, I explore how patterning similar suspended membranes can be used to enable new transducer geometries. Specifically, by producing cuts around the perimeter of a graphene membrane, the mechanical stiffness can be changed from being dominated by the built-in stress and elastic modulus of the sheet to being driven by the bending stiffness of a graphene beam.

In the first section of this chapter, I describe a method to reduce the resonant frequency and broaden the frequency response for graphene resonators by patterning azimuthal flexures into the membrane. I then assess the use of these softened resonators for acoustic transduction. In the second sections, I describe the use of a similar patterned graphene/PMMA bimorph architecture for electron beam induced rotational actuation.

5.1 Patterned Graphene for Softened Acoustic Transducers

This section is based on unpublished ideas formed in collaboration Donez Horton-Bailey and Dr. Hu Long under the supervision of Prof. Alex Zettl.

Suspended graphene has previously been demonstrated as an excellent system for acoustic transducers. [203,204] Speakers and microphones comprised of suspended membranes of thick multilayer graphene have been shown to possess a wide-band frequency response in both the standard audio and ultrasonic ranges. Moreover, these devices demonstrate a nearly flat frequency response without the need for compensating electronics.

These graphene acoustic transducers, as described in the literature and sketched in **Figure 5.1**(a), consist of a suspended graphene membrane separated by spacers on each side from two air permeable electrodes. In order to achieve wide-band, audio-frequency responses (100 Hz-100 kHz) from these mechanical resonators they must be 1-10 millimeters in diameter. In this regime, an overall reduction in the resonance frequency is achieved versus the smaller graphene resonators reported in the literature[126,205–207] due to the large size of the suspended membrane and the frequency response is broadened due to an increase in damping.
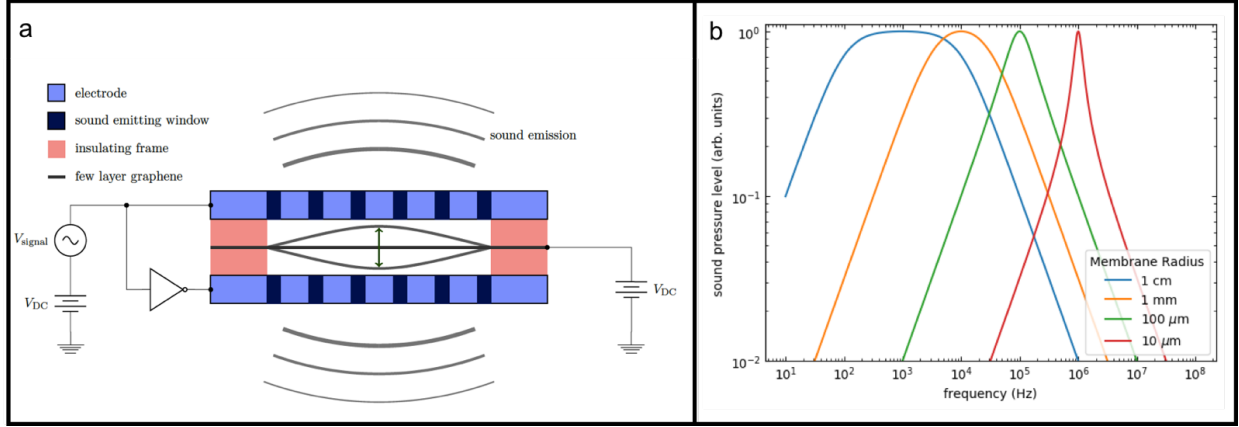
Figure 5.1 Schematic of a graphene acoustic transducer and its frequency response as its size varies. (a) A schematic showing the geometry of the graphene speaker studied in References [203,204]. A graphene membrane is suspended between two perforated electrodes. An AC signal on the electrodes is used to oscillate the membrane to produce acoustic waves. (b) A calculation depicting the calculated frequency response graphene membranes with varying radii and constant thickness (50 nm) and stress. Figure prepared in collaboration with Donez Horton-Bailey.

The reduction in resonant frequency and increase in bandwidth can be understood by considering the radial dependence of the transducer frequency response. The amplitude of oscillation at a given frequency for a circular suspended graphene membrane is a function of its resonant frequency and quality factor (Q) as defined by the Lorentz distribution:

$$A(f) = \frac{\frac{f}{f_0}}{\sqrt{\left(\frac{f}{f_0}\right)^2 + Q\left(\left(\frac{f}{f_0}\right)^2 - 1\right)^2}}$$

For this geometry, the resonant frequency is given as a function built-in stress on the membrane (σ), its mass per unit area (ρ), and the radius (r) of the circle. Moreover, it can be re-expressed as a function of only the radius and a reference measured resonant frequency ($f_0(R)$).

$$f_0(r) = \frac{1}{r}\sqrt{\frac{\sigma}{2\pi\rho}} = \frac{R}{r} \times f_0(R)$$

Like the resonance frequency, the quality factor has been observed to vary inversely proportionally to the radius of the graphene membrane.[207] Q can therefore be expressed either as a function of the damping (D) and the resonant frequency or as a function of only the radius and a reference measured quality factor.

As calculated in **Figure 5.1**(b) (based on the reference f_0 and Q values from Reference [207]), if the membrane is made smaller, the graphene transducer resonance frequency migrates above the audible regime and the FWHM of the response shrinks several orders of magnitude due to a decrease in dissipation. Therefore, in this configuration, the transducer cannot be made any smaller than the 1-10 mm while maintaining its audio-frequency response.

The ability to reduce the diameter of graphene acoustic transducers to between one micron and one millimeter would enable new applications and increase the yield of production for graphene speakers. One strategy that has been previously employed to change the properties of nanomaterial mechanical systems is the modification of their geometry and mass distribution. For example, previous work from the Zettl group has demonstrated the use of mass loading [208,209] and length tuning [210] to reduce and raise the resonant frequency of one-dimensional carbon nanotube resonators. In two-dimensional systems, similar strategies exist. The art of kirigami, which is cutting paper by a known design, has been used since ancient times to alter the mechanical compliance of a sheet. Similar manipulations have been realized at the micron scale by Blees et al in single layer graphene. [201]

In order to find a new route to reduce the size of the graphene acoustic transducers, we explore the use of patterned graphene to increase the bandwidth and reduce the resonance frequency of graphene membranes smaller than 1 mm. We approached this by developing a pattern in which a rigid central membrane is supported by a set of flexible springs that drive the transducers motion. Figure 5.2(a) shows the design we considered; in this configuration, several azimuthal flexures are created by cutting overlapping Z-shaped arcs along the outer edge of a circular area. In this way, the mechanics of the entire membrane is dominated not by the built-in tension of the membrane but rather the bending-stiffness of the flexures.

Figure 5.2(b)-(c) demonstrates how the flexures allows for the softening of the membrane under a static load both in a paper model (b) and simulated in COMSOL (by Dr. Hu Long). When a force is applied orthogonally to the plane of the membrane, the narrow flexures lift opposite the direction of the force while the central area is only minimally deformed. In this geometry, the effective spring constant of this deflection can be seen to depend totally on the bending modulus of the flexure.

The patterned graphene transducer shown in Figure 5.2(d) has two modes of operation. The first mode in converts electrical signals to acoustic waves while the second converts acoustic waves to electrical signals. These mechanisms are identical as those for the unpatterned device.

The actuator is used to generate acoustic waves by applying an AC voltage (with a DC offset) between the electrodes and the membrane (the AC voltage is inverted between the top and bottom electrode). The AC voltage capacitively couples to the membrane causing it to oscillate with the AC signal due to the electrostatic force on the membrane. As the membrane moves in and out of its original plane, the air is pushed producing sound.

By running this same mechanism in reverse, sounds can be used to generate an AC voltage. Incoming acoustic waves oscillate the suspended graphene membrane which is in turn amplified by a DC voltage. By measuring an AC voltage signal at the electrodes, electrical oscillations can be measured as sound excites the motion of the actuator. This allows for the device to also be used as a microphone.
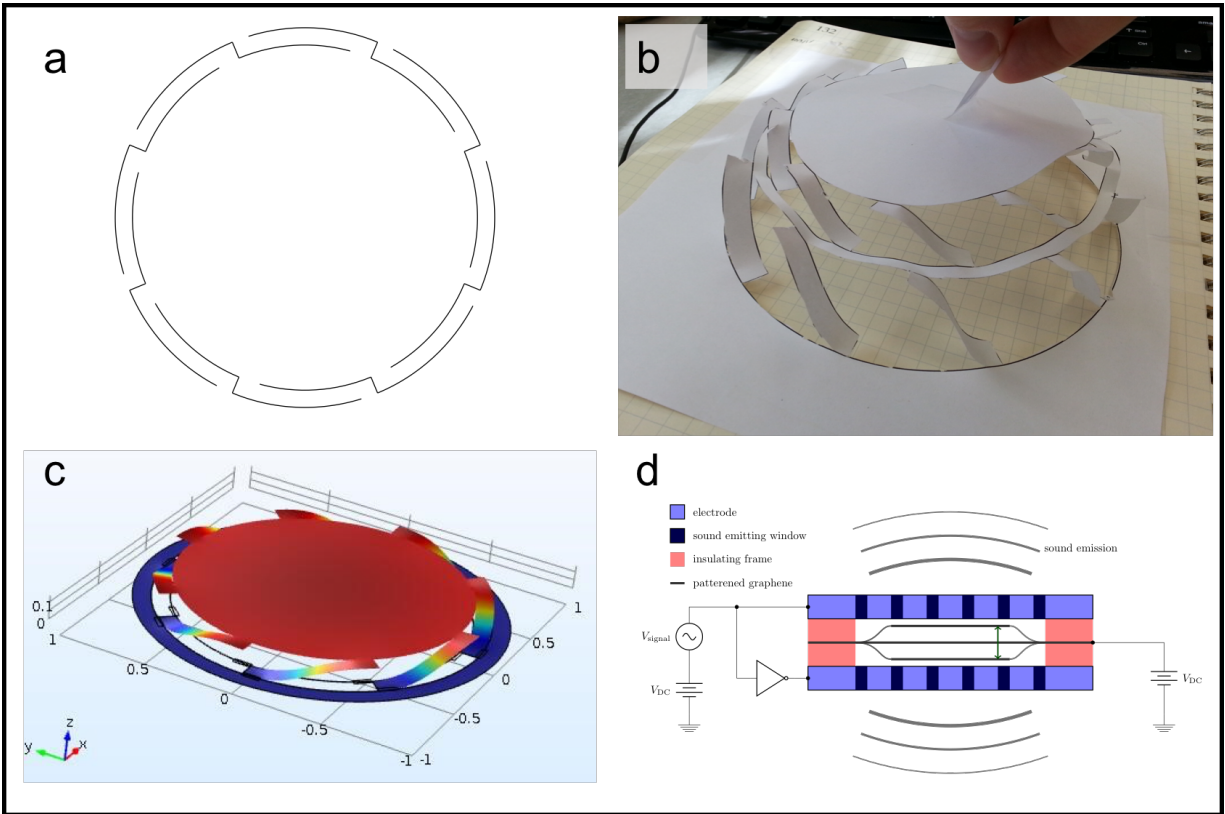
Figure 5.2 Design of a softened membrane. (a) The design studied for patterning graphene to soften its membrane. This combination of radial and azimuthal cuts allows for the rigid central plate to lift and rotate as shown in (b) in a paper model. (c) A COMSOL simulation in which a uniform force is applied to graphene membrane. The majority of the deformation occurs in the outer cuts, confirming an increased compliance of the speaker. (d) shows a schematic of patterned graphene loudspeaker device. The speaker behaves similarly to the one in Figure 5.1(a), but the changes mode shapes as the full displacement moves into the flexures as sketched. Figure prepared in collaboration with Donez Horton-Bailey and Dr. Hu Long.
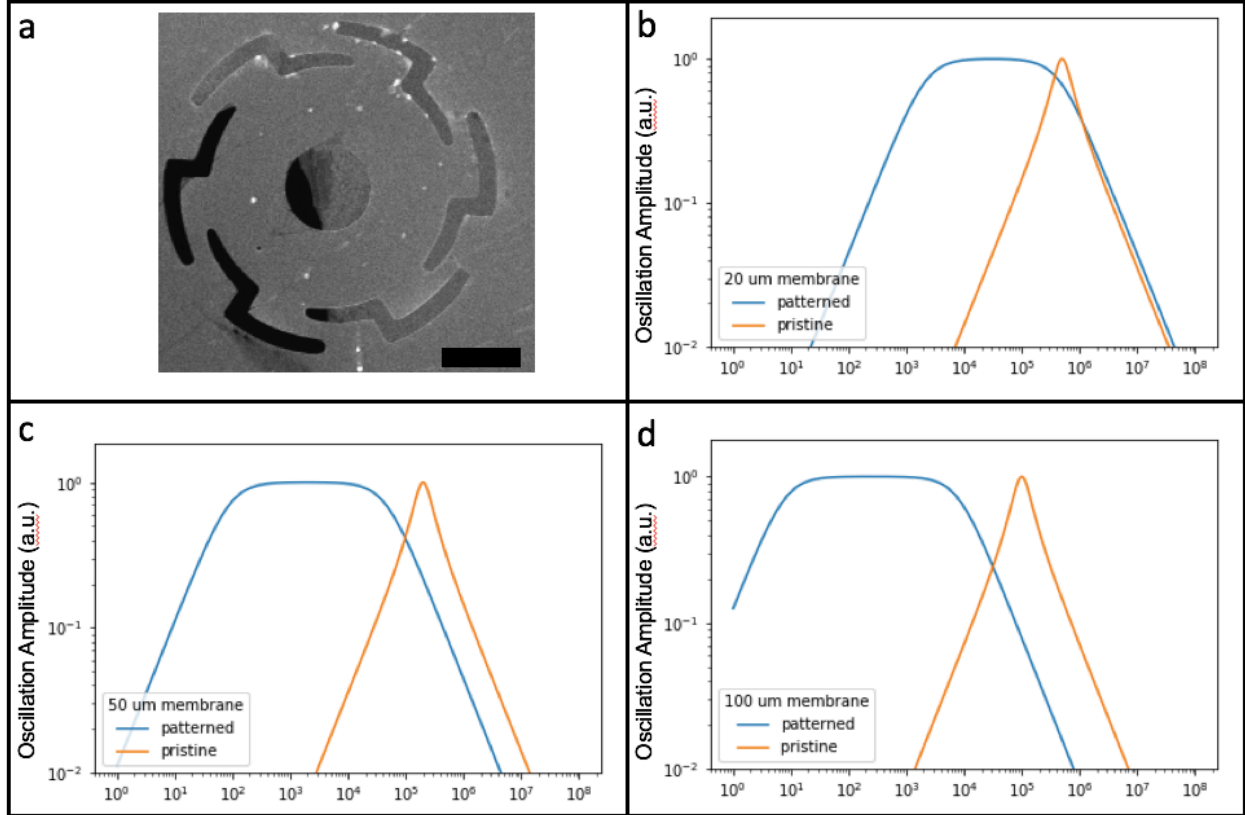
Figure 5.3 The AC mechanical effect of patterning a graphene membrane. (a) An example SEM image of a multilayer graphene softened transducer. The transducer was fabricated as shown in Figure 5.4(b). (b)-(d) show the calculated frequency response of pattern in (a) versus that of the unpatterned membrane for radii of (b) 20 μm, (c) 50 μm and (d) 100 μm. The patterned actuators consistently demonstrate enhanced resonances at reduced and broadened frequencies – lending to applicability for acoustic applications. (a) Scale bar is 5 μm. Figure prepared in collaboration with Donez Horton-Bailey.

An example SEM image of a multilayer graphene softened transducer is shown in Figure 5.3(a). This transducer was fabricated using the process shown in Figure 5.4(b). The resonant frequency of these patterned graphene is calculated and plotted as shown in Figure 5.3(b)-(d). The frequency is deduced as a function of the effective spring constant of the 8 flexures in parallel where each flexure is considered as two single clamped beams in series.

$$f_0 = \sqrt{\frac{8\,k_{eff}}{m}} = \sqrt{\frac{8 \times \frac{1}{2}\left(\frac{1}{4}Ew\dfrac{t^3}{\left(\frac{1}{2}L\right)^3}\right)}{m}} = \sqrt{\frac{8Ewt^3}{mL^3}}$$

Where E is the Young's modulus for graphite, m and h are the mass and thickness of the membrane, L and w are the length and width of the flexure, and $\frac{1}{4}Ew\frac{t^3}{(L)^3}$ is the effective spring constant for a singly clamped beam. For the calculation in Figure 5.3(b)-(d, we use E= 1 TPa, t = 40 nm, w = 5μm, and L = 2πR/8, and assume the same damping as for the patterned membrane as the pristine membrane (i.e. $f_0 \times Q$) is constant between the two for a given radius). We find

that for the 20, 50, and 100 μm radius graphene membranes considered, the transducer amplitude is at its maximum value and relatively flat across the entire audible range (~$10^2 - 10^4$ Hz). Moreover, the smaller of the two patterned transducers maintain this response well into the ultrasonic region.

5.2 PMMA on Graphene Rotational Actuators Enabled by Strain Relaxation

This section is based on our previously published work in Reference [211].

In this section, I report a novel angular displacement graphene-based mechanical device that uses only a conventional scanning electron microscope (SEM) or electron beam lithography system, common to many standard fabrication facilities, to both drive and detect its motion. The device consists of a patterned PMMA (poly(methyl methacrylate)) on graphene laminate, and rotational actuation is enabled by relaxation of the built in strain of the graphene. Azimuthal flexures support a central membrane, and compression of the membrane, via electron irradiation[212], produces rotation. The method demonstrates that irradiation from a conventional scanning electron microscope or electron beam lithography tool can be used to control the motion and rotation of suspended membranes, suggesting that this technique can be exploited for numerous applications. The actuation relies only on the ability to tune the elastic modulus of the PMMA, and therefore this device may lend itself to being driven by other means [213–215].

Figure 5.4 illustrates the process for the fabrication of suspended PMMA on graphene angular displacement actuators on commercially available holey silicon nitride (Norcada) or copper foil. First, four to eight layer stacks of commercially available single-layer graphene (Grolltex) are prepared on copper foil by repeatedly using a conventional PMMA assisted wet transfer [51,119]. This sequential transfer ensures spatial homogeneity of the mechanical properties of our multilayer graphene film.

Next, for the devices on silicon nitride (Figure 5.4(a)), the multilayer graphene is transferred. In order to reduce the built-in tension for the graphene membrane, we use a polymer free wet transfer to suspend the four layer graphene. In this process, the copper substrate is dissolved from below the four-layer graphene in sodium persulfate solution and the free-floating graphene is rinsed in three deionized water baths. The graphene is then scooped onto a 200 nm thick holey silicon nitride membrane. The suspended graphene is spin-coated with 250 nm of PMMA (molecular weight = 950k) dissolved at 4% weight in anisole (A4) and hard baked at 185 ºC.

The PMMA is then patterned with the actuator shape using electron beam lithography and developed in a 3:1 mixture of isopropanol and methyl isobutyl ketone. We use a newly developed pattern (Figure 1(a iv)) that is comprised of a central membrane supported by eight flexures such that when the flexures compress rotation is induced The graphene is then etched to the same shape as the PMMA by exposure to oxygen plasma with two steps of 60 seconds of 50 W at 50 sccm O_2 plus 20 seconds of 40 W at 20 sccm O_2.

For the devices prepared on copper foil (Figure 5.4(b)), the multilayer graphene is left on the growth substrate. First, the multilayer graphene is coated with PMMA using the same recipe detailed above. Next, electron beam lithography is performed to generate arrays of the actuator pattern and the graphene is patterned using a similar oxygen plasma etch. Finally, the copper is

selectively etched below the graphene actuator by floating the sample with its top side facing down on sodium persulfate (1mg/ml) for approximately 30 minutes.
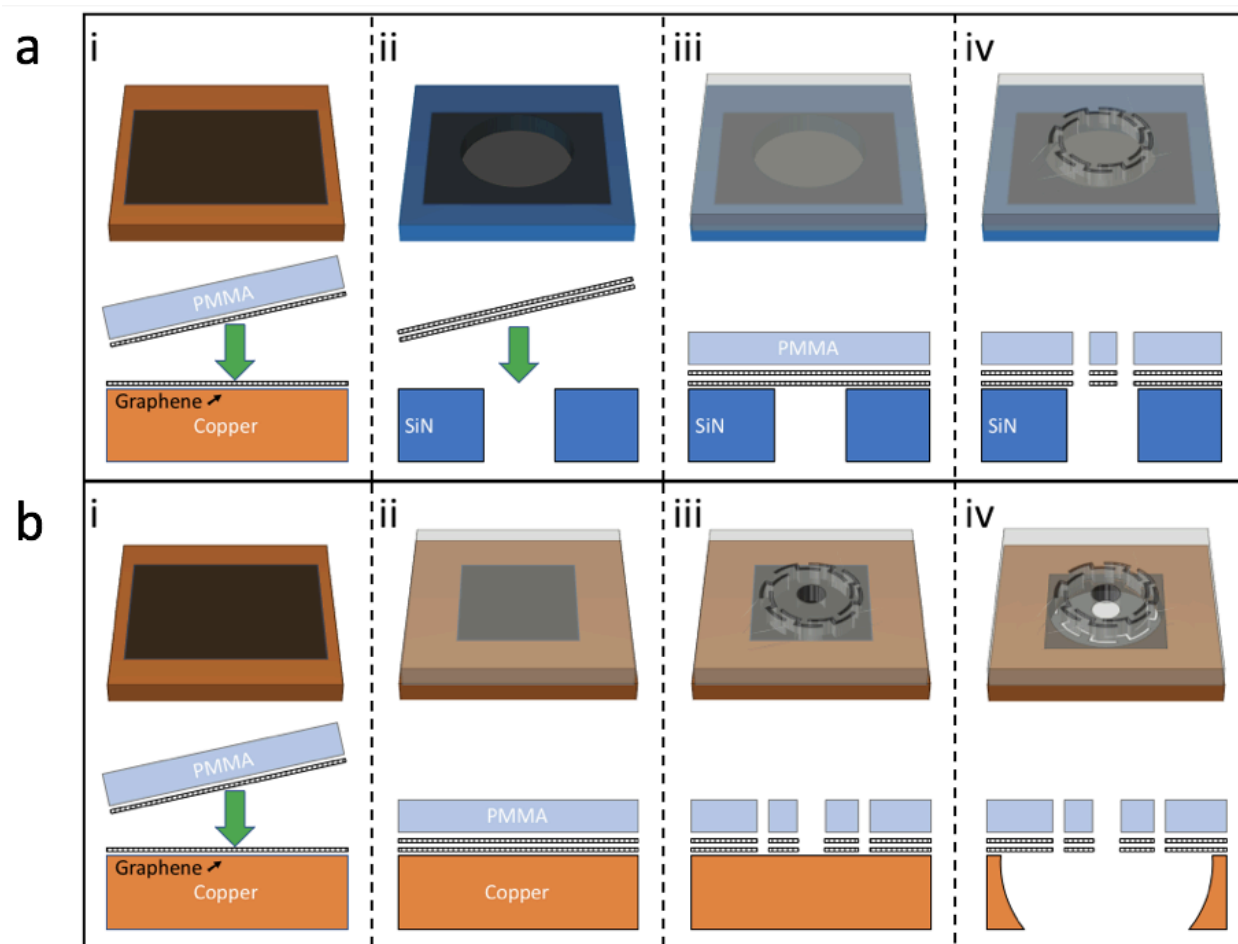
Figure 5.4 The process used to fabricate the PMMA on graphene angular displacement structures on (a) Silicon Nitride membranes and (b) copper foils. (a) (i) First several layers of graphene are transferred sequentially onto a graphene monolayer on copper foil, leaving a four to eight layer stack of graphene on the foil, (ii) the copper foil is dissolved and the graphene multilayers are transferred to holey silicon nitride, (iii) the graphene is coated with PMMA, and (iv) the PMMA is patterned using electron beam lithography and the graphene is etched by plasma. (b)) (i) Several layers of graphene are transferred sequentially onto a commercially available graphene monolayer on copper foil, (ii) the multilayer graphene is left on the copper foil and coated with PMMA, (iii) the PMMA is patterned using electron beam lithography and the graphene is etched by plasma, (iv) the copper is etched below the patterned graphene with a sodium persulfate wet etch. Figure reprinted from our previously published work in Reference [211].
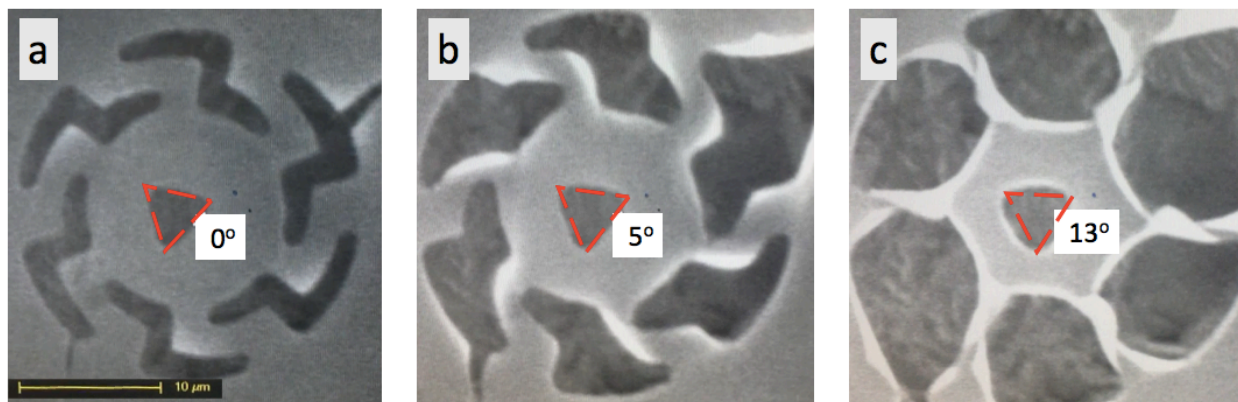
Figure 5.5 PMMA on graphene actuator as it rotates under SEM irradiation. This device is suspended over a hole in copper. (a) The graphene rotational actuator in its initial state, (b) the graphene rotational actuator after it has been exposed to ~1 x 10^{15} e⁻/cm² causing it to twist 5°, (c) the actuator has reached its final rotation of 13° after being exposed to ~3 x 10^{15} e⁻/cm². Scale bar is 10 microns. Figure reprinted from our previously published work in Reference [211].

After the fabrication of the suspended PMMA on graphene device, its rotation can be controlled using electron beam irradiation. The actuators are loaded into an SEM operating at 5 kV with a beam current of 1.0 nA over a roughly 1000 μm² area. The motion can be simultaneously driven and imaged using the electron beam.

Figure 5.5 shows a suspended PMMA on multilayer graphene device (with a copper trench) as it undergoes angular displacement due to electron exposure. A triangle is patterned in the middle of the central membrane in order to track the angle of the actuator. Figure 5.5(a) shows the initial configuration of the device before it is driven. In Figure 5.5(b), the flexures supporting the central membrane begin to compress after the device is irradiated by ~1 x 10^{15} e⁻/cm², and the triangle at the center of the membrane is seen to be rotated by 5°. In Figure 5.5(c), the flexures are fully compressed and have folded over allowing the actuator to reach its full displacement after the device is irradiated by 3 x 10^{15} e⁻/cm².

Figure 5.6 sketches the mechanism for angular displacement of the graphene actuator. Suspended graphene has been shown to have its mechanical properties dominated by a large built in tension [205,216,217]. This stress pulls inward on the PMMA on graphene flexures. As the PMMA is irradiated by the electron beam, the coordination of its polymer chains is reduced causing a decrease in its molecular weight and elastic modulus. This reduction in elastic modulus allows the built-in stress of the graphene membrane to compress and fold the PMMA. The stress relaxation rotates the graphene transducer as shown schematically in Figure 5.6 and experimentally in Figure 5.5.

In order to confirm that the built in stress of the graphene produces the observed membrane angular displacement, we fabricate a batch of actuators over 10 μm holes and remove the PMMA by annealing at 350 °C in a ~1 Torr H_2 environment [218]. This simulates the condition of reducing the elastic modulus of the PMMA to zero. Figure 4 shows the device before (optical image) and after (SEM) the removal of the PMMA. Before the PMMA is removed, the suspended PMMA on graphene holds its patterned structure. When the PMMA is removed, the graphene relaxes under its built-in tension. This results in a ~15° rotation as the arc of the flexures fully compress. There is also compression and folding in both central membrane and the flexures. This confirms

that the rotation of the graphene actuator is driven by the built-in stress in the graphene membrane

This mechanism highlights the potential versatility of our method. First, we have found that electron irradiation can be used to selectively and controllably relax the stress in suspended PMMA on graphene stacks. While we have used this effect to drive pre-patterned angular displacement actuators, this same principle could be used to write stress-strain field into pristine PMMA on graphene stacks, thereby controlling the mechanical [219] and electrical [220–222] properties of the membrane or its 3D morphology [223]. Given the maturity of electron beam writing technologies, near arbitrary patterns can be generated over large scales.

Also, we have found using our specific angular displacement actuator pattern that a simple reduction in the rigidity of our PMMA layer can result in mechanical motion. This suggests that any phenomena that tunes the elastic modulus of a polymer on graphene could produce similar motion. Effects like temperature [215], solution environment [213,223], and light irradiation [214] could all be detected by this device or used to drive its motion.

We have demonstrated a novel PMMA on graphene angular displacement actuator that can be driven using a convention SEM. By reducing the rigidity of the PMMA, the built-in stress of the graphene causes a compression of the flexures in our pattern yielding a controlled twist. This method is broadly applicable to other structures which can benefit from precise stress relaxation or can be driven by other processes which soften polymers.
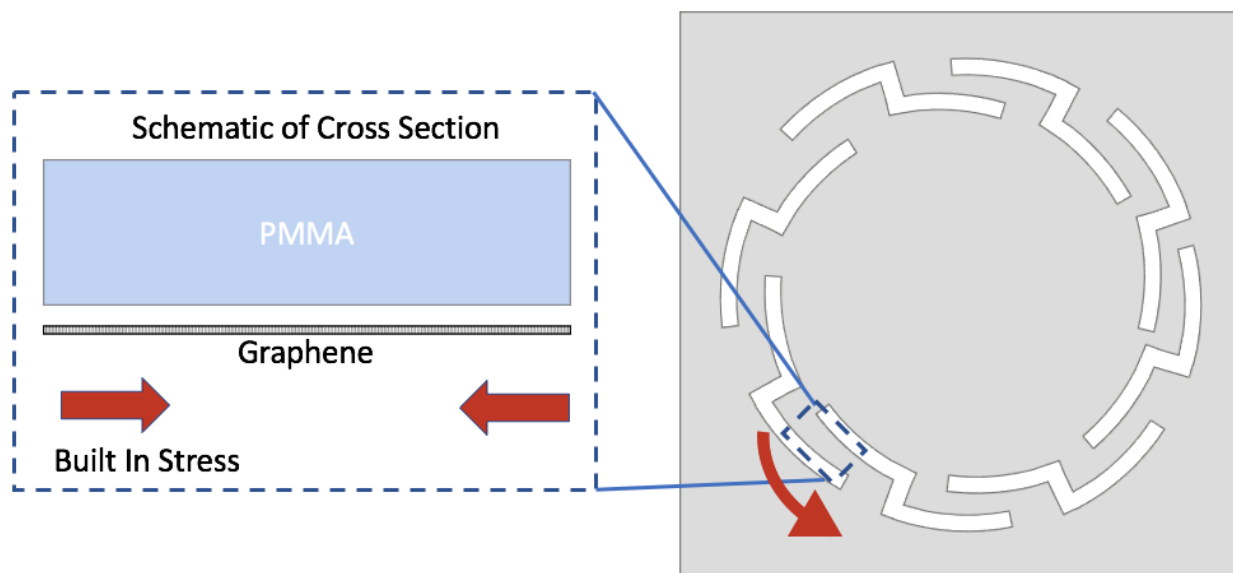
Figure 5.6 Rotational actuator schematic. An illustration of the rotation mechanism of the actuator. (Right) Eight PMMA on graphene flexures support a central membrane. (Left) The much thicker PMMA dominates the structural properties of the stack while the underlying graphene has a built in compressional strain as shown by the two red arrows on the left. When the PMMA is made less rigid by electron beam exposure, compression of the flexures result in rotation as shown by the red arrow on the right. Figure reprinted from our previously published work in Reference [211].
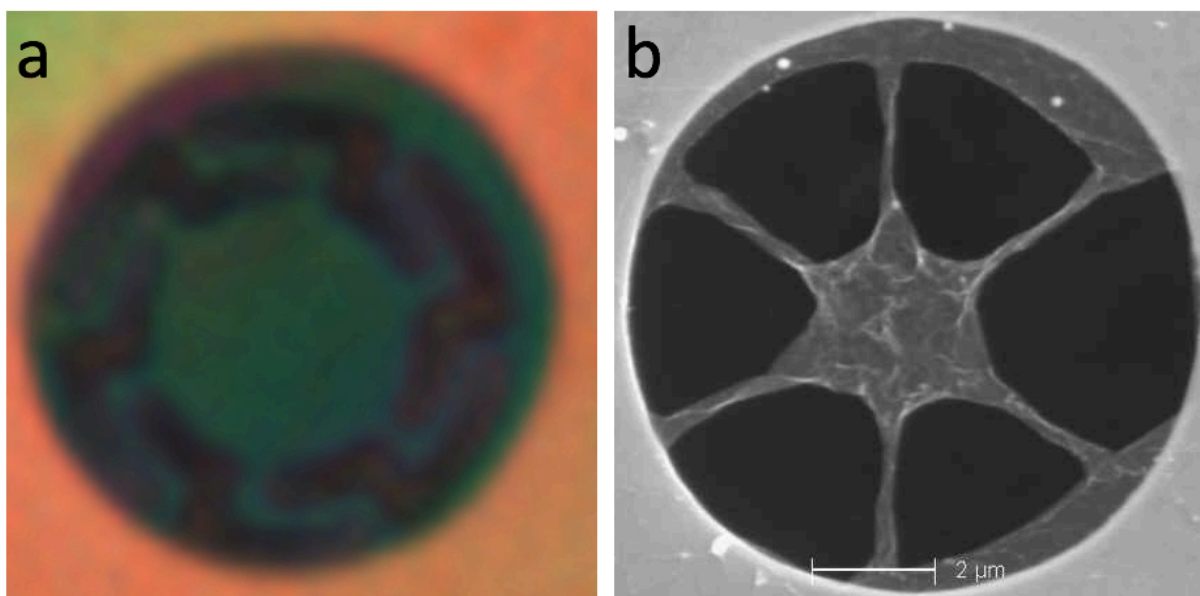
Figure 5.7 The effect of removing the PMMA from the PMMA on graphene stack. (a) An optical image of a patterned PMMA on graphene stack. (b) An SEM image of the relaxed graphene after the PMMA is removed. The hole is 10 μm in diameter in each image. Figure reprinted from our previously published work in Reference [211].

114

References:

1. Pakdel, A., Zhi, C., Bando, Y. & Golberg, D. Low-dimensional boron nitride nanomaterials. *Mater. Today* **15,** 256–265 (2012).

2. Hebard, A. F. *et al.* Superconductivity at 18 K in potassium-doped C60. *Nature* **350,** 600–601 (1991).

3. Ishigami, M., Sau, J. D., Aloni, S., Cohen, M. L. & Zettl, A. Observation of the Giant Stark Effect in Boron-Nitride Nanotubes. *Phys. Rev. Lett.* **94,** 56804 (2005).

4. Park, C.-H. & Louie, S. G. Energy Gaps and Stark Effect in Boron Nitride Nanoribbons. *Nano Lett.* **8,** 2200–2203 (2008).

5. Novoselov, K. S. *et al.* Electric field effect in atomically thin carbon films. *Science* **306,** 666–9 (2004).

6. Anderson, P. Hall effect in the two-dimensional Luttinger liquid. *Phys. Rev. Lett.* **67,** 2092–2094 (1991).

7. Geim, A. K. Graphene: status and prospects. *Science* **324,** 1530–4 (2009).

8. Kroto, H. W., Heath, J. R., O'Brien, S. C., Curl, R. F. & Smalley, R. E. C60: Buckminsterfullerene. *Nature* **318,** 162–163 (1985).

9. Iijima, S. Helical microtubules of graphitic carbon. *Nature* **354,** 56–58 (1991).

10. Mermin, N. D. Crystalline Order in Two Dimensions. *Phys. Rev.* **176,** 250–254 (1968).

11. Fasolino, A., Los, J. H. & Katsnelson, M. I. Intrinsic ripples in graphene. *Nat. Mater.* **6,** 858–861 (2007).

12. Novoselov, K. S. *et al.* Two-dimensional atomic crystals. *Proc. Natl. Acad. Sci. U. S. A.* **102,** 10451–3 (2005).

13. Meyer, J. C. *et al.* The structure of suspended graphene sheets. *Nature* **446,** 60–63 (2007).

14. Wang, Y. *et al.* Observing atomic collapse resonances in artificial nuclei on graphene. *Science* **340,** 734–7 (2013).

15. Son, Y.-W., Cohen, M. L. & Louie, S. G. Energy Gaps in Graphene Nanoribbons. *Phys. Rev. Lett.* **97,** 216803 (2006).

16. Bai, J., Zhong, X., Jiang, S., Huang, Y. & Duan, X. Graphene nanomesh. *Nat. Nanotechnol.* **5,** 190–194 (2010).

17. Jessen, B. S. *et al.* Lithographic band structure engineering of graphene. *Nat. Nanotechnol.* **14,** 340–346 (2019).

18. Geim, A. K. & Grigorieva, I. V. Van der Waals heterostructures. *Nature* **499,** 419–425 (2013).

19. Liu, Y. *et al.* Van der Waals heterostructures and devices. *Nat. Rev. Mater.* **1,** 16042 (2016).

20. Solís-Fernández, P., Bissett, M. & Ago, H. Synthesis, structure and applications of graphene-based 2D heterostructures. *Chem. Soc. Rev.* **46,** 4572–4613 (2017).

21. Butler, S. Z. *et al.* Progress, Challenges, and Opportunities in Two-Dimensional Materials Beyond Graphene. *ACS Nano* **7,** 2898–2926 (2013).

22. Gupta, A., Sakthivel, T. & Seal, S. Recent development in 2D materials beyond graphene. *Prog. Mater. Sci.* **73,** 44–126 (2015).

23. Katsnelson, M. I., Novoselov, K. S. & Geim, A. K. Chiral tunnelling and the Klein paradox in graphene. *Nat. Phys.* **2,** 620–625 (2006).

24. Bolotin, K. I. *et al.* Ultrahigh electron mobility in suspended graphene. *Solid State Commun.* **146,** 351–355 (2008).

25. Lee, C., Wei, X., Kysar, J. W. & Hone, J. Measurement of the elastic properties and intrinsic strength of monolayer graphene. *Science* **321,** 385–8 (2008).

26. Georgakilas, V. *et al.* Functionalization of Graphene: Covalent and Non-Covalent Approaches, Derivatives and Applications. *Chem. Rev.* **112,** 6156–6214 (2012).

27. Pacilé, D., Meyer, J. C., Girit, Ç. Ö. & Zettl, A. The two-dimensional phase of boron nitride: Few-atomic-layer sheets and suspended membranes. *Appl. Phys. Lett.* **92,** 133107 (2008).

28. Watanabe, K., Taniguchi, T. & Kanda, H. Direct-bandgap properties and evidence for ultraviolet lasing of hexagonal boron nitride single crystal. *Nat. Mater.* **3,** 404–409 (2004).

29. Bhimanapati, G. R., Glavin, N. R. & Robinson, J. A. 2D Boron Nitride: Synthesis and Applications. *Semicond. Semimetals* **95,** 101–147 (2016).

30. Gilbert, S. M. *et al.* Alternative Stacking Sequences in Hexagonal Boron Nitride. (2018).

31. Handschin, C. *et al.* Point contacts in encapsulated graphene. *Appl. Phys. Lett.* **107,** 183108 (2015).

32. Dean, C. R. *et al.* Boron nitride substrates for high-quality graphene electronics. *Nat. Nanotechnol.* **5,** 722–726 (2010).

33. Eichler, J. & Lesniak, C. Boron nitride (BN) and BN composites for high-temperature applications. *J. Eur. Ceram. Soc.* **28,** 1105–1109 (2008).

34. Weng, Q., Wang, X., Wang, X., Bando, Y. & Golberg, D. Functionalized hexagonal boron nitride nanomaterials: emerging properties and applications. *Chem. Soc. Rev.* **45,** 3989–4012 (2016).

35. Garcia, A. G. F. *et al.* Effective Cleaning of Hexagonal Boron Nitride for Graphene Devices. *Nano Lett.* **12,** 4449–4454 (2012).

36. Zhou, Z. *et al.* DNA Translocation through Hydrophilic Nanopore in Hexagonal Boron Nitride. **3,** 13770–13773 (2013).

37. Mak, K. F., Lee, C., Hone, J., Shan, J. & Heinz, T. F. Atomically Thin MoS_2: A New Direct-Gap Semiconductor. *Phys. Rev. Lett.* **105,** 136805 (2010).

38. Radisavljevic, B., Radenovic, A., Brivio, J., Giacometti, V. & Kis, A. Single-layer MoS2 transistors. *Nat. Nanotechnol.* **6,** 147–150 (2011).

116

39. Desai, S. B. *et al.* MoS2 transistors with 1-nanometer gate lengths. *Science* **354,** 99–102 (2016).

40. Manzeli, S., Ovchinnikov, D., Pasquier, D., Yazyev, O. V. & Kis, A. 2D transition metal dichalcogenides. *Nat. Rev. Mater.* **2,** 17033 (2017).

41. Gilbert, S. M. *et al.* Alternative stacking sequences in hexagonal boron nitride. *2D Mater.* (2019). doi:10.1088/2053-1583/ab0e24

42. Gilbert, S. M. *et al.* Fabrication of Subnanometer-Precision Nanopores in Hexagonal Boron Nitride. *Sci. Rep.* **7,** 15096 (2017).

43. Ayari, A., Cobas, E., Ogundadegbe, O. & Fuhrer, M. S. Realization and electrical characterization of ultrathin crystals of layered transition-metal dichalcogenides. *J. Appl. Phys.* **101,** 14507 (2007).

44. Watanabe, K., Taniguchi, T. & Kanda, H. Direct-bandgap properties and evidence for ultraviolet lasing of hexagonal boron nitride single crystal. *Nat. Mater.* **3,** 404–409 (2004).

45. Edelberg, D. *et al.* Approaching the Intrinsic Limit in Transition Metal Diselenides via Point Defect Control. *Nano Lett.* **19,** 4371–4379 (2019).

46. Edelberg, D. *et al.* Hundredfold Enhancement of Light Emission via Defect Control in Monolayer Transition-Metal Dichalcogenides. (2018).

47. Anzai, Y. *et al.* Broad range thickness identification of hexagonal boron nitride by colors. *Appl. Phys. Express* **12,** 55007 (2019).

48. S. Roddaro, *, P. Pingue, V. Piazza, V. Pellegrini, and & Beltram, F. The Optical Visibility of Graphene: Interference Colors of Ultrathin Graphite on SiO2. (2007). doi:10.1021/NL071158L

49. Golla, D. *et al.* Optical thickness determination of hexagonal boron nitride flakes. *Appl. Phys. Lett.* **102,** 161906 (2013).

50. Li, H. *et al.* Optical Identification of Single- and Few-Layer MoS2 Sheets. *Small* **8,** 682–686 (2012).

51. Li, X. *et al.* Large-area synthesis of high-quality and uniform graphene films on copper foils. *Science* **324,** 1312–4 (2009).

52. Kim, K. K. *et al.* Synthesis of Monolayer Hexagonal Boron Nitride on Cu Foil Using Chemical Vapor Deposition. *Nano Lett.* **12,** 161–166 (2012).

53. Song, L. *et al.* Large Scale Growth and Characterization of Atomic Hexagonal Boron Nitride Layers. *Nano Lett.* **10,** 3209–3215 (2010).

54. Lee, Y.-H. *et al.* Synthesis of Large-Area MoS$_2$ Atomic Layers with Chemical Vapor Deposition. *Adv. Mater.* **24,** 2320–2325 (2012).

55. Zhan, Y., Liu, Z., Najmaei, S., Ajayan, P. M. & Lou, J. Large-Area Vapor-Phase Growth and Characterization of MoS$_2$ Atomic Layers on a SiO$_2$ Substrate. *Small* **8,** 966–971 (2012).

56. Zhou, J. *et al.* A library of atomically thin metal chalcogenides. *Nature* **556,** 355–359 (2018).

57. Bae, S. *et al.* Roll-to-roll production of 30-inch graphene films for transparent electrodes. *Nat. Nanotechnol.* **5,** 574–578 (2010).

58. Kobayashi, T. *et al.* Production of a 100-m-long high-quality graphene transparent conductive film by roll-to-roll chemical vapor deposition and transfer process. *Appl. Phys. Lett.* **102,** 23112 (2013).

59. Brown, L. *et al.* Polycrystalline Graphene with Single Crystalline Electronic Structure. *Nano Lett.* **14,** 5706–5711 (2014).

60. Hao, Y. *et al.* The Role of Surface Oxygen in the. *Science (80-.).* **342,** 720–723 (2013).

61. Liu, Z. *et al.* In-plane heterostructures of graphene and hexagonal boron nitride with controlled domain sizes. *Nat. Nanotechnol.* **8,** 119–124 (2013).

62. Gong, Y. *et al.* Vertical and in-plane heterostructures from WS2/MoS2 monolayers. *Nat. Mater.* **13,** 1135–1142 (2014).

63. Liu, Z. *et al.* Direct Growth of Graphene/Hexagonal Boron Nitride Stacked Layers. *Nano Lett.* **11,** 2032–2037 (2011).

64. Zhang, C. *et al.* Direct growth of large-area graphene and boron nitride heterostructures by a co-segregation method. *Nat. Commun.* **6,** 6519 (2015).

65. Levendorf, M. P. *et al.* Graphene and boron nitride lateral heterostructures for atomically thin circuitry. *Nature* **488,** 627–632 (2012).

66. Wang, L. *et al.* Growth and Etching of Monolayer Hexagonal Boron Nitride. *Adv. Mater.* **27,** 4858–4864 (2015).

67. Lu, G. *et al.* Synthesis of large single-crystal hexagonal boron nitride grains on Cu-Ni alloy. *Nat. Commun.* **6,** (2015).

68. Chen, X., Zhang, L. & Chen, S. Large area CVD growth of graphene. *Synth. Met.* **210,** 95–108 (2015).

69. Fang, W., Hsu, A. L., Song, Y. & Kong, J. A review of large-area bilayer graphene synthesis by chemical vapor deposition. *Nanoscale* **7,** 20335–20351 (2015).

70. Li, Q. *et al.* Growth of Adlayer Graphene on Cu Studied by Carbon Isotope Labeling. *Nano Lett* **13,** 41 (2013).

71. Alem, N. *et al.* Atomically thin hexagonal boron nitride probed by ultrahigh-resolution transmission electron microscopy. *Phys. Rev. B* **80,** 155425 (2009).

72. Bernal, J. D. The Structure of Graphite. *Proc. R. Soc. A Math. Phys. Eng. Sci.* **106,** 749–773 (1924).

73. Warner, J. H., Rümmeli, M. H., Bachmatiuk, A. & Büchner, B. Atomic Resolution Imaging and Topography of Boron Nitride Sheets Produced by Chemical Exfoliation. *ACS Nano* **4,** 1299–1304 (2010).

74. Paine, R. T. & Narula, C. K. Synthetic routes to boron nitride. *Chem. Rev.* **90,** 73–91 (1990).

75. PEASE, R. S. Crystal Structure of Boron Nitride. *Nature* **165,** 722–723 (1950).

76. Ooi, N., Rairkar, A., Lindsley, L. & Adams, J. B. Electronic structure and bonding in hexagonal boron nitride. *J. Phys. Condens. Matter* **18,** 97–115 (2006).

77. Liu, L., Feng, Y. P. & Shen, Z. X. Structural and electronic properties of *h* -BN. *Phys. Rev. B* **68,** 104102 (2003).

78. Hu, M. L., Yin, J. L., Zhang, C. X., Yu, Z. & Sun, L. Z. Electronic structures and optical properties of hexagonal boron nitride under hydrostatic pressures. *J. Appl. Phys.* **109,** 73708 (2011).

79. Constantinescu, G., Kuc, A. & Heine, T. Stacking in Bulk and Bilayer Hexagonal Boron Nitride. *Phys. Rev. Lett.* **111,** 36104 (2013).

80. Ribeiro, R. M. & Peres, N. M. R. Stability of boron nitride bilayers: Ground-state energies, interlayer distances, and tight-binding description. *Phys. Rev. B* **83,** 235312 (2011).

81. Fujimoto, Y. & Saito, S. Band engineering and relative stabilities of hexagonal boron nitride bilayers under biaxial strain. *Phys. Rev. B* **94,** 245427 (2016).

82. Marom, N. *et al.* Stacking and Registry Effects in Layered Materials: The Case of Hexagonal Boron Nitride. *Phys. Rev. Lett.* **105,** 46801 (2010).

83. Hu, M. L., Yu, Z., Yin, J. L., Zhang, C. X. & Sun, L. Z. A DFT-LDA study of electronic and optical properties of hexagonal boron nitride under uniaxial strain. *Comput. Mater. Sci.* **54,** 165–169 (2012).

84. Baroni, S., de Gironcoli, S., Dal Corso, A. & Giannozzi, P. Phonons and related crystal properties from density-functional perturbation theory. *Rev. Mod. Phys.* **73,** 515–562 (2001).

85. Wu, X., Vanderbilt, D. & Hamann, D. R. Systematic treatment of displacements, strains, and electric fields in density-functional perturbation theory. *Phys. Rev. B* **72,** 35105 (2005).

86. Laturia, A., Van de Put, M. L. & Vandenberghe, W. G. Dielectric properties of hexagonal boron nitride and transition metal dichalcogenides: from monolayer to bulk. *npj 2D Mater. Appl.* **2,** 6 (2018).

87. Haubner, R., Wilhelm, M., Weissenbacher, R. & Lux, B. in 1–45 (Springer, Berlin, Heidelberg, 2002). doi:10.1007/3-540-45623-6_1

88. Balmain, W. H. Bemerkungen über die Bildung von Verbindungen des Bors und Siliciums mit Stickstoff und gewissen Metallen. *J. für Prakt. Chemie* **27,** 422–430 (1842).

89. Zhai, X. & Jin, G. Asymmetric bandgaps and Landau levels in a Bernal-stacked hexagonal boron-nitride bilayer. *J. Phys. Condens. Matter* **26,** 15304 (2014).

90. Kim, C.-J. *et al.* Stacking Order Dependent Second Harmonic Generation and Topological Defects in *h* -BN Bilayers. *Nano Lett.* **13,** 5660–5665 (2013).

91. Aggoune, W. *et al.* Dimensionality of excitons in stacked van der Waals materials: The example of hexagonal boron nitride. *Phys. Rev. B* **97,** 241114 (2018).

92. Ji, Y. *et al.* Chemical Vapor Deposition Growth of Large Single-Crystal Mono-, Bi-, Tri-Layer Hexagonal Boron Nitride and Their Interlayer Stacking. *ACS Nano* **11,** 12057–

12066 (2017).

93. Warner, J. H., Rümmeli, M. H., Bachmatiuk, A. & Büchner, B. Atomic Resolution Imaging and Topography of Boron Nitride Sheets Produced by Chemical Exfoliation. *ACS Nano* **4,** 1299–1304 (2010).

94. Khan, M. H. *et al.* Carbon- and crack-free growth of hexagonal boron nitride nanosheets and their uncommon stacking order. *Nanoscale* **8,** 15926–15933 (2016).

95. Gilbert, S. M. M., Liu, S., Schumm, G. & Zettl, A. *Nanopatterning Hexagonal Boron Nitride with Helium Ion Milling: Towards Atomically-Thin, Nanostructured Insulators*. *MRS Advances* **3,** 327–331 (Materials Research Society, 2018).

96. Ji, Y. *et al.* Chemical Vapor Deposition Growth of Large Single-Crystal Mono-, Bi-, Tri-Layer Hexagonal Boron Nitride and Their Interlayer Stacking. *ACS Nano* **11,** 12057–12066 (2017).

97. Liu, K. *et al.* Evolution of interlayer coupling in twisted molybdenum disulfide bilayers. *Nat. Commun.* **5,** 4966 (2014).

98. Shevitski, B. *et al.* Dark-field transmission electron microscopy and the Debye-Waller factor of graphene. *Phys. Rev. B* **87,** 45417 (2013).

99. Ping, J. & Fuhrer, M. S. Layer Number and Stacking Sequence Imaging of Few-Layer Graphene by Transmission Electron Microscopy. *Nano Lett* **12,** 26 (2012).

100. Pham, T. *et al.* Nanoscale structure and superhydrophobicity of sp^2-bonded boron nitride aerogels. *Nanoscale* **7,** 10449–10458 (2015).

101. Horn, F. H. Some Electrical and Optical Properties of Simple Rhombohedral Boron. *J. Appl. Phys.* **30,** 1611–1612 (1959).

102. Pham, T. *et al.* Formation and Dynamics of Electron-Irradiation-Induced Defects in Hexagonal Boron Nitride at Elevated Temperatures. *Nano Lett.* **16,** 7142–7147 (2016).

103. Alem, N. *et al.* Vacancy growth and migration dynamics in atomically thin hexagonal boron nitride under electron beam irradiation. *Phys. status solidi - Rapid Res. Lett.* **5,** 295–297 (2011).

104. Kotakoski, J., Jin, C. H., Lehtinen, O., Suenaga, K. & Krasheninnikov, A. V. Electron knock-on damage in hexagonal boron nitride monolayers. *Phys. Rev. B* **82,** 113404 (2010).

105. Jin, C., Lin, F., Suenaga, K. & Iijima, S. Fabrication of a Freestanding Boron Nitride Single Layer and Its Defect Assignments. *Phys. Rev. Lett.* **102,** 195505 (2009).

106. Sutter, P., Lahiri, J., Albrecht, P. & Sutter, E. Chemical Vapor Deposition and Etching of High-Quality Monolayer Hexagonal Boron Nitride Films. *ACS Nano* **5,** 7303–7309 (2011).

107. Kidambi, P. R. *et al.* In Situ Observations during Chemical Vapor Deposition of Hexagonal Boron Nitride on Polycrystalline Copper. *Chem. Mater.* **26,** 6380–6392 (2014).

108. Nie, S. *et al.* Growth from below: bilayer graphene on copper by chemical vapor deposition. *New J. Phys.* **14,** 93028 (2012).

109. Yang, Y. *et al.* Creating a Nanospace under an h-BN Cover for Adlayer Growth on Nickel(111). *ACS Nano* **9,** 11589–11598 (2015).

110. Zhao, R., Zhao, X., Liu, Z., Ding, F. & Liu, Z. Controlling the orientations of h-BN during growth on transition metals by chemical vapor deposition. *Nanoscale* **9,** 3561–3567 (2017).

111. Gibb, A., Alem, N. & Zettl, A. Low pressure chemical vapor deposition synthesis of hexagonal boron nitride on polycrystalline metal foils. *Phys. status solidi* **250,** 2727–2731 (2013).

112. Hemmi, A. *et al.* High quality single atomic layer deposition of hexagonal boron nitride on single crystalline Rh(111) four-inch wafers. *Rev. Sci. Instrum.* **85,** 35101 (2014).

113. Schulz, F. *et al.* Epitaxial hexagonal boron nitride on Ir(111): A work function template. *Phys. Rev. B* **89,** 235429 (2014).

114. Zhao, R., Zhao, X., Liu, Z., Ding, F. & Liu, Z. Controlling the orientations of h-BN during growth on transition metals by chemical vapor deposition. *Nanoscale* **9,** 3561–3567 (2017).

115. Göhring, H., Fabrichnaya, O., Leineweber, A. & Mittemeijer, E. J. Thermodynamics of the Fe-N and Fe-N-C Systems: The Fe-N and Fe-N-C Phase Diagrams Revisited. *Metall. Mater. Trans. A* **47,** 6173–6186 (2016).

116. Do, T. *et al.* Improving Structural Integrity with Boron-based Additives for 3D Printed 420 Stainless Steel. *Procedia Manuf.* **1,** 263–272 (2015).

117. Lin, Z. *et al.* 2D materials advances: from large scale synthesis and controlled heterostructures to improved characterization techniques, defects and applications. *2D Mater.* **3,** 42001 (2016).

118. Wang, J., Ma, F. & Sun, M. Graphene, hexagonal boron nitride, and their heterostructures: properties and applications. *RSC Adv.* **7,** 16801–16822 (2017).

119. Gannett, W. *et al.* Boron nitride substrates for high mobility chemical vapor deposited graphene. *Appl. Phys. Lett.* **98,** 242105 (2011).

120. Gao, L. *et al.* Repeated growth and bubbling transfer of graphene with millimetre-size single-crystal grains using platinum. *Nat. Commun.* **3,** 699 (2012).

121. Regan, W. *et al.* A direct transfer of layer-area graphene. *Appl. Phys. Lett.* **96,** 113102 (2010).

122. Pizzocchero, F. *et al.* The hot pick-up technique for batch assembly of van der Waals heterostructures. *Nat. Commun.* **7,** 11894 (2016).

123. Toyoda, S., Uwanno, T., Taniguchi, T., Watanabe, K. & Nagashio, K. Pinpoint pick-up and bubble-free assembly of 2D materials using PDMS/PMMA polymers with lens shapes. *Appl. Phys. Express* **12,** 55008 (2019).

124. Castellanos-Gomez, A. *et al.* Deterministic transfer of two-dimensional materials by all-dry viscoelastic stamping. *2D Mater.* **1,** 11002 (2014).

125. Koenig, S. P., Boddeti, N. G., Dunn, M. L. & Bunch, J. S. Ultrastrong adhesion of graphene membranes. *Nat. Nanotechnol.* **6,** 543–546 (2011).

126. Bunch, J. S. *et al.* Impermeable Atomic Membranes from Graphene Sheets. *Nano Lett.* **8,** 2458–2462 (2008).

127. Boddeti, N. G. *et al.* Graphene Blisters with Switchable Shapes Controlled by Pressure and Adhesion. *Nano Lett.* **13,** 6216–6221 (2013).

128. Yuk, J. M. *et al.* High-resolution EM of colloidal nanocrystal growth using graphene liquid cells. *Science (80-.).* **335,** 61–64 (2012).

129. Steinhauser, Georg, Buchtela, K. in *Handbook of Radioactivity Analysis (Third Edition)* (2012).

130. Iberi, V. *et al.* Nanoforging Single Layer MoSe2 Through Defect Engineering with Focused Helium Ion Beams. *Sci. Rep.* **6,** 30481 (2016).

131. Chen, J.-H. *et al.* Controlled growth of a line defect in graphene and implications for gate-tunable valley filtering. *Phys. Rev. B* **89,** 121407 (2014).

132. Alem, N. *et al.* Subangstrom Edge Relaxations Probed by Electron Microscopy in Hexagonal Boron Nitride. *Phys. Rev. Lett.* **109,** 205502 (2012).

133. Halbertal, D. *et al.* Imaging resonant dissipation from individual atomic defects in graphene. *Science* **358,** 1303–1306 (2017).

134. Tran, T. T., Bray, K., Ford, M. J., Toth, M. & Aharonovich, I. Quantum Emission From Hexagonal Boron Nitride Monolayers. *arXiv* **11,** (2015).

135. Rasool, H. I., Ophus, C. & Zettl, A. Atomic Defects in Two Dimensional Materials. *Adv. Mater.* **27,** 5771–5777 (2015).

136. Girit, Ç. Ö. *et al.* Graphene at the Edge: Stability and Dynamics. *Science (80-.).* **323,** (2009).

137. Robertson, A. W. *et al.* Atomic Structure of Graphene Subnanometer Pores. (2015). doi:10.1021/ACSNANO.5B05700

138. Meyer, J. C., Chuvilin, A., Algara-Siller, G., Biskupek, J. & Kaiser, U. Selective Sputtering and Atomic Resolution Imaging of Atomically Thin Boron Nitride Membranes. *Nano Lett.* **9,** 2683–2689 (2009).

139. Gibb, A. L. *et al.* Atomic Resolution Imaging of Grain Boundary Defects in Monolayer Chemical Vapor Deposition-Grown Hexagonal Boron Nitride. *J. Am. Chem. Soc.* **135,** 6758–6761 (2013).

140. Venkatesan, B. M. & Bashir, R. Nanopore sensors for nucleic acid analysis. *Nat. Nanotechnol.* **6,** 615–624 (2011).

141. Heerema, S. J. & Dekker, C. Graphene nanodevices for DNA sequencing. *Nat. Nanotechnol.* **11,** 127–136 (2016).

142. Dekker, C. Solid-state nanopores. *Nat. Nanotechnol.* **2,** 209–215 (2007).

143. Deamer, D., Akeson, M. & Branton, D. Three decades of nanopore sequencing. *Nat. Biotechnol.* **34,** 518–524 (2016).

144. Kowalczyk, S. W. *et al.* Modeling the conductance and DNA blockade of solid-state nanopores. *Nanotechnology* **22,** 315101 (2011).

145. Haynes, T. *et al.* Electric-Field-Driven Translocation of ssDNA through Hydrophobic Nanopores. *ACS Nano* **12,** 8208–8213 (2018).

146. Garaj, S., Liu, S., Golovchenko, J. A. & Branton, D. Molecule-hugging graphene nanopores. *Proc. Natl. Acad. Sci.* **110,** 12192–12196 (2013).

147. Merchant, C. A. *et al.* DNA Translocation through Graphene Nanopores. (2010). doi:10.1021/NL101046T

148. Schneider, G. F. *et al.* DNA Translocation through Graphene Nanopores. (2010). doi:10.1021/NL102069Z

149. Acosta, V. & Hemmer, P. Nitrogen-vacancy centers: Physics and applications. *MRS Bull.* **38,** 127–130 (2013).

150. Wang, J. *et al. Coherence times of precisely depth controlled NV centers in diamond.* (2015).

151. Tran, T. T., Bray, K., Ford, M. J., Toth, M. & Aharonovich, I. Quantum emission from hexagonal boron nitride monolayers. *Nat. Nanotechnol.* **11,** 37–41 (2015).

152. Koenig, S. P., Wang, L., Pellegrino, J. & Bunch, J. S. Selective molecular sieving through porous graphene. *Nat. Nanotechnol.* **7,** 728–732 (2012).

153. Hu, S. *et al.* Proton transport through one-atom-thick crystals. *Nature* **516,** (2014).

154. Zhao, J. *et al.* Etching gas-sieving nanopores in single-layer graphene with an angstrom precision for high-performance gas mixture separation. *Sci. Adv.* **5,** eaav1851 (2019).

155. Kidambi, P. R. *et al.* A Scalable Route to Nanoporous Large-Area Atomically Thin Graphene Membranes by Roll-to-Roll Chemical Vapor Deposition and Polymer Support Casting. *ACS Appl. Mater. Interfaces* **10,** 10369–10378 (2018).

156. Cohen-Tanugi, D. & Grossman, J. C. Water Desalination across Nanoporous Graphene. *Nano Lett.* **12,** 3602–3608 (2012).

157. Surwade, S. P. *et al.* Water desalination using nanoporous single-layer graphene. *Nat. Nanotechnol.* **10,** 459–464 (2015).

158. Heiranian, M., Farimani, A. B., Aluru, N. R., Lee, R. & Agre, P. Water desalination with a single-layer MoS2 nanopore. *Nat. Commun.* **6,** 8616 (2015).

159. O'Hern, S. C. *et al.* Selective ionic transport through tunable subnanometer pores in single-layer graphene membranes. *Nano Lett.* **14,** (2014).

160. Wang, L. *et al.* Molecular valves for controlling gas phase transport made from discrete ångström-sized pores in graphene. *Nat. Nanotechnol.* **10,** 785–790 (2015).

161. Kidambi, P. R. *et al.* Nanoporous Atomically Thin Graphene Membranes for Desalting and Dialysis Applications. *Adv. Mater.* **29,** 1700277 (2017).

162. Emmrich, D. *et al.* Nanopore fabrication and characterization by helium ion microscopy. *Appl. Phys. Lett.* **108,** 163103 (2016).

163. Warner, J. H., Rümmeli, M. H., Bachmatiuk, A. & Büchner, B. Atomic Resolution Imaging and Topography of Boron Nitride Sheets Produced by Chemical Exfoliation. *ACS Nano* **4,** 1299–1304 (2010).

164. Ryu, G. H. *et al.* Atomic-scale dynamics of triangular hole growth in monolayer hexagonal boron nitride under electron irradiation. *Nanoscale* **7,** 10600–5 (2015).

165. Hopkinson, D. G. *et al.* Formation and Healing of Defects in Atomically Thin GaSe and InSe. *ACS Nano* **13,** 5112–5123 (2019).

166. Zobelli, A., Gloter, A., Ewels, C. P., Seifert, G. & Colliex, C. Electron knock-on cross section of carbon and boron nitride nanotubes. *Phys. Rev. B* **75,** 245402 (2007).

167. Kotakoski, J., Jin, C. H., Lehtinen, O., Suenaga, K. & Krasheninnikov, A. V. Electron knock-on damage in hexagonal boron nitride monolayers. doi:10.1103/PhysRevB.82.113404

168. Choi, S. *et al.* Engineering and Localization of Quantum Emitters in Large Hexagonal Boron Nitride Layers. *ACS Appl. Mater. Interfaces* **8,** 29642–29648 (2016).

169. Chen, X. *et al.* High-quality sandwiched black phosphorus heterostructure and its quantum oscillations. *Nat. Commun.* **6,** 7315 (2015).

170. Lee, G.-H. *et al.* Highly Stable, Dual-Gated MoS $_2$ Transistors Encapsulated by Hexagonal Boron Nitride with Gate-Controllable Contact, Resistance, and Threshold Voltage. *ACS Nano* **9,** 7019–7026 (2015).

171. Nanda, G., Goswami, S., Watanabe, K., Taniguchi, T. & Alkemade, P. F. A. Defect Control and *n* -Doping of Encapsulated Graphene by Helium-Ion-Beam Irradiation. *Nano Lett.* **15,** 4006–4012 (2015).

172. Tsen, A. W. *et al.* Nature of the quantum metal in a two-dimensional crystalline superconductor. *Nat. Phys.* **12,** 208–212 (2016).

173. Cao, Y. *et al.* Unconventional superconductivity in magic-angle graphene superlattices. *Nature* **556,** 43–50 (2018).

174. Raja, A. *et al.* Coulomb engineering of the bandgap and excitons in two-dimensional materials. *Nat. Commun.* **8,** 15251 (2017).

175. Utama, M. I. B. *et al.* A dielectric-defined lateral heterojunction in a monolayer semiconductor. *Nat. Electron.* **2,** 60–65 (2019).

176. Forsythe, C. *et al.* Band structure engineering of 2D materials using patterned dielectric superlattices. *Nat. Nanotechnol.* **13,** 566–571 (2018).

177. Pham, T. *et al.* Formation and Dynamics of Electron-Irradiation-Induced Defects in Hexagonal Boron Nitride at Elevated Temperatures. *Nano Lett.* **16,** (2016).

178. Kim, K. *et al.* Atomically perfect torn graphene edges and their reversible reconstruction. *Nat. Commun.* **4,** 2723 (2013).

179. Liu, S. *et al.* Boron Nitride Nanopores: Highly Sensitive DNA Single-Molecule Detectors. *Adv. Mater.* **25,** 4549–4554 (2013).

180. Cretu, O., Lin, Y.-C. & Suenaga, K. Inelastic electron irradiation damage in hexagonal boron nitride. *Micron* **72,** 21–27 (2015).

181. Nam, S. *et al.* Graphene Nanopore with a Self-Integrated Optical Antenna. *Nano Lett.* **14,** 5584–5589 (2014).

182. Cretu, O. *et al.* Structure and Local Chemical Properties of Boron-Terminated Tetravacancies in Hexagonal Boron Nitride. *Phys. Rev. Lett.* **114,** 75502 (2015).

183. Bellunato, A. *et al.* Chemistry at the Edge of Graphene. *ChemPhysChem* **17,** 785–801 (2016).

184. Lv, W., Chen, M. & Wu, R. The impact of the number of layers of a graphene nanopore on DNA translocation. *Soft Matter* **9,** 960–966 (2013).

185. Wang, L. *et al.* One-dimensional electrical contact to a two-dimensional material. *Science* **342,** 614–7 (2013).

186. Sinitskii, A. *et al.* High-Yield Synthesis of Boron Nitride Nanoribbons *via* Longitudinal Splitting of Boron Nitride Nanotubes by Potassium Vapor. *ACS Nano* **8,** 9867–9873 (2014).

187. Erickson, K. J. *et al.* Longitudinal Splitting of Boron Nitride Nanotubes for the Facile Synthesis of High Quality Boron Nitride Nanoribbons. *Nano Lett.* **11,** 3221–3226 (2011).

188. Han, M. Y., Özyilmaz, B., Zhang, Y. & Kim, P. Energy Band-Gap Engineering of Graphene Nanoribbons. *Phys. Rev. Lett.* **98,** 206805 (2007).

189. Liu, S. *et al.* Boron Nitride Nanopores: Highly Sensitive DNA Single-Molecule Detectors. *Adv. Mater.* **25,** 4549–4554 (2013).

190. Feng, J. *et al.* Identification of single nucleotides in MoS2 nanopores. *Nat. Nanotechnol.* **10,** 1070 (2015).

191. Fischbein, M. D. & Drndić, M. Electron beam nanosculpting of suspended graphene sheets. *Appl. Phys. Lett.* **93,** 113107 (2008).

192. Deng, Y. *et al.* Precise fabrication of a 5nm graphene nanopore with a helium ion microscope for biomolecule detection. (2016). doi:10.1088/1361-6528/28/4/045302

193. Li, Y., Zhou, Z., Zhang, S. & Chen, Z. MoS ₂ Nanoribbons: High Stability and Unusual Electronic and Magnetic Properties. *J. Am. Chem. Soc.* **130,** 16739–16744 (2008).

194. Chen, S. *et al.* Monolayer MoS ₂ Nanoribbon Transistors Fabricated by Scanning Probe Lithography. *Nano Lett.* **19,** 2092–2098 (2019).

195. Fox, D. *et al.* Helium ion microscopy of graphene: beam damage, image quality and edge contrast. *Nanotechnology* **24,** 335702 (2013).

196. Zhou, Y., Fox, D. S. & Zhang, H. in 245–262 (Springer, Cham, 2016). doi:10.1007/978-3-319-41990-9_11

197. Fox, D., Chen, Y., Faulkner, C. C. & Zhang, H. Nano-structuring, surface and bulk modification with a focused helium ion beam. *Beilstein J. Nanotechnol.* **3,** 579–585 (2012).

198. Schneider, G. F. *et al.* Tailoring the hydrophobicity of graphene for its use as nanopores for DNA translocation. *Nat. Commun.* **4,** 326–328 (2013).

199. Ribeiro-Palau, R. *et al.* Twistable electronics with dynamically rotatable heterostructures. *Science (80-.).* **361,** 690–693 (2018).

200. Park, C.-H., Son, Y.-W., Yang, L., Cohen, M. L. & Louie, S. G. Electron Beam

Supercollimation in Graphene Superlattices. *Nano Lett.* **8,** 2920–2924 (2008).

201. Blees, M. K. *et al.* Graphene kirigami. *Nature* **524,** 204–207 (2015).

202. Kim, K. *et al.* Multiply folded graphene. *Phys. Rev. B* **83,** 245433 (2011).

203. Zhou, Q. & Zettl, A. Electrostatic graphene loudspeaker. *Appl. Phys. Lett.* **102,** 223109 (2013).

204. Zhou, Q., Zheng, J., Onishi, S., Crommie, M. F. & Zettl, A. K. Graphene electrostatic microphone and ultrasonic radio. *Proc. Natl. Acad. Sci. U. S. A.* **112,** 8942–6 (2015).

205. Chen, C. *et al.* Performance of monolayer graphene nanomechanical resonators with electrical readout. *Nat. Nanotechnol.* **4,** 861–867 (2009).

206. Zande, A. M. van der *et al.* Large-Scale Arrays of Single-Layer Graphene Resonators. *Nano Lett.* **10,** 4869–4873 (2010).

207. Barton, R. A. *et al.* High, Size-Dependent Quality Factor in an Array of Graphene Mechanical Resonators. *Nano Lett.* **11,** 1232–1236 (2011).

208. Begtrup, G. E., Gannett, W., Yuzvinsky, T. D., Crespi, V. H. & Zettl, A. Nanoscale Reversible Mass Transport for Archival Memory. *Nano Lett.* **9,** 1835–1838 (2009).

209. Kim, K., Jensen, K. & Zettl, A. Tuning Nanoelectromechanical Resonators with Mass Migration. *Nano Lett.* **9,** 3209–3213 (2009).

210. K. Jensen, J. Weldon, H. Garcia, and & Zettl*, A. Nanotube Radio. (2007). doi:10.1021/NL0721113

211. Gilbert, S. M., Molnar, A., Horton-Bailey, D., Yao, H. Y. & Zettl, A. Strain-controlled Graphene-Polymer Angular Actuator. *MRS Adv.* 1–7 (2019). doi:10.1557/adv.2019.276

212. Cho, S. O. & Jun, H. Y. Surface hardening of poly(methyl methacrylate) by electron irradiation. *Nucl. Instruments Methods Phys. Res. Sect. B Beam Interact. with Mater. Atoms* **237,** 525–532 (2005).

213. Papanu, J. S., Hess, D. W., Soane (Soong), D. S. & Bell, A. T. Swelling of poly(methyl methacrylate) thin films in low molecular weight alcohols. *J. Appl. Polym. Sci.* **39,** 803–823 (1990).

214. Jin, Y., Harrington, D., Rachford, A. A. & Rack, J. J. Stimulating changes in the elastic modulus of polymer materials by molecular photochromism. *RSC Adv.* **4,** 62920–62925 (2014).

215. Abdel-Wahab, A. A., Ataya, S. & Silberschmidt, V. V. Temperature-dependent mechanical behaviour of PMMA: Experimental analysis and modelling. *Polym. Test.* **58,** 86–95 (2017).

216. Changyao Chen & Hone, J. Graphene nanoelectromechanical systems. *Proc. IEEE* **101,** 1766–1779 (2013).

217. Alemán, B. *et al.* Polymer-free, low tension graphene mechanical resonators. *Phys. status solidi - Rapid Res. Lett.* **7,** 1064–1066 (2013).

218. Rasool, H. I., Ophus, C., Klug, W. S., Zettl, A. & Gimzewski, J. K. Measurement of the intrinsic strength of crystalline and polycrystalline graphene. *Nat. Commun.* **4,** 2811

(2013).

219. Zhang, K. & Arroyo, M. Understanding and strain-engineering wrinkle networks in supported graphene through simulations. *J. Mech. Phys. Solids* **72,** 61–74 (2014).

220. Zhu, S.-E., Krishna Ghatkesar, M., Zhang, C. & Janssen, G. C. A. M. Graphene based piezoresistive pressure sensor. *Appl. Phys. Lett.* **102,** 161904 (2013).

221. Smith, A. D. *et al.* Electromechanical Piezoresistive Sensing in Suspended Graphene Membranes. *Nano Lett.* **13,** 3237–3242 (2013).

222. Kumar, M. & Bhaskaran, H. Ultrasensitive Room-Temperature Piezoresistive Transduction in Graphene-Based Nanoelectromechanical Systems. *Nano Lett.* **15,** 2562–2567 (2015).

223. Teshima, T. F. *et al.* Self-Folded Three-Dimensional Graphene with a Tunable Shape and Conductivity. *Nano Lett.* **19,** 461–470 (2019).